BENDING CHARACTERISTICS AND STRETCH BENDABILITY OF MONOLITHIC AND LAMINATED SHEET MATERIALS

Bending Characteristics and Stretch Bendability of Monolithic and Laminated Sheet Materials

By

GANESH N. GOVINDASAMY, M.S.

A Thesis

Submitted to the School of Graduate Studies

in Partial Fulfillment of the Requirements

for the Degree

Doctor of Philosophy

McMaster University

DOCTOR OF PHILOSOPHY (2015) McMaster University

Department of Mechanical Engineering Hamilton, Ontario

TITLE	BENDING CHARACTERISTICS AND STRETCH BENDABILITY OF MONOLITHIC AND LAMINATED SHEET MATERIALS
AUTHOR	Ganesh Govindasamy, M.S. (Indian Institute of Technology Madras, India)
SUPERVISOR	Dr. Mukesh Jain
NUMBER OF PAGES	xxxi; 246

Dedicated to my

Parents, Teachers and Well Wishers.

Abstract

Bending deformation characteristics of monolithic, bi-layer and tri-layer laminate sheet materials are studied using Analytical and FE models in this work. The analytical model, based on advanced theory of pure bending considers von Mises yielding, Ludwik hardening law and Bauschinger effect for various laminate constituent thickness ratios. The principal stresses and strains through the thickness and, change in relative thickness at specified bend curvatures are obtained as a function of increasing curvature during bending. Additionally, 2D and 3D finite element (FE) based models for bending are developed to overcome simplifications of the analytical models such as the effect of specimen width on strain distribution. Further, to experimentally assess and validate bending characteristics from the analytical models, a new experimental bend test-jig that is closer to pure bending is developed. The experimental set-up is an open concept design that allows access to the tensile surface as well as through-thickness region for recording and analyzing strains using an online strain mapping system based on digital image correction (DIC) method. Experimental bending is carried out on annealed AA2024 monolithic aluminum alloy sheet and Steel/Aluminum (SS400/AA1050) bi-layer laminate sheet at different thickness ratios. The model and experiments are studied in terms of stress and strain distribution as a function of relative thickness for different clad to matrix thickness ratios.

Further the case of simultaneous bending and stretching over small radius bending is analyzed for limit strain prediction using an existing limit strain criterion based on major strain acceleration. An angular stretch bend test is used to subject an hour-glass shaped

AA20240-O aluminum sheet specimen to simultaneous stretching and bending deformation while continuously imaging the critical tensile surface region using an optical camera. The strain development in the critical region is subsequently analyzed using digital image correlation (DIC) method. The effect of DIC parameters such as facet size, facet step, and effect of curve fitting procedures on limit strain are studied. An average limit strain of 0.2 is obtained for AA2024 for a facet size of 9x9 pixels, a facet step of 5 pixels and by applying a 5th order polynomial curve fit to the strain data. The results obtained are comparable with a limit strain of the material. The results are compared with a commercially available tri-layer laminate sheet material Alclad 2024 that has 80 μm thin layer of soft AA1100 on both surfaces of harder AA2024 core material. An improved stretch bendability limit strain of 0.24 for Alclad 2024 tri-layer specimen was predicted by utilizing the major strain acceleration criterion. The thin AA1100 protective layer produced a positive effect on the stretch bendability of Alclad 2024 when compared with monolithic AA2024 specimen.

Acknowledgements

After completing the thesis, I look behind with gratitude, the efforts and concern of the people who helped me through this journey. First and foremost I would like to thank my supervisor Dr. Mukesh Jain for his invaluable expertise, guidance and encouragement throughout my studies. The scientific insights I gained during the research and coursework projects persist in me as an essential learning experience.

I extend my thanks to my supervisory committee members Dr. Joseph McDermid, Dr. Eugene Ng and Dr. Marek Niewczas for their critical reviews that helped in shaping this thesis.

I thank the faculty members of the Department of Mechanical Engineering for their thoughts and encouragement. Many thanks to the Mechanical Engineering office staff Vania Loyzer, Florence Rosato and Lily Sazz-Fayter for their kind and constant support during my studies. The friendly support of the technical staff, Ron Lodewyks, J.P Talon, Jim Maclaren, Mark MacKenzie, Michael Lee, Joe Verhaeghe and Doug Culley is remembered with gratitude.

I am very grateful to my colleagues Dr. Anantheshwara, Dr. Mitukiewicz, Gowei Zhoug, Kevin Mclaren, Keyvan Hosseinkhani, Mahmoud Marzouk, Dr. Huamiao Wang, Nick Andreae, Dr. G. Prasath, Dr. Jeyakumar and Dr. Yuossef Ziada for their valuable and timely suggestions. I am obliged to my family and friends for the unwavering support and encouragement they offered to pursue my passion. My heartfelt thanks to my wife Ramya and son Anbaran for their patience, understanding and support over these years.

Table of Contents

List of Figures

List of Tables

Nomenclature

σ_0	yield strength
K_1, K_2	strength coefficient of matrix and clad
n_{L1}, n_{L2}	strain hardening exponent of matrix and clad (Ludwik hardening law)
r	general radius of curvature of a fiber
r_m	radius of curvature of the mid surface.
r_i, r_y	inside and outside radius of curvature of bent sheet, respectively
r_n	current radius of curvature of neutral surface
r_u	radius of curvature of unstretched fiber
r_b	radius of curvature of laminate boundary fiber
t, t_o	deformed and original laminate thickness, respectively
t_c	thickness of clad layer
q_1	clad to matrix thickness ratio (t_c/t)
$\bar{\varepsilon}$	effective strain
$\bar{\sigma}$	effective stress
X	applied stress in uniaxial tension
ε_θ	tangential strain
ε_r	radial strain
ε_w	width strain
ε_p	compressive pre-strain
σ_θ	tangential stress
σ_r	radial stress

σ_w	width stress
σ_x	stress component along x-coordinate
σ_y	stress component along y-coordinate
σ_z	stress component along z-coordinate
F	constant of anisotropy used in Hill's 1948 yield criteria
G	constant of anisotropy used in Hill's 1948 yield criteria
H	constant of anisotropy used in Hill's 1948 yield criteria
L	constant of anisotropy used in Hill's 1948 yield criteria
M	constant of anisotropy used in Hill's 1948 yield criteria
N	constant of anisotropy used in Hill's 1948 yield criteria
ε_t	thickness strain used in Hill's 1948 yield criteria
R_0	plastic strain ratio (anisotropy value) at 0 degree to the rolling direction
R_{90}	plastic strain ratio (anisotropy value) at 90 degrees to the rolling direction
η	relative thickness, t/t_o
ρ	relative radius of curvature of neutral surface, r_n/r_u,
κ	relative curvature, t/r_m
λ	volume fraction of material in analytical model for pure bending
λ_n	volume fraction of material between neutral radius and inner radius
α	bend angle in analytical model for pure bending
θ	rotation angle in analytical model for pure bending
R	radius of curvature in FE-MPC model
L	distance between nodes in FE-MPC model

Chapter 1
Introduction

With increasing demands on the performance of materials for automotive and industrial applications, there has been growing interest in laminate sheets of dissimilar materials. Laminated or clad composites are capable of overcoming the performance limitations of monolithic sheets by tailoring the properties of its constituent layers. In the context of press forming, it is useful to understand to what extent the sheet laminate materials can be press formed and the modifications that occur in the known formability theory for monolithic materials due to the presence of two or more layers when they are subjected to different stress states.

1.1. Bending Characteristics of Laminated Sheet Materials

Among the various press forming processes, bending is a critical process that is widely applied in the sheet metal industry. Theoretical study of pure bending of monolithic sheets has been studied extensively in the past. In sheet bending the specimen undergoes simultaneous tension and compression in different regions resulting in three principal stresses namely, the tangential stress (σ_θ), radial stress (σ_r) and width stress (σ_w) and different stress states at the edge and mid-width section regions. A schematic of a bend specimen with the bend line at the centre is shown in Figure 1. Pure bending process

imposes uniform curvature throughout the specimen without the action of any external forces, such as friction and die reaction forces. Many analytical models have been proposed to predict the pure bending characteristics of monolithic sheets. A review of several mathematical models is presented in Chapter 2. As compared to monolithic sheet material, few studies exist on the analysis of the bending characteristics of laminate sheet materials. A comprehensive assessment of the analytical models via suitable laboratory-based experiments or using more rigorous finite element simulations of the lab-based experiments is often lacking. In the present work, a similar modeling approach based on advanced bending theory has been applied to well-bonded laminate sheet materials where the focus has been on studying the roles of laminate material properties and respective thickness ratios of constituent layers on bendability characteristics. No interface delamination has been assumed for simplicity.

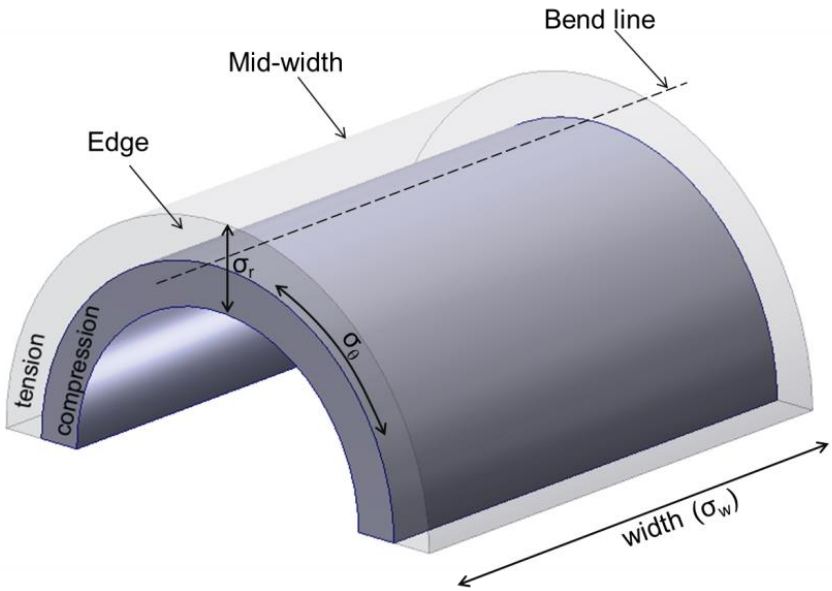

Figure 1. Schematic of a bent specimen with principal stresses shown as σ_θ (tangential stress), σ_r (radial stress) and σ_w (width stress).

1.2. Stretch-bending and its Limit Strain Prediction

Stretch-bending, a simultaneous stretching and bending operation, is commonly utilized in sheet forming processes to make components. Stretch-bending state also exists in the failure of critical punch profile radius region of sheet during cup drawing. Many theories of plastic instability in the form of diffuse or localized necking of sheet material exist in the literature for in-plane deformation. However, few such criteria have been assessed for stretch bending involving small radius bends where bending strains are superimposed with either tension on the convex surface, or compression on the concave surface. Specific forming tests that simulate stretch-bending have been proposed in the literature such as angular stretch-bending test (ASBT). A limit strain criterion to predict the onset of failure is required to specify the forming limit in stretch bending.

1.3. Objectives of Present Research

Based on the above consideration, this research is aimed at three objectives that are precisely to validate the bending characteristics from a mathematical model for pure bending of monolithic sheet using experimental and FE based method, extending the model and validation to bi-layer and tri-layer laminate sheets and thirdly to predict the limit strain under stretch bending of sheets using a strain acceleration criterion. A test jig that is capable of simulating pure bending of sheet by the rotary action of a holding clamp and pivoted joints is used in the test. The experimental strain data under bending and stretch-bending are obtained using digital image correlation (DIC) based optical strain

measurement technique. Finally, an angular stretch-bending test rig is used to perform stretch-bend test until the material failure. The definition and motivation of the objectives are discussed below.

1.3.1. Objective - 1

Development of a mathematical model to determine the bending characteristics of laminate sheet materials.

Key Issues and Motivation

A comprehensive mathematical model for bending of laminate materials that is capable of predicting the through thickness tangential and radial stress and strain distribution is not available in the literature. Development of a model by incorporating suitable material properties, hardening law, Bauschinger effect, would aid in more accurate prediction of the bending deformation for laminate materials.

1.3.2. Objective - 2

Development of experimental test method for validation of pure bending models and comparing experimental results with FE based models.

Key Issues and Motivation

In spite of several mathematical models being available in the literature none have been satisfactorily validated due to limitations in through-thickness strain measurement in

sheet bending. Plastic deformation and particularly strain localization in bending is concentrated in a very small region. A new method is needed for such measurements. Such a method needs to be not only developed but its accuracy and limitations need to be assessed. FE based models can provide data for comparison purposes.

1.3.3. Objective - 3

Prediction of limit strain in stretch-bending based on available and applicable theories

Key Issues and Motivation

Many theories of plastic instability in the form of diffuse or localized necking of sheet material exist in the literature. However, few such criteria have been assessed for stretch bending involving small radius bends where bending strains are superimposed with either tension on the convex surface, or compression on the concave surface. Experimental angular stretch bending test is employed to characterize strain history and limit strain of an aluminum sheet material undergoing stretch-bending with the aid of an in-situ optical strain measurement system based on the digital image correlation (DIC) method. A number of methods based on DIC technique have been proposed for general limit strain prediction in the literature. A strain acceleration criterion proposed by Situ et al. (Situ, Jain and Metzger, 2011) has been successfully utilized for predicting strain localization under various stretching, drawing and plane strain deformation conditions. Its applicability for stretch bending is to be studied in the present work.

1.4. Organization of the Thesis

The objectives of the thesis stated in Chapter 1 are followed by the Literature review section on analytical models on pure bending in Chapter 2. Several models based on advanced theory of bending, and other approaches such as FE modeling on monolithic and laminated sheets are discussed. A review of different sheet bending test methods in the literature and their feasibility in acquiring strain data are presented. Lastly, experimental tests methods to measure the stretch bendability of sheet materials are discussed. The analytical and FE models pertaining to bending characteristics are presented in Chapter 3 and 5 respectively. The details of a bend test fixture that could facilitate in-situ optical strain measurement during bending are discussed in Chapter 4. Apart from large strain bending, a fast and reliable method to predict the limit strain of the material based on a strain acceleration method using major strain data from the tensile surface in a stretch bending test has been studied on monolithic and tri-layer laminate sheet material. The results of the numerical models and experimental test on pure bending and bend stretching are presented and discussed in Chapter 6. Several bending characteristics that are obtained through analytical and FE models are validated wherever possible by experimental tests using DIC strain measurement. The limit strain in stretch bending is studied for different parameters such as facet size and the implication on major strain history by data fitting and choice of time scale. Finally, the effectiveness of DIC method in evaluating the limit strain between monolithic and tri-layer laminate sheet material is assessed from the experimental study. The conclusions on the results obtained from different bending and stretch-bending studies are presented in Chapter 7.

Chapter 2
Literature Review

2.1. Review of Analytical Models of Pure Bending of Sheet Materials

Many classical theories exist on the elastic and plastic bending of monolithic beams and plates. Ludwik, established the first modern engineering theory for plastic bending of non-work hardening materials using four assumptions (Ludwik, 1903).

a) Plane cross section remains plane during bending
b) The transverse stress (radial stress) is ignored
c) The neutral layer coincides with the mid-plane during bending
d) Applied bending moment is equal to the moment causing elastic recovery upon removal of load.

Over the years, except for the first assumption all others assumptions have been found to be invalid for large plastic strain, small radius, bending of wide sheets. The original theory of Ludwik is now classified as “elementary” theory of bending.

2.1.1. Pure Bending Models Based on Advanced Theory of Bending for Monolithic Sheets

Based on Ludwik's work, Hill (Hill, 1950) and Lubahn and Sachs (Lubahn and Sachs, 1950) independently formulated the first advanced bending theory that provided not only the tangential through-thickness stress distribution (σ_t) but also the radial stress (σ_r) distribution and movement of the neutral axis towards the centre of curvature of the during bending. The theory of plane strain bending for rigid perfectly-plastic materials, formulated by Hill, described the through-thickness neutral fiber movements as shown in Figure 2(a). The advanced bending models start with the differential form of equilibrium equation in terms of the above stress components, and together with a material constitutive equation and boundary conditions, obtain closed form solutions for tangential and radial stress distributions through the sheet thickness. Figure 2(b,c) show the through -thickness stresses and relative thickness change from the works of Hill (1950) and Lubahn and Sachs(1950) respectively. Thinning of the specimen upon bending is observed through a reduction in relative thickness as shown in Figure 2(d). These studies have led to an understanding of the presence of a zone of tangential stress reversal where the stresses are initially compressive but change to tensile as the specimen curvature is increased and as the neutral axis migrates towards the center of curvature of the bend. This original formulation assumed, for simplicity, a rigid – perfectly plastic material and did not allow for thickness change in bending, as observed experimentally. Drucker investigated the influence of shear force on plastic bending of rectangular

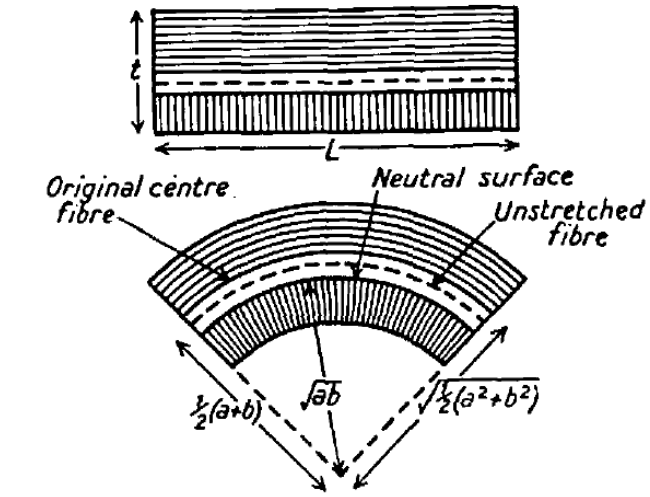

(a)

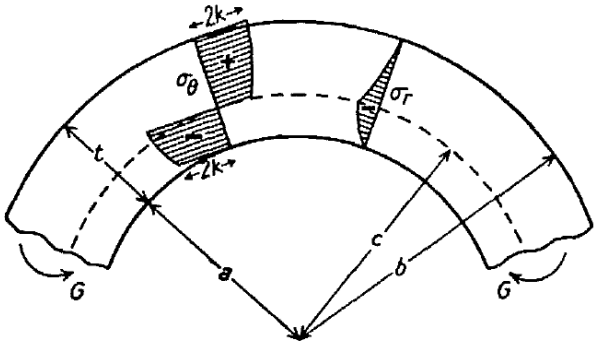

(b)

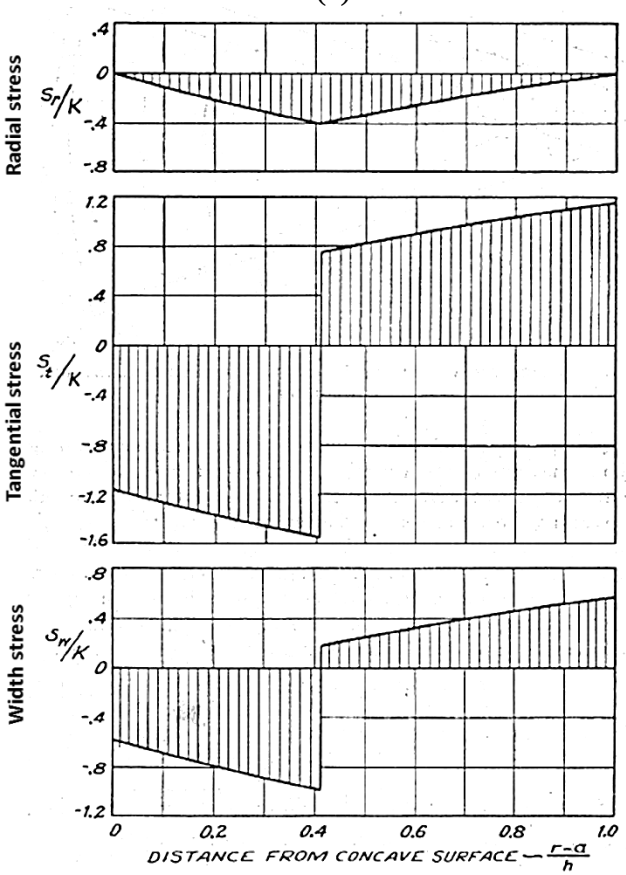

(c)

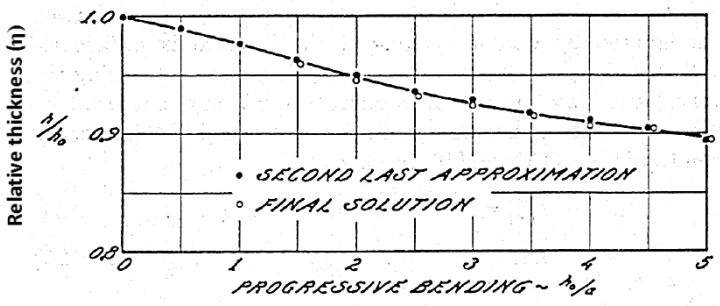

(d)

Figure 2. Through-thickness bending characteristics, (a) Bending model developed by Hill, 1950, (b) through thickness tangential and radial stress distribution in Hill's model; (c) through thickness tangential, radial and width stress distribution; (d) relative thickness distribution Lubahn and Sachs, 1950.

cantilever beam and found that the interaction between shear and bending moment is not significant (Drucker, 1956). It was found that there was only 10% reduction in moment for a shear force equal to half the shear force in fully plastic yielding case. Following Drucker, the next significant contribution to plane strain sheet bending was made by Proksa (1959), who used Hill's concepts of fiber movement as well as his suggested displacement equations in developing the theory of plane strain bending of rigid-linear hardening materials. Martin and Tsang applied Proksa's model to model the plastic bending of sheets by considering die friction effects (Martin and Tsang, 1966). The work examined the validity of using a pure moment bending theory in bending with transverse load and friction at freely supported ends. A geometric model to obtain the forces acting while bending was proposed and solved to obtain the bending moment expression containing the geometric variables. Crafoord (Crafoord, 1967) extended the advanced plane strain bending model to rigid non-linear work hardening materials while adopting a constant flow stress model for fibers located in the region between the neutral and unstretched planes. By employing a numerical technique, he was able to compute the bending moment, thickness reduction and stress distribution as a function of curvature in bending. Other early attempts at modeling pure bending of sheet materials was carried by Dadras and Majlessi (Dadras and Majlessi, 1982), who developed two numerical models for the plane strain plastic bending of rigid–strain hardening materials. The work refined the moment curvature prediction by considering the thickness change effects that was neglected in the earlier works. Model 1 considered a linear stress strain behavior for fibers in reversed bending and involved numerical computations similar to that of

Crafoord's 1967 solution. Model 2 was an extension of Proksa's analysis (Proksa, 1959) to the case of rigid work hardening material where they considered material behavior in terms of Ludwik's strain hardening equation. The thickness region of the bending specimen was sub-divided into three radial zones namely the Zone 1 (outer surface radius to mid-thickness plane radius), Zone 2 (mid-thickness plane radius to neutral plane radius), Zone 3 (neutral plane radius to inner surface radius). Based on fiber movement, the relative thickness change and relative curvature of the sheet upon bending was deduced. The tangential and radial stress distribution at different radii of curvature is shown in Figure 3(a). It was concluded that the overall pattern of bending moment variations with deformation is greatly affected by the rate of work hardening but changes only slightly with strength level. More recently, Zhu developed a model for pure bending of wide plates based on isotropic and kinematic hardening theories of plasticity (Zhu, 2007). The work compared the relative thickness and non-dimensional moment with curvature and determined that large curvature bending resulted in significant reduction in thickness (Figure 3(b)). The work also compared his work with earlier bending models developed using the deformation and flow theories of plasticity and shell theory (which neglect transverse stress). Model parameters, namely, effect of anisotropy, strength coefficient and thickness change were, however not considered in Zhu's model. Secondly, the model did not present the methodology to obtain stress distribution during bending.

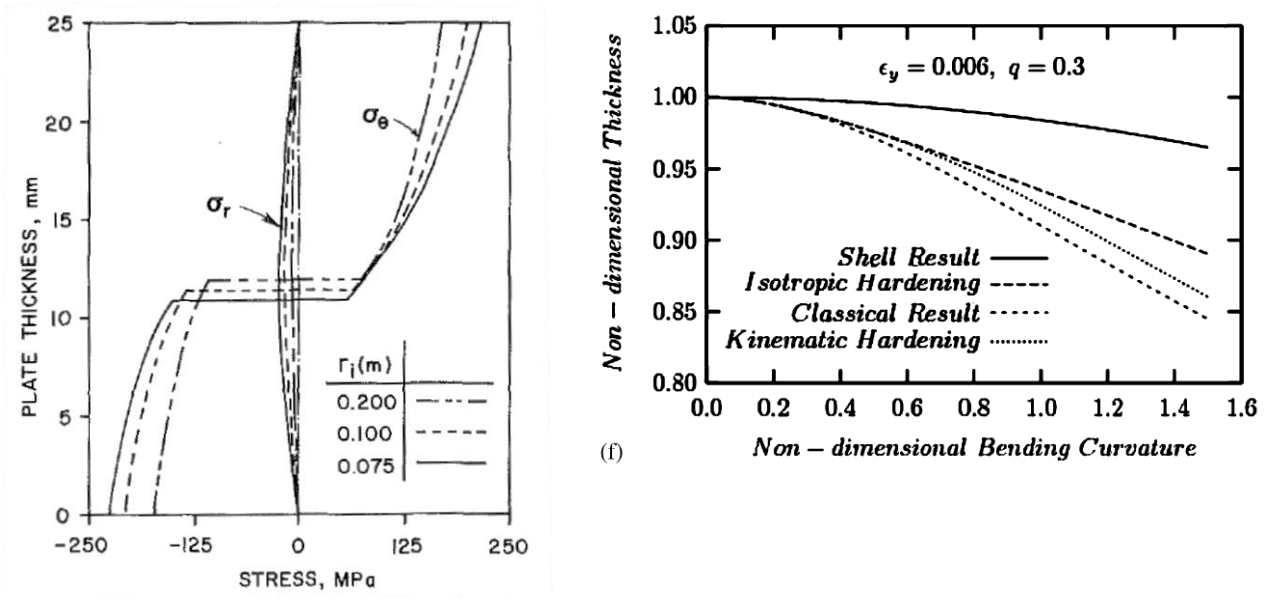

(a) (b)

Figure 3. Bending characteristics plots, (a) tangential and radial stress distribution at different radii of curvature (Dadras and Majlessi, 1982); (b) non-dimensional thickness versus non-dimensional bending curvature of a wide plate made of a material with 'isotropic hardening' or 'kinematic hardening (Zhu, 2007).

2.1.2. Tan's Pure Bending Model

Tan et al., investigated the pure bending of sheet by further analyzing the three zones of bending by including material plastic anisotropy in the model (Tan, Persson and Magnusson, 1995). As earlier studies, the model considered plane strain pure bending of monolithic sheets and divided the specimen thickness into 3 characteristics zones, as shown in Figure 4. The zones consist of regions (i) from outer radius r_y to unstretched fiber r_u (marked zone I), (ii) unstretched fiber to neutral fiber r_n (zone III) and (iii) neutral fiber to inner radius r_i (zone II).

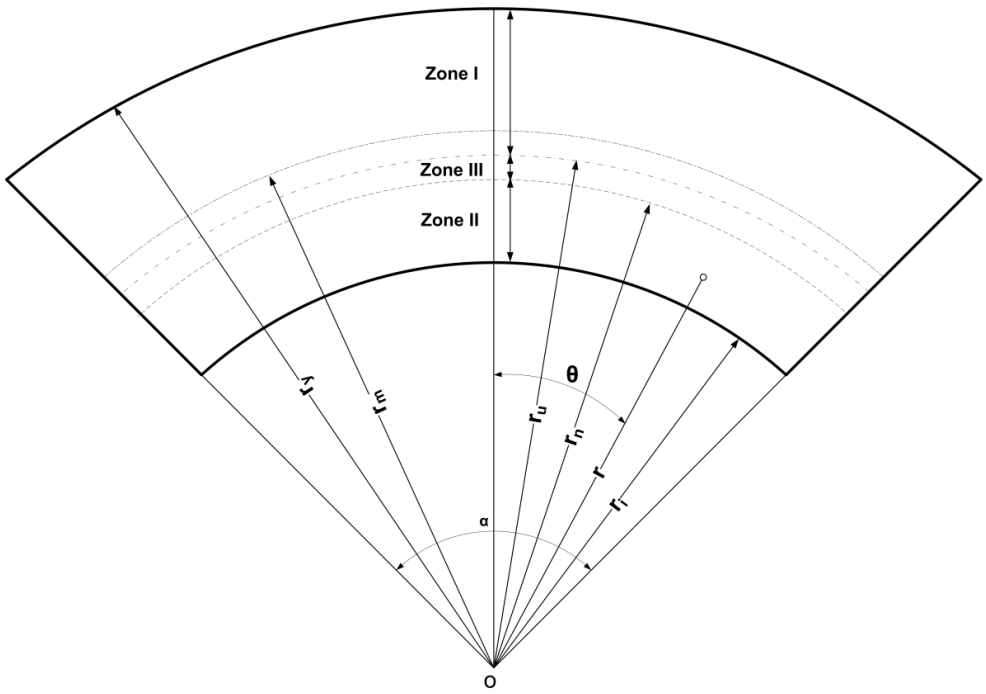

Figure 4. Through-thickness classification of zones in Tan et al. (1995) model.

The kinematics of the model was based on solving a system of ordinary differential equations (or ODEs) representing volume constancy condition in terms of thickness and curvature to obtain the current radius of neutral fiber (r_n). A Runge-Kutta numerical method was used to solve the ODE equation. Once the neutral fiber radius was determined all other radii were fixed and the logarithmic strains of interest are obtained with respect to the unstretched fiber radius (r_u). The radial stress and tangential stresses were obtained from the governing equilibrium equation and Hill's quadratic anisotropic yield criterion (Hill, 1950). The model utilized two different hardening laws, namely Voce (Voce, 1955) and Ludwik (Ludwik, 1903). The Voce model (referred as Model 1 in Tan's paper) was developed without Bauschinger effect and the Ludwik model (referred as Model II) considered Bauschinger effect.

2.1.2.1. Bauschinger effect in Tan's Bending Model

Material thinning in bending in Tan's model was mainly due to Bauschinger effect and effects of strain hardening and anisotropy on material thinning were found to be minimal. Bauschinger effect refers to the reduction in yield strength of a material upon reverse loading from tension to compression or vice versa (Figure 5 (a)). In bending, the effect is observed due to shift in neutral fiber position causing the fibers to reverse load to tension from compression (Figure 5(b)). The effect of Bauschinger effect can be best described by choosing the appropriate kinematic hardening hypothesis for the material. The modification of Ludwik hardening law to address Bauschinger effect is explained in the work of Tan et al. (Tan, Magnusson and Persson, 1994). BE is measured as difference between forward stress (at which unloading begins) and reverse yield stress ($\sigma_f - \sigma_r$) (see Figure 6). The curve OAB is obtained from tension test and curve OCD-EF is obtained from compression – tension test.

Ludwik hardening law is expressed as, $\sigma_f = \sigma_o + k\left|\varepsilon_p\right|^n$ (2-1)

For the case of isotropic hardening, $\sigma_f = \sigma_r$

For the case of kinematic hardening, $\left|\sigma_f\right| + \left|\sigma_r\right| = 2\left|\sigma_o\right|$

Bauschinger effect in Ludwik hardening form is expressed as, $\sigma_r = \sigma_o - k\left|\varepsilon_p\right|^n$ (2-2)

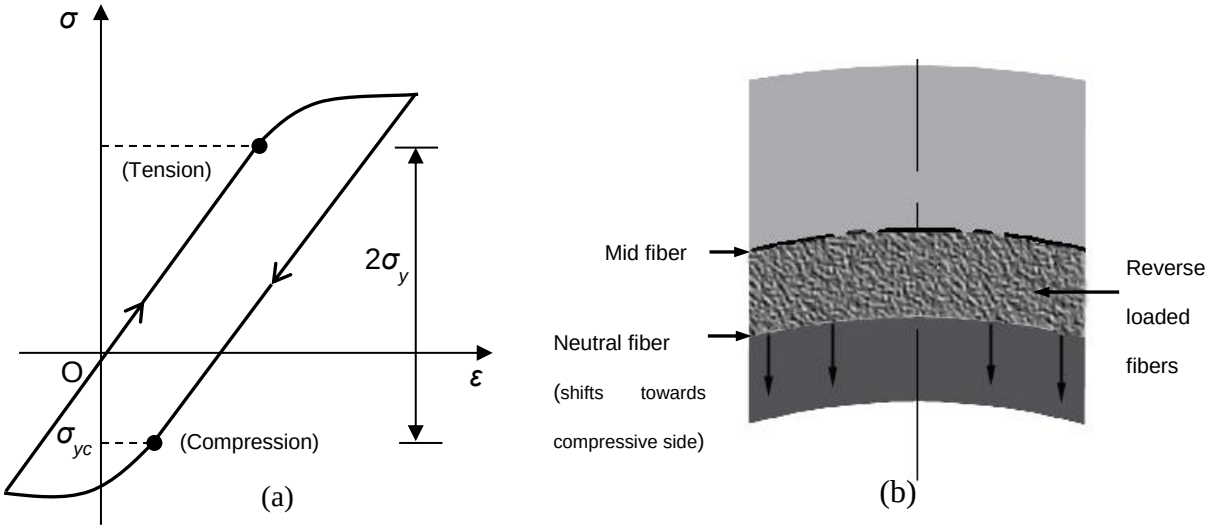

Figure 5. Stress reversal in bending, (a) Bauschinger effect seen as diminishing yield stress in the stress strain plot; (b) reverse loading of fibers due to shift in neutral fiber.

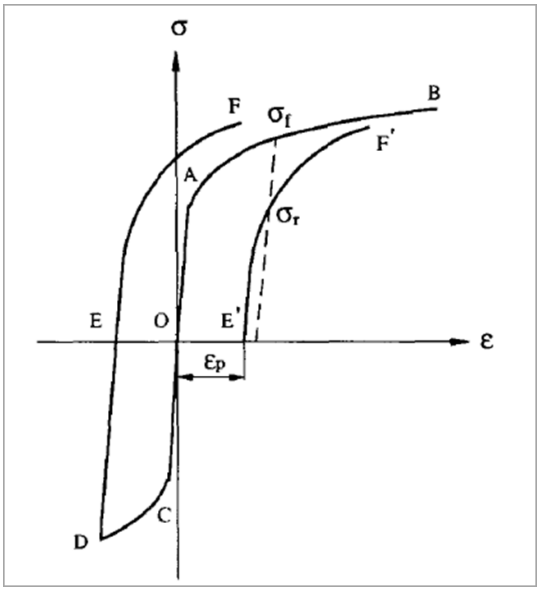

Figure 6. Schematic stress-strain curve. E'F' is the reverse flow curve replotted with the prestrain positive and OAB is the initial tensile curve (Tan et al. 1994).

2.1.2.2. Bending Characteristics from Tan's Model

A detailed description of Tan's model and derivations of equations are presented in Chapter 3. However, some general bending characteristics are summarized here. Tan et al. introduced material anisotropy (or *r* value) in the advanced theory of sheet bending by implementing the Hill's quadratic anisotropic yield criterion. In this work, material thinning in bending was attributed mainly to Bauschinger effect and strain hardening. The application of anisotropy parameters in Tan et al. was based on the assumption that the tension and compression zones through the thickness act as plane strain tensile and compressive elements. Hill presented a theory of plastic anisotropy to describe the characteristic of different yield strength in different orientations (Hill, 1948), anisotropy yield criteria. According to Hill's theory, the anisotropic yield criterion is expressed in the form,

$$2f(\sigma_{ij}) = F(\sigma_y - \sigma_z)^2 + G(\sigma_z - \sigma_x)^2 + H(\sigma_x - \sigma_z)^2 + 2L\tau_{yz}^{\ 2} + 2M\tau_{zx}^{\ 2} + 2N\tau_{xy}^{\ 2} = 1 \quad (2\text{-}3)$$

where x, y and z axes are chosen coincident with the axes of anisotropy and F, G, H, L, M and N are constants of anisotropy.

Equivalent stress is expressed as,

$$\bar{\sigma} = \frac{\sqrt{3}}{2}\left[\frac{\left[F(\sigma_y - \sigma_z)^2 + G(\sigma_z - \sigma_x)^2 + H(\sigma_x - \sigma_z)^2 + 2L\tau_{yz}^{\ 2} + 2M\tau_{zx}^{\ 2} + 2N\tau_{xy}^{\ 2}\right]}{F + H + G}\right]^{1/2} \quad (2\text{-}4)$$

Equivalent strain increment is,

$$\overline{d\varepsilon} = \sqrt{\frac{2}{3}(F+H+G)}\left[\frac{\left[F(Gd\varepsilon_y - Hd\varepsilon_z)^2 + G(Hd\varepsilon_z - Fd\varepsilon_x)^2 + H(Fd\varepsilon_x - Gd\varepsilon_y)^2\right]}{(FG+GH+HF)^2} + \frac{2d\gamma^2{}_{yz}}{L} + \frac{2d\gamma^2{}_{zx}}{M} + \frac{2d\gamma^2{}_{xy}}{N}\right]^{1/2} \quad (2\text{-}5)$$

Where the anisotropy constants R_0 and R_{90} are expressed as,

$$R_0 = \frac{d\varepsilon_y}{d\varepsilon_z} = \frac{\varepsilon_w{}^0}{\varepsilon_t{}^0} = \frac{H}{G}$$

$$R_{90} = \frac{d\varepsilon_x}{d\varepsilon_z} = \frac{\varepsilon_w{}^{90}}{\varepsilon_t{}^{90}} = \frac{H}{F}$$

Based on the anisotropy expressions from Hill's criterion, the anisotropic constants C_o and C_{90} are defined based in the directions of bend axis with respect to the rolling direction (refer to Figure 7).

(i) Bend axis parallel to RD

$$C = C_0 = \left[\frac{(1+R_0)(R_{90}/R_0 + R_{90})}{(1+R_0+R_{90})}\right]^{1/2} \quad (2\text{-}6)$$

(ii) Bend axis perpendicular to RD

$$C = C_{90} = \left[\frac{(1+R_0)(1+R_{90})}{(1+R_0+R_{90})}\right]^{1/2} \quad (2\text{-}7)$$

If an isotropic material is assumed, then $R_0 = R_{90} = 1$ and $C = 2\sqrt{3}$.

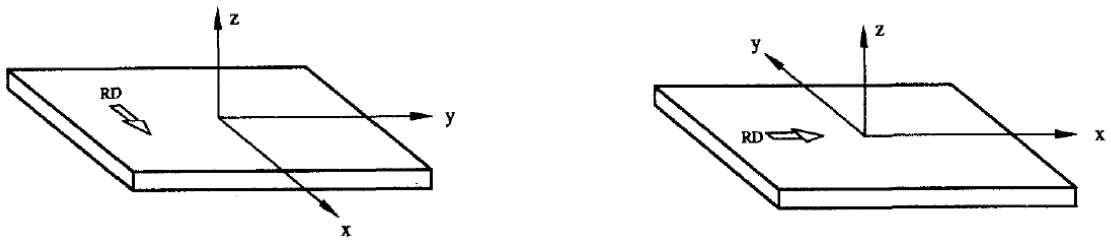

Figure 7. Orientation of coordinates and sheet rolling direction (RD) in Tan et al., (1995) model.

Case (I): If the width is coincident with the rolling direction, then $d\varepsilon_x = 0$. The condition of volume constancy gives $d\varepsilon_y = - d\varepsilon_z$. The equivalent stress and the equivalent strain with respect the tangential and radial stress components, in the case of plane strain are, respectively,

$$\bar{\sigma} = \left\{ \frac{3}{2} \left[\frac{(1 + R_0 + R_{90})}{(1 + R_0)(1 + R_{90} + R_{90}/R_0)} \right]^{1/2} \right\} (\sigma_\theta - \sigma_r) \tag{2-8}$$

$$\bar{\varepsilon} = \left\{ \frac{2}{3} \left[\frac{(1 + R_0)(1 + R_{90} + R_{90}/R_0)}{(1 + R_0 + R_{90})} \right]^{1/2} \right\} \varepsilon_\theta \tag{2-9}$$

Case (II): If the width is perpendicular to the rolling direction, then $d\varepsilon_y = 0$.

$$\bar{\sigma} = \left\{ \frac{3}{2} \left[\frac{(1 + R_0)(1 + R_{90})}{(1 + R_{90})(1 + R_0 + R_0/R_{90})} \right]^{1/2} \right\} (\sigma_\theta - \sigma_r) \tag{2-10}$$

$$\bar{\varepsilon} = \left\{ \frac{3}{2} \left[\frac{(1+R_{90})(1+R_0+R_0/R_{90})}{(1+R_0+R_{90})} \right]^{1/2} \right\} \varepsilon_\theta \tag{2-11}$$

According to Tan's model the effective stress in plane strain bending is equal to the effective stress in uniaxial tension. Based on the assumption, the differential component of equilibrium equation in bending (Equation (3-6)) is represented in terms of the equivalent stress ($\bar{\sigma}$) and anisotropy factor (C).

$$r \frac{d\sigma_r}{dr} = \pm C\bar{\sigma} \begin{cases} + r \geq r_n \\ - r < r_n \end{cases} \tag{2-12}$$

The equivalent stress is later substituted with material constitutive laws (Ludwik or Voce) according to the tension and compression zones. In the case of isotropic assumption, R_0 = R_{90} = 1 and C= $2/\sqrt{3}$. A detailed description of the isotropic case of Tan's model with Bauschinger effect incorporated is presented in section 3.1. Bending characteristics namely, the tangential and radial stresses, relative thicknesses and relative curvature of neutral fiber for the Voce and Ludwik models are obtained from the model Figure 8(a-d). The model plots showed that anisotropy had negligible effect in terms of stresses and relative thickness. The same is observed in the tangential stress and radial stress plot Figure 8 (e-f) for AA5052 specimen for two different anisotropy factors, C_0=1.288 and C_{90}=1.11 (refer to Table 1. in Tan et al. paper for properties). It is to be noted that, in Tan et al. (Tan, Persson and Magnusson, 1995), the tangential stress plots in Figure 8(a,b) of their paper have been incorrectly labelled for the Voce and Ludwik models, respectively.

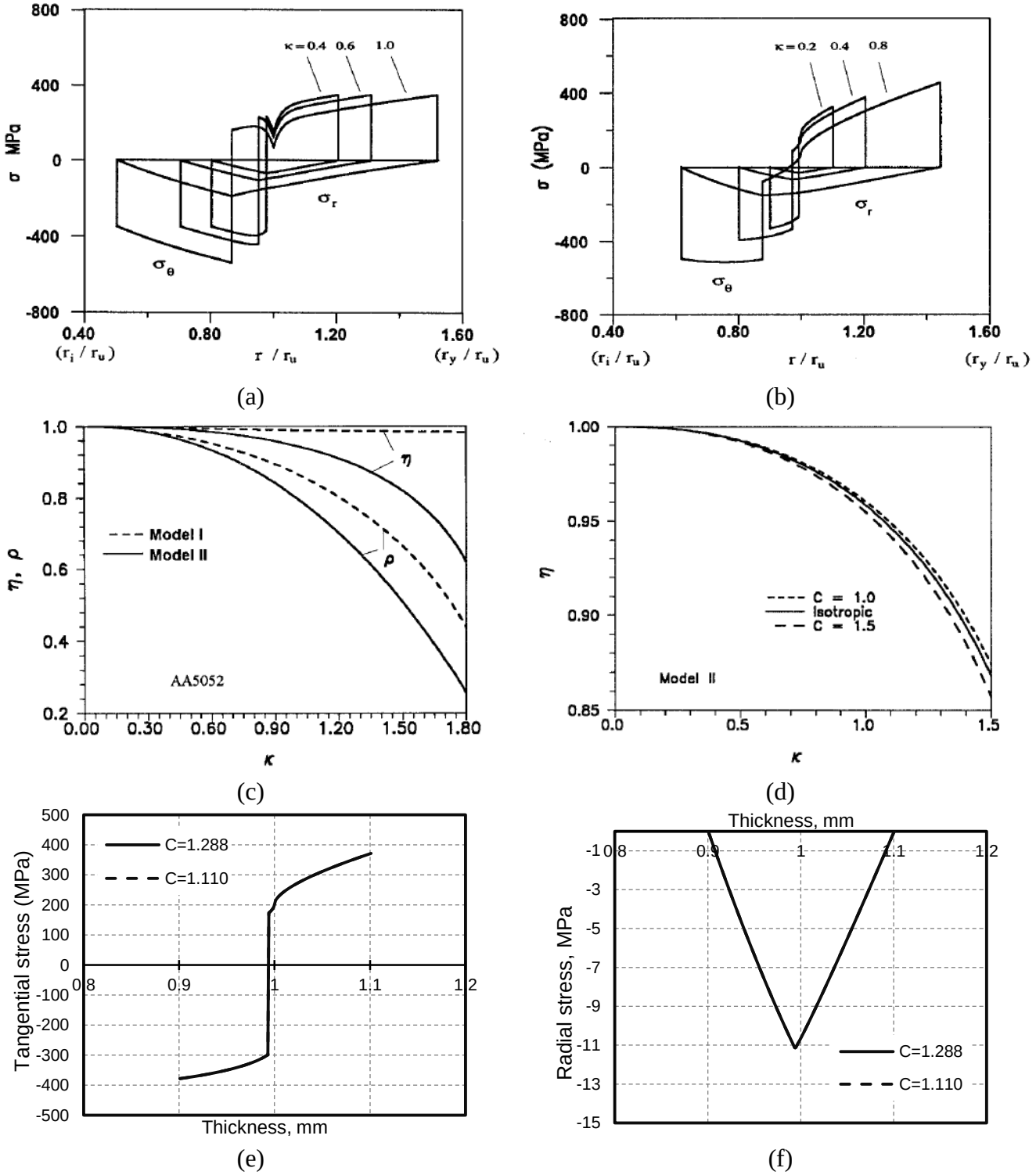

Figure 8. Through-thickness bending characteristic plots from Tan's model for AA5052 (Tan et al., 1995).

2.1.3. Summary of Bending Models Based on Advanced Theory of Bending

A comparison of the various models of sheet bending with respect to important parameters and bend characteristics is shown in Table 1. These models are based on a largely similar method of analyzing the fiber movement during bending to that derived by Hill (Hill, 1950) and Lubahn and Sachs (Lubahn and Sachs, 1950) in their 'advanced' bending theory.

Table 1. Comparison of bending models on monolithic sheets.

Bending Models / Factors	Lubhan and Sachs, 1950	Martin and Tsang, 1966	Dadras and Majlessi, 1982	Tan et al., 1995	Zhu, 2007
Plane strain condition	✓	✓	✓	✓	✓
Strain hardening	-	-	✓	✓	✓
Strength coefficient	-	-	✓	✓	-
Anisotropy	-	-	-	✓	-
Stress equilibrium condition	✓	✓	✓	✓	✓
Neutral axis shift	✓	✓	✓	✓	✓
Unstretched axis	-	✓	✓	✓	-
Bauschinger effect	-	-	-	✓	✓
Stress distribution	✓	-	✓	✓	✓
Strain distribution	✓	✓	-	-	✓
Relative thickness	✓	✓	✓	✓	✓
Relative curvature	-	✓	✓	✓	-
Relative curvature of Neutral fiber	✓	-	✓	✓	✓
Moment versus Curvature	-	✓	✓	✓	✓
Die friction effect	-	✓	-	-	-

From the comprehensive study of various models, it was observed that Tan et al. (Tan, Persson and Magnusson, 1995) model was more better in describing the pure bending phenomena than the rest of the models. The advantages of Tan's model is that the model considered most of the relevant parameters for pure bending as shown in Table. 1. The model is also capable of predicting the tangential and radial stress distribution through the numerical integration method proposed first by Verguts and Sowerby (Verguts and Sowerby, 1975). The model utilizes the basic Ludwik hardening law to express the kinematic hardening and Bauschinger effect due to shift in neutral fiber. Apart from stress distribution, the model also predicted the change in thickness and relative curvature during bending that is necessary to describe the mechanics of sheet bending.

2.1.4. Other Approaches on Bending Modeling

For completeness, other approaches to bend modeling development are reviewed here. A comprehensive V-bending model that was not based on advanced bending theory was developed by Wang et al. (Wang, Kinzel and Altan, 1993) to determine the bending characteristics in terms of force versus stroke and bending moment versus curvature. The approach to bend analysis was different from others in that the length of bend specimen included not only the region in contact with the bending mandrel but also the region between the die and mandrel. Thus the bend length was divided into elastic, elastic-plastic and plastic zones (Figure 9) while the other models identify the zones horizontally (refer to Figure 2(b)). The model considered the effective stresses and strain, anisotropy factor,

friction coefficient, elastic and plastic components of the moment equations and the die geometry in determining the moment equations in each zone. The relation between the lengths of each zone is obtained from the moments, through which the bend angle variation of the specimen is calculated. An algorithm is developed to obtain the moment versus curvature plots. Some deficiencies in the model are the exclusion of various parameters at different stages such as the thickness variations while bending. Overall the results are comparable with their limited experimental results in bending moment and spring back angle. Another plane strain bending model for an elastic-plastic condition considering anisotropy and based upon Hill's quadratic yield criterion and its associated normality flow rule was developed by Chakrabarty et al. (Chakrabarty, Lee and Chan, 2001). This paper compared the moment versus curvature with the (Wang, Kinzel and Altan, 1993) model that neglected the elastic component while calculating the moment. A semi analytical process model for air bending was developed by Heller and Kleiner (Heller and Kleiner, 2006). In this model the sheet specimen was divided into piecewise segments for calculating the bending moments. With the segmental data, simulation of bending moment for the entire specimen length was performed. The experimental and simulation results were in close agreement (deviating by only 2%) with the average bend angles. Further, the model predicted the thinning effect through drop in relative thickness for steel and aluminum alloy materials as shown in Figure 10. The relative thickness results were compared with experimental tests on v-bending that showed greater decrease in the relative thickness compared to model predictions. However, characteristics plots

that describe the tangential and radial stresses, strains, thickness change or their experimental validations have not been reported in these latter studies.

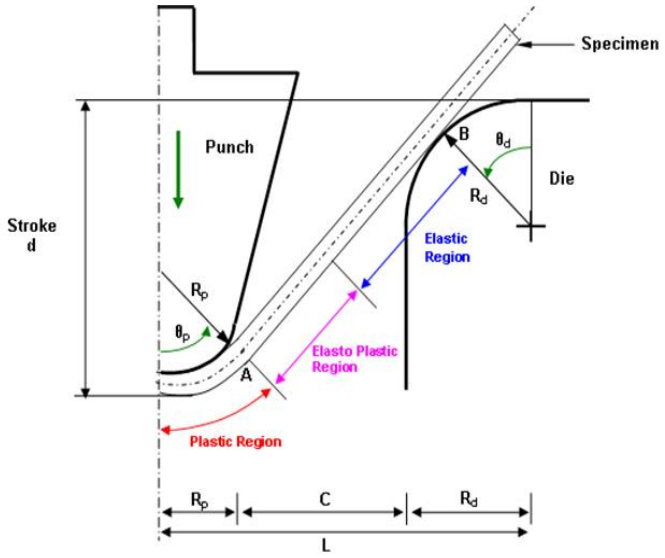

Figure 9. Schematic of Wang et al. (1993) bending model.

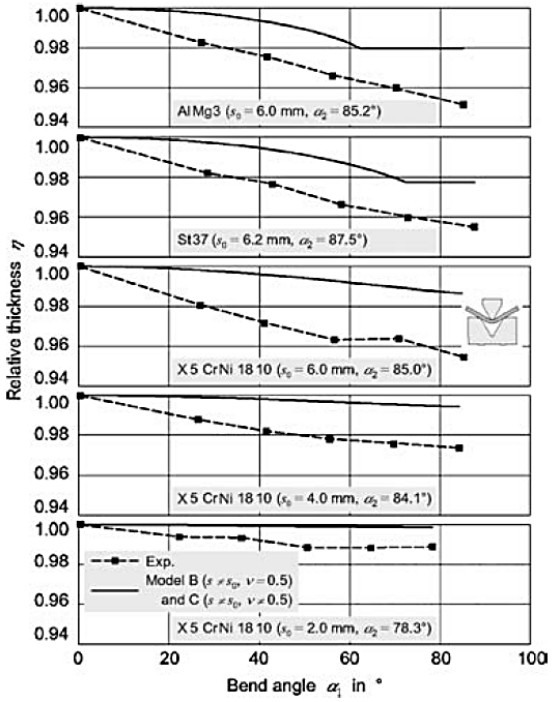

Figure 10. Model plot showing the change in relative thickness in v-bending (Heller and Kleiner, 2006)

2.2. Laminated Sheet Materials

Laminated sheet material have been developed to exploit the beneficial properties of the distinct constituent layers in a single product. Several methods to manufacture laminate sheets have been in practice for many years. One of the earliest applications of laminated composites is known to be in the development of armors made of layers of bronze, tin and gold that combines the aesthetics of gold and penetration resistance of bronze and tin (Lesuer et al., 1996). A classic example is the Japanese Samurai swords made through solid state welding of high carbon steel with soft iron as illustrated in Figure 11. Forging was done at 1000°C, at which temperature both steels are softer and the oxide skin is readily broken. After heat treatment, the final product consisted of a hard high carbon steel casing with a tough iron core that inhibits cracking of the tool during use (Figure 11). The various methods to manufacture laminate sheets and bonding mechanisms, are discussed in this section.

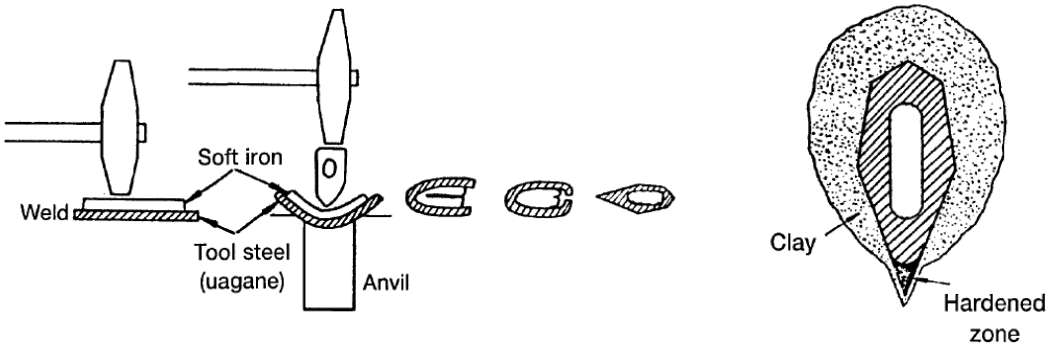

(a) (b)

Figure 11. (a) Solid state welding (forging) of high carbon steel (case) with soft iron (core), (b) Heat treatment by covering with clay, (Lesuer et al., 1996).

2.2.1. Production of Laminate Sheet Materials

Laminated metal composites can be fabricated by many techniques, which may be broadly categorized into three groups namely (i) bonding, (ii) deposition and (iii) spray forming. Bonding techniques are widely used in components materials in sheet and plate form that are solid state bonded at the interfaces. Deposition techniques involve molecular scale transportation of component materials to form sequential layers. Spray forming techniques involve direct deposition of molten metals of the component materials into a laminate form. Table 2 describes the various processing mechanism in making the sheet laminates. The schematic of different bonding techniques are shown in Figure 12(a-f).

Table 2. Classification of various processing mechanism in making the sheet laminates.

Bonding			
Process	Mechanism	Example	Reference
Roll bonding	Layer ore stacked and deformed by rolling. Bonding established through extrusion of virgin metal into the cracks of the fractured surface due to deformation	1. Copper –Nickel; Iron-Nickel; Mg-Cadmium; Al- Zinc etc. 2. AA2024 – AA1100 (Alclad)	1. (McEwan and Milner, 1962) 2. (Liu et al., 2008)
Adhesive bonding	Epoxy adhesives or solders bond the layers	1. Al layers were bonded with epoxy adhesives 2. Mild steel layers soldered with Tin-Lead-Silver solder	1. (Alice and Danesh, 1978) 2. (Embury, 1967)
table continued in next page…….			

Explosive welding	Explosively impacting one metallic mass onto another under controlled conditions. The impact energy causes solid-state bonding.	Copper and aluminum explosively welded	(Mamalis et al., 1998)
Diffusion bonding	Application of compressive stress at elevated temperature that bonds the layers. Metallic bonding is attained by interdiffusion; grain growth and recrystallization	1.Diffusion bonding of layers of Al- Ti-25Al-10Ni sheets. 2. Cladding of stainless steel on aluminum and carbon steel	1. (Wu, Wei and Koo, 1998) 2. (Deqing, Ziyuan and Ruobin, 2007)
Deposition			
Chemical vapour deposition (CVD)	Substrate material is exposed to vapours of one or more volatile precursors, which react and/or decompose on the substrate surface to produce the desired deposit	silicon deposition over nickel, tungsten, titanium	(Smith, 1995)
Physical vapour deposition (PVD) and Sputtering	Deposition of one metal by condensation and vaporization of the film material onto the substrate material	Nickel – Copper laminated with thickness ratio of 9:1	(Tench and White, 1984)
Spray Forming			
Spray forming	Atomized spraying powder particulates of the metal/compound over the liquid metal	Silicon carbide particles were periodically injected into liquid AA6061 aluminum alloy To produce AA6061 – 6061-SiC laminate	(Wu et al., 1995)

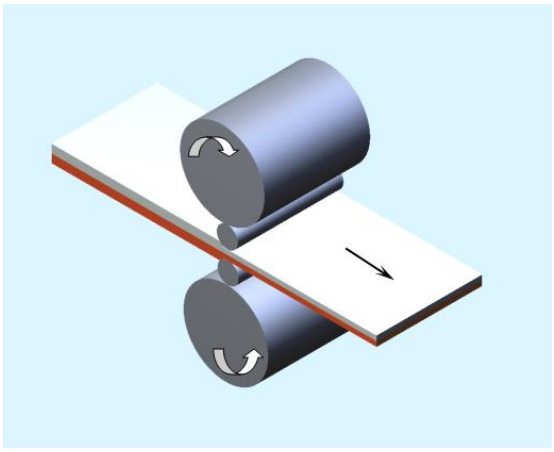

(a)

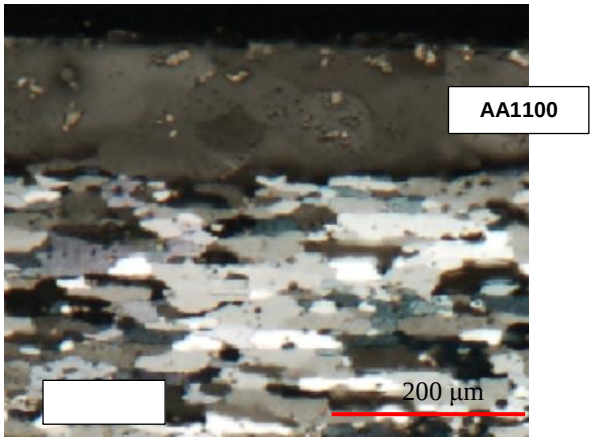

(b)

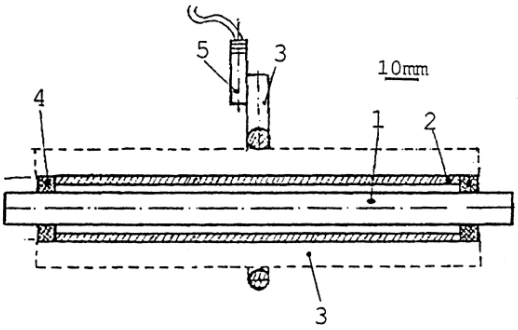

(c)

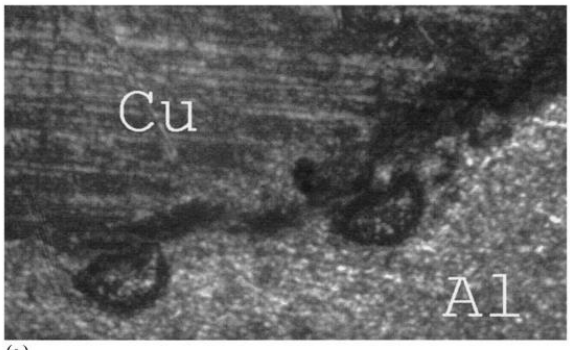

(d)

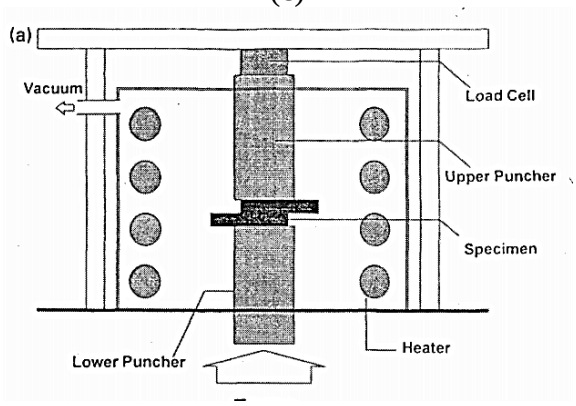

(e)

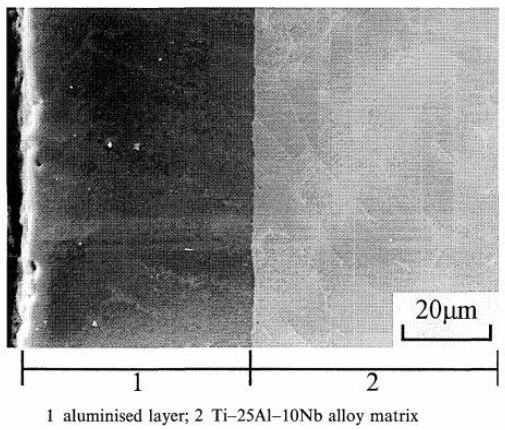

(f)

Figure 12. Schematic of different lamination processes (a) roll bonding process, (b) optical micrograph of roll bonded AA2024/AA1100 specimen; (c)explosive welding process; (d) optical micrograph of explosive welded copper aluminum (Mamalis et al, 1998); (e) diffusion bonding process, (f) aluminm titanium alloy joint (Wu et al. 1998).

2.2.2. Clad Sheet Production by Direct Chill Cast (Fusion) Process

Hot roll bonding has generally been the process for producing large length scale clad sheets such as Alclad 2024 developed by Alcoa (Liu et al., 2008). This conventional process has many additional manufacturing steps. The clad and matrix layers have to be scalped, pre-heated, roll bonded, trimmed to required dimensions. Futher, an oxide interface layer between the clad layers becomes inevitable. This multi-step process is cost intensive that has led to the development of low cost and high efficient manufacturing process for cladded aluminum sheets. A new technique of simultaneous continuous casting of aluminum alloy known as direct chill casting (commerically known as Fusion Process) has been successful in producing bi-layer and tri-layer aluminum alloy clad sheets ((Novelis Global Research, 2005)). During process startup, the liquid core alloy is poured into the opening delimited by the mold, the chill bar, and the starter block. A solid core shell is formed and extracted as the starter block is withdrawn at a given casting speed. The liquid clad alloy is then poured into the clad side of the mold and makes first contact with the solid shell immediately below the chill bar. Further cooling of the clad ingot below the mold takes place via an array of water jets shown. A schematic of the physical fusion process setup and a DC cast aluminum alloy specimen are shown in Figure 13(a-b). This method is different from conventional casting process by means of using cooling plates in traditional mold. The cooling plates served as divider walls that divide the chamber of the mold into three separate ones to mate three melts different alloy compositions. Another difference is that the solidification near the composite interface can be controlled. This provides a relatively ideal temperature distribution in the region

near the composite interface and ensures that three –layer composite ingots can be produced by semi-continuous casting. The major advantage of this process is that it can produce an absolutely clean and oxide-free interface between the layers that is not possible through conventional roll bonding process. A direct chill cast AA4045/AA3003 clad sheet is shown in Figure 13(f) (Caron et al., 2014) .

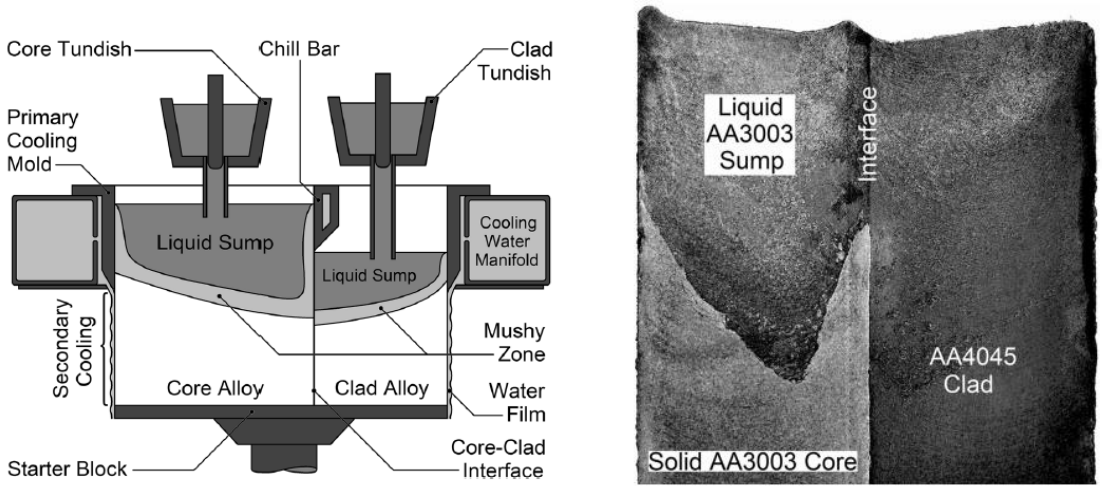

(a) (b)

Figure 13. Novelis Fusion process to produce continuous direct chill cast aluminum alloy ingots (Novelis Global Research, 2005)); (a) DC casting process and (b) AA4045/AA3003 DC cast clad specimen (Caron et al. 2012).

2.3. Bending of Clad Sheet Materials

2.4. Mathematical Modeling of Bending Characteristics of Clad Sheet Materials

As compared to monolithic sheet material, few analytical studies have been carried out on bending characteristics of clad sheet materials. One of the early notable works on

modeling the bending of clad sheets was carried by Verguts and Sowerby (Verguts and Sowerby, 1975). In this work on 304 stainless steel cladded with AA3003 aluminum, the deformation history of each individual fiber through the thickness of the sheet metal was tracked through three main equations namely the stress equilibrium equation, yield condition and Proksa's thickness change equations (Proksa, 1959). Solving the three equations leads to determination of strains and stresses (i.e., deformation history) through the thickness of the sheet and bending moment at each stage of deformation. In addition, the variation of the total sheet thickness as well as the thickness of each laminate could be calculated during deformation. However, this work had a simplified approach to account for Bauschinger effect for fibers overtaken by neutral axis. The assumption considered the yield stress of the fiber after stress reversal was constant and equal to the original yield stress of the material. This resulted in higher flow stress values in reverse loading for determining the stress distribution across thickness. Another related work on the pure plastic bending of laminate sheets in plane strain condition was investigated by Majlessi and Dadras (Majlessi and Dadras, 1983), assuming rigid strain hardening material behavior. The work predicted the distribution of tangential and radial stress for three and two layer laminates. A detailed analysis of the changes in thickness ratios of the core and clad was conducted with various layer combinations of soft core and hard clad materials and vice versa. For example, for bi-layer laminate with strong core and weak clad, a reduction in overall thickness due to bending was observed. In the weak core and strong clad, overall thickening was usually noticed. But no experimental validation of the analysis was conducted. Even though the model predicted the fiber movement, this work

assumed a linear stress – strain model for fibers in reversed loading. Secondly, the basic material properties were simulated and no anisotropy effect was considered in the models. Digitized stress plot from their work in Figure 14(a) represents a non-strain hardening bi-layer material with a strong inner layer and weak outer layer. The magnitude of stress in the inner layer represented by a-b-c-d-e denoting the stronger inner layer drops to f-g-h for the weak outer layer. In contrast, Figure 14(b) represents a tri-layer material with weak outer layers and a stronger inner core layer. The stress value drops in d-e-f-g representing the weaker core layer. Further, the reason for constant stress value at d-e is not explained by the authors.

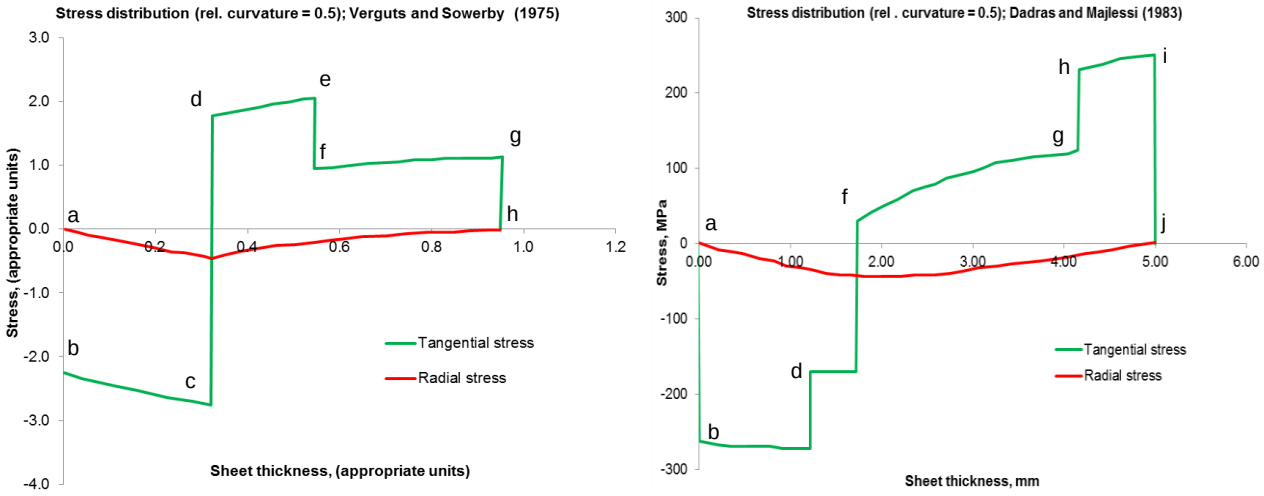

(a) (b)

Figure 14. Stress distribution plots, (a) Bi-layer laminate by Verguts and Sowerby (1975), (b) Tri-layer laminate by Dadras and Majlessi (1983).

More recently, bending of stainless steel aluminum clad sheet was experimentally studied by Yilamu et al. (Yilamu et al., 2010) where change in sheet thickness for different relative positions of steel and aluminum were determined. The thickness change during bending was found to be dependent on the relative positions of the strong and weak layers. For example, for steel inner and aluminum outer layer ($Steel_{in}/Al_{out}$) a reduction in thickness was obtained and vice versa for $Al_{in}/Steel_{out}$ combination (see Figure 15). For increased thinning during bending, the neutral layer is preferred in the stronger layer and the tensile stress is preferred in the weak outer layer causing it to elongate and thin down rather than fracture. A numerical analysis was carried for thickness change during bending using the Yohisda-Uemori kinematic hardening model (Yoshida and Uemori, 2002). A schematic of tangential stress distribution through the specimen thickness from the model is shown in Figure 16. The figure shows the bending stress distribution through the thickness of the specimen based on the geometrical arrangement of aluminum and steel layers. The magnitude of stress is shown across the thickness with steel layer showing higher tangential stress compared to aluminum.

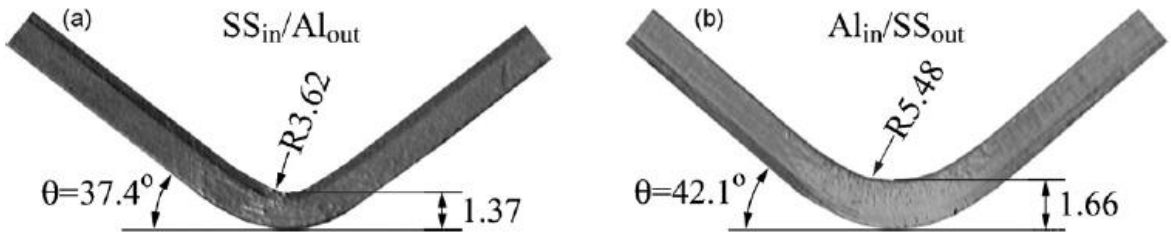

(a) (b)

Figure 15. Schematic illustration of mechanism of changes in thickness, bending radius and bending angle of bent clad sheet for the case of (a) SS_{in}/Al_{out} and (b) Al_{in}/SS_{out} (Yilamu et al. 2010).

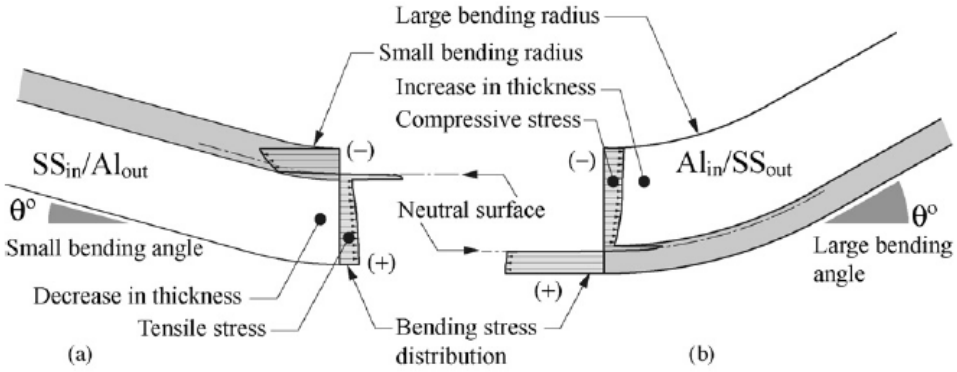

Figure 16. Schematic illustration of mechanism of changes in thickness, bending radius and bending angle of bent clad sheet for the case of (a) SS_{in}/Al_{out} and (b) Al_{in}/SS_{out} (Yilamu et al. 2010).

2.5. Finite Element Model of Pure Bending of Monolithic and Laminated Sheet Materials.

An early pure bending FE model was developed by Triantafyllidis et al. (Triantafyllidis and Needleman, 1982). The objective was to numerically study the development of shear bands in a plate subject to pure bending. The effect of initial periodic imperfection in a plate subjected to pure bending for different material constitutive conditions namely, elastic-plastic and non-linear elastic models, was studied. The maximum moment condition (Figure 17(a)) was correlated with the preferential growth of a localized pattern of undulations (Figure 17(b)). The initial imperfections lead to the development of surface undulations on both the tensile and compressive sides of the specimen and subsequently shear bands initiated at points of strain concentration induced by these

surface undulations (Figure 17(b)). An interesting observation was that the surface undulations in the compressive side occurred prior to the maximum moment while that for tensile surface occurs after the maximum moment was achieved. Further, it was concluded that, in pure bending, the shear bands propagate from the free surface of the specimen and typically stopped inside the specimen.

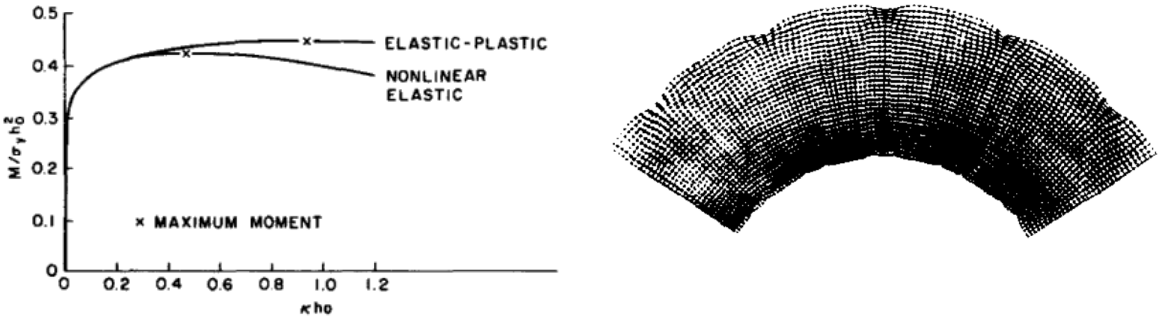

(a) (b)

Figure 17. Pure bending model results, (a) Moment vs. curvature plots; (b) bent specimen with undulations on the free surfaces (Triantafyllidis et al. 1982).

A pure bending FE model was developed by Patel (Patel, 2006) where sheet was bent using bending moment only and without any axial, shear and torsional forces. A difficulty that arises in modeling plastic sheet bending is that it is prone to exhibit plastic hinge effect. Plastic hinging is a plastic instability state in bending that is comparable to necking in tension. It requires the use of multi-point constraints (MPC) on the sheet nodes in order to achieve uniform pure bending. The MPC method is governed by a set of analytical equations required to constrain the movements of the nodes in the specimen without causing any significant reaction forces on the sheet. Figure 18(a) shows an illustration of

the concept proposed by Patel. The nodes of the central fiber are constrained to make them lie on a circle. The first node along the central fiber is subject to symmetrical boundary conditions. The second node is free to move as dictated by the loading. All the nodes on the central fiber of the sheet to the right of the second node follow the deformation of the second node as shown in Figure 18(a). A set of analytical equations (not described here) were used to constrain the movements of the nodes in the central row as described in Figure 18(b). Furthermore, the constraining equations did not constrain the radius of curvature of bend and eliminated any significant reaction forces on the sheet. The MPC subroutine was utilized within Abaqus© FE software and the simulation output where a sheet is deformed into a completely circular shape is shown in Figure 19.

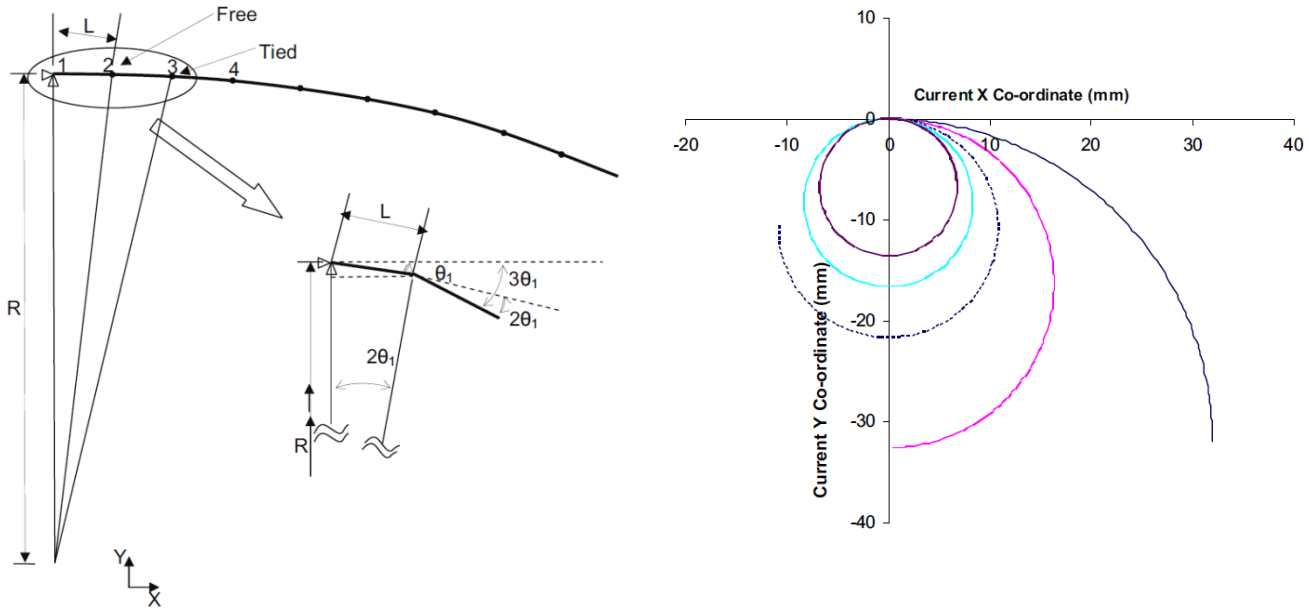

(a) (b)

Figure 18. Geometric relationship between the location of the free node and the other nodes along the centerline of the sheet; (b) curvature of centerline nodes of the sheet at different stages of bending, (Patel, 2006).

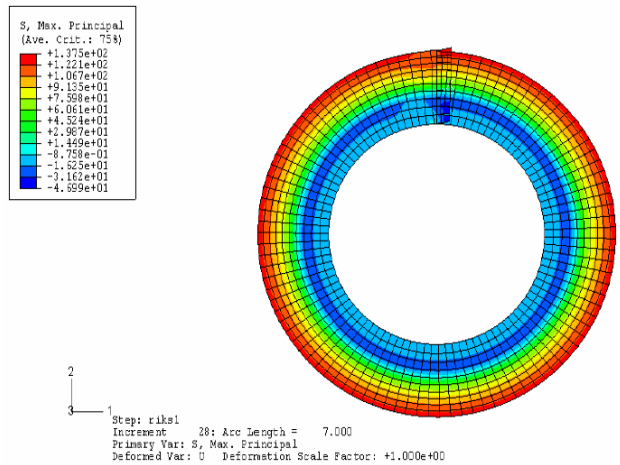

Figure 19. Pure bending simulation using 2D elements (Patel, 2006).

Another FE model for pure bending of a dual phase steel sheet material was recently developed by Bettaieb et al. (Bettaieb et al., 2010). The objective was to study the bendability of metallic sheets using a combined GTN (Gurson-Tvergaard-Needleman) model (Tvergaard and Needleman, 1984) and Thomason (Thomason, 1990) material damage models to predict the coalescence of voids in bending. Such models are continuum based but involve microstructural parameters such as void fraction for onset of plastic instability in bending. Bending model considered mixed isotropic-kinematic hardening law and studied the combined effects of initial geometrical imperfection and damage evolution on the bendability. The sheet was divided into two parts, one that was subjected to bending and the other that underwent bending and stretching (Figure 20 (a)). Due to the symmetry of the sheet only half of the bend sample was modeled by applying a vertical displacement to the right end of the sheet while keeping the left end fixed. The work did not present any result on the limit strain or limiting curvature in bending but showed the distribution of voids in terms of void volume fraction (f) across the thickness

of the specimen as shown in (Figure 20 (b)). The void volume fraction (*f*) increased with bending curvature and promoted damage development. The tangential and radial stress distribution in pure bending is shown in Figure 21.

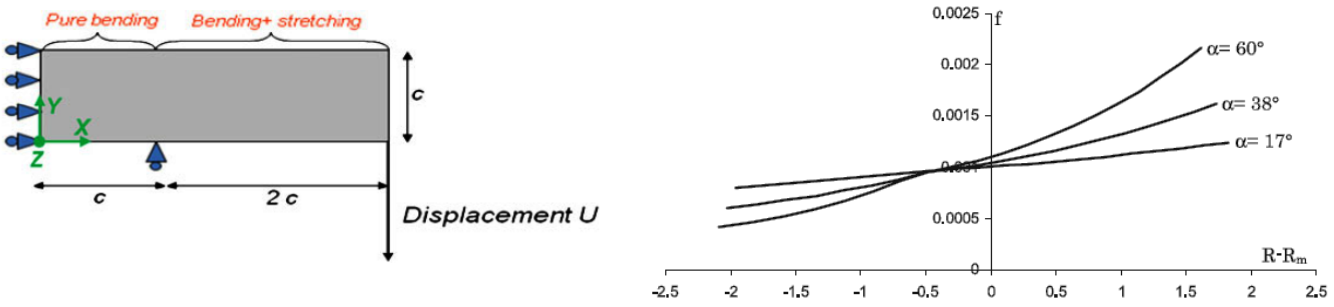

(a) (b)

Figure 20. Pure bending FE model, (a) boundary condition; (b) void volume fraction (*f*) distribution. (Bettaieb et al., 2010).

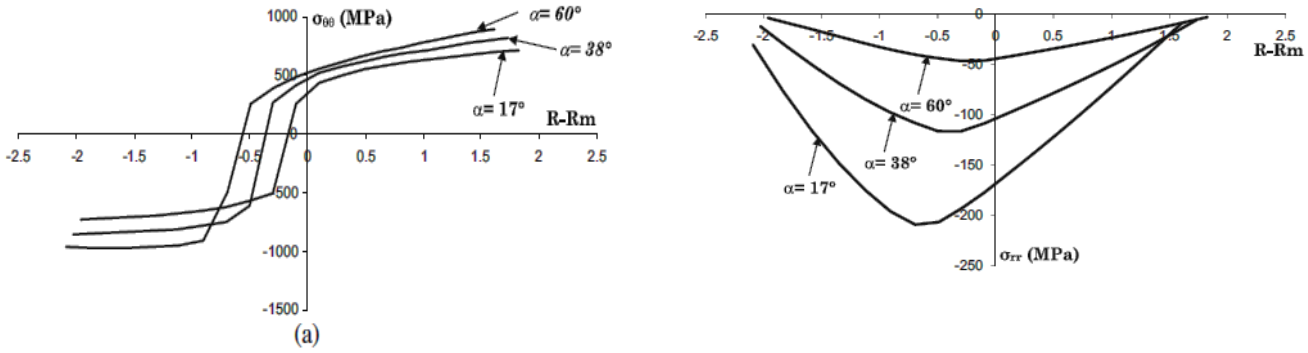

(a) (b)

Figure 21. Bending characteristics from pure bending model, (a) tangential and (b) radial stress plots (Bettaieb et al., 2010) (α – bend angle).

2.6. Review of Sheet Bending Test Methods

Bending test methods essentially involve a certain span or length of test specimen that is simply supported or clamped at the ends. The specimen is subjected to loading perpendicular to its plane (thus giving rise to moment) to a small radius typical of plastic sheet bending. An experimental test rig to simulate pure bending through application of moment alone, and in the absence of frictional or other tensile forces, is required for validation of theoretical models. A challenge for the experimentalist is to measure plastic strain in bending of a thin sheet (automotive panel sheet for stamping is typically 1 mm or less in thickness) that has a strong gradient from tension to compression through the thickness. Two noteworthy test designs from literature are illustrated in Figure 22 and Figure 23 and briefly described below. The first method developed by Hill and Zapel (Hill and Zapel, 1962), and later adapted by Guijosa et al. (Guijosa et al., 2012), Perdujin and Hoogenboom (Perduijn and Hoogenboom, 1995), Yoshida et al. (Yoshida, Urabe and Toropov, 1998)(see Figure 22(b)), and by Doig et al. (Doig et al., 2010), uses an assembly of 4 parallel side-by-side rollers to convert axial tensile force supplied by the test system into a rotational force for the rollers. The rotary motion of the roller assembly is controlled by several belts around pairs of rollers which not only connect the rollers together but also provide tension between them. The two outer rollers are attached with pin joints to a test machine that applies the axial force while the two inner rollers accommodate the test specimen and move in the opposite direction at a constant angular velocity to cause bending of the specimen (see Figure 22(a)). The specimen is mounted with screws on (and across) the 2 inner rollers with the bend line placed symmetrically

between the rollers and aligned to the axis of the rollers. The design appears capable of producing pure bending in thin sheets although some frictional sliding between sheet tensile surface and the rollers is expected. However, proponents of this design concept [(Guijosa et al., 2012), (Yoshida, Urabe and Toropov, 1998)] have also not utilized the test to carry out in-situ measurements of specimen deformation characteristics. The second design, shown in Figure 23, developed by Marciniak and Kuczynski (Marciniak and Kuczynski, 1979), consists of top and bottom assemblies attached to the top and bottom grips respectively of a tensile test frame. The top assembly consists of a pair of links to which a specimen clamping fixture is mounted via four pins. The clamping fixture consists of a pair of symmetrical upper and lower platens for clamping specimen with rows of bolts on each side. Each of the two upper platens take the form of a curved 'knee' shape over which a cable wraps around to attach the top and bottom assemblies to complete the loading train. The bottom assembly is simply a symmetrical horizontal beam, the two ends of which receive cables (assumed non-deformable during testing) from the upper assembly. When the upper grip is fixed and lower grips of the test system are pulled downwards, the two cables on either side of the clamped specimen are subjected to tension thus rotating the clamps in opposite directions about the two lower pivot points, and causing the specimen to bend. The specimen bend line is kept free from contact and spacing between the inner edges of the clamps is kept close enough to achieve a state of pure bending. The design, while more robust and rigid compared to the previous one, appears to be limited in terms of providing a clear viewing of the tensile surface of the test specimen. Another variant of this test design was developed by Weiss

et al. (Weiss et al., 2010) (see Figure 22(c)), that was able to produce small radius bends as the clamp rotation was arrested. However, no camera based measurements were carried out from the exposed surfaces. Strain measurements across the two exposed surfaces require the cameras to move in tandem with the specimen. This was not possible in the methods proposed by Weiss et al. (Weiss et al., 2010) and Yoshida et al. (Yoshida, Urabe and Toropov, 1998) in spite of their open designs. A number of other bend tests exist in the literature, but they utilize bending mandrels and dies to subject the material to bending (for example, V-bending). This system of loading invariably causes the specimen to not only bend but also stretch as it conforms to the radii of the bending mandrel and die and offer no viewing opportunity of the tensile surface as the specimen bends (Doig et al., 2010).

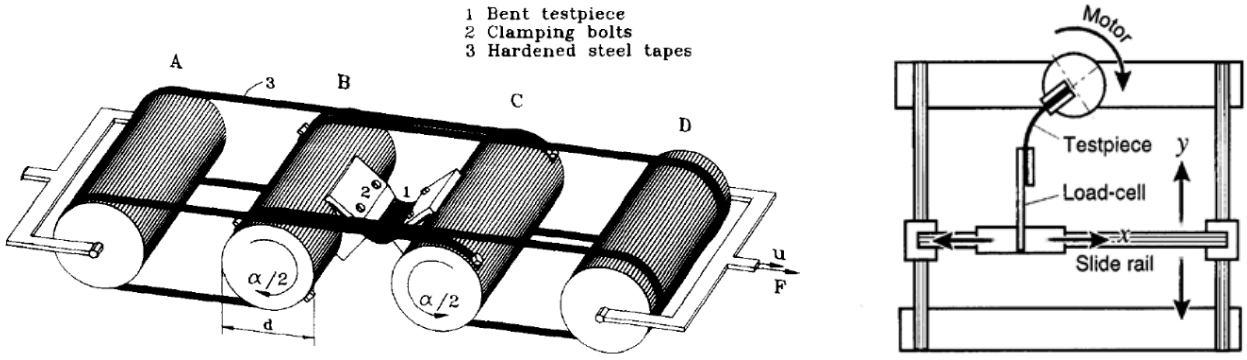

(a) (b)

(figure continued on next page)

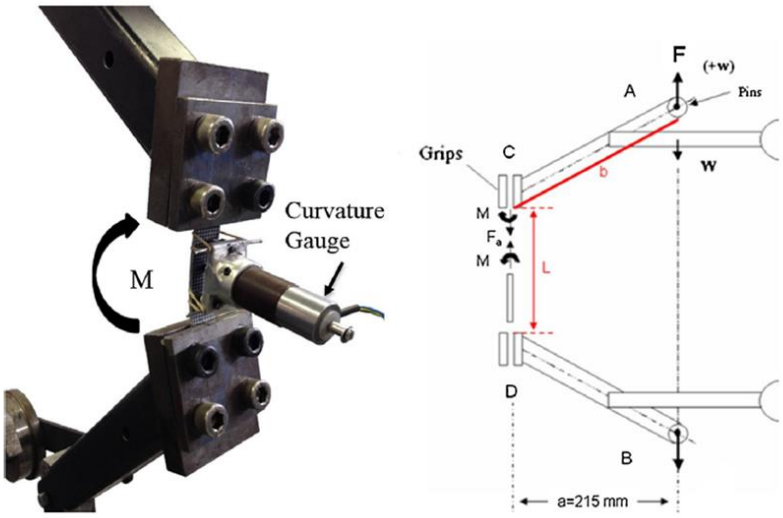

(c)

Figure 22. Bend test design proposed by (a)Perjudin and Hoogenboom (1995); (b) Yoshida et al. (1998); (c) Weiss et al. (2010).

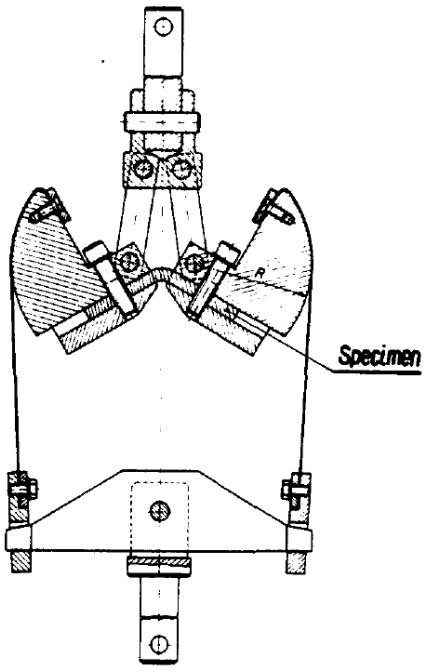

Figure 23. Bend test design proposed by Marciniak and Kuczynski (1979).

It is to be noted that most available test methods in the literature appear to subject sheet material to large radius (or small curvature) bending. Significant plastic bending for sheet forming applications such as hemming, however, requires that the sheet is bent to a very small radius of the order of 1-2 mm (i.e., large curvature). Additionally, it is highly desirable for model validation to be able to observe relevant regions of the test specimen and to allow for in-situ displacement, curvature and possibly strain measurement during bending.

2.7. Experimental Approaches to Acquiring Bend Data

Experimental approaches for bend test data typically consists of a macroscopic response by recording the bend force, corresponding punch displacement and rotation. Local measurements in the bend region such as by micro-hardness measurement and grid based strain measurements have been utilized on post-test bend specimens (Geist and Parker, 1984). Strain measurement across the through-thickness section in bending is often difficult especially for thin laminates. Bosia et al. (Bosia et al., 2004) used embedded fiber Bragg grating sensor and embedded strain gauges between the laminated layers for through-thickness strain measurements in a three point bend test. The results were also compared with 2D and 3D finite element (FE) models of three point bend test. The measurement method and the FE models confirmed the presence of non-linearity in through-thickness strain distribution that is typically not predicted with existing composite laminate theories. A recent online strain measurement technique based on

digital image correlation (DIC) principle has been employed to make continuous strain measurement in the highly curved bend region (Marzouk, Shankar and Jain, 2014). The surface of the deforming specimen is initially applied with a speckle pattern (i.e., a stochastic pattern). The deformation of the pattern is recorded during the test using CCD cameras. Camera images of the deformed region are converted to gray scale images which as subsequently analyzed for grey level changes in the sub-region from image to image. The limitation of this optical method is that it requires unhindered access by the cameras to the region of interest on the specimen. The image is divided into small rectangular areas or facets which have a large numbers of speckles on them (see Figure 24). Change in the intensity of the speckle pattern within each facet is correlated with initial or between adjacent images to yield a displacement map. For this purpose, a software converts the displacement of the random dots to a change in pixel intensity of the gray scale and then to a displacement vector field. By analyzing the displacement vectors within the entire image, the maximum correlation in each window corresponds to the actual displacement of the pattern. Further, by comparing the facets in the current image with those of the previous image, the shift, rotation and distortion of the facets can be calculated, so that the incremental and total strain can be obtained. The major advantages of this technique are (i) a full field strain map of region of interest on the specimen is obtained which is not possible with conventional methods; (ii) a continuous measurement of strain data can be made and (iii) the method is rapid and low cost provided suitable cameras and associated hardware and DIC analysis software are available.

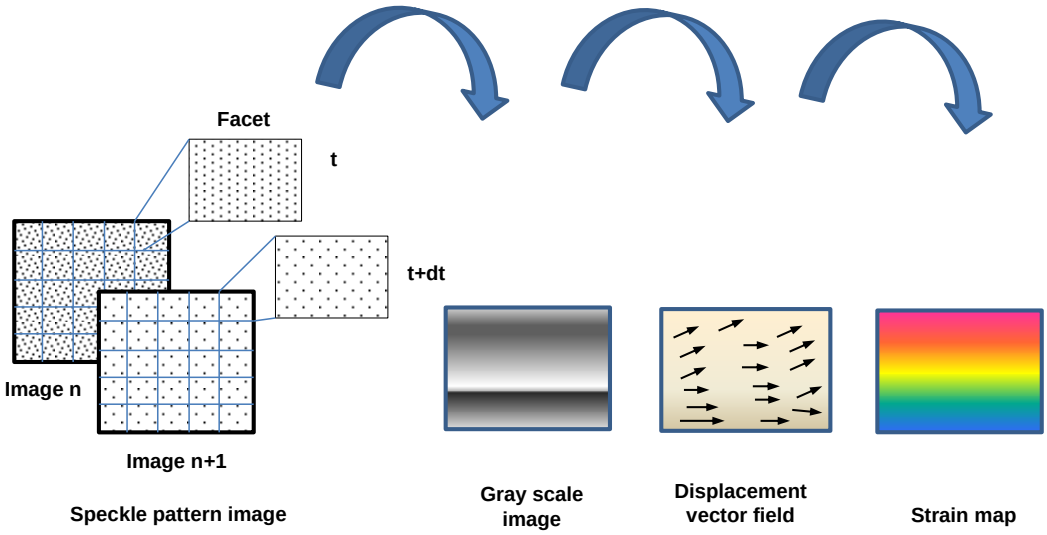

Figure 24. Schematic of Aramis strain measurement principle.

2.8. Plastic Instability Criteria for Determining Limit Strain

Instability study in metal forming is critical in determining the limit strains or the extent to which the specimen could be usefully deformed. Such limit strain analysis in bending has been studied only to a limited extent in the past. Bendability or the bending limit is often defined as the initiation of an observable fissuring or crack growth by unaided eye in the outer fiber of the tensile zone for a specimen bent to a minimum bending radius and for a given initial thickness (r_{min}/t). Bend tests using a set of bending mandrels with decreasing radii are typically used to determine the minimum radius to which material can be bent without fracture. This simple test method however lacks precise determination of limit strain as no strain measurements are carried out. Many theories of plastic instability in the form of diffuse or localized necking of sheet material exist in the literature. Considère, proposed basic criteria for necking during tensile deformation when

a material's cross-sectional area decreases by a greater proportion than the material strain hardens (Considère, 1885). The work of Considère, and Swift (Swift, 1952) for diffuse necking, Hill (Hill, 1952) and Marciniak and Kuczynski (Marciniak and Kuczynski, 1967) for localized necking from more than 40 or more years ago has been extensively referred to in the literature (Hosford and Duncan, 1999). These theories typically assume plane stress state in the sheet and most of the applications are to situations involving either in-plane stretching or large radius out-of-plane biaxial stretching conditions. A number of new theoretical approaches have been suggested in the recent years for analyzing plastic instability and flow localization processes in sheet material such as vertex theory (Storen and Rice, 1975), development of shear bands (Triantafyllidis and Needleman, 1982), through-thickness shear criterion (Eyckens, Bael and Houtte, 2009), non-planar stress states (Allwood and Shouler, 2009) and many have similar restrictions (Antolovich and Armstrong, 2014). Many of these criteria make use of macroscopic (or non-local) conditions, for example, a load maximum in the case of Hill's theory for onset of plastic instability. A number of recent studies have presented and utilized strain localization criteria, applied to critical region of the sheet for limit strain prediction during FLD determination (Geiger and Merklein, 2003), (Situ, Jain and Metzger, 2011), (Martínez-Donaire, García-Lomas and Vallellano, 2014). The latter approaches are quite promising but their application to small radius bending is still lacking. In this context, the method proposed by Situ et al. is noteworthy because of its strong physical basis. This method is discussed next.

2.8.1. Maximum Major Strain Acceleration Criterion for Predicting Limit Strain

A recent limit strain predicting criterion, by analyzing the major strain history of the surface of the sheet specimen from finite element simulations and DIC based experimental strain data was developed by Situ et al. (Situ, Bruhis and Jain, 2006). Strain measurement by DIC is based on series of images that reflect the spatial transformation of the specimen surface. The method offers the advantage of providing a complete history of strain at temporal and spatial scales in the critical stretch-bend region. This capability of DIC method to observe strain localization process provides an opportunity to predict the onset of necking and thereby limit strain of the material in Situ et al. (Situ, Jain and Metzger, 2011). The strain history plot of a strain localized region and its vicinity in a uniaxial tensile specimen is shown in (Figure 25). The major strain history shows the rise in the strain magnitude at the stage of diffuse necking and peak in the localized region (Situ, 2008). In this work, major strain distribution of a localized neck and its vicinity from a deformed specimen was obtained and plotted as a function of time (Figure 26(a)) as well as first derivative of major strain (i.e., major strain rate) and second derivative of major strain (i.e., major strain acceleration). The instant at which an inflection point occurred in the major strain rate curve, i.e., a peak in the major strain acceleration (Figure 26(b)), was proposed as onset of localized necking. The criterion was employed with both experimental DIC-based strain field data and FE model data and the approach was applied to predict FLD using hemispherical punch stretching test.

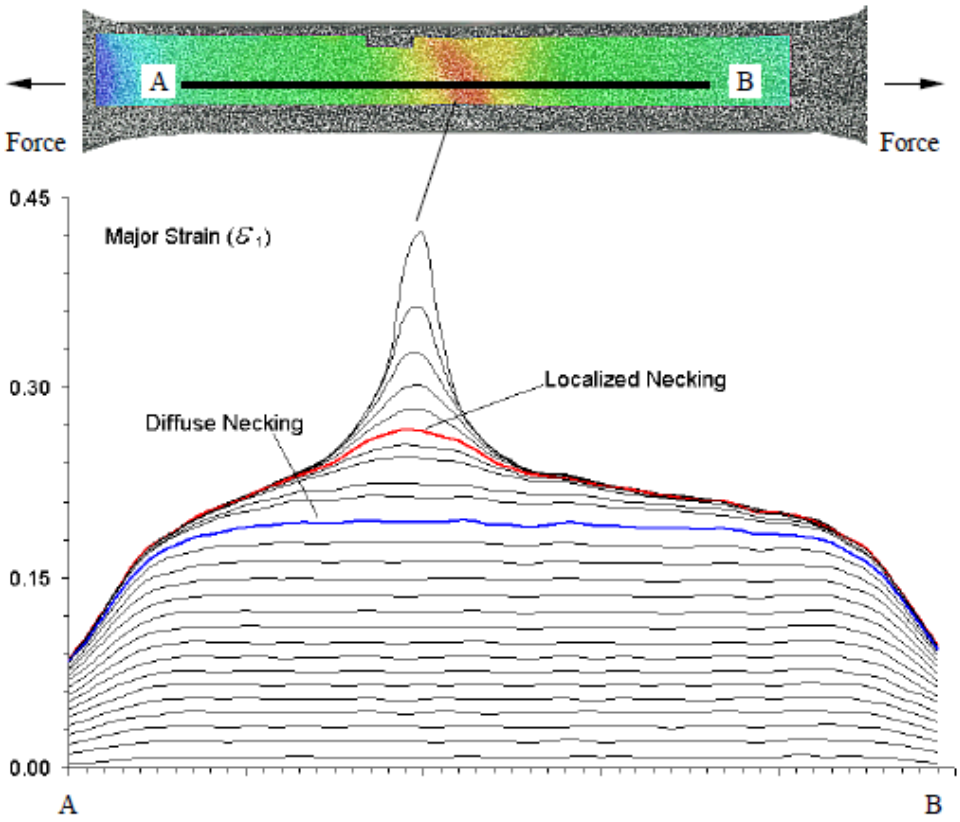

Figure 25. Strain history from ARAMIS indicating diffuse necking and localized necking for a uniaxial tensile test specimen (AA6111-T4, 1 mm thickness) (Situ, 2008).

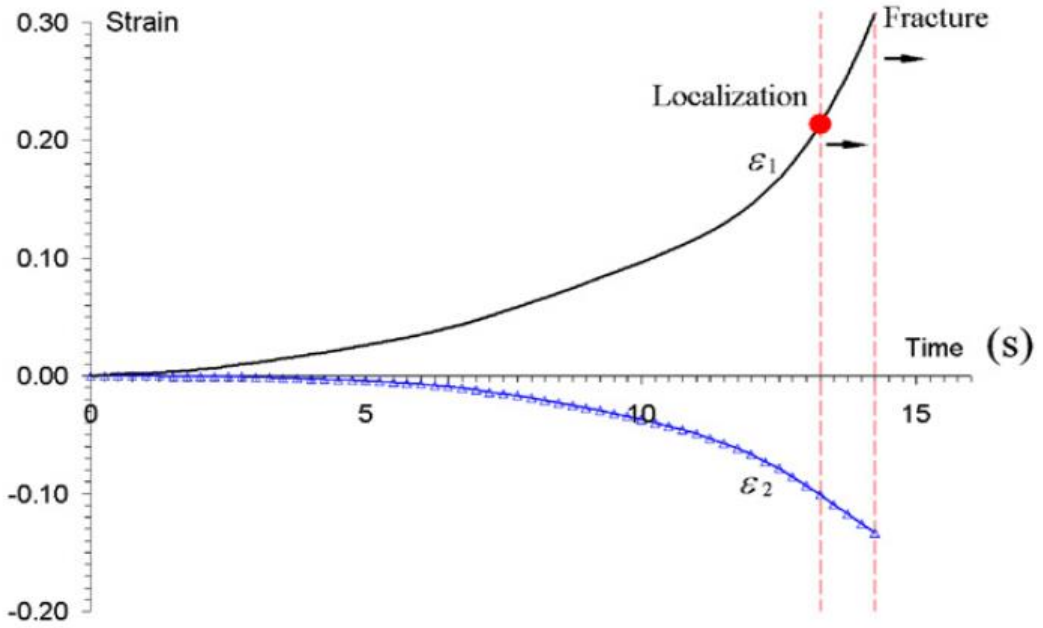

(a)

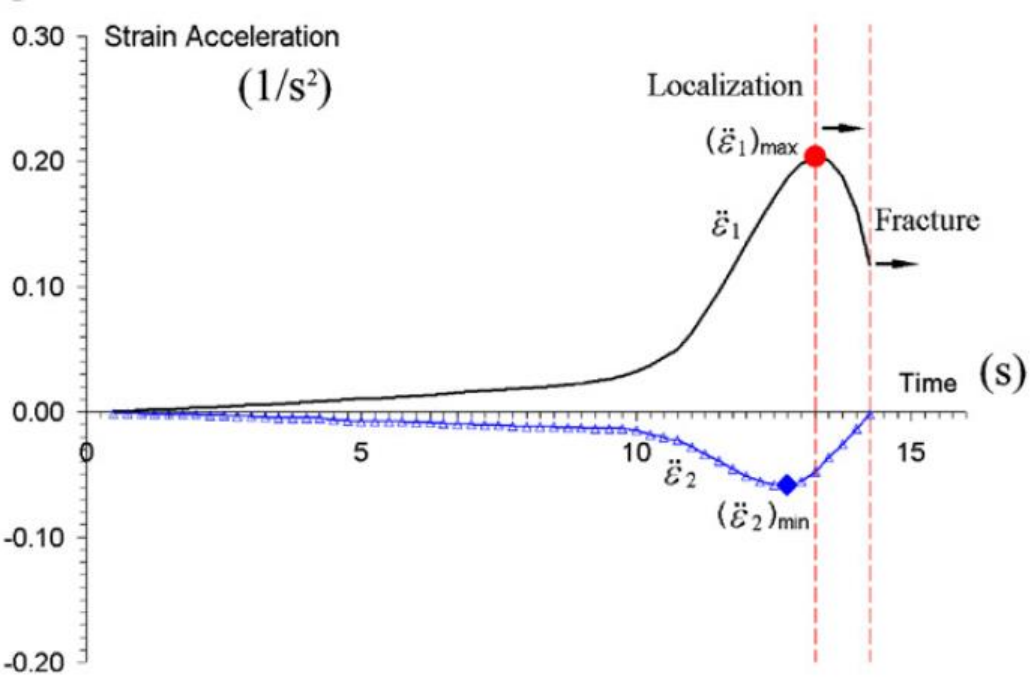

(b)

Figure 26. Limit strains prediction from the (a) major strain plot that corresponds to the peak in (b) strain acceleration plot obtained from the strain history for AA6111-T4 punch stretching FE model (Situ, Jain and Metzger, 2011).

2.8.2. Plastic Instability Criteria Applied to Limit Strain in Stretch Bending

Stretch-bending, a simultaneous stretching and bending operation, is commonly utilized in sheet forming process to make components. Stretch-bending state also exists in the failure of sheet in the critical punch profile radius region of sheet during cup drawing. Sheet stretching is often performed at the end of bending operation to reduce springback. Swift was perhaps first to theoretically study the mechanics of plastic bending under tension in 1948 (Swift, 1948). Mathematical expressions for tension in the specimen due to bending and friction were derived to predict the thinning in the circumferential direction. However, no study on plastic instability due to bending was conducted. Kruijf et al. (Kruijf, Peerlings and Geers, 2009) also analyzed the effect of bending on stretchability of the sheet where a Considère type criterion was analytically deduced to predict onset of necking under several simplifying assumptions. A finite element based analysis was made to study the effect of stretching before, during, and after bending. The criterion proposed by Kruijf et al. predicted that simultaneous stretching and bending improved the sheet stretchability, whereas a sequential operation, such as stretching followed by bending, had a detrimental effect on stretchability. However, such predictions were based on fracture strain and no strain localization in the form of a neck was predicted. Based on a so-called angular stretch bend test (or ASBT), Yoshida et al. (Yoshida et al., 2005) developed a theoretical model (see Figure 27(a)) to predict the limit wall stretch and forming height required to measure the forming limit criteria prescribed by the Aluminum Association (Aluminum Association, 1998). The analytical model developed a relationship that represents the limit wall stretch L_{max}/L_0 (L_{max}: limit wall

length of a sheet, L_0: initial wall length) in terms of the limit outer surface true strain (ε_{of}). The limit wall stretch varied with strain hardening exponent (n) value of the material and non-dimensional bending curvature. An increasing n value and bending curvature increased the limit wall stretch and outer surface limit strain (ε_{of}) (see Figure 27(b)). Yoshida et al. also noted that a standard FLD may not be suitable for analyzing material deformation behavior in the vicinity of sharp radius bends.

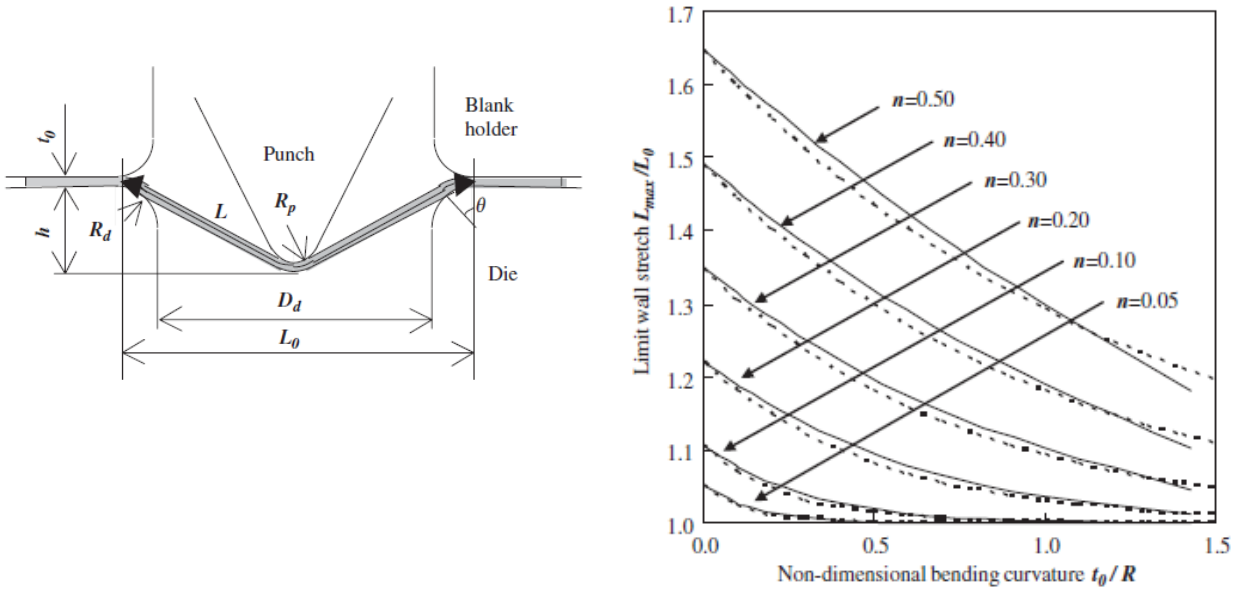

(a) (b)

Figure 27. Bending model of Yoshida et al., (a) Schematic of stretch bending test , (b) relationship plot explaining the effect of strain hardening effect on limit wall stretching ratio (Yoshida et al. 2005).

In this context, Wu et al. (Wu et al., 2006) developed a bending forming limit curve (or BFLC) based on so-called stretch bendability index (or SBI) proposed by Sriram et al. (Sriram et al., 2003). The stretch bendability index is a ratio of limit strain in uniaxial

tension to the major membrane strain in the unsupported sidewall region. The purpose of this index was to isolate the stretching effect from that of stretch bending. For example, a maximum SBI value of 1 means no bending effect on stretching. Under stretch bending state, the failure is assumed to occur if the following criterion is satisfied,

$$\left(\frac{\varepsilon^{bending}}{\varepsilon^{fracture_{bend}}}\right)^{\alpha} + \left(\frac{\varepsilon^{tension}}{\varepsilon^{fracture_{tension}}}\right)^{\beta} = 1$$

Where α and β are exponents in the above expression to be determined from test data. From curve fitting to experimental data it was found that the SBI increased with increasing punch radius to sheet thickness ratio. In other words, larger the bending radius or smaller the sheet thickness, the larger was the value of SBI.

The applicability of general forming limit curve (or FLC) is more suited for relatively flat regions of parts where tool with a large radius punch are employed to create larger curvatures over panel surfaces, resulting in only a small bending effect. In many situations, however, stretch-bending is inevitable as the sheet is bent to smaller radii, such as for hemming, part styling and stiffening, and springback control. The work of Wu et al. was able to capture the movement of failure location from the side wall to punch nose area as bending curvature increased. However, the model was based on several overly simplifying assumptions such as thin shell theory, and no thickness change in bending. These assumptions caused deviation from the measured strain values and BFLC was

simply shifted downward from the conventional FLC depending on the severity of SBI parameter while no shape change occurred in the FLC.

To account for bending, an alternative approach to conventional FLC representation has been suggested in the form of a so-called "concave side rule" (or CSR) (Tharret and Stoughton, 2003). This rule attempts to take into account inhomogeneous through-thickness deformation that occurs in stretch-bending. It is assumed that onset of necking occurs on the convex side when strain on the concave side of the sheet (i.e., sheet-punch contact side) reaches the forming limit strain of conventional FLC. However, experimental work of Kitting et al. (Kitting et al., 2009), as mentioned earlier, showed that limit strains based on CSR were well above the measured values.

In spite of availability several stretch bendability criteria in the literature; few have been assessed for stretch bending involving small radius bends where bending strains are superimposed with either tension on the convex surface, or compression on the concave surface. Plastic instability in stretch-bending operations is governed by tool geometric considerations (such as bending tool radius, clamping conditions) that result in large curvature and, significant out-of-plane deformation. Plastic instability is also related to global constitutive material properties, as well as microstructure and crystallographic texture of the sheet. While local microstructure and texture based parameters play a crucial role in affecting the limit strain bending and stretch-bending (Davidkov et al., 2012) (Marzouk, Shankar and Jain, 2014), their incorporation into practical, industrially useful, limit strain prediction tools has been challenging. It is to be noted that the

prediction of limit strain in sheet forming involves not only a suitable plastic instability criterion but also consideration of stress state as well as material specific yield criterion, material constitutive law, and surface condition. Recently, a theoretical study of stretch-bending involving effects of different constitutive models, yield criteria, anisotropy, Bauschinger effect was carried out by He et al. (He et al., 2013). However, a comprehensive laboratory-based experimental study involving all of the above with experimental tooling and strain measurement in the critical region is still lacking for assessment of stretch-bendability of sheet materials.

2.8.3. Experimental Test Designs for Stretch Bending

Hemispherical punch based stretching test (or Nakazima test), typically used for forming limit diagram (FLD) determination, does not quite simulate the stretch-bend conditions typically encountered in actual stampings. Therefore, specific forming tests that simulate stretch-bending have been proposed in the literature (Swift, 1948) (Baba and Tozawa, 1964) (Kruijf, Peerlings and Geers, 2009). Swift was first to develop a bend-stretching test jig in which a sheet sample was wrapped around a cylindrical roller and pulled by clamps using a screw mechanism as shown in Figure 28. The test set-up was utilized to study the effect of tension due to bending and friction on sheet thinning and springback after removal of the load. The experimental set-up in this earlier study, however, was inadequate, since full field strain measurement methods were in their infancy in 1948, for studying aspects of strain localization and limit strain prediction in stretch bending. The

next experimental advance in stretch-bend test design involved an angular stretch bend test (ASBT) first developed by Uko et al. (Uko, Sowerby and Duncan, 1977) in 1977 and later adapted by Demeri (Demeri, 1981) in 1981 (Figure 29(a)). The test design offered several advantages such as ability to mount the test jig on a standard mechanical test system or to a forming press. The test jig itself was designed to be rigid and simple, and similar to the well-known and commonly available hemispherical punch stretching (HPS) test jig. ASBT jig consisted of a bending mandrel (or punch), and upper and lower clamping plates (or dies) with suitable lock-beads for clamping the sheet specimen. The mandrel or punch was angular in shape with a straight edge in one direction and a small radius in the perpendicular direction. The punch passed through the central hole in the dies to contact and stretch-bend the specimen from the bottom surface. Evolving convex shaped tensile surface of the deforming specimen could be viewed from the top (or bottom, depending upon the design) in this rather open design as shown in Figure 29(b). The strain was concentrated in a small stretch-bend region around the mandrel profile radius. The test design offered several advantages such as ability to mount the test jig on a standard mechanical test system or to a forming press. However, in the works of Uko et al. (Uko, Sowerby and Duncan, 1977) and Demeri (Demeri, 1981), no continuous strain measurement were carried out during the test to analyze the nature of evolving strains in the neck (and failure) region.

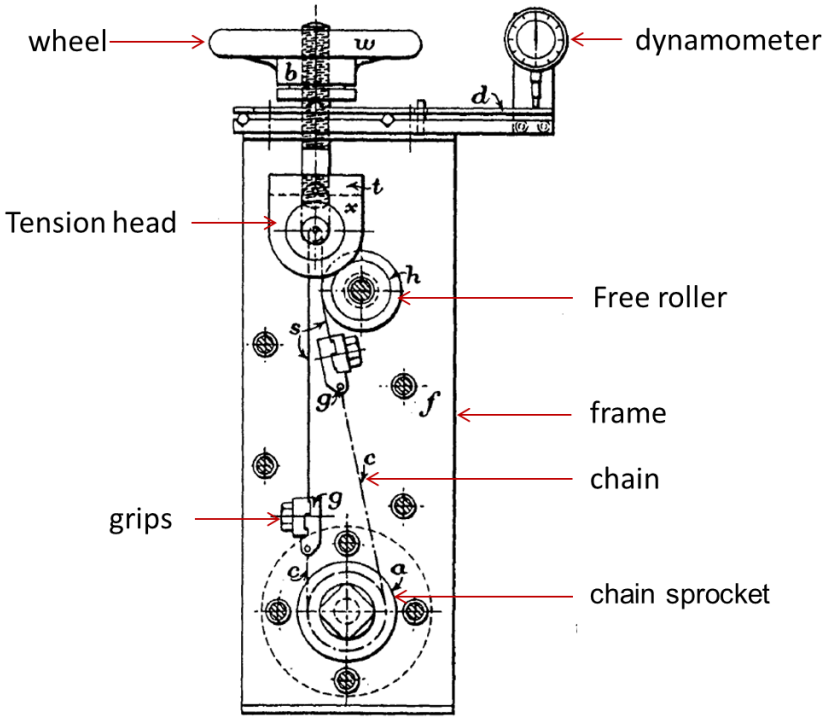

Figure 28. Stretch-bend test design by Swift (Swift, 1948).

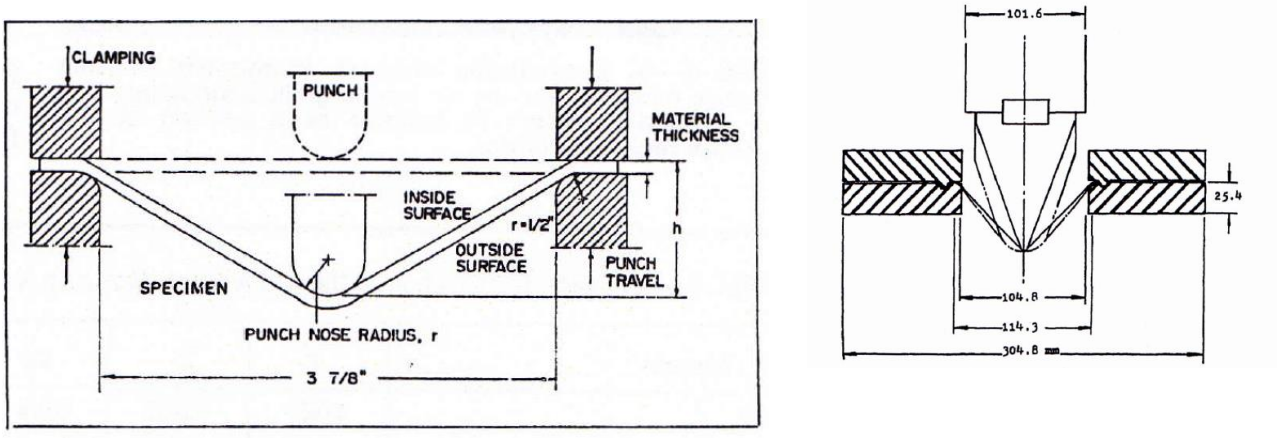

(a) (b)

Figure 29. Schematic of punch die set for (a) angular stretch bending by Uko, 1977 and (b) hemispherical stretch bending by Demeri, 1981.

2.9. Strain Measurements on Stretch-bent Specimens

2.9.1. Post-test Measurements from Imprinted Grid Patterns

Strain measurement in bending with sharper mandrel profile radius has posed a challenge to any conventional strain measurement method. The major strain is localized in the small bend region with significant strain gradient in through-thickness direction at the bend line. Uko et al. (Uko, Sowerby and Duncan, 1977) measured post-test strain along the convex and concave sides of the ASBT specimen using a circular grid pattern of 0.96 mm diameter that was imprinted using photo-resist etching method. Sufficiently thick sheet specimen of 5.96 mm thickness were chosen to allow for through-thickness strain measurements from the edge of the specimen. The major (i.e., circumferential) strain was localized in the stretch-bend region and the maximum occurred at the bend line Figure 30(a). Effective fracture strain from the test was significantly lower than that from uniaxial tensile tests. The final stage in stretch-bending appeared to be a characteristic of plastic instability process rather than fracture. A smaller punch radius resulted in higher limit strain and a larger gradient in the major strain distribution along the circumferential direction as shown in Figure 30(b). Similar grid-based strain measurements were carried out by Demeri (Demeri, 1981) to study the effect of specimen curvature and thickness on stretch-bending using a hemispherical stretch-bending test (HSBT) that uses hemispherical punch instead of angular punch (Demeri, 1986). Demeri's work reported an important observation by comparing limit strain based on limiting height between HSBT and ASBT tests. In HSBT test, the limit strain increased with increasing material thickness due to increased material availability and increased uniformity in strain

distribution. In contrast the limit strain decreased with increasing thickness is ASBT where the specimen encountered more bending (i.e. lower R/t ratio) and increased through thickness strain gradient that contributes to early failure. The same was concluded in the works of Yoshida et al. (Yoshida et al., 2005) and Martínez-Palmeth (Martínez-Palmeth et al., 2013).

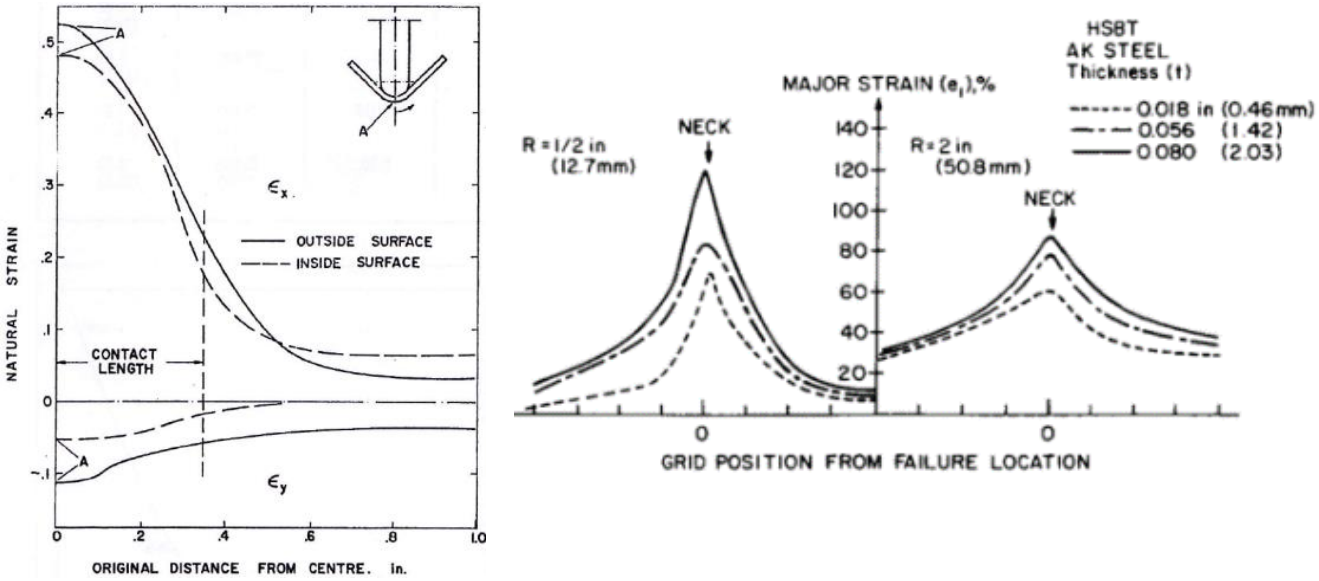

(a) (b)

Figure 30. Major strain distribution from tensile and compressive sides of HSLA steel ASBT specimen along (a) longitudinal (i.e., circumferential) (specimen thickness, t = 5.26 mm), strains measured by a periodic grid pattern, and (b) thickness on strain distributions for two punch radii for AK steel. All results are taken from Uko et al. (Uko, Sowerby and Duncan, 1977).

2.9.2. In-situ Measurements Using DIC Technique

Kitting et al. (Kitting et al., 2009) recently conducted ASBT with different punch geometries where DIC technique was used for continuous strain measurements on the

convex surface to validate the so-called “concave side rule” (or CSR) for stretch-bending. This rule is discussed in a later section. The deformed specimens showed significant strain gradient in the stretch-bend region depending upon the punch geometry. The small radii punches shifted the forming limits to higher strains compared to the forming limits of homogenous in-plane deformation processes. The study stressed the significance of through thickness strain gradient in assessing the formability under stretch bending. It was concluded that CSR was not able to estimate formability for a wide range of punch radii in stretch bending. The study stressed the significance of through thickness strain gradient in assessing the formabilty under stretch bending. The test was also simulated using FE method. The major strain showed appreciable correlation between the DIC data (dotted line) and FE model (thicker line) at the bend line as shown in Figure 31. However, differences were also noted between the FE model and DIC data at the specimen edges and in between the edge and pole. Other information on DIC parameters such as facet size, facet steps and speckle pattern size to assess the quality of DIC analysis were not available. Martínez-Palmeth et al. (Martínez-Palmeth et al., 2013) measured fracture strain in hemispherical stretch bend test (HSBT) using a range of punch diameters and DIC method. Major strain distribution along a section line passing across the dome was utilized for curve fitting to determine peak major strain along the line. In general, larger necking strains were received with decreasing punch radius.

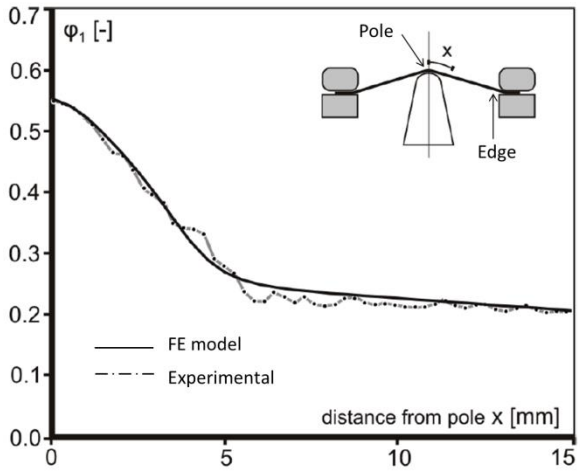

Figure 31. Major strain distribution from tensile surface along longitudinal axis from experiments and FE model (Kitting et al., 2009).

2.9.3. Strain Calculation by Numerical Method

A numerical model for comparing strain distributions in the inner and outer surfaces and mid-thickness region of a stretch-bend specimen was developed by McClintock et al. (McClintock, Zhou and Wierzbicki, 1993). The model predicted the effect of increasing bend angle, curvature and bending moment on plastic instability. It was concluded that necking will occur in plane strain under constant applied tension and increasing bending curvature when the tensile force can no longer be maintained. In other words, increasing curvature reduced the tensile force for necking. The strains were compared at the outer surface, mid-thickness layer and inner surface of the specimen that showed highest strain at the outer surface and least at the inner surface. Another FE-based stretch-bending model by He et al., based on Yoshida-Uemori kinematic hardening constitutive model , predicted major strain distribution across the outer surface, mid-thickness layer, and inner surface in a stretch-bend specimen (He et al., 2013). The major strain distribution across

the three regions followed a similar pattern (Figure 32). However, this study showed continuous increase in the magnitude of strains in all three regions in contrast to the work of McClintock et al. where the strains dropped at the inner surface.

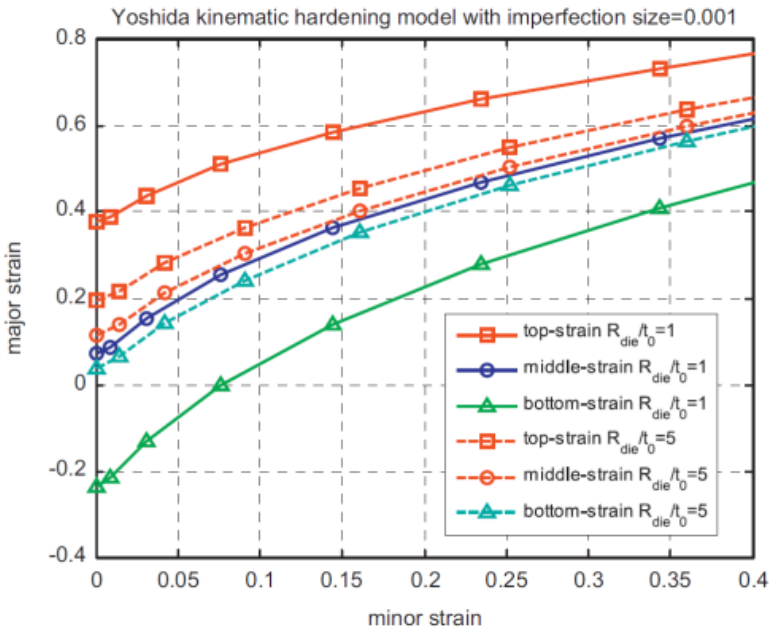

(a)

Figure 32. Evolution of major strain distribution across outer surface, mid-thickness layer and inner surface for DP600 steel sheet (He, et al., 2013).

A compilation of maximum major strain obtained from various experimental and numerical methods for different materials is shown in Table 3. When comparing the maximum strains to the tensile elongation, it should be noted that, in many studies, the stretch-bent material could attain almost twice the strain to that from uniaxial tension.

In spite of the many studies on stretch-bending, as noted above, a reliable method of detecting the onset of necking or fracture in stretch bending is still not available. A strain

localization criterion based on measured continuous local strain data up to fracture in a stretch-bend test using DIC technology would serve well. Therefore, applicability of a strain acceleration criterion from Situ et al. (Situ, Jain and Metzger, 2011) based on spatial and temporal development of strains in the critical stretch-bend region is studied in this work.

Table 3. Maximum major strain in stretch-bending obtained by various methods compared to the tensile elongation

Material	Thickness, mm	Tensile elongation %	Maximum major strain (rounded to closest approximation)	Method	Reference
HSLA steel	5.26 mm	36%	0.5	Grid pattern	(Uko, Sowerby and Duncan, 1977)
1008AK steel	1.04 mm	40%	0.8	Grid pattern	(Tharret and Stoughton, 2003)
AK steel (punch radius = 12.7 mm)	1.42 mm	44%	1.1	Grid pattern	(Demeri, 1986)
HSLA steel	1.2 mm	28%	0.5	DIC	(Martínez-Palmeth et al., 2013)
General material condition	normalized	Y.S/E = 0.002	0.45	Numerical	(McClintock, Zhou and Wierzbick, 1993)
DP600	normalized	24%	0.7	FE model	(He et al., 2013)
H340 LAD steel	1.5 mm	25%	0.55	FE model and DIC	(Kitting et al., 2009)
DP600 steel	1.4 mm	22%	0.40	FE model	(Lopez and van den Boogard, 2011)

2.10. Summary of Literature Review

Several models of pure bending of monolithic sheet materials are available in literature, yet theory is still lacking on laminated sheet materials. More notably, a detailed

experimental study to validate the pure bending models is not available in literature. It is also inferred that a comprehensive model and experimental validation method to fully characterize bending of wide sheets that has different stress states in the edge and mid-width section is not available. Similarly, several criteria and test methods to predict the limit strain in in-plane deformation processes are available, yet only few have been reported on stretch bending of sheet material. Likewise a limit strain prediction criterion applicable to stretch bending of laminated sheet materials is not yet reported. Further, the conventional strain measurement methods are not suitable for measuring strain on thin sheet specimens and not capable of obtaining full-field strain data. The current work is aimed to address these deficiencies in theory and experimental strain measurement in bending and stretch-bending of laminated sheet material.

Chapter 3
Analytical Modeling of Pure Bending

This chapter presents details related to analytical modeling of pure bending of monolithic and laminated sheet materials. The analytical model is a 2 dimensional analysis of plane strain bending based on advanced theory of bending. The basic framework of the analytical model for laminated sheet is based on plane strain pure bending of monolithic sheet from the work of Tan et al. The following assumptions are made.

a) Plane sections remain plane as the sheet deforms, i.e., there is no lateral deformation to cause edge effect.
b) Uniform moment is transmitted across the specimen, i.e., moment is not accumulated at a particular region of strain accumulation.
c) Pure bending results in uniform curvature across the span of the specimen.
d) There is no superimposed tension or compression on the sheet.
e) Strain rate and temperature effect are not considered.
f) Bending occurs in the plane strain condition and no specimen edge effect is considered.

Additional assumptions related to choice of yield criterion and hardening law are discussed later along with the model formulation.

3.1. Tan's 3 Zone Model for Pure Bending of Monolithic Sheet

The analytical model of Tan et al. for pure plane strain bending of a monolithic sheet considered three zones across the specimen thickness. The zones were categorized by dividing the thickness with respect to outer radius (r_y), un-stretched fiber (r_u), neutral fiber (r_n) and inner radius (r_i). The model utilized Ludwik hardening law for tension, compression and reverse loaded zones. The Bauschinger effect in reverse loaded zone was captured by modified Ludwik law as described by Tan et al. (Tan, Magnusson and Persson, 1994). The hardening law was applied to the tension and compression zones with their material hardening parameters obtained from tensile tests. The model kinematics were based on solving a system of ordinary differential equations representing relative thickness and curvature to obtain the current value of the radius of neutral fiber. Subsequently, other radii of interest were obtained through which the logarithmic strain values of the zones are calculated. The radial stress and tangential stresses were obtained from the governing equilibrium equation and Hill's quadratic anisotropic yield criterion. Because of the close relationship of new bending model for laminated sheet to the work of Tan et al., for monolithic sheet, the mathematical development of Tan's model is presented in the following sub-sections.

3.1.1. Equilibrium Equation of Pure Bending

Consider a wide specimen undergoing plane strain bending as shown in Figure 33(a). Consider a specimen shown in shaded area Figure 33(b) for force analysis:

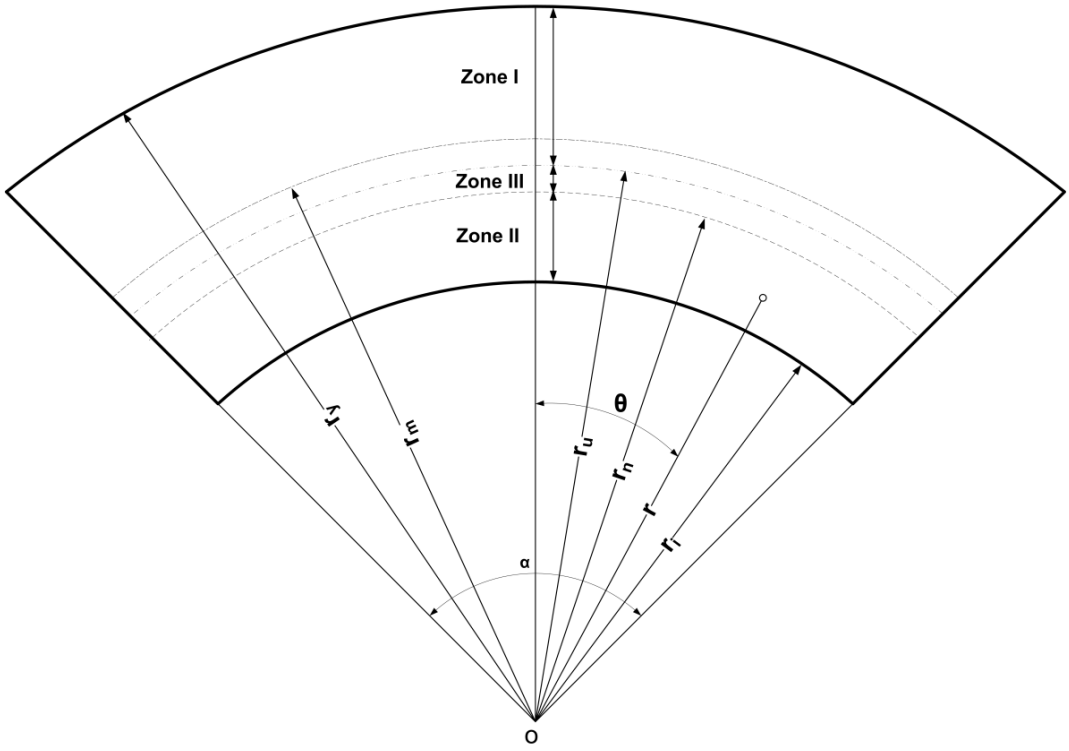

(a)

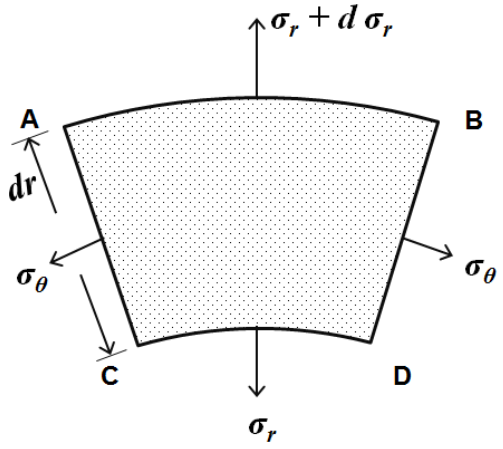

(b)

Figure 33. Tan et al.'s pure bending model (a) classification of zones in analytical pure bending model for monolithic sheet; (b) stresses acting on an element (A-B-C-D) of the bend specimen.

Force acting on upper side $= (\sigma_r + d\sigma_r)(r + dr)d\theta$ (3-1)

Force acting on lower side $= \sigma_r r d\theta$ (3-2)

Equating the left and right side forces = $\sigma_\theta dr$ (3-3)

Radial forces on the top face, F_t $= (\sigma_r + d\sigma_r)(r + dr)d\theta$

$= (r\sigma_r + rd\sigma_r + \sigma_r dr + drd\sigma_r)d\theta$

or $F_t \approx (r\sigma_r + rd\sigma_r + \sigma_r dr)d\theta$ (neglecting smaller order quantity, $drd\sigma_r$)

Radial forces on the bottom face, $F_b = (\sigma_r r d\theta + rd\sigma_r + \sigma_r dr) + 2(\sigma_\theta dr)\sin(d\theta/2)$

or $F_b \approx (\sigma_r r d\theta + \sigma_\theta drd\theta)$ (considering $Sin(d\theta/2) \approx (d\theta/2)$)

Force equilibrium in the radial direction ($F_t = F_b$) gives,

$$(r\sigma_r + rd\sigma_r + \sigma_r dr)d\theta = \sigma_r r d\theta + \sigma_\theta drd\theta \quad (3\text{-}4)$$

$$rd\sigma_r d\theta = \sigma_\theta drd\theta - \sigma_r drd\theta$$

$$r\frac{d\sigma_r}{dr} = \sigma_\theta - \sigma_r \quad (3\text{-}5)$$

The equilibrium equation of pure bending is generally represented in the form,

$$\frac{d\sigma_r}{dr} = \frac{\sigma_\theta - \sigma_r}{r} \tag{3-6}$$

3.1.2. Hill's Thickness Change Equation

In order to maintain volume constancy during bending, the strain increment from Hill's bending theory is given as,

$$\mathrm{d}\varepsilon_\theta = \text{-}\mathrm{d}\varepsilon_\mathrm{r} = \frac{dt}{t} = -\left(1 - \frac{r_n^{\,2}}{r_i r_y}\right)\frac{d\alpha}{2\alpha} \tag{3-7}$$

where, α is the bend angle. The Hill's general theory of pure bending shows that the neutral layer r_n, which initially coincides with the middle surface r_m moves towards the inner surface r_i during bending.

3.1.3. Tangential Strain Equation

During neutral axis shift there exists a surface that has been compressed and then elongated by the same amount to regain its initial length. The layer is known as unstretched surface layer corresponding to a radial distance of r_u. Therefore the true tangential strain of an element located at radius r is defined as,

$$\varepsilon_\theta = \ln\left(\frac{r}{r_u}\right) \tag{3-8}$$

3.1.4. Proska's Relative Thickness - Curvature Relation

Relative curvature (η) = $\frac{t}{r_m} = \frac{r_y - r_i}{(r_y + r_i)/2}$

(3-9)

Relative curvature (κ) = $\frac{t}{r_m} = \frac{r_y - r_i}{(r_y + r_i)/2}$

$$\kappa = \frac{t}{r_m} = \frac{2(r_y - r_i)}{r_y + r_i}$$

(3-10)

Radius of curvature of neutral fiber (ρ) = $\frac{r_n}{r_u}$

(3-11)

From volume constancy, r_u . *to* = r_m . *t*

$$r_u = r_m . \left(\frac{t}{t_o} \right)$$

$$r_u = r_m . \eta$$

(3-12)

$$r_u = \frac{(r_y + r_i)}{2} . \frac{(r_y - r_i)}{t_o}$$

Radius of unstretched fiber *(r_u):*

$$r_u = \frac{(r_y^{\,2} - r_i^{\,2})}{2.t_o}$$

(3-13)

From the definition of relative curvature, we derive the radius of inner and outer fiber as,

$$r_i = r_m(1-\kappa/2) \tag{3-14}$$

$$r_y = r_m(1+\kappa/2) \tag{3-15}$$

From the definition of radius of curvature of neutral fiber,

$$r_n = r_m.\eta.\rho \tag{3-16}$$

The volume fraction of the material contained between the fiber of radius r and inside radius r_i is defined as,

$$\lambda = \frac{r^2 - r_i^2}{r_y^2 - r_i^2} \tag{3-17}$$

Therefore the volume fraction of material between the neutral radius and inner radius is given as,

$$\lambda_n = \frac{r_n^2 - r_i^2}{r_y^2 - r_i^2} \tag{3-18}$$

Substituting the appropriate radius terms,

$$\lambda_n = \frac{r_m^2\eta^2\rho^2 - r_m^2(1-\kappa/2)^2}{r_m^2(1+\kappa/2)^2 - r_m^2(1-\kappa/2)^2}$$

$$\lambda_n = \frac{\eta^2\rho^2 - (1-\kappa/2)^2}{2\kappa} \tag{3-19}$$

By volume constancy relation, $r_u \,.\, t_o = r_m \,.\, t$ and Equation (3-9) we obtain,

$$r_u = r_m.\eta \tag{3-20}$$

Now tangential strain is given as,

$$\varepsilon_\theta = \ln\left(\frac{r}{r_y}\right) = \ln\left(\frac{r}{r_m}\right) - \ln\eta \tag{3-21}$$

From equation (3-18),

$$r^2 = \lambda(r_y{}^2 - r_i{}^2) + r_i{}^2$$

Dividing both sides by $r_m{}^2$

$$\frac{r^2}{r_m{}^2} = \frac{\lambda(r_y{}^2 - r_i{}^2)}{r_m{}^2} + \frac{r_i{}^2}{r_m{}^2} = \frac{\lambda[r_m{}^2(1+\kappa/2)^2 - r_m{}^2(1+\kappa/2)^2}{r_m{}^2} + \frac{r_m{}^2(1+\kappa/2)^2}{r_m{}^2}$$

$$\frac{r^2}{r_m{}^2} = 2\lambda\kappa + (1-\kappa/2)^2$$

Taking log on both sides,

$$\ln\frac{r}{r_m} = \frac{1}{2}\ln[(1-\kappa/2)^2 + 2\lambda\kappa] \tag{3-22}$$

Substituting equation (3-22) into equation (3-21),

$$\varepsilon_\theta = \frac{1}{2}\ln[(1-\kappa/2)^2 + 2\lambda\kappa] - \ln\eta \tag{3-23}$$

Now, the tangential strain ε_θ is a function of relative curvature (κ), relative thickness (η) and volume fraction (λ). Partially differentiating ε_θ, with respect to κ, η and λ,

$$d\varepsilon_\theta = \left(\frac{\partial \varepsilon_\theta}{\partial \kappa}\right) d\kappa + \left(\frac{\partial \varepsilon_\theta}{\partial \eta}\right) d\eta + \left(\frac{\partial \varepsilon_\theta}{\partial \lambda}\right) d\lambda \tag{3-24}$$

Assuming that the volume fraction of material λ is a constant i.e. (λ=constant),

$$d\varepsilon_\theta = \left(\frac{\partial \varepsilon_\theta}{\partial \kappa}\right) d\kappa + \left(\frac{\partial \varepsilon_\theta}{\partial \eta}\right) d\eta \tag{3-25}$$

Substituting for ε_θ from equation (3-23),

$$d\varepsilon_\theta = \frac{1}{2}\left[\frac{-(1-\kappa/2)+2\lambda}{(1-\kappa/2)^2+2\lambda\kappa}\right] d\kappa - \frac{d\eta}{\eta} \tag{3-26}$$

At the neutral surface ($\lambda=\lambda_n$), the circumferential strain increment equals zero, i.e., $d\varepsilon_\theta = 0$. Applying it to ((3-26), the following equation is obtained,

$$\frac{d\eta}{d\kappa} = -\frac{\eta}{2}\left[\frac{1-2\lambda_n-\kappa/2}{(1-\kappa/2)^2+2\lambda_n\kappa}\right] \tag{3-27}$$

From equation (3-19) we have,

$$\lambda_n = \frac{\eta^2\rho^2 - (1-\kappa/2)^2}{2\kappa}$$

$$2\kappa\lambda_n = \eta^2\rho^2 - (1-\kappa/2)^2 \tag{3-28}$$

By rearranging the terms in equation (3-27) and substituting equation (3-28),

$$\frac{d\eta}{d\kappa} = -\frac{\eta}{2}\left[\frac{1-2\lambda_n-\kappa/2}{(1-\kappa/2)^2+2\lambda_n\kappa}\right] = -\frac{\eta}{2\kappa}\left[\frac{\kappa-2\lambda_n\kappa-\kappa^2/2}{(1-\kappa/2)^2+2\lambda_n\kappa}\right]$$

$$\frac{d\eta}{d\kappa} = -\frac{\eta}{2\kappa}\left[\frac{1-\kappa^2/4}{\eta^2\rho^2}-1\right] \tag{3-29}$$

3.1.5. Stress Equations: Ludwik Power Hardening Law

Von Mises yield criterion

$$\sigma_{ys}\left(=\bar{\sigma}\right) = \frac{1}{\sqrt{2}}\left[(\sigma_1-\sigma_2)^2+(\sigma_2-\sigma_3)^2+(\sigma_3-\sigma_1)^2\right]^{1/2} \tag{3-30}$$

In case of uniaxial tension along rolling direction,

$$\bar{\sigma} = \frac{1}{\sqrt{2}}\left[(\sigma_1-0)^2+(0-0)^2+(0-\sigma_1)^2\right]^{1/2}$$

$$\bar{\sigma} = \frac{\sqrt{2}}{\sqrt{2}}\sigma_1$$

Therefore, effective stress is the applied stress (X),

$$\bar{\sigma} = \sigma_1 = X$$

Similarly, effective strain,

$$\bar{\varepsilon} = \varepsilon_1$$

For the case of plane strain bending,

Von Mises effective stress,

$$\bar{\sigma} = \frac{\sqrt{3}}{2}\left(\sigma_\theta - \sigma_r\right) \tag{3-31}$$

Von Mises effective strain,

$$\bar{\varepsilon} = \int \sqrt{\frac{2}{3} d\varepsilon_{ij} d\varepsilon_{ij}} \tag{3-32}$$

$$d\varepsilon_{ij} = \begin{vmatrix} d\varepsilon_\theta & 0 & 0 \\ 0 & d\varepsilon_r & 0 \\ 0 & 0 & 0 \end{vmatrix} = \begin{vmatrix} d\varepsilon_\theta & 0 & 0 \\ 0 & -d\varepsilon_\theta & 0 \\ 0 & 0 & 0 \end{vmatrix}$$

$$d\varepsilon_{ij}.d\varepsilon_{ij} = \begin{vmatrix} d\varepsilon_\theta & 0 \\ 0 & -d\varepsilon_\theta \end{vmatrix} . \begin{vmatrix} d\varepsilon_\theta & 0 \\ 0 & -d\varepsilon_\theta \end{vmatrix} = \left(d\varepsilon_\theta^{\,2} + d\varepsilon_\theta^{\,2}\right) = 2d\varepsilon_\theta^{\,2}$$

Therefore,

$$\bar{\varepsilon} = \sqrt{\frac{2}{3}} . \int \sqrt{2 d\varepsilon_\theta^{\,2}}$$

$$\bar{\varepsilon} = \frac{2}{\sqrt{3}}\left(\varepsilon_\theta\right) \tag{3-33}$$

The equivalent stress is obtained from von Mises criterion

$$\bar{\sigma} = \frac{1}{\sqrt{2}}\left[(\sigma_\theta - \sigma_w)^2 + (\sigma_w - \sigma_r)^2 + (\sigma_r - \sigma_\theta)^2\right]^{1/2}$$

In plane strain bending,

$$\sigma_w = \frac{\sigma_\theta + \sigma_r}{2}$$

Therefore,

$$\bar{\sigma} = \frac{1}{\sqrt{2}}\left[\left(\sigma_\theta - \frac{\sigma_\theta + \sigma_r}{2}\right)^2 + \left(\frac{\sigma_\theta + \sigma_r}{2} - \sigma_r\right)^2 + (\sigma_r - \sigma_\theta)^2\right]^{1/2}$$

$$\bar{\sigma} = \frac{\sqrt{3}}{2}(\sigma_\theta - \sigma_r) \tag{3-34}$$

According to Tan's model the effective stress and strain in plane strain bending is equal to the effective stress and strain in uniaxial tension.

$$\bar{\sigma} = X = \frac{\sqrt{3}}{2}(\sigma_\theta - \sigma_r)$$

$$(\sigma_\theta - \sigma_r) = \frac{2}{\sqrt{3}} X \tag{3-35}$$

$$\bar{\varepsilon} = \varepsilon_1 = \frac{2}{\sqrt{3}}\varepsilon_\theta \tag{3-36}$$

Through-thickness region of the monolithic sheet is classified as tension, compression and reverse loaded zone as shown in Figure 34. The hardening law is applied to the equivalent stress for each of the zones as shown in Table 4.

Equating the equilibrium equation (3-6) and effective stress equation (3-34) gives the following differential equation for the radial stress,

$$r\frac{d\sigma_r}{dr} = +\frac{2}{\sqrt{3}}\bar{\sigma} \tag{3-37}$$

On, substituting Ludwik hardening law for the effective stress at appropriate zones, one obtains the following differential equations.

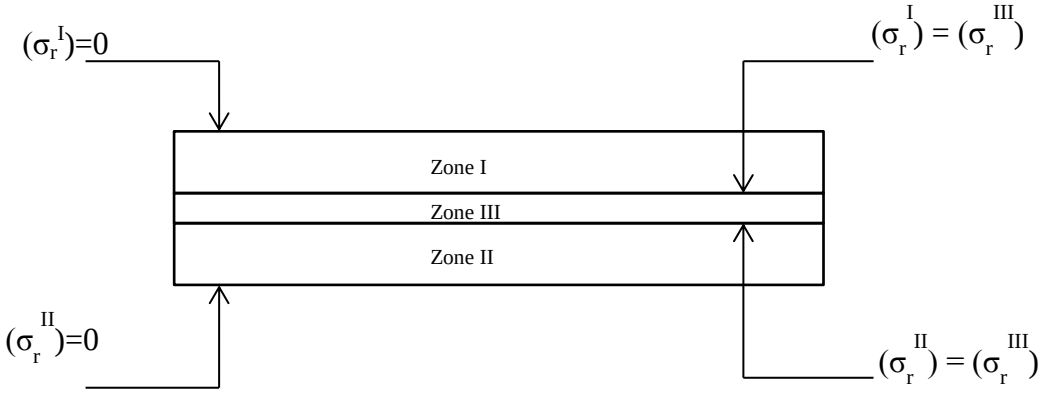

Figure 34. Boundary condition used for monolithic bend specimen.

Table 4. Ludwik hardening law forms applied to different zones through the thickness.

Zone I: $r_u \leq r \leq r_y$	$\sigma = \sigma_0 + K(\varepsilon)^{n_L}$	$\varepsilon = \ln\left(\frac{r}{r_u}\right)$
Zone II: : $r_i \leq r \leq r_n$	$\sigma = \sigma_0 + K(\varepsilon)^{n_L}$	$\varepsilon = \ln\left(\frac{r_u}{r}\right)$
Zone III: $r_n \leq r \leq r_u$ (Reverse hardening due to B.E)	$\sigma = \sigma_0 - K\lvert\varepsilon_p\rvert^{n_L}$ ε_p – Compressive pre-strain	$\varepsilon = \ln\left(\frac{r_u}{r}\right)$

ZONE I (Tension)

$$r\frac{d\sigma_r}{dr} = \frac{2}{\sqrt{3}}\left[\sigma_0 + K\left(\varepsilon_p\right)^{n_L}\right]$$

$$r\frac{d\sigma_r}{dr} = \frac{2}{\sqrt{3}}\left[\sigma_0 + K\left(\frac{2}{\sqrt{3}}\varepsilon_\theta\right)^{n_L})\right]$$

$$r\frac{d\sigma_r}{dr} = \frac{2}{\sqrt{3}}\left[\sigma_0 + K\left(\frac{2}{\sqrt{3}}\ln\frac{r}{r_u}\right)^{n_L}\right] \qquad (3\text{-}38)$$

ZONE II (Compression)

$$r\frac{d\sigma_r}{dr} = -\frac{2}{\sqrt{3}}\left[\sigma_0 + K\left(\frac{2}{\sqrt{3}}\ln\frac{r_u}{r}\right)^{n_L}\right] \qquad (3\text{-}39)$$

ZONE III (Compression →Tension)

$$r\frac{d\sigma_r}{dr} = \frac{2}{\sqrt{3}}\left[\sigma_0 - K\left(\frac{2}{\sqrt{3}}\ln\frac{r_u}{r}\right)^{n_L}\right] \qquad (3\text{-}40)$$

3.1.6. Radial Stress – Ludwik Law

(i) **ZONE I** : $r_u \le r \le r_y$

$$r\frac{d\sigma_r}{dr} = \frac{2}{\sqrt{3}}\left[\sigma_0 + K\left(\frac{2}{\sqrt{3}}\ln\frac{r}{r_u}\right)^{n_L}\right]$$

$$d\sigma_r = \sigma_0 \frac{2}{\sqrt{3}}\left(\frac{dr}{r}\right) + K\frac{2}{\sqrt{3}}\left(\frac{2}{\sqrt{3}}\right)^{n_L}\left(\ln\frac{r}{r_u}\right)^{n_L}\left(\frac{dr}{r}\right)$$

On integration between the limits $r=r$ and $r=r_y$

$$\int_{\sigma_r}^{0} d\sigma_r = \sigma_0 \frac{2}{\sqrt{3}}\int_{r}^{r_y}\frac{dr}{r} + K\left(\frac{2}{\sqrt{3}}\right)^{n_L+1}\int_{r}^{r_y}\frac{\left(\ln\frac{r}{r_u}\right)^{n_L}}{r}\,dr$$

$$\int\frac{(\ln ax)}{x}dx = \frac{(\ln ax)^{n+1}}{n+1}$$

$$(0-\sigma_r) = \sigma_0\frac{2}{\sqrt{3}}\left(\ln\frac{r_y}{r}\right) + K\left(\frac{2}{\sqrt{3}}\right)^{n_L+1}\left[\frac{\left(\ln\frac{r}{r_u}\right)^{n_L+1}}{n_L+1}\right]_r^{r_y}$$

$$\sigma_r^{\ I} = -k_1\left(\ln\frac{r_y}{r_u} - \ln\frac{r}{r_u}\right) - k_2\left[\left(\ln\frac{r_y}{r_u}\right)^{n_L+1} - \left(\ln\frac{r}{r_u}\right)^{n_L+1}\right] \qquad (3\text{-}41)$$

$$k_1 = \frac{2}{\sqrt{3}}\sigma_0$$

$$k_2 = \frac{K}{n_L+1}\left(\frac{2}{\sqrt{3}}\right)^{n_L+1}$$

(ii) **<u>ZONE II</u>** : $r_i \le r \le r_n$

$$r\frac{d\sigma_r}{dr} = -\frac{2}{\sqrt{3}}\left[\sigma_0 + K\left(\frac{2}{\sqrt{3}}\ln\frac{r_u}{r}\right)^{n_L}\right]$$

$$d\sigma_r = -\sigma_0\frac{2}{\sqrt{3}}\left(\frac{dr}{r}\right) - K\left(\frac{2}{\sqrt{3}}\right)^{n_L+1}\left(\ln\frac{r_u}{r}\right)^{n_L}\left(\frac{dr}{r}\right)$$

On integration between the limits $r=r$ and $r=r_i$

$$\int_0^{\sigma_r} d\sigma_r = -\sigma_0\frac{2}{\sqrt{3}}\int_{r_i}^{r}\frac{dr}{r} - K\left(\frac{2}{\sqrt{3}}\right)^{n_L+1}\int_{r_i}^{r}\frac{\left(\ln\frac{r_u}{r}\right)^{n_L}}{r}\,dr$$

$$\int\frac{1}{x}\left(\ln\frac{1}{x}\right)^n dx = -\frac{\left(\ln\frac{1}{x}\right)^{n+1}}{n+1}$$

$$\sigma_r^{\,II} = \sigma_0\frac{2}{\sqrt{3}}\left(\ln\frac{r_i}{r}\right) + K\left(\frac{2}{\sqrt{3}}\right)^{n_L+1}\int_{r}^{r_i}\frac{\left(\ln\frac{r_u}{r}\right)^{n_L}}{r}\,dr$$

$$\sigma_r^{\,II} = k_1\left(\ln\frac{r_u}{r} - \ln\frac{r_u}{r_i}\right) - k_2\left[\left(\ln\frac{r_u}{r_i}\right)^{n_L+1} - \left(\ln\frac{r_u}{r}\right)^{n_L+1}\right] \qquad (3\text{-}42)$$

(iii) **<u>ZONE III</u>**: $r_n \le r \le r_u$

$$r\frac{d\sigma_r}{dr} = \frac{2}{\sqrt{3}}\left[\sigma_0 - K\left(\frac{2}{\sqrt{3}}\ln\frac{r_u}{r}\right)^{n_L}\right]$$

$$d\sigma_r = \sigma_0\frac{2}{\sqrt{3}}\frac{dr}{r} - K\left(\frac{2}{\sqrt{3}}\right)^{n_L+1}\left(\ln\frac{r_u}{r}\right)^{n_L}\frac{dr}{r}$$

On integration between the limits $r=r$ and $r=r_u$

$$\int_{\sigma_r^{III}}^{\sigma_r^{I}} d\sigma_r = \sigma_0\frac{2}{\sqrt{3}}\int_{r}^{r_u}\frac{dr}{r} - K\left(\frac{2}{\sqrt{3}}\right)^{n_L+1}\int_{r}^{r_u}\left(\ln\frac{r_u}{r}\right)^{n_L}\frac{dr}{r}$$

$$\sigma_r^{\ I} - \sigma_r^{\ III} = k_1\left(\ln\frac{r_u}{r}\right) + k_2\left[\left(\ln\frac{r_u}{r_u}\right)^{n_L+1} - \left(\ln\frac{r_u}{r}\right)^{n_L+1}\right]$$

$$-\sigma_r^{\ III} = k_1\left(\ln\frac{r_u}{r}\right) - k_2\left(\ln\frac{r_u}{r}\right)^{n_L+1} - \sigma_r^{\ I}$$

At $r=r_u$

$$\sigma_r^{\ I} = -k_1\left(\ln\frac{r_y}{r_u}\right) - k_2\left[\left(\ln\frac{r_y}{r_u}\right)^{n_L+1}\right]$$

$$-\sigma_r^{\ III} = k_1\left(\ln\frac{r_u}{r}\right) - k_2\left(\ln\frac{r_u}{r}\right)^{n_L+1} + k_1\left(\ln\frac{r_y}{r_u}\right) + k_2\left[\left(\ln\frac{r_y}{r_u}\right)^{n_L+1}\right]$$

$$\sigma_r^{\ III} = -k_1\left(\ln\frac{r_y}{r_u} + \ln\frac{r_u}{r}\right) - k_2\left[\left(\ln\frac{r_y}{r_u}\right)^{n_L+1} - \left(\ln\frac{r_u}{r}\right)^{n_L+1}\right]$$

(3-43)

It is to be noted that the radial stresses are expected to be continuous across the zonal interfaces. The continuity of radial stress at the neutral fiber that shifts during the bending process is obtained by setting $r = r_n$ in the radial stress equations for those zones which meet at the neutral fiber. By equating the stresses at the neutral fiber boundary (eg: $\sigma_r^{\ II} = \sigma_r^{\ III}$), the Λ parameter necessary for Proksa's thickness – curvature relation (Proksa, 1959) is obtained. The summary of radial and tangential stresses at each zone is shown in Table 5.

3.1.7. Equality Condition

For $r = r_n$

$$\sigma_r^{II} = k_1\left[\left(\ln\frac{r_u}{r_n}\right)-\left(\ln\frac{r_u}{r_i}\right)\right]-k_2\left[\left(\ln\frac{r_u}{r_i}\right)^{n_L+1}-\left(\ln\frac{r_u}{r_n}\right)^{n_L+1}\right]$$

$$\sigma_r^{II} = k_1\left(\ln\frac{r_i}{r_n}\right)-k_2\left[\left(\ln\frac{r_u}{r_i}\right)^{n_L+1}-\left(\ln\frac{r_u}{r_n}\right)^{n_L+1}\right] \qquad (3\text{-}44)$$

and

$$\sigma_r^{III} = -k_1\left(\ln\frac{r_y}{r_u}+\ln\frac{r_u}{r_n}\right)-k_2\left[\left(\ln\frac{r_y}{r_u}\right)^{n_L+1}-\left(\ln\frac{r_u}{r_n}\right)^{n_L+1}\right]$$

$$\sigma_r^{III} = -k_1\left(\ln\frac{r_y}{r_n}\right)-k_2\left[\left(\ln\frac{r_y}{r_u}\right)^{n_L+1}-\left(\ln\frac{r_u}{r_n}\right)^{n_L+1}\right] \qquad (3\text{-}45)$$

Equating σ_r^{II} and σ_r^{III}

$$k_1\left(\ln\frac{r_i}{r_n}\right)-k_2\left[\left(\ln\frac{r_u}{r_i}\right)^{n_L+1}-\left(\ln\frac{r_u}{r_n}\right)^{n_L+1}\right] = -k_1\left(\ln\frac{r_y}{r_n}\right)-k_2\left[\left(\ln\frac{r_y}{r_u}\right)^{n_L+1}-\left(\ln\frac{r_u}{r_n}\right)^{n_L+1}\right]$$

$$\frac{r_n^{\,2}}{r_i.r_y} = \exp\left[\frac{k_2}{k_1}\left[\left(\ln\frac{r_y}{r_u}\right)^{n_L+1}-\left(\ln\frac{r_u}{r_i}\right)^{n_L+1}\right]\right] \qquad (3\text{-}46)$$

Now substituting for the dimensionless parameters,

$$\frac{\rho^2\eta^2 r_m^{\,2}}{\left[\left(1-\frac{\kappa}{2}\right).r_m\right]\left[\left(1+\frac{\kappa}{2}\right).r_m\right]} = \exp\left[\frac{k_2}{k_1}\left[\left(\ln\frac{1+\frac{\kappa}{2}}{\eta}\right)^{n_L+1}-\left(\ln\frac{\eta}{1-\frac{\kappa}{2}}\right)^{n_L+1}\right]\right]$$

Let, $\dfrac{k_2}{k_1}\left[\left(\ln\dfrac{1+\frac{\kappa}{2}}{\eta}\right)^{n_L+1}-\left(\ln\dfrac{\eta}{1-\frac{\kappa}{2}}\right)^{n_L+1}\right] = \Lambda$

$$\frac{\rho^2\eta^2}{\left(1-\frac{\kappa^2}{4}\right)} = \exp[\Lambda] \tag{3-47}$$

3.1.8. Thickness Change Equation

From Equation (3-29),

$$\frac{d\eta}{d\kappa} = -\frac{\eta}{2\kappa}\left[\frac{1-\kappa^2/4}{\eta^2\rho^2}-1\right]$$

Substituting from Equation (3-47), gives the equation for relative thickness.

$$\frac{d\eta}{d\kappa} = -\frac{\eta}{2\kappa}[\exp(-\Lambda)-1] \tag{3-48}$$

Table 5. Summary of radial and tangential stress equation for pure bending of monolithic sheet.

Radial Stress	Tangential Stress
$\sigma_r^{\ I} = -k_1\left(\ln\frac{r_y}{r_u}-\ln\frac{r}{r_u}\right)-k_2\left[\left(\ln\frac{r_y}{r_u}\right)^{n_L+1}-\left(\ln\frac{r}{r_u}\right)^{n_L+1}\right]$	$\sigma_\theta^{\ I} = \frac{2}{\sqrt{3}}\left[\sigma_0 + K\left(\frac{2}{\sqrt{3}}\ln\frac{r}{r_u}\right)^{n_L}\right]+\sigma_r^{\ I}$
$\sigma_r^{\ II} = k_1\left(\ln\frac{r_u}{r}-\ln\frac{r_u}{r_i}\right)-k_2\left[\left(\ln\frac{r_u}{r_i}\right)^{n_L+1}-\left(\ln\frac{r_u}{r}\right)^{n_L+1}\right]$	$\sigma_\theta^{\ II} = -\frac{2}{\sqrt{3}}\left[\sigma_0 + K\left(\frac{2}{\sqrt{3}}\ln\frac{r_u}{r}\right)^{n_L}\right]+\sigma_r^{\ II}$
$\sigma_r^{\ III} = -k_1\left(\ln\frac{r_y}{r_u}+\ln\frac{r_u}{r}\right)-k_2\left[\left(\ln\frac{r_y}{r_u}\right)^{n_L+1}-\left(\ln\frac{r_u}{r}\right)^{n_L+1}\right]$	$\sigma_\theta^{\ III} = \frac{2}{\sqrt{3}}\left[\sigma_0 - K\left(\frac{2}{\sqrt{3}}\ln\frac{r_u}{r}\right)^{n_L}\right]+\sigma_r^{\ III}$

The derived stress and relative thickness equations were coded using Matlab© to obtain the characteristic plots for AA2024 monolithic sheet (3.12 mm thick) monolithic sheets. The flow chart explaining the kinematics of the model to obtain the stresses by solving the ODE equation for relative thickness and curvature is shown in Figure 35.

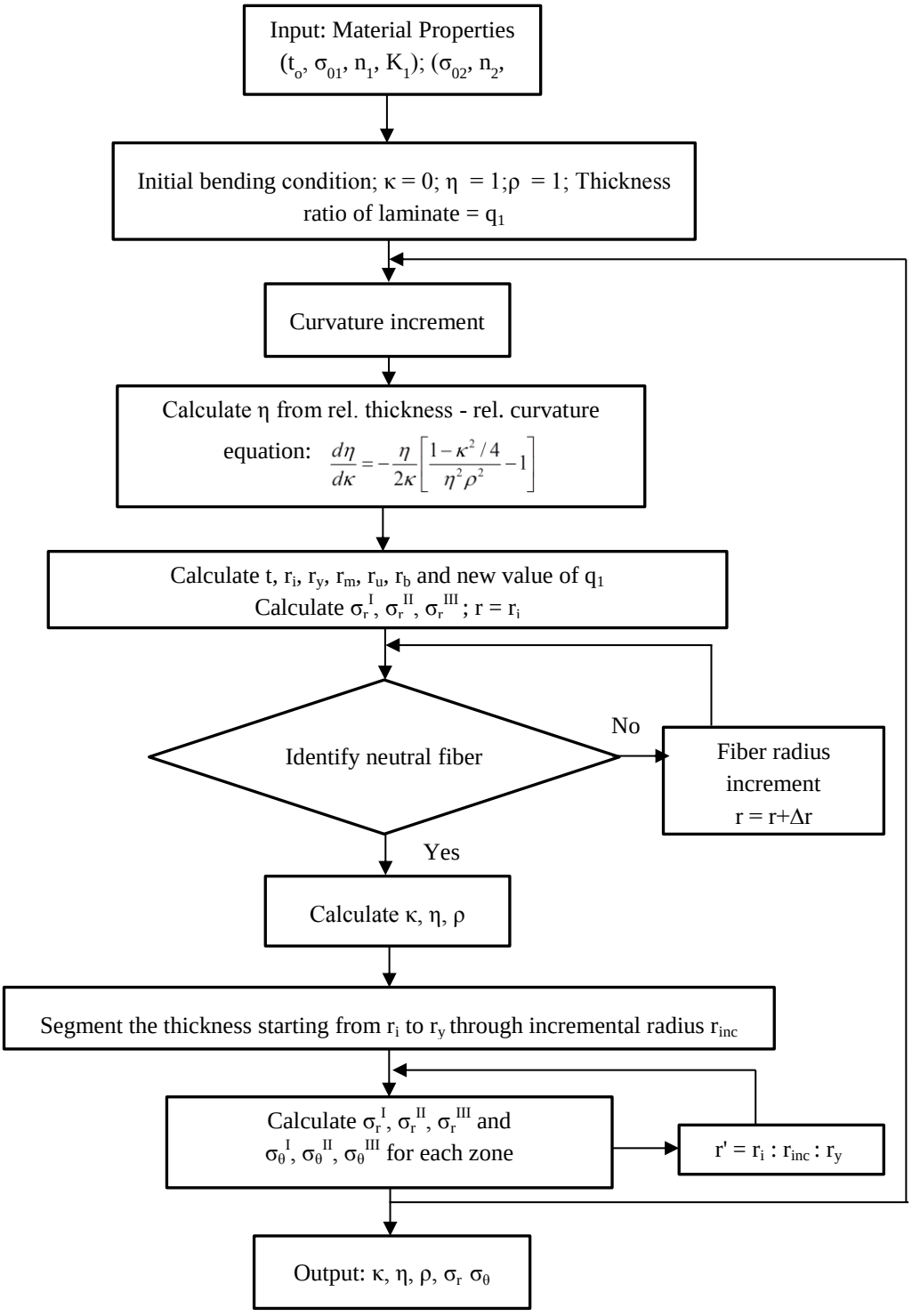

Figure 35. Flowchart showing the calculation steps of Tan's bending model.

3.2. Development of a 4 Zone Model for Pure Bending of Bi-layer Laminates

The derived model equations for the bi-layer and tri-layer laminate follow the same methodology as that for monolithic sheet. For bending of bi-layer laminates, an additional boundary radius parameter (r_b) between the clad and the matrix has been introduced in the framework of Tan et al. model. The bi-layer specimen is termed C-T and C-C when the softer clad layer is on tension and compression sides respectively. The schematic diagrams and corresponding boundary conditions for C-T and C-C bi-layer specimens are shown in Figure 36(a) and Figure 37(a) respectively. The corresponding boundary conditions based on radial stresses are shown in Figure 36(b) and Figure 37(b) respectively. The differential equations for four zone bi-layer laminate models for C-T and C-C cases are presented in Table 6 and Table 7 respectively.

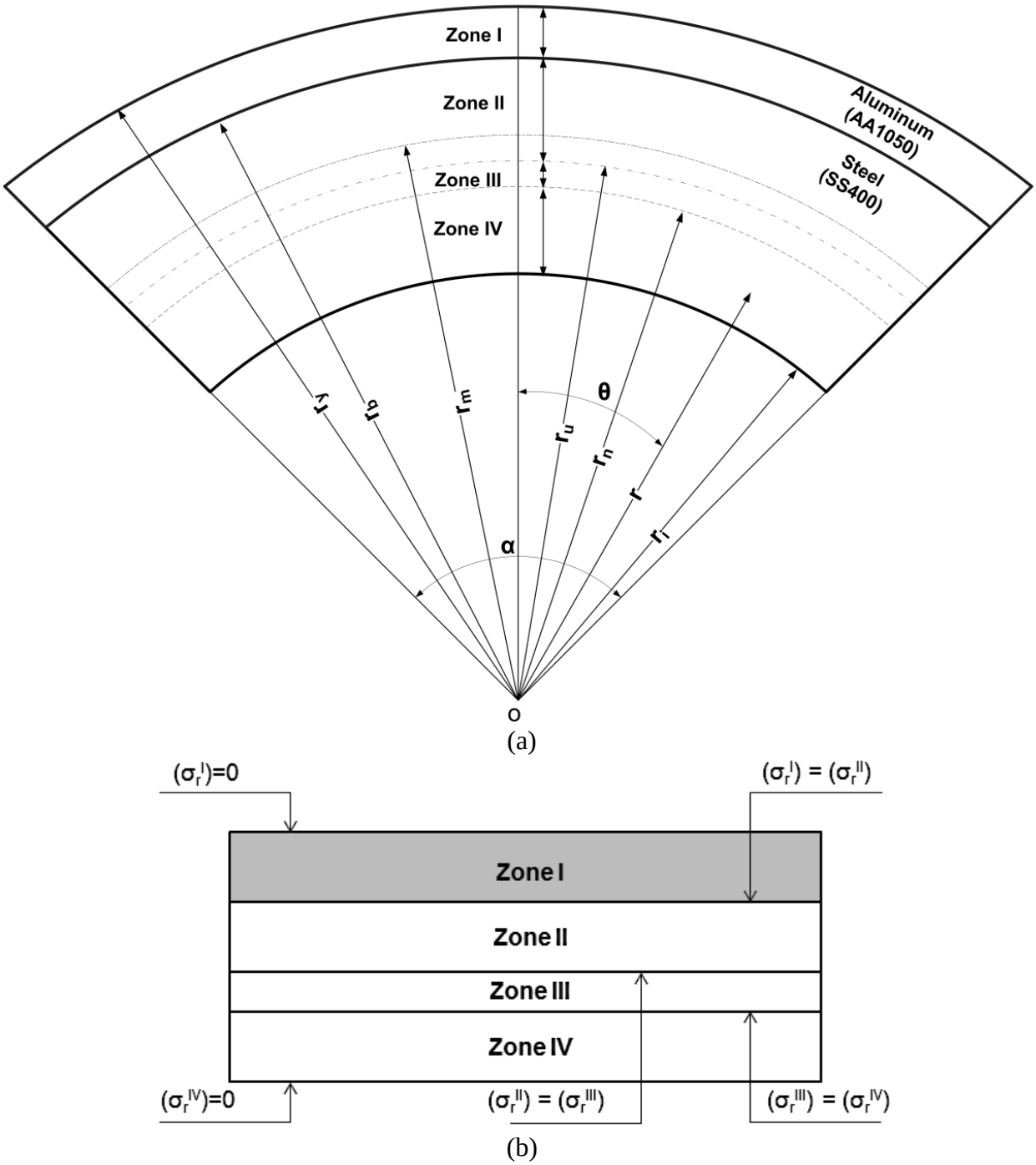

Figure 36. Pure bending model for bi-layer (C-T) laminate, (a) classification of plastic zones; (b) corresponding boundary conditions at zone interfaces.

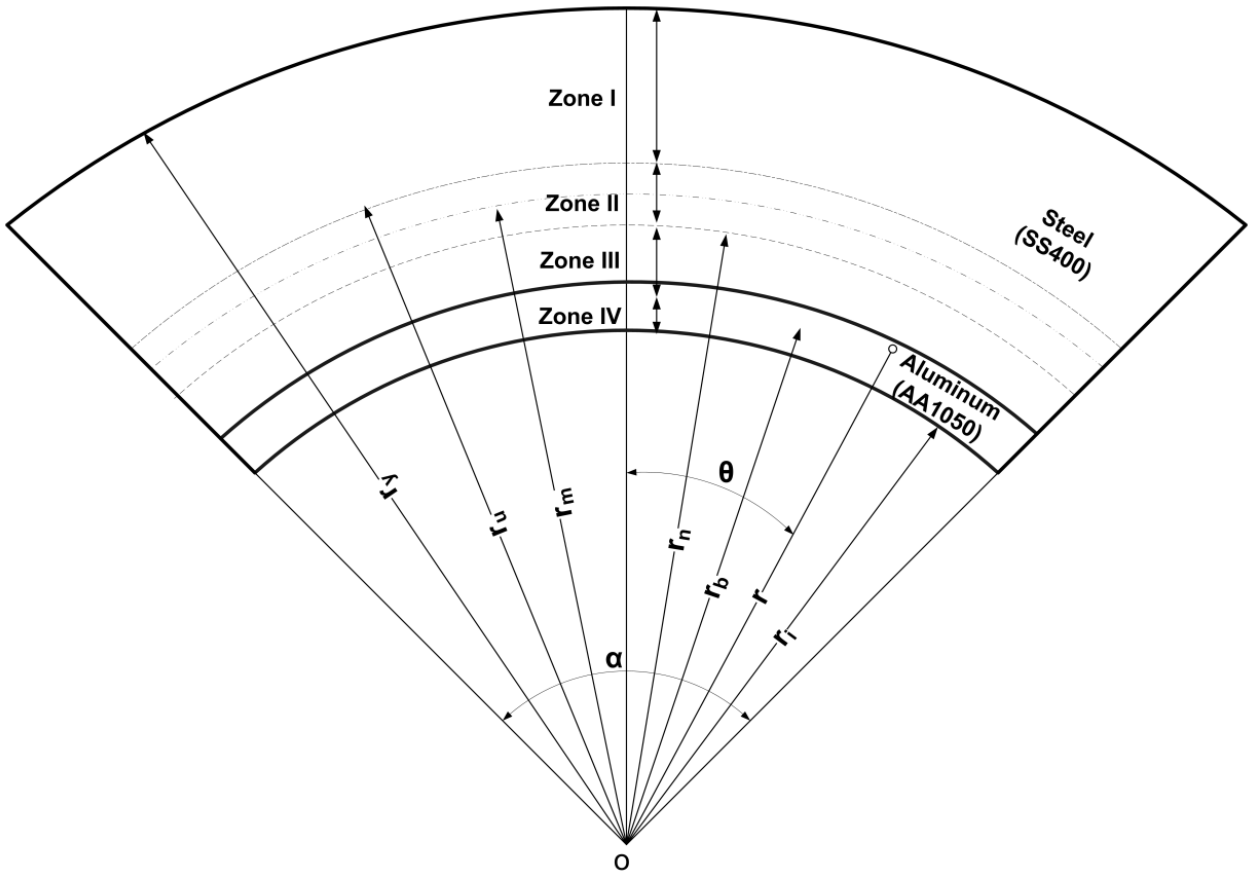

Figure 37. Pure bending model for bi-layer (C-C) laminate, (a) classification of plastic zones; (b) corresponding boundary conditions at zone interfaces.

Table 6. Mathematical expressions for radial stress at each plastic zone for C-T specimen with boundary condition at zone interfaces.

	Ludwik Model	Tangential strain
Zone I $r_y \geq r \geq r_b$	$r\frac{d\sigma_r}{dr} = \frac{2}{\sqrt{3}}\left[\sigma_{02} + K_{L2}\left(\bar{\varepsilon}\right)^{n_{L2}}\right]$	$\varepsilon_\theta = \ln\left(\frac{r}{r_u}\right)$
Zone II $r_b \geq r \geq r_u$	$r\frac{d\sigma_r}{dr} = \frac{2}{\sqrt{3}}\left[\sigma_{01} + K_{L1}\left(\bar{\varepsilon}\right)^{n_{L1}}\right]$	$\varepsilon_\theta = \ln\left(\frac{r}{r_u}\right)$
Zone III $r_u \geq r \geq r_n$	$r\frac{d\sigma_r}{dr} = \frac{2}{\sqrt{3}}\left[\sigma_{01} - K_{L1}\left(\varepsilon_p\right)^{n_{L1}}\right]$	$\varepsilon_\theta = \ln\left(\frac{r_u}{r}\right)$
Zone IV $r_n \geq r \geq r_i$	$r\frac{d\sigma_r}{dr} = -\frac{2}{\sqrt{3}}\left[\sigma_{01} + K_{L1}\left(\bar{\varepsilon}\right)^{n_{L1}}\right]$	$\varepsilon_\theta = \ln\left(\frac{r_u}{r}\right)$

Table 7. Mathematical expressions for radial stress at each zone for C-C specimen with boundary condition at zone interfaces.

	Ludwik Model	Tangential strain
Zone I $r_y \geq r \geq r_u$	$r\frac{d\sigma_r}{dr} = \frac{2}{\sqrt{3}}\left[\sigma_{02} + K_{L2}\left(\bar{\varepsilon}\right)^{n_{L1}}\right]$	$\varepsilon_\theta = \ln\left(\frac{r}{r_u}\right)$
Zone II $r_u \geq r \geq r_n$	$r\frac{d\sigma_r}{dr} = \frac{2}{\sqrt{3}}\left[\sigma_{01} - K_{L1}\left(\varepsilon_p\right)^{n_{L1}}\right]$	$\varepsilon_\theta = \ln\left(\frac{r_u}{r}\right)$
Zone III $r_n \geq r \geq r_b$	$r\frac{d\sigma_r}{dr} = -\frac{2}{\sqrt{3}}\left[\sigma_{01} + K_{L1}\left(\bar{\varepsilon}\right)^{n_{L1}}\right]$	$\varepsilon_\theta = \ln\left(\frac{r_u}{r}\right)$
Zone IV $r_b \geq r \geq r_i$	$r\frac{d\sigma_r}{dr} = -\frac{2}{\sqrt{3}}\left[\sigma_{02} + K_{L2}\left(\bar{\varepsilon}\right)^{n_{L2}}\right]$	$\varepsilon_\theta = \ln\left(\frac{r_u}{r}\right)$

The thickness of clad layer and clad to matrix thickness ratio are expressed by symbols t_c and q_1 respectively. The parameter r_b can be represented in terms of other known parameters as shown below. For C-T specimen,

$$q_1 = \frac{t_c}{t} = \frac{r_y - r_b}{\eta \cdot t_0} \tag{3-49}$$

$$r_b = \left(1 + \frac{\kappa}{2}\right) \cdot r_m - q_1 \cdot \eta \cdot t_0 \tag{3-50}$$

and, for C-C specimen,

$$q_1 = \frac{t_c}{t} = \frac{r_b - r_i}{\eta \cdot t_0} \tag{3-51}$$

$$r_b = \left(1 - \frac{\kappa}{2}\right) \cdot r_m - q_1 \cdot \eta \cdot t_0 \tag{3-52}$$

3.3. Development of a 5 Zone Model for Pure Bending of Tri-layer Laminates

For the tri-layer laminates the zones are categorized by dividing the thickness with respect to outer radius (r_y), unstretched fiber (r_u), neutral fiber (r_n) and inner radius (r_i). For tri-layer laminate sheets, additional boundary radii parameters (r_a and r_b) between the clad and the matrix are defined, making it a five zone model. The schematic diagrams for tri-layer specimens and corresponding boundary condition are shown in Figure 38(a) and (b) respectively. The differential equations for five zone tri-layer laminate model are presented in Table 8.

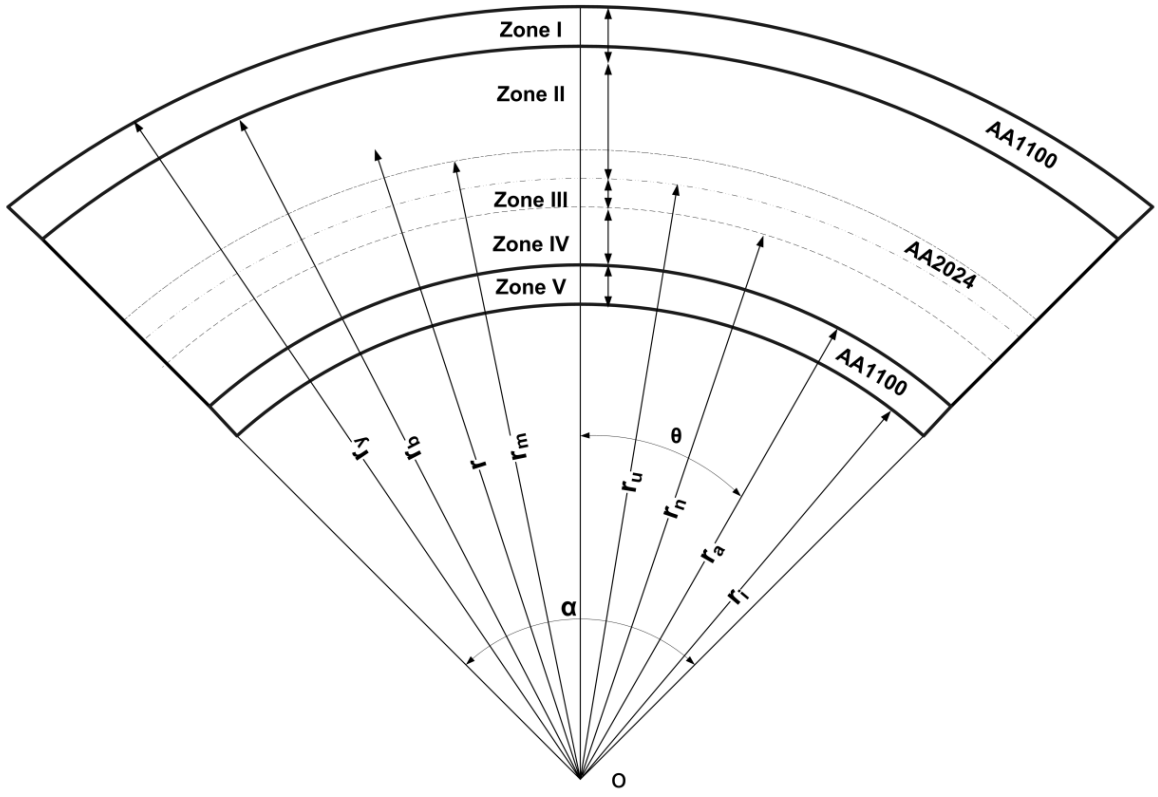

(a)

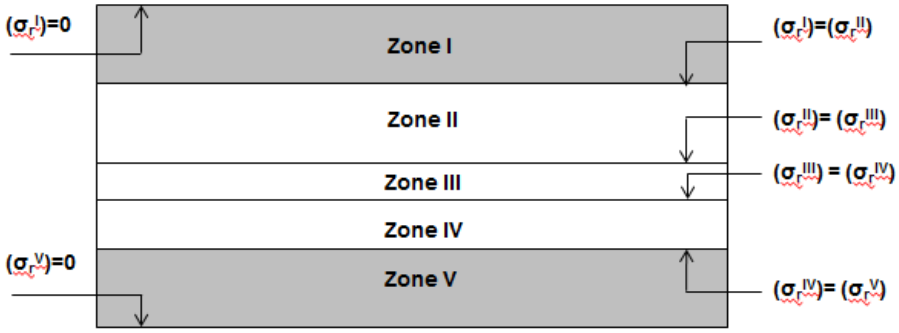

(b)

Figure 38. Pure bending model for tri-layer laminate, (a) classification of plastic zones (b) corresponding boundary conditions at zone interfaces.

Table 8. Differential expression for radial stress at each plastic zone for tri-layer specimen with boundary condition at zone interfaces.

	Ludwik Model	Tangential strain
Zone I $r_y \geq r \geq r_b$	$r\frac{d\sigma_r}{dr} = +\frac{2}{\sqrt{3}}\left[\sigma_{02} + K_2\left(\bar{\varepsilon}\right)^{n_{L2}}\right]$	$\varepsilon_\theta = \ln\left(\frac{r}{r_u}\right)$
Zone II $r_b \geq r \geq r_u$	$r\frac{d\sigma_r}{dr} = \frac{2}{\sqrt{3}}\left[\sigma_{01} + K_1\left(\bar{\varepsilon}\right)^{n_{L1}}\right]$	$\varepsilon_\theta = \ln\left(\frac{r}{r_u}\right)$
Zone III $r_u \geq r \geq r_n$	$r\frac{d\sigma_r}{dr} = \frac{2}{\sqrt{3}}\left[\sigma_{01} - K_1\left(\varepsilon_p\right)^{n_{L1}}\right]$	$\varepsilon_\theta = \ln\left(\frac{r_u}{r}\right)$
Zone IV $r_n \geq r \geq r_a$	$r\frac{d\sigma_r}{dr} = -\frac{2}{\sqrt{3}}\left[\sigma_{01} + K_1\left(\bar{\varepsilon}\right)^{n_{L1}}\right]$	$\varepsilon_\theta = \ln\left(\frac{r_u}{r}\right)$
Zone V $r_a \geq r \geq r_i$	$r\frac{d\sigma_r}{dr} = -\frac{2}{\sqrt{3}}\left[\sigma_{02} + K_2\left(\bar{\varepsilon}\right)^{n_{L2}}\right]$	$\varepsilon_\theta = \ln\left(\frac{r_u}{r}\right)$

Further, the value of the radius of boundary fiber (r_b) between the clad and the matrix is represented in terms of other known parameters. The thickness of clad layers and clad to matrix thickness ratio are expressed by symbols (t_{c1}, t_{c2}) and (q_1, q_2) respectively. The parameters r_a and r_b can be represented in terms of other known parameters as follows:

$$q_1 = \frac{t_{c1}}{t} = \frac{r_y - r_b}{\eta.t_0}$$

$$r_b = r_y - q_1.\eta.t_0 \qquad (3\text{-}53)$$

$$r_y = \left(1 + \frac{\kappa}{2}\right).r_m$$

$$r_b = \left(1 + \frac{\kappa}{2}\right).r_m - q_1.\eta.t_0 \qquad (3\text{-}54)$$

$$q_2 = \frac{t_{c2}}{t} = \frac{r_a - r_i}{\eta . t_0}$$

(3-55)

$$r_a = q_2 . \eta . t_0 + r_i$$

$$r_i = \left(1 - \frac{\kappa}{2}\right) . r_m$$

$$r_a = q_2 . \eta . t_0 + \left(1 - \frac{\kappa}{2}\right) . r_m$$

(3-56)

3.4. Summary of Chapter

The analytical models for bi-layer and tri-layer laminates sheet were developed based on advanced theory of bending. The final forms of radial and tangential stress equations for the 4 zones bilayer and 5 zones tri-layer laminates along with the Λ parameter for relative thickness are summarized in Appendix A. Matlab code for one case of bi-layer laminate C-T case is presented in the Appendix B. Convergence check for the bi-layer and tri-layer models was carried out by applying the same material properties to the laminate and matrix layers. The results are shown in Appendix D. Further, to validate the model results, experimental test method using a rotary test fixture and DIC strain measurement was developed. This work is presented in Chapter 5.

Chapter 4
Experimental Methodology

This chapter presents experimental details pertaining to bend testing and experimental strain measurement. Experimental validation of the numerical bending models was performed using a rotary bend test rig that was capable of producing pure bending with uniform curvature. The test rig was an open concept design that exposed the outside tensile surface for strain measurement. The bend test fixture offered several advantages compared to other designs discussed in the literature review. Strain measurements were carried along the through-thickness and width directions of the specimen using the DIC based optical method.

4.1. Tensile Material Properties of Chosen Sheet Materials

4.1.1. Uniaxial Tensile Test

Tensile material properties for the constituent materials for the laminate, AA1100, AA2024, AA1050 and SS400, were determined from uniaxial tensile tests. AA2024 and AA1100 were received as cold rolled sheet and SS400/AA1050 bi-layer plate was received in explosively welded form. An image of sample SS400/AA1050 bi-layer plate laminate is shown in Figure 39. Tensile specimens were cut from the plate using EDM from the blank material taken at 0 degrees to the rolling direction in the case of AA2024

and AA1100. The specimens were heat treated to fully annealed state according to ASM heat treatment standard as listed in Table 9. The test specimens were cut to 1 inch gauge length (25.4 mm) and 0.25 inch gauge width (6.35 mm) according to ASTM-E8 subsize standard (Figure 40) (ASTM-E8, 2008). Load displacement traces were obtained using a uniaxial MTS hydraulic press (250 kN) under cross head velocities of 2.54 mm/min (initial strain rate 0.1 /min) and 25.4 mm/min (initial strain rate 1 /min) to failure. Strain calculations were carried out using digital image correlation (DIC) technique using standard facet size times facet step (15 x 13) in Aramis Gom (Gom-mbH, 2001). The uniaxial tensile stress–strain curves for AA2024, AA1100, AA1050 and SS400 at different initial strain rates are shown in Figure 41. Plastic portion of the plot was identified using proof stress (0.2% strain) intersection. This data was then subjected to nonlinear least square fitting using the Gauss Newton algorithm in Matlab curve fit tool box to obtain the Ludwik hardening law parameters. A sample curve fit plot and quality of curve fit for AA2024 0.1/min tensile plot is shown in Figure 42 and Table 10, respectively. The summary of yield strength and Ludwik parameters is shown in Table 11.

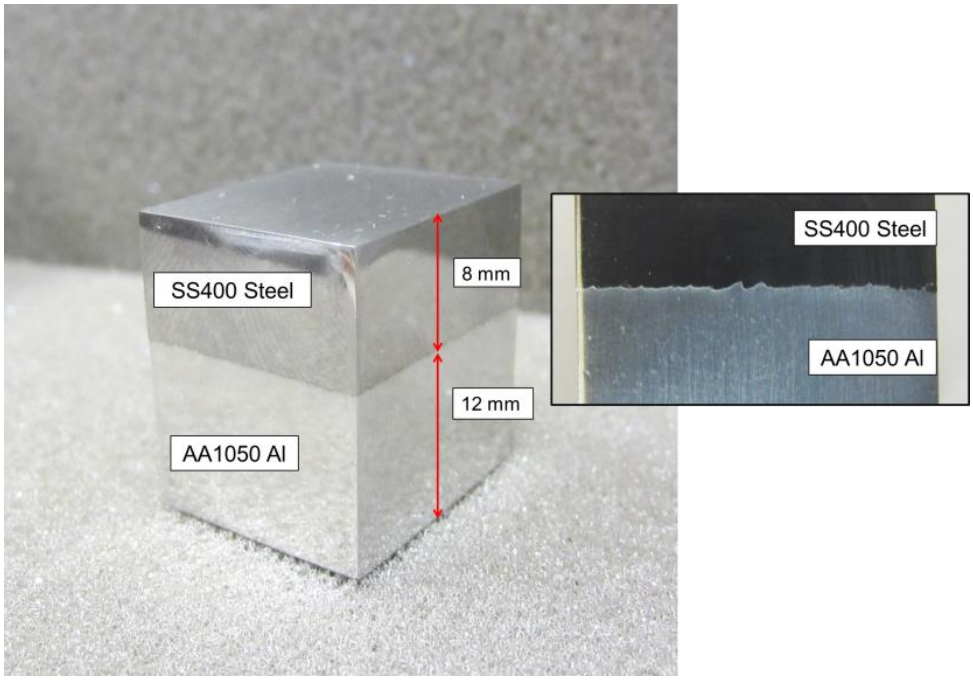

(a)

Figure 39. As received sample view of SS400-AA1050 steel-aluminum bi-layer laminate bonded by explosive welding.

Table 9. Heat treatment parameters for chosen experimental materials (ASM International, 1991).

Material	Annealing Temperature	Annealing Time
AA2024	686 K	2 hours
AA1100	616 K	2 hours
SS400	1163 K	2 hours
AA1050	616 K	2 hours

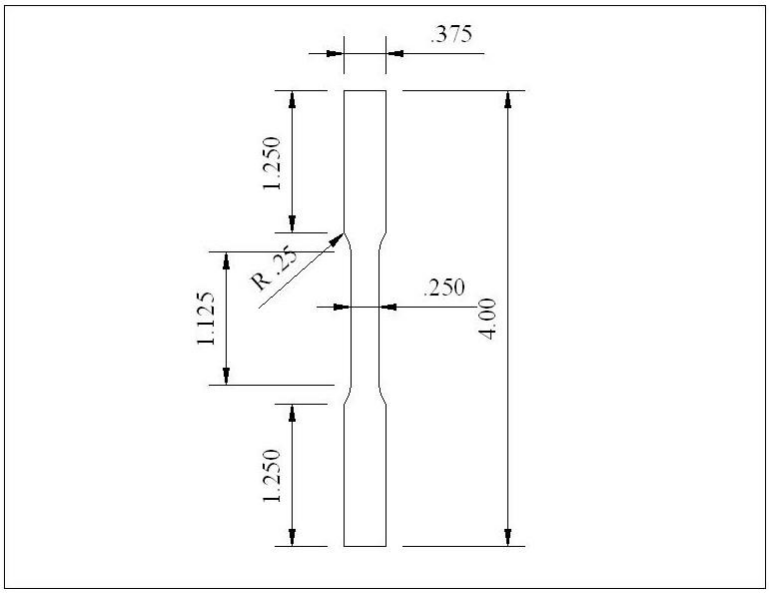

Figure 40. Tensile test specimen dimensions (ASTM-E8 subsize specimen). All dimensions are in inches.

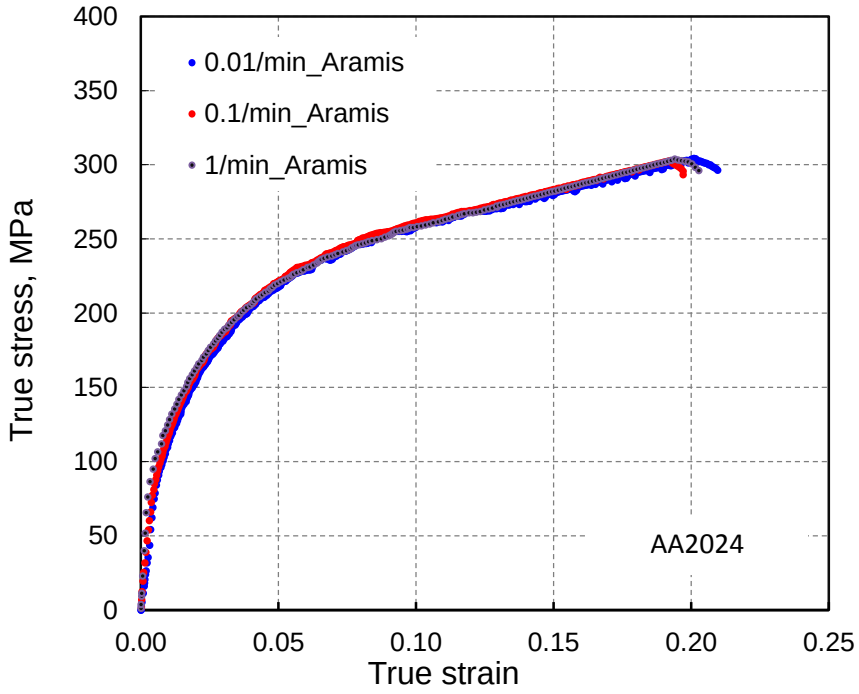

(a)

(figure continued on next page)

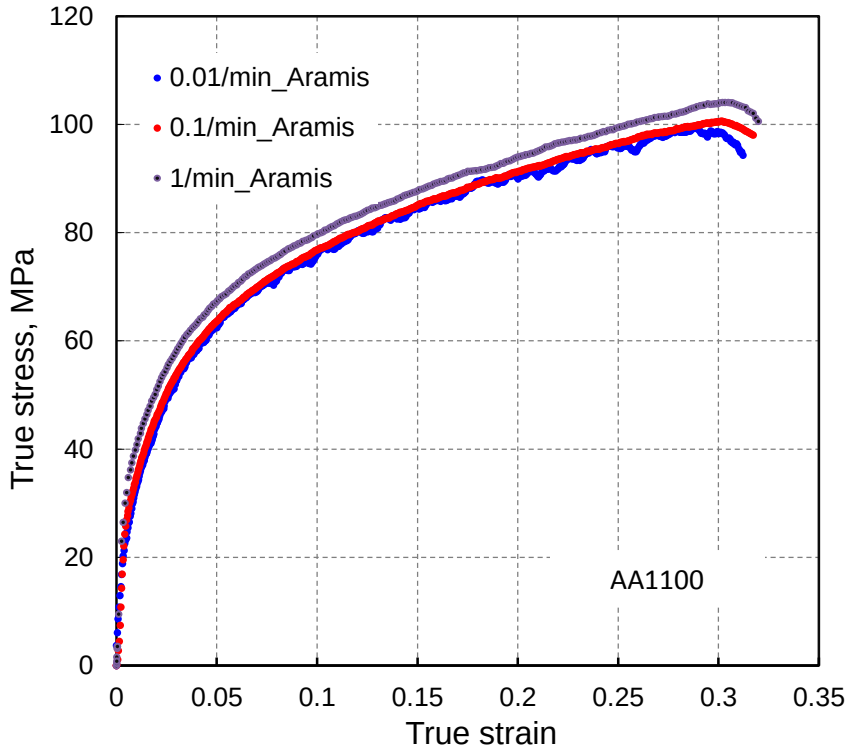

(b)

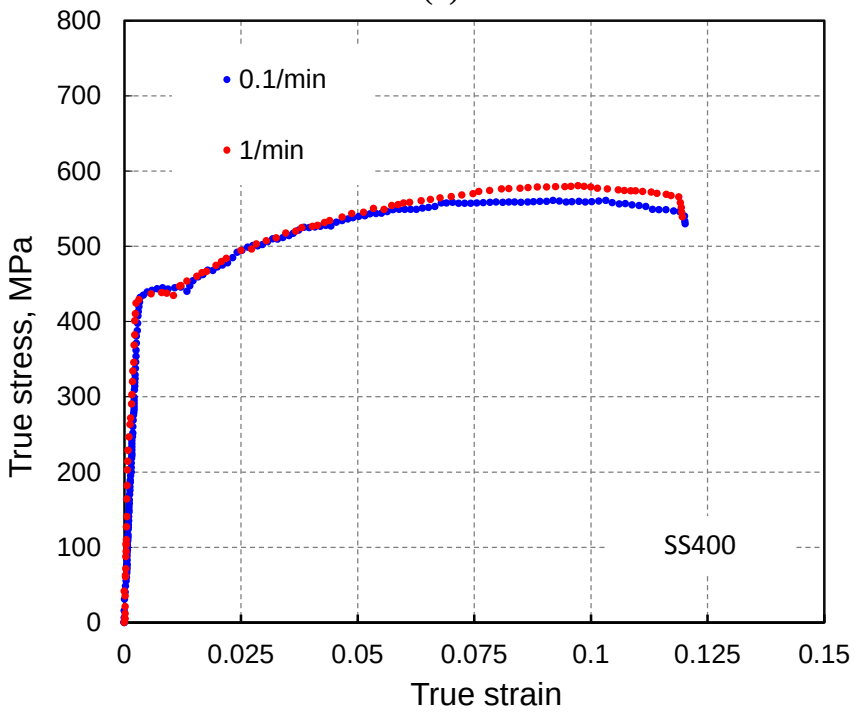

(c)

(figure continued on next page)

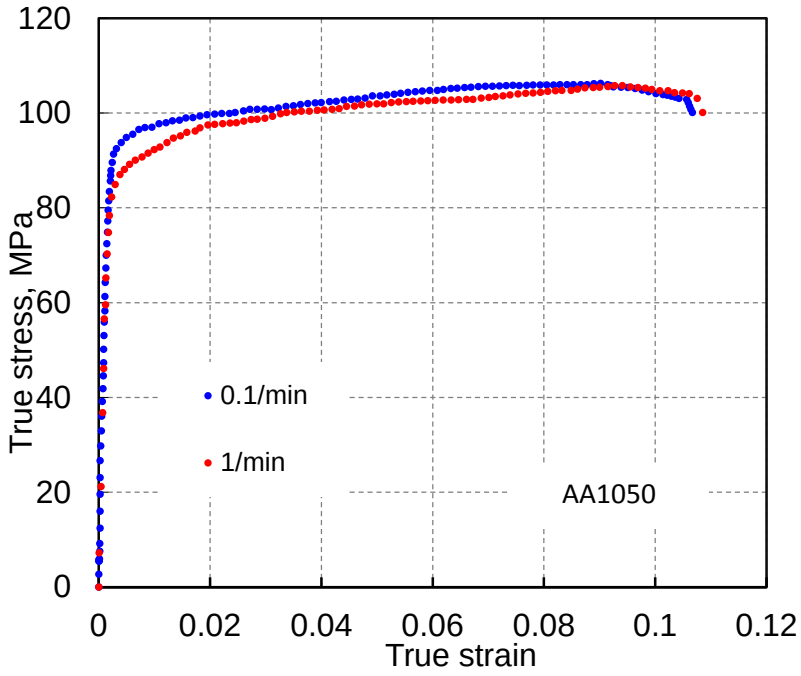

(d)

Figure 41. Uniaxial tensile stress–strain curves for (a) AA2024, (b) AA1100, (c) SS400 and (d) AA1050 at different initial strain rates.

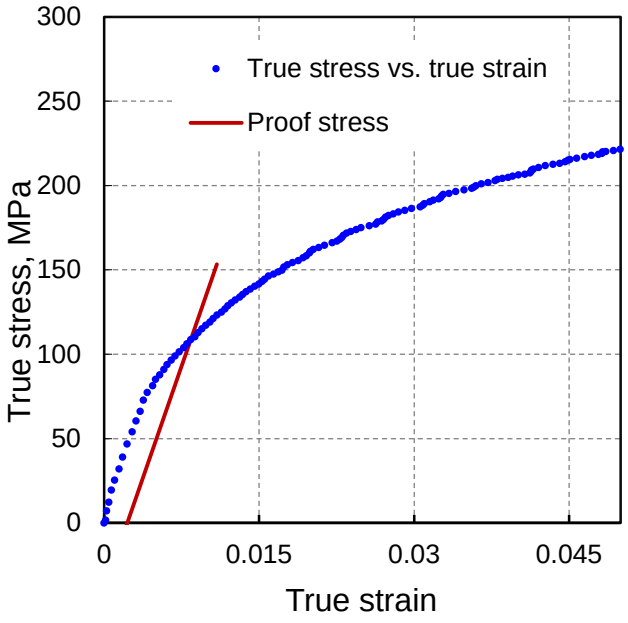

(a)

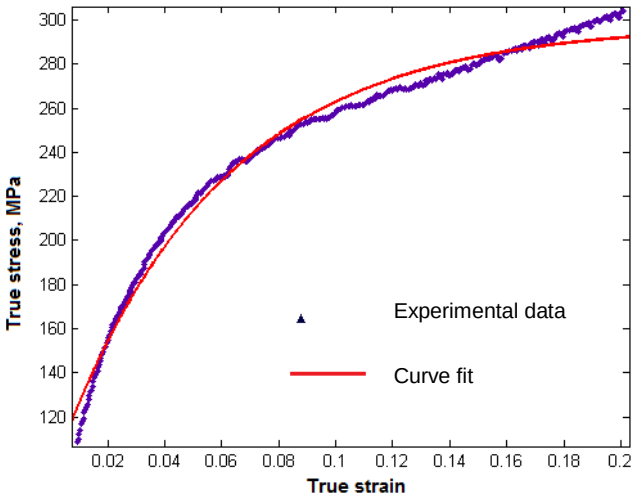

(b)

Figure 42. Tensile property determination, (a) obtaining yield stress by proof stress intersection; (b) non-linear curve fit using Matlab on AA2024 0.1/min tensile plot.

Table 10. Matlab curve fit results for AA2024 0.1/min tensile plot for Ludwik law.

Ludwik hardening law	$\sigma = \sigma_o + K_L(\varepsilon)^{nL}$
Coefficients (with 95% confidence bounds)	K_L =456.4 MPa (441.6, 471.2) n_L = 0.4745 (0.4604, 0.4886) σ_o = 101 MPa
Goodness of fit (sum of squares due to error)	1.367e+004
R-square	0.9679
Adjusted R-square	0.9676

Table 11. Ludwik hardening law parameters from tensile test.

	Ludwik Hardening Parameters		
	σ_o, *MPa*	K_L, *MPa*	n_L
AA2024	101	456	0.48
AA1100	30	127	0.45
AA1050	90	58	0.53
SS400	438	1132	0.83

4.2. Bending Experiments

4.2.1. Rotary Bend Test Fixture and Test Conditions

The test fixture consisted of 4 steel angled arms (2 pairs) that were attached to the top of servo-hydraulic mechanical test system via a cylindrical adapter and a rectangular steel block (see Figure 43). The top ends of the angled arms were pivoted using pins within the steel block. The pivoting connections made the angled arm rotate as the specimen was bent, eliminating stretching forces on the specimen. The bottom ends of the angled arms were attached to a clamp mechanism (one pair on each side of the specimen as shown in

Figure 43(a). These ends were also pivoted to the angled arm using a pinned connection that rotated the clamps to transmit uniform moment across the specimen as indicated by circular arc shape of the initially bent specimen. A bending mandrel was mounted to an actuator located below the suspended bending assembly. The test procedure involved moving the bending mandrel upwards until it came in line contact with the clamped specimen to begin the experiment. Upon further advancement of the mandrel, the pivoting action occurred at the two ends of the each of the four angled arms and the entire specimen length was subjected to pure bending in the early stage of bending. The specimen exhibited uniform curvature in the vicinity of the bending mandrel and non-uniform curvature away from the bending mandrel and towards the two grips (Figure 43 (c)). With continued upward motion of the bending mandrel, specimen grips came in contact with the sides of the bending mandrel which arrested the rotation of the grips resulting in pure stretching of the specimen to fracture in the specimen-mandrel contact region (see Figure 43(d,e)). This rather 'open' design enabled not only attainment of near pure bending condition but also allowed camera access to both the edges and tensile surface of the specimen. The test rig was mounted on a MTS 150KN uniaxial tensile testing system. V-shaped grooves were made on the specimen ends in a separate operation to position them in the clamp grips with similar V-shaped grooves. The specimen was tightened in the grips using threaded bolts. The proposed rotary bend test design was capable of producing 3 stages in bending, namely, (i) initial uniform curvature (i.e., pure bending), (ii) subsequent non-uniform curvature, and (iii) final stretching of the specimen to fracture.

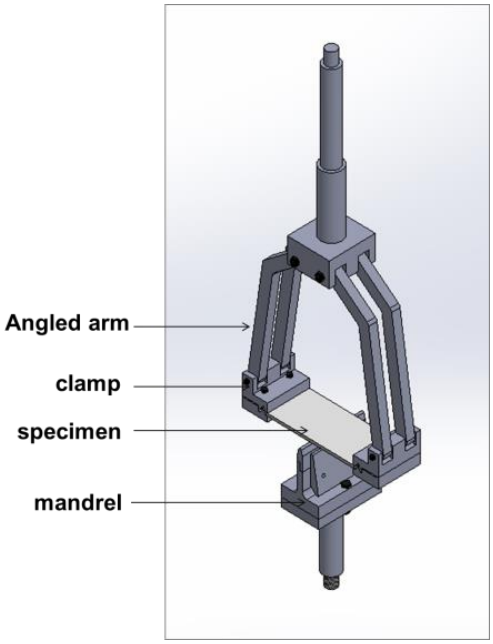

(a)

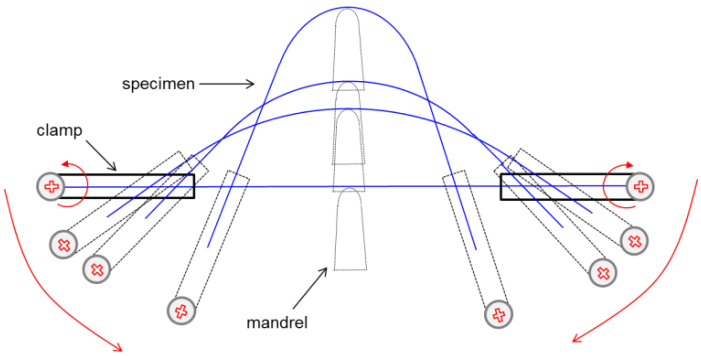

(b)

(c)

(d)

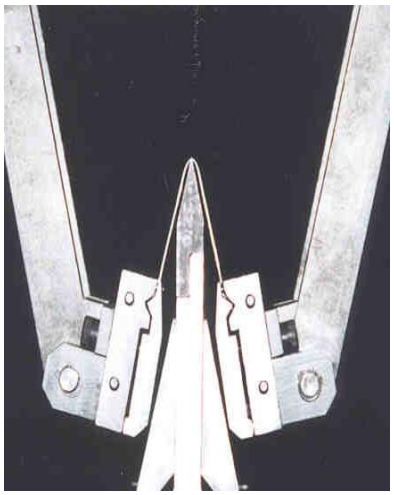

(e)

Figure 43. Experimental bend testing, (a) schematic of rotary bending test rig; (b) specimen curvatures in progressive bending (c) pure bending stage (uniform curvature); (d) bending with non-uniform curvature away from the mandrel; (e) stretching stage. Note that a thinner (1.25 mm) specimen is used to show the stretching stage in Figure 43(e).

However, pure bending region (and thus effective bending length) continued to decrease as the bending progressed (see Figure 43(b)). The material in contact with the bending mandrel stayed in pure bending state up to large plastic strains. For curvature calculation and strain mapping using DIC, a relatively smaller effective bend length (24 mm) in the uniform curvature region was considered instead of the entire specimen length.

Load versus displacement trace for a 1.25 mm thick AA2024 (annealed) specimen is shown in Figure 44 where 3 distinct stages of deformation can be identified. The first stage was characterized by pure bending wherein the entire specimen was bent close to a uniform curvature from the designed rotating clamp and rotating arm mechanism. The normal reaction force across the mid-span of the test specimen was negligible in this first stage of bending. This stage ends at an inflection point between the first and second knee as shown in Figure 44. The second stage involved non-uniform curvature of the specimen but still could be considered uniform curvature close to pure bending in the vicinity of the bending mandrel, as shown earlier in Figure 43(c). This stage occurred between the inflection point and the second knee. The third stage started at the second knee once the clamp rotation was arrested by the bending mandrel. In this stage pure stretching of the bent specimen occurs with rapid increase in load leading to fracture of the specimen. A similar curve up to the stretching stage was received for 3.12 mm sheet. This is shown as an inset in Figure 44.

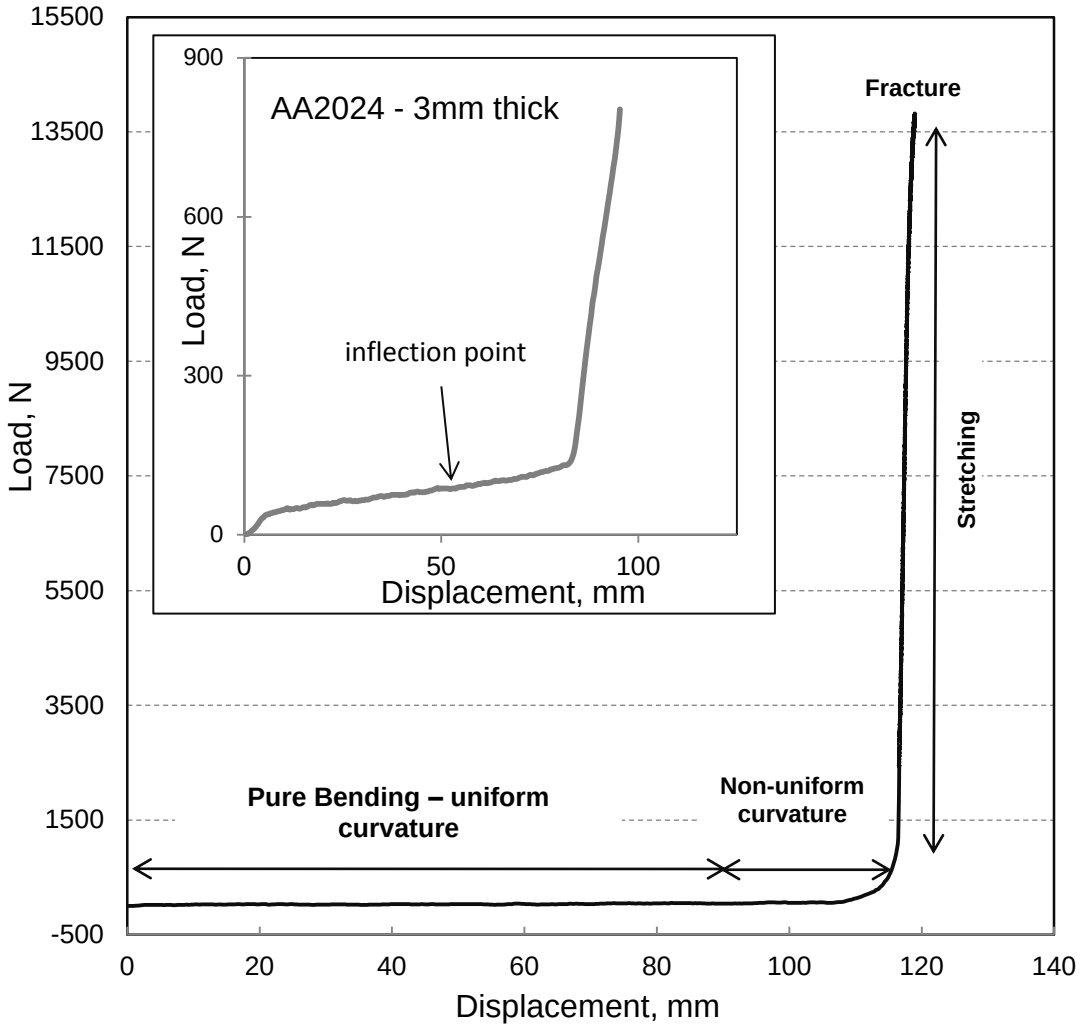

Figure 44. A typical load versus displacement trace from bending test on AA2024 (annealed) sheet of 1.25 mm. Inset to the figure shows, for comparison, another load versus displacement curve for 3.2 mm thick AA2024 sheet.

4.2.2. Strain Measurement using DIC

An online strain measurement procedure based on the DIC method was utilized to obtain full-field strain measurements (i.e., strain maps) using the commercially available Aramis system from Gom (Gom-mbH, 2001). DIC method of strain mapping is a non-contact

technique that uses high resolution digital camera images to track the gray level change of the speckles in small facets (constituting the image) during deformation at regular intervals. By comparing the facets (typically 15 pixels × 15 pixels in the present work) in the current image with the previous reference image or with the initial reference image, the incremental or total strains were obtained. For utilizing the DIC method, the specimen was applied with a fine speckle pattern in the undeformed state over the tensile surface as well as in the thickness region using an air brush. The average speckle size was measured to be 165 μm. Two separate cameras with 1.3 megapixels resolution were used to record the images of size 1280 pixels x 1024 pixels from the two regions (Figure 45). The cameras were mounted such that they were able to move with the punch to maintain a constant distance from the imaged region of the specimen to keep the image in focus during the test. For the pure bending test, a punch speed of 1 mm/sec was selected and camera image acquisition rate was set at 1 frame per second (fps). The initial specimen thickness and width of the AA2024 specimen were chosen to be 3.12 mm and 40 mm and for bi-layer SS400/AA1050 specimens were chosen to be 4 mm and 40 mm respectively. The SS400/AA1050 specimens were machined from a thicker bi-layer plate stock to 10% and 25% clad to matrix thickness ratio using wire EDM machining. Images from through-thickness section and tensile surface were recorded by the two cameras and their corresponding strain maps are shown in Figure 46 and Figure 47 respectively.

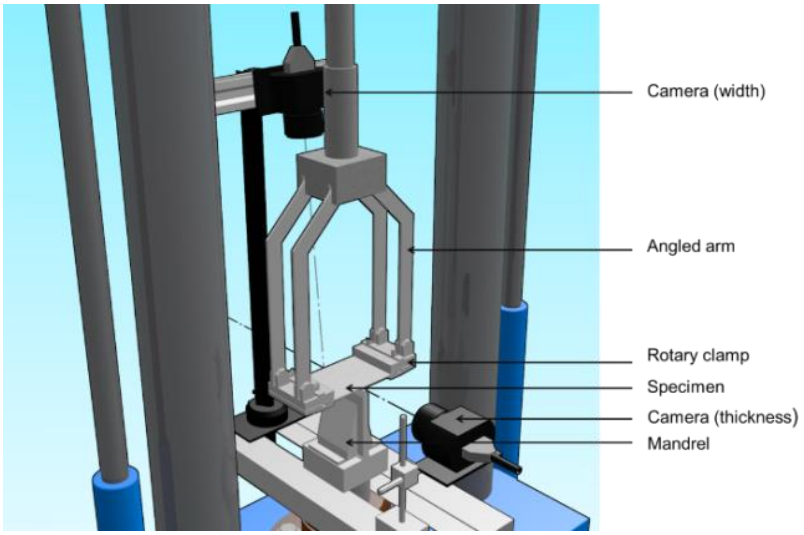

(a)

(b)

Figure 45. Experimental bend test jig, (a) schematic of bend test rig and camera arrangement for strain measurement, (b) experimental test set-up.

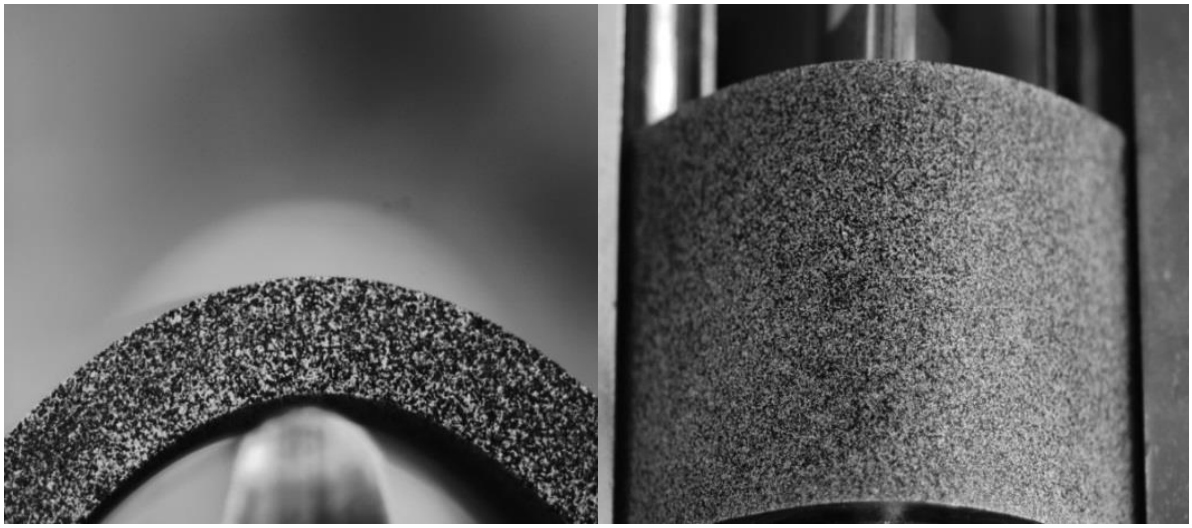

Figure 46. Images from a typical bent specimen with speckle pattern across the specimen, (a) through-thickness and (b) tensile surface regions.

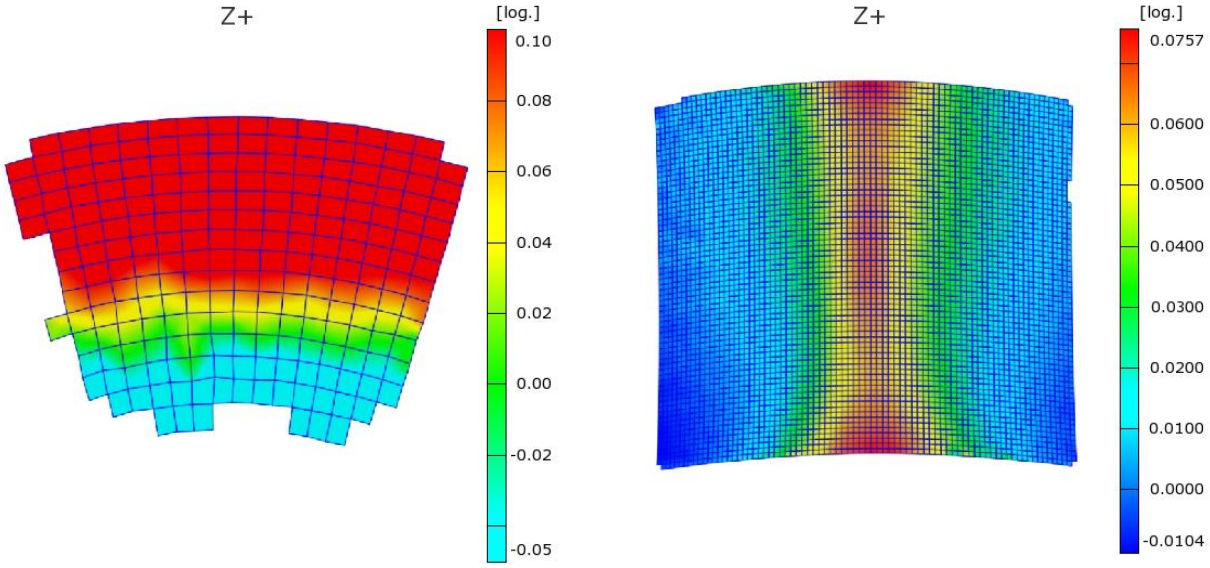

(a) (b)

Figure 47. DIC based strain map of (a) through-thickness and (b) tensile surface regions.

4.2.3. Thickness Measurement using Optical Microscopy

Specimen thickness measurements were carried out on bend specimens using an optical microscope to acquire relative thickness data as a function of curvature. For this purpose, five specimens, bent at progressively decreasing inner radius of curvature r_i = 73 mm, 32 mm, 17 mm, 7 mm, and 3.5 mm, as shown in see Figure 48(a), were cut through the

(a)

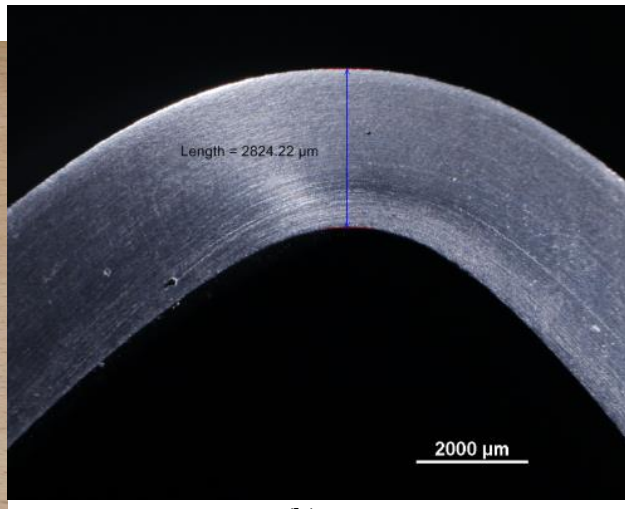

(b)

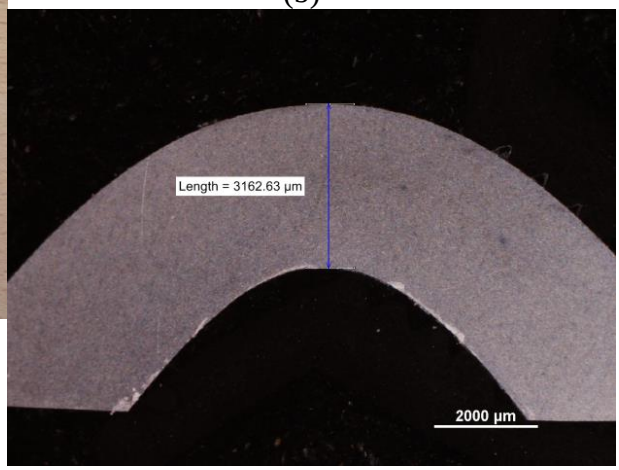

(c)

Figure 48. AA2024 specimens bent to different radii, (a) full specimen images, (b) microscopic cross sectional view of bend specimen (r_i=3.5 mm) from the (b) edge, and (c) mid-section.

thickness at mid-width. Microscopic examination was carried using Nikon optical microscope at a magnification of 10×. The cross section of a bend specimen (r_i= 3.5 mm) across the edge and mid-width are shown in Figure 48(b) and (c) respectively.

4.2.4. Thickness Measurements Across Specimen Width

Prior to thickness measurement, the bi-layer interface was observed with an optical microscope to assess the interface characteristics in the un-deformed and deformed (bent) state, and especially the possibility of de-bonding between layers. The images were observed at two different magnifications of 100× and 1000× in the VHX Keyence optical microscope. Perfect bonding between explosively welded SS400/AA1050 bi-layer was seen before and after deformation as shown in Figure 49.

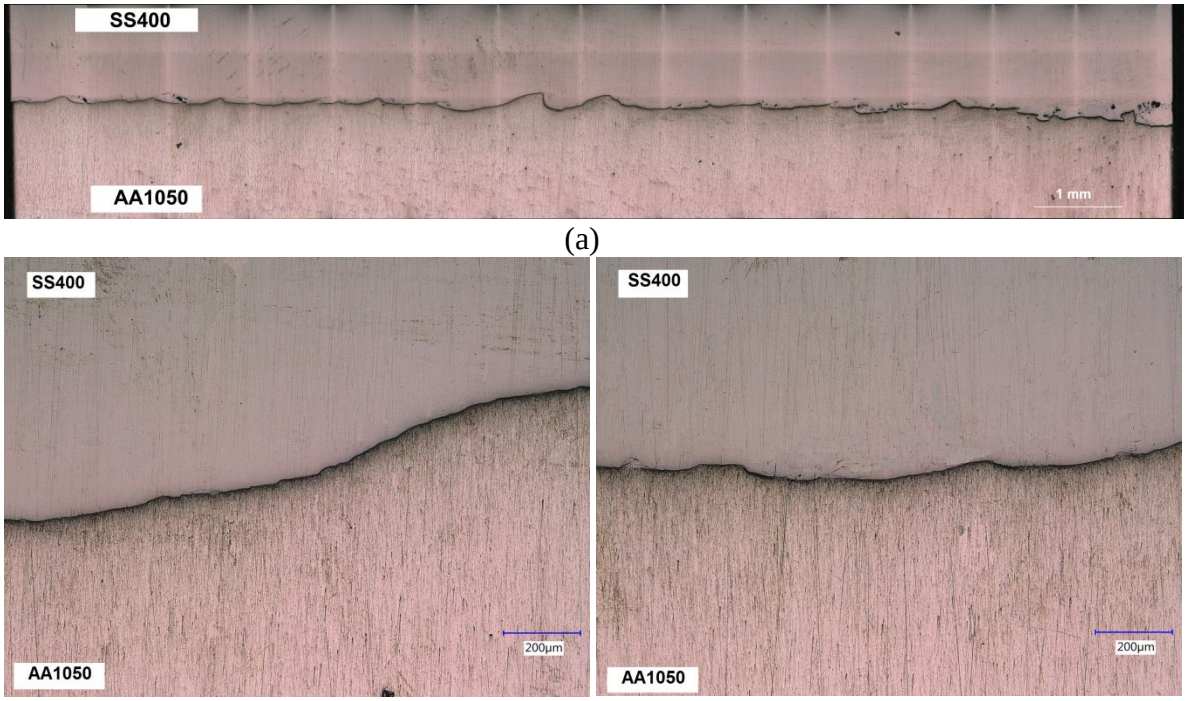

Figure 49. Optical microscope images of SS400/AA1050 specimen (a) specimen cross section before deformation at 100×; (b) un-deformed magnified at 1000X ; (c) bent specimen at 1000×.

The variation of thickness across the width of the specimen at the bend line was obtained from thickness measurements from optical microscopic images of cut AA2024, SS400 C-T and C-C specimens as shown in Figure 50 (a),(b) and (c), respectively. The curling effect at the edges is clearly evident in the photographs. The dark and light layers in the Figure 50(b,c) represent SS400 steel and 1050 aluminum layers, respectively.

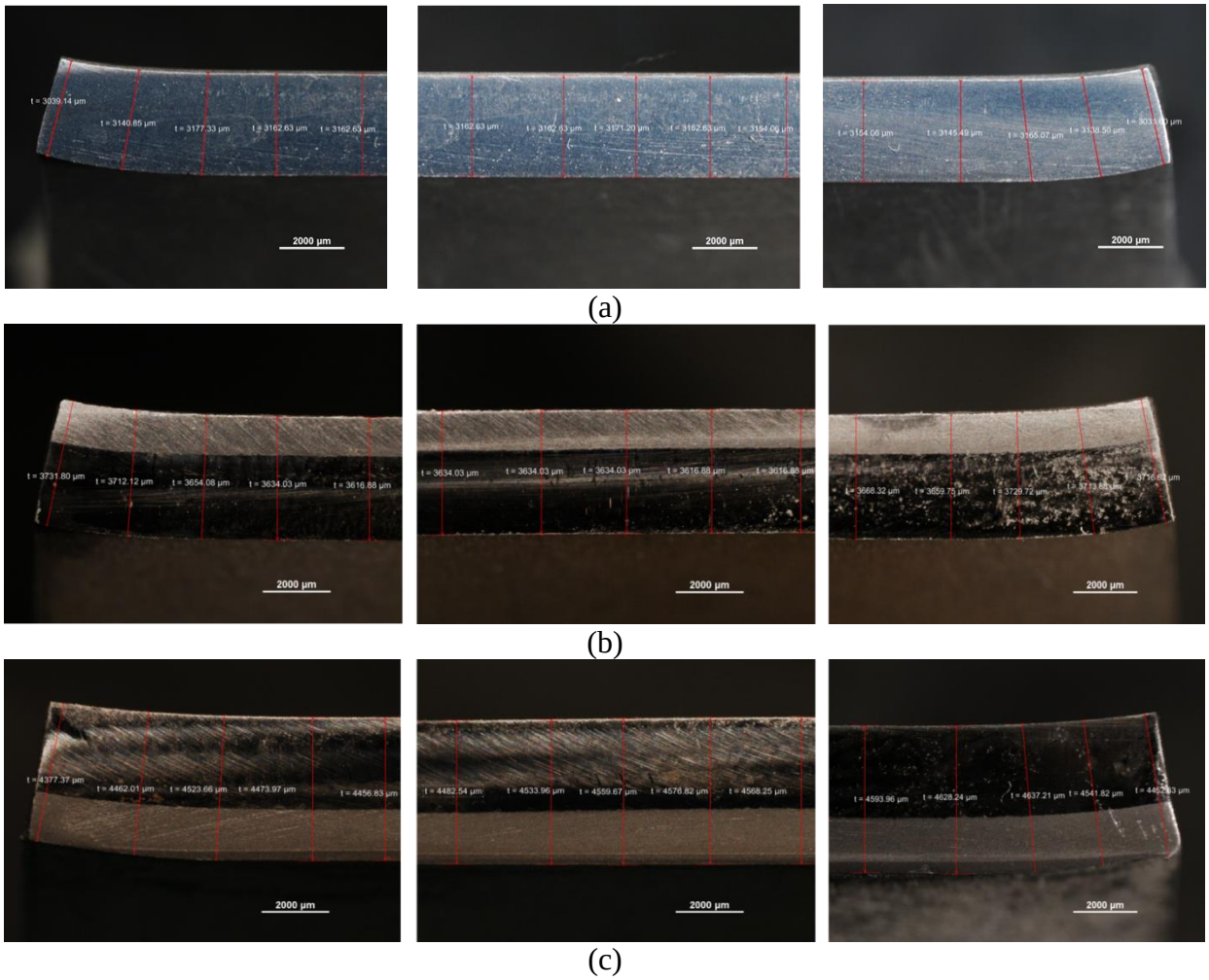

Figure 50. Thickness measurements across the specimen width at the bend line from cut specimen for (a) AA2024 monolithic specimen for inner radius of 3.5 mm, (b) C-T and (c) C-C specimens for inner radius of 25 mm.

4.3. Stretch-Bending Test for Bendability Study

4.3.1. Angular Stretch-bend Test Details

The test set-up of ASBT, described in Figure 51 from Demeri (Demeri, 1981), was adopted in the present work. ASBT jig consisted of a bending mandrel (or punch), and upper and lower clamping plates (or dies) with suitable lock-beads for clamping the sheet specimen. The details of the tooling are described earlier in section 2.8.3. Hourglass shaped test specimens from AA2024 sheet of 1.25mm thickness were machined using WEDM process with gauge width 22.8 mm and radius 50.4 mm. The punch width and radius were 25.4 mm and 1.5 mm respectively. The test specimen was fully annealed at 686 K for 2 hours. The punch, specimen and clamping plates were mounted on a MTS 200 kN double-action mechanical testing system (see Figure 53(a-b)). Rubber sheet cushion was used between the specimen and clamping plate to provide cushioning effect in the clamped region of the specimen to avoid fracture at the beads. The tests were conducted at an actuator velocity of 1.5 mm/min and a clamping load of 75 kN. The specimens were deformed to fracture as shown in Figure 53(c). DIC system was employed to characterize strain history and limit strain of an aluminum sheet material undergoing stretch-bending.

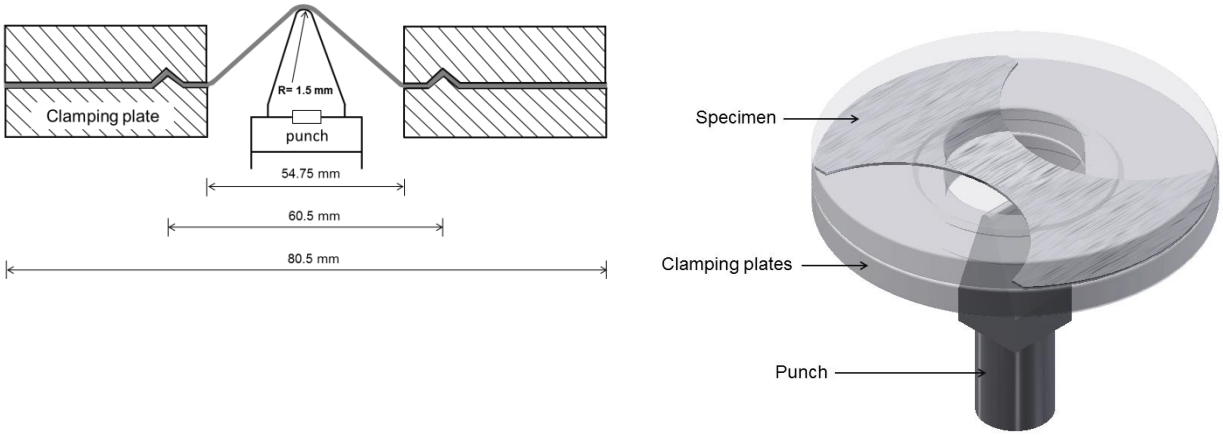

(a) (b)

Figure 51. Schematic of ABST tooling, (a) 2D and (b) 3D models from Demeri (Demeri, 1981).

The limit strain study was extended to a commercially available tri-layer laminate, Alclad 2024. The laminate is produced by hot roll bonding of AA2024 as matrix and a thin layer (80μm) of AA1100 as clad material on either side of the matrix for corrosion resistance purposes. The material finds its application in aerospace structures owing to high strength and fatigue resistance property of AA2024 and better corrosion resistance property of AA1100. The hot roll bonding mechanism of Alclad 2024 is explained in the work of Liu et al. (Liu et al., 2008). A microscopic image of the through thickness section of Alclad 2024 laminate of 1.25 mm thickness is shown in Figure 52. AA2024 at T3 temper condition is very hard and less ductile for stretch-bending test in the tempered state. Therefore the material for the test specimens was fully annealed at 686 K for 2 hours and furnace cooled following ASM heat treatment standard for AA2024 material (ASM International, 1991). The optical micrographs of the crack regions of AA2024 and Alclad 2024 stretch bent specimens are shown in Figure 54 (a,b) respectively. While necking

type of fracture is observed in the AA1100 layer of Alclad 2024 specimen that is typical to ductile materials, a brittle fracture at the hard AA2024 specimen is seen.

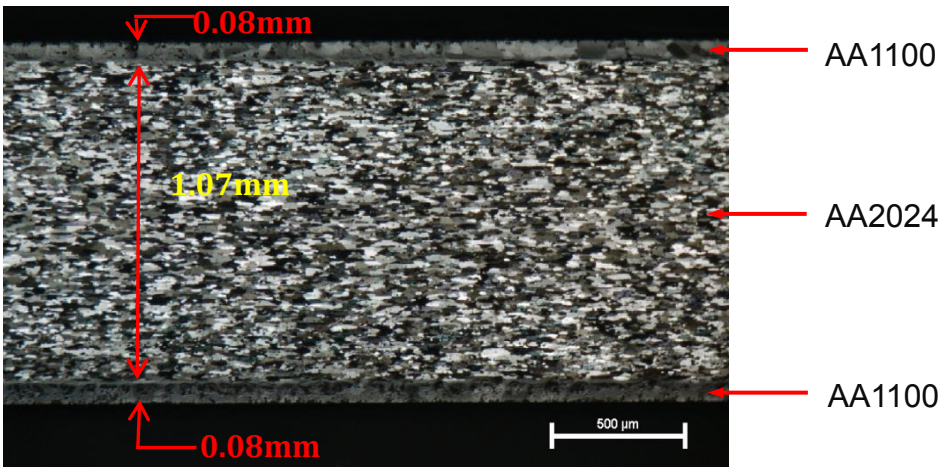

Figure 52.Optical image of Alclad 2024-T3 specimen cross section (thickness 1.25 mm).

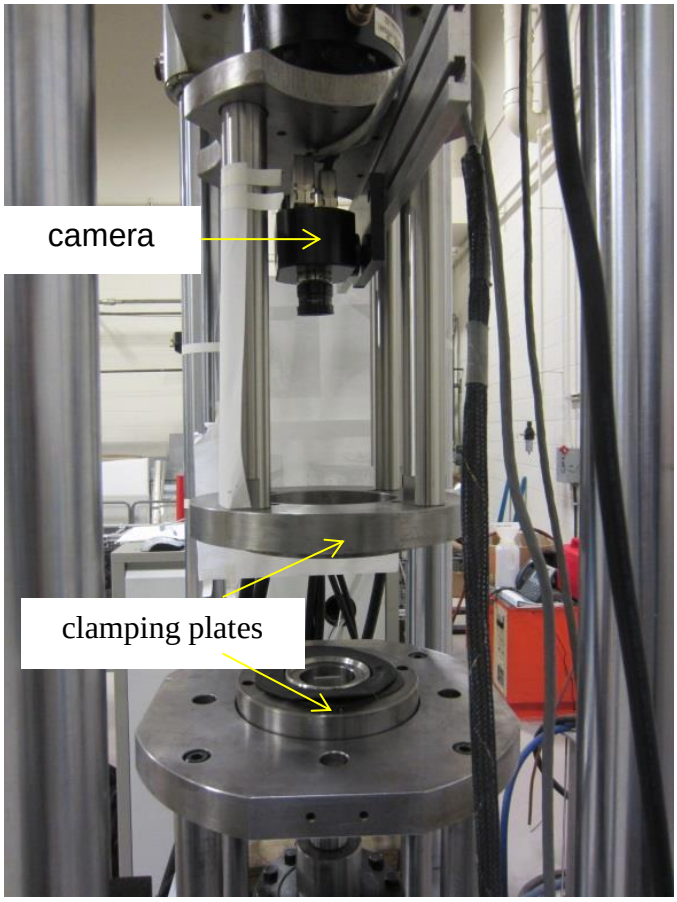

(a)

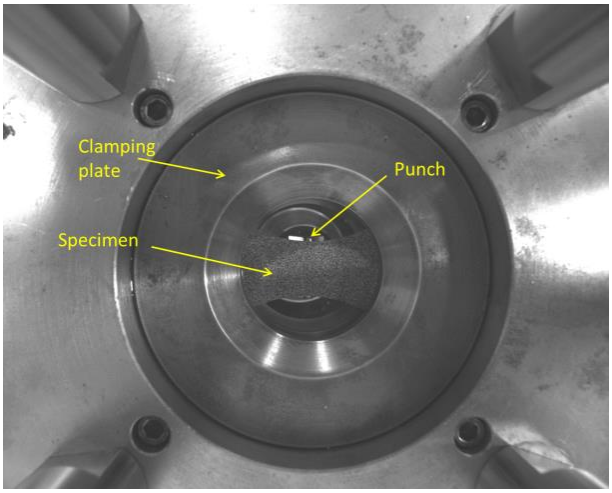

(b)

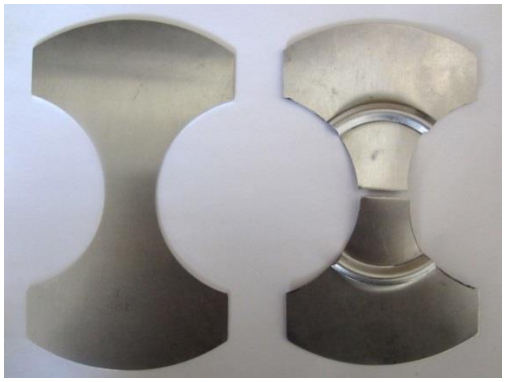

(c)

Figure 53. ASBT test details, (a) experimental test set-up with camera mounted above the test-jig for strain measurement, (b) camera view of tensile surface of deformed test specimen, and (c) specimen before the test and after fracture.

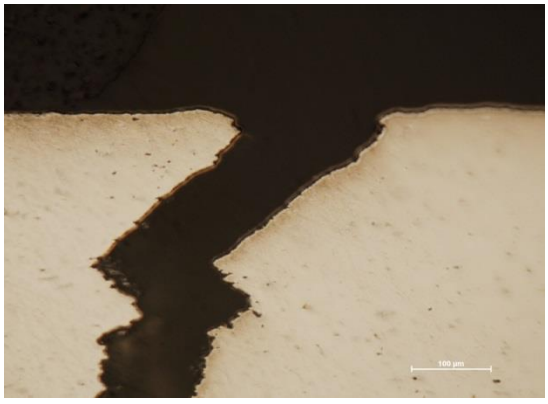

(a)

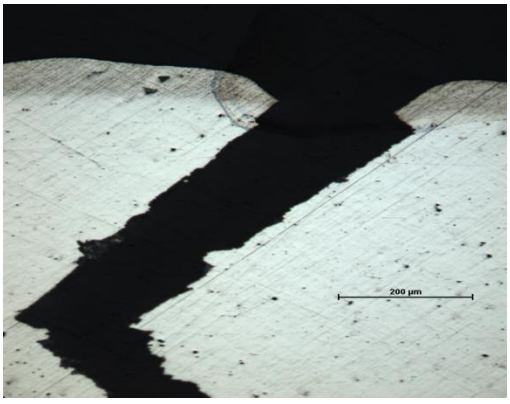

(b)

Figure 54. Optical micrographs showing the crack region of (a) AA2024 and (b) Alclad 2024 stretch bent specimens.

4.3.2. Experimental Strain Measurement Considerations

Strain measurements at the outer convex surface were carried out using DIC-method based Aramis® online strain measurement system from GoM (Gom-mbH, 2001). For utilizing the DIC method, the specimen was applied with a fine speckle pattern using a spray paint over the flat surface. First a fine coat of white paint was sprayed followed by a fine spray of black paint from a pressurized canister attached to an air brush. The black and white layers were applied to enhance image contrast and to minimize the average speckle size. The deformation stages were recorded at 3 frames/sec using Aramis high resolution digital camera mounted directly above the specimen (see earlier Figure 53(a)). The camera was fixed at a distance of 450 mm from the specimen to overcome loss of focus due out-of-plane deformation of the specimen during the test.

Despite several advantages of DIC measurement, obtaining high-fidelity quantitative information is necessary for local strain data. The fidelity of strain data is dependent upon several factors such as (i) optics of camera and stochastic (i.e., random speckle) pattern, (ii) image processing parameters (facet size and facet step), and (iii) length scale of interest (continuum or grain scale) (Amini and Kumar, 2014). The success in DIC relies on overcoming the limitations in composing the matching macroscopic continuum scale speckle pattern size for the microstructure of the material. Polycrystalline material such as aluminum is heterogeneous at the microscopic scale and hence the speckle size and facet size should correspond to the grain size to avoid local fluctuations. In other words, on continuum mechanics scale, it is suitable to have several grains spanning a single facet rather than a single grain spanning several facets. The AA2024 material after annealing

revealed an average grain size of 50µm, a speckle pattern with stochastic gray and white dots was spray painted to obtain an average speckle size of 165µm. This could accommodate 3-4 grains. The grain size and speckle size was then correlated with the facet size in terms of pixels. The DIC method used high resolution camera of 1.3 mega pixels that rendered images of size 1280 pixels x 1024 pixels along the dimensions of width and height. For example, for a selection of 9 pixel × 9 pixel facet size, a facet dimension of 1285 µm (~ 1.3 mm) was obtained. The dimensional ratio of grain size to speckle size to facet size for this case would be 1 : 3 : 3.25 as schematically shown in Figure 55(a). The ratio indicates that there were adequate grains and speckles within the facet that would generate reasonable strain compared to far-field applied strain. Overlapping of facets is necessary to uniquely identify each facet and to obtain correlation. The overlap distance, otherwise known as facet step is inversely proportional to the distance between centroids of adjacent facets. The general rule of thumb for better strain resolution is that the facet step should be half of the facet size (Amini and Kumar, 2014). Optical micrographs of surface of AA2024-O sheet with fine speckle pattern and Aramis DIC facet size-step for 9 x 9 pixels with a facet step of 5 pixels are shown in Figure 55(b, c) and a typical Aramis strain map is shown in Figure 55(d) respectively. The Matlab code to extract major strain data from Aramis strain output file is presented in Appendix C.

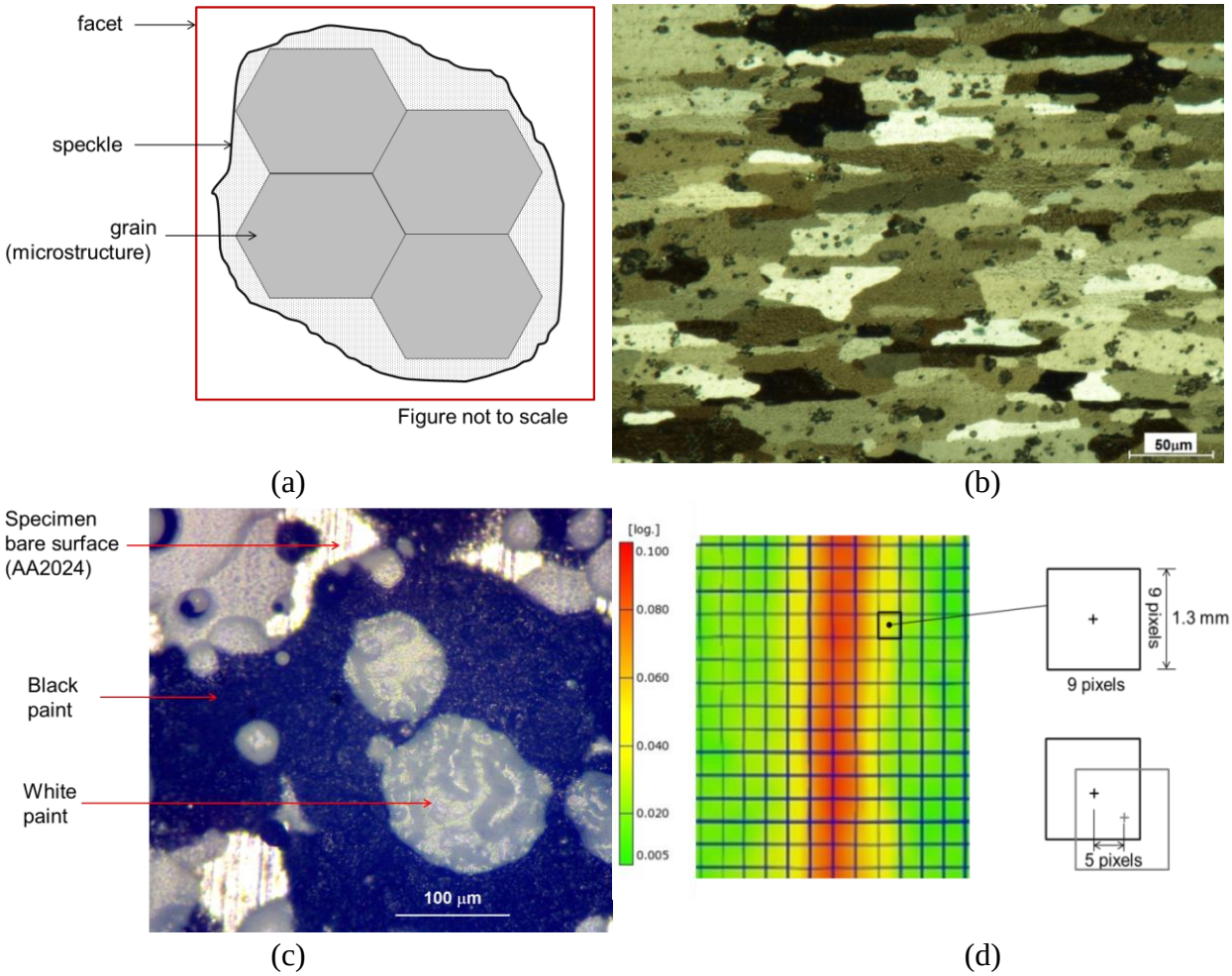

Figure 55. DIC based strain measurements, (a) schematic of length scales of facet, speckle and grain, (b) optical micrograph of AA2024-O sheet material from long transverse (or LT) plane, (c) higher magnification image of speckles (100X), (d) Aramis DIC strain map for facet size of 9 x 9 pixels and facet step of 5 pixels.

4.4. Summary of Chapter

The experimental test method describing the rotary bend text fixture, angular stretch bending and DIC strain measurement were discussed. However, strain data could only be obtained from the surface of the specimen in the bending tests. FE models for bending were developed to obtain data from sections across width and are presented in Chapter 5.

Chapter 5
Finite Element Models of Bending

This chapter presents several different FE models of bending to compare and contrast with analytical model and experimental bend test results. FE models do offer some clear advantages in understanding the mechanics of sheet bending.

5.1. Finite Element Models of Bending

Current analytical models, including the previous work of Tan et al., are based on the assumption that plane sections remain plane during the entire process. This assumption is difficult to fulfill in wide sheet bending experiments. Loss of plane strain condition leads to inevitable anti-clastic curvature development at the specimen edges. In order to check for the validity of the analytical model assumptions, two FE based models using Abaqus FE modeling software (version 6.8.3), (Dassault Systemes, 2008) were developed. The first FE model was a two dimensional (2D) plane strain bending model that utilized multi-point constraint (MPC) to attain a uniform curvature of the specimen. The second FE model was developed for three dimensional (3D) bending to simulate the laboratory experimental set up as closely as possible. FE models provide strain data for any section of interest (edge or centre of the specimen at the bend line) and the data could be obtained at any desirable position within the test specimen unlike the experimental test where data

was often difficult to obtain from the entire through thickness region due to speckle pattern degradation and consequent breakdown of DIC calculations.

5.1.1. Two Dimensional FE model using Multi-Point Constraints (FE-MPC)

Two dimensional plane strain bend test model was developed first for its simplicity to compare it with the analytical model. Pure bending was achieved in the specimen by constraining the mid fiber nodes to make them lie on a circle. The theoretical framework was adopted from the work of Patel as illustrated in Figure 56 (Patel, 2006). One end of the specimen was constrained and a pressure load was applied at the other end to avoid element damage. The left most node was held stationary and the next node acted as a 'free' master node. The following nodes to the right of this node were all slave nodes that were tied to the master node. As the master node was displaced, the slave nodes moved in an angular manner so as to form a circular arc. CPE4R element, a 4-node bilinear plane strain quadrilateral element with reduced integration and hourglass control, was selected for model development. Static Riks algorithm was used for deformation steps and Abaqus/Standard solver was utilized. A total of 4000 elements were used with 40 elements through the thickness of the specimen. The model bend specimen at two stages of bending is shown in Figure 57.

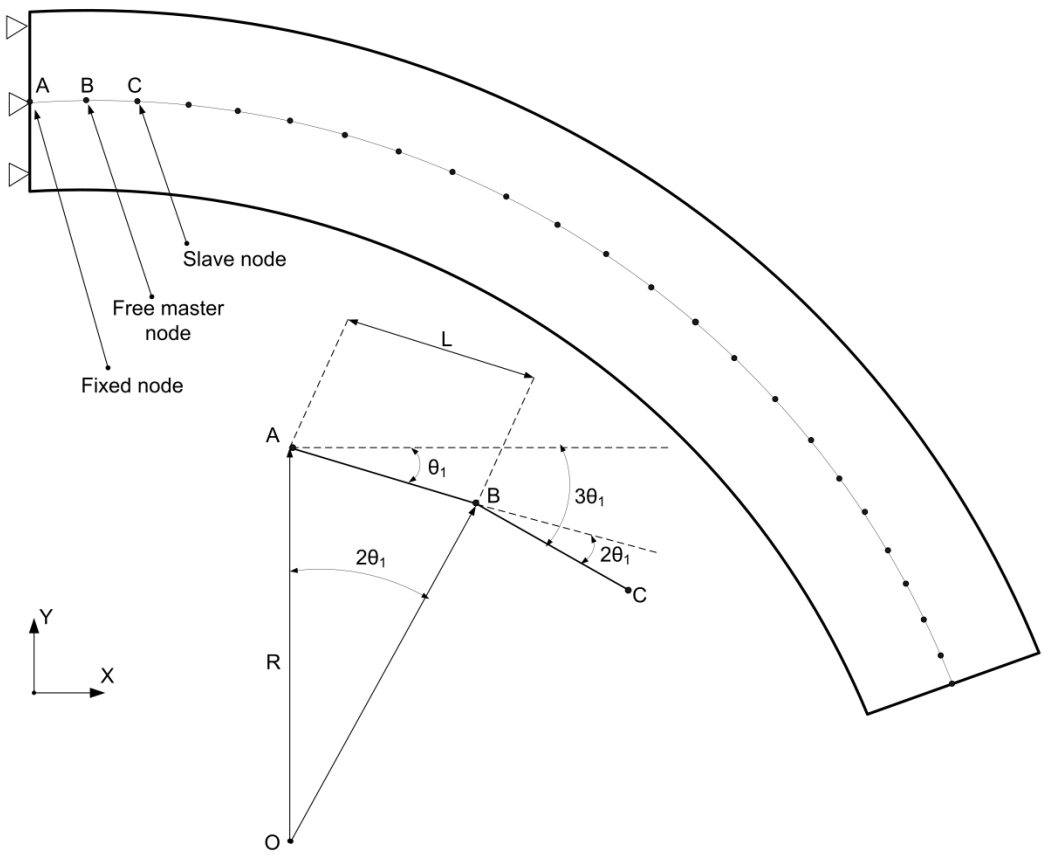

Figure 56. Two dimensional FE model by multi-point constraints (FE-MPC) (Patel, 2006).

The governing equations for the model were based on radius R, Length L, and angle θ (see Figure 56) and the following geometrical relationships:

$$R = \frac{L\cos\theta_1}{\sin 2\theta_1} \tag{5-1}$$

$$L = \sqrt{\left((x_2 - x_1)^2 - (y_2 - y_1)^2\right)} \tag{5-2}$$

$$\theta_1 = \tan\left(\frac{(y_2 - y_1)}{(x_2 - x_1)}\right) \tag{5-3}$$

The X and Y coordinates of node *i* (along the central row) were obtained using the following expression,

$$x_1 = R\sin(2i\theta_i)$$

$$y_1 = R\cos((2i\theta_i) - 1)$$

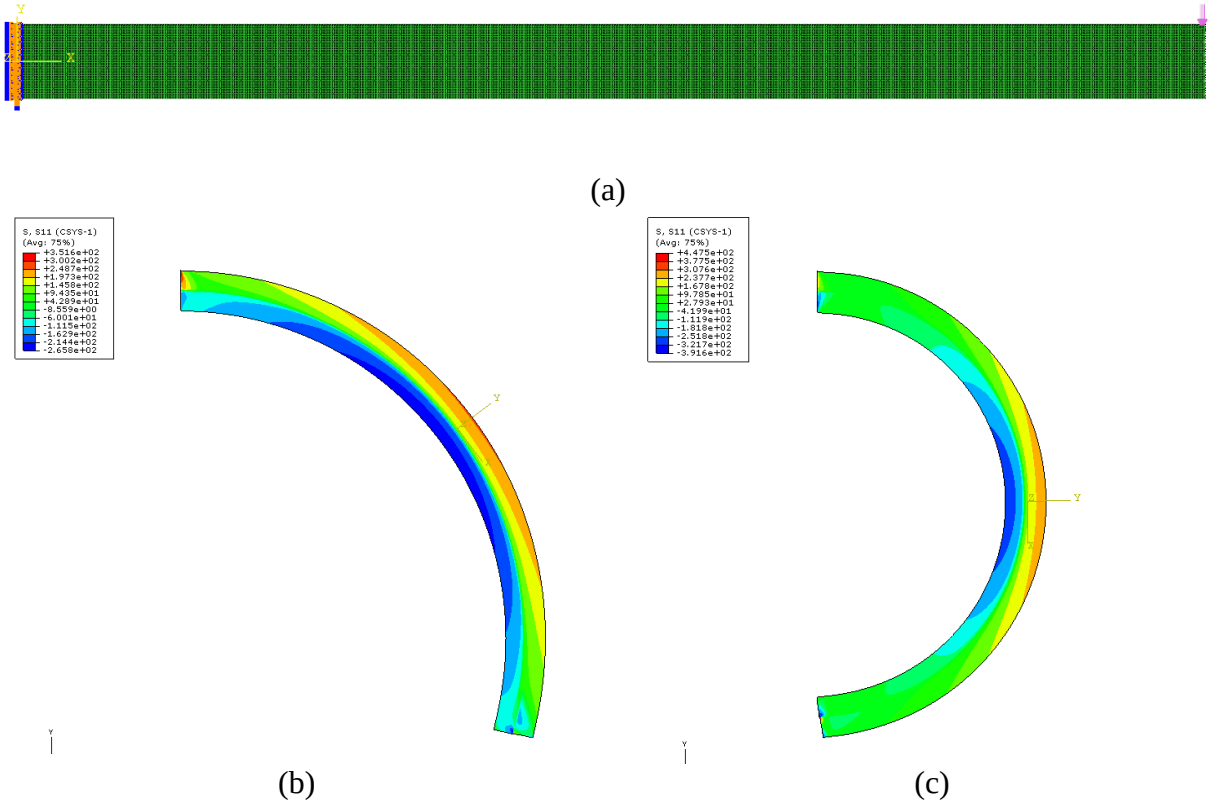

(a)

(b) (c)

Figure 57. FE-MPC model for pure bending using multi-point constraints; (a) undeformed specimen showing edge constraint and loading, (b), (c) bent specimen at different stages of bending.

5.1.2. Three-dimensional FE Model of Bending with Non-Uniform Curvature (FE-NUC)

The 3D model geometry (for specimen and punch) and loading were based on the experimental geometry and loading conditions discussed earlier in Chapter 4. Minor modifications to the clamp-arm design were made to avoid clamping step in the simulation. It is to be noted that the clamped region of the specimen was significantly away from the bend line and no sliding of the specimen within the clamped region occurred during the test. The specimen edge was tied to the rectangular element edge that exhibited the same action as that of the clamp. Likewise the top end of the angular arm was suspended at the reference point instead of pivoting at the steel block. An 8 node linear brick element with reduced integration (C3D8R element in Abaqus/Explicit) and hourglass control was used in the simulation process. Clamp, angular arm and punch were considered as analytical rigid (i.e., non-deformable) bodies. A total of 12 elements through the thickness and 40 elements through the width of the specimen were used to keep the size of the model manageable. Kinematic contact was considered between the specimen and the punch (i.e., bending mandrel) mating surfaces with a coefficient of friction value of 0.3. Material properties of AA2024 including stress-strain curve, as presented in section 4.3, were utilized with the isotropic Mises finite strain plasticity constitutive model in Abaqus/Explicit. The data points for Ludwik hardening law were obtained from the curve fit parameters of the experimental tensile data. A schematic of the test fixture and FE model output at different stages of bending is shown in Figure 58.

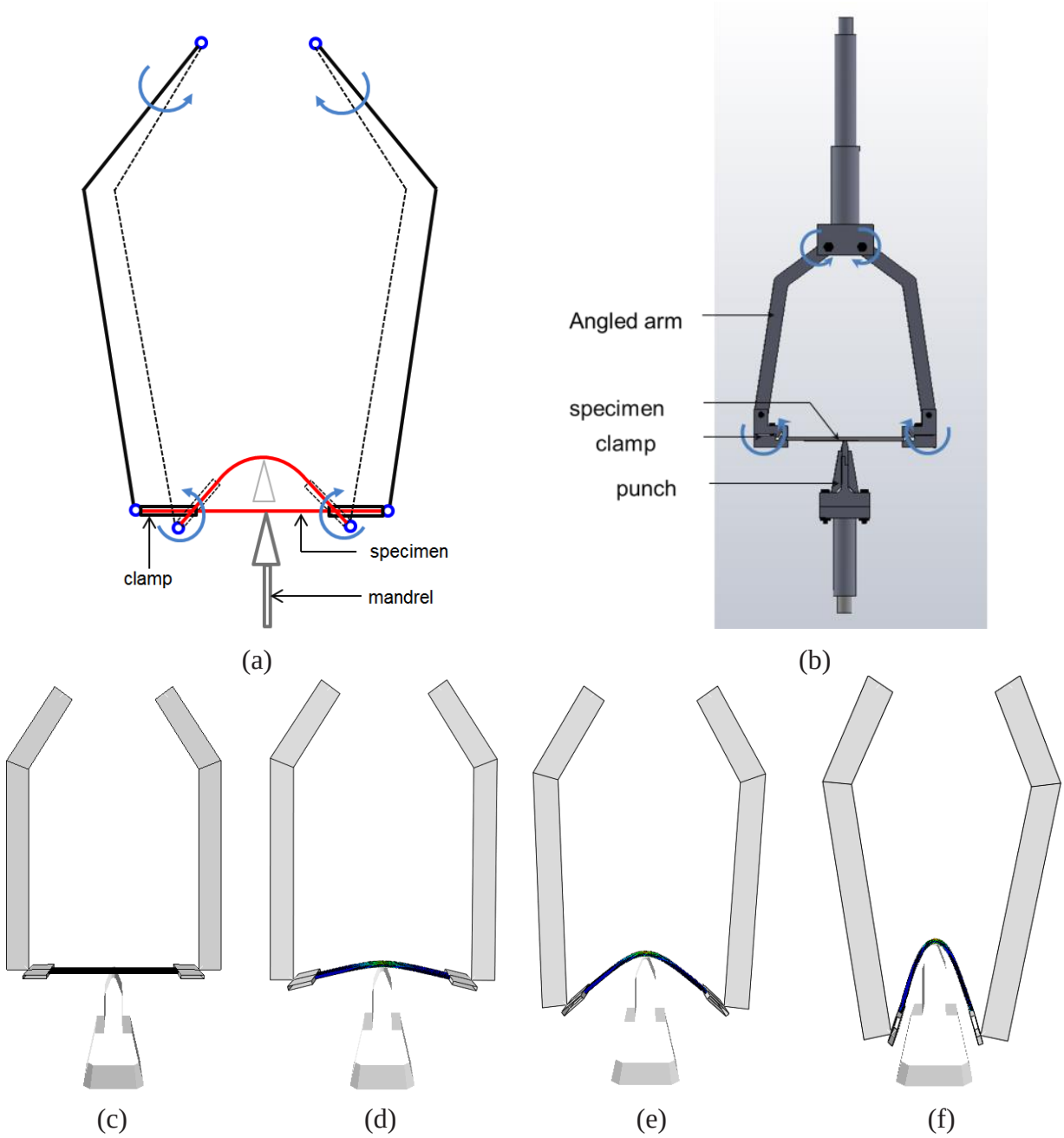

Figure 58. FE model results of rotary bend testing, (a-b) schematic of the test fixture; (c-f) FE model output at different stages of bending.

A schematic representation of stress states in punch based bending is shown in Figure 59. A deformed specimen from the 3D model at an intermediate bending stage is presented in Figure 60(a) where the development of anticlastic curvature (Figure 60(b)) and punch penetration along the compressive side of the specimen (Figure 60 (c,d)) can be observed. This is due to the differences in stress state along the edge (uniaxial tension and compression) and mid-section (plane strain tension and compression) that is typical of small radius bending.

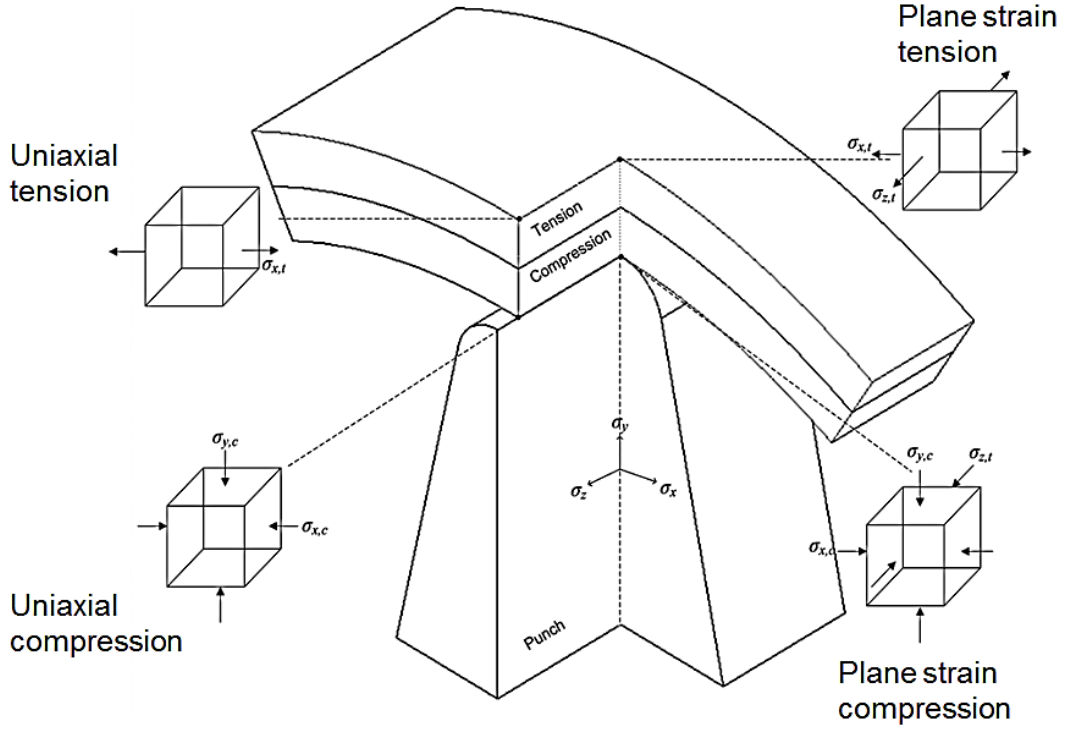

Figure 59. Schematic representation of stress states at the edge and mid-width sections of punch based bending.

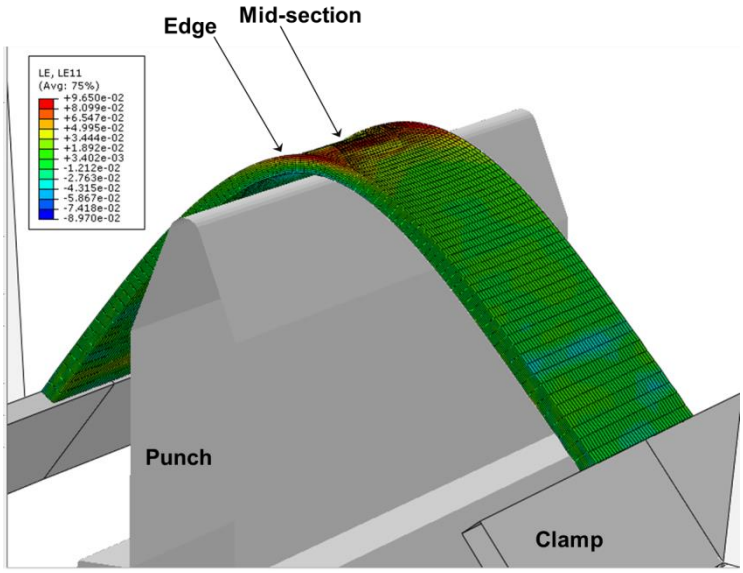

(a)

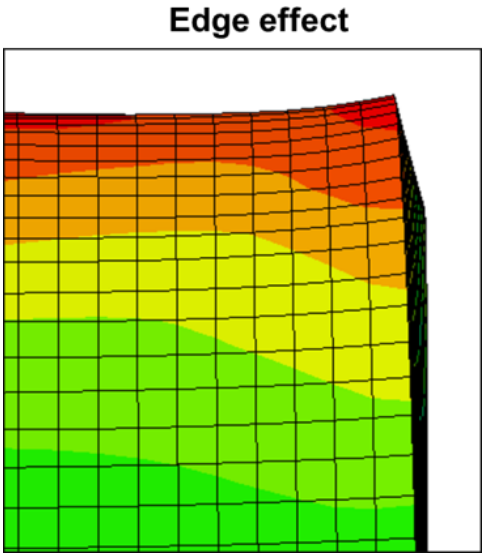

(b)

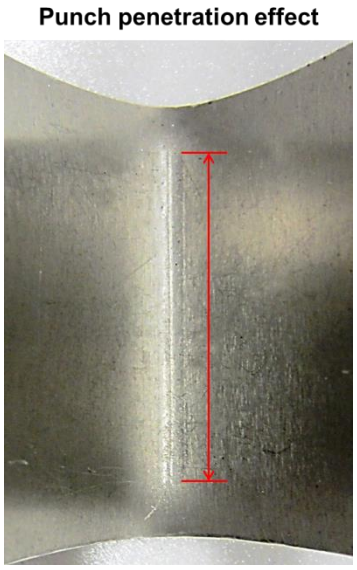

(c)

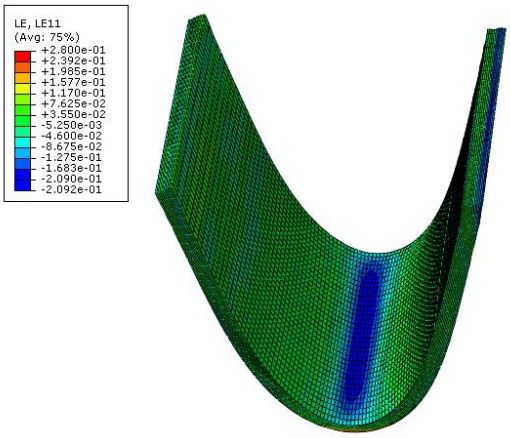

(d)

Figure 60. Three dimensional FE model for bending (FE-NUC), (a) model setup, (b) edge effect, (c) experimentally observed punch penetration effect on the compressive side, and (d) model predicted punch penetration region.

5.1.3. Shear Force and Bending Moment from the FE Model

The shear force and bending moment imposed by the rotary bend tester on the specimen was studied using Abaqus FE/Explicit 3D model using 2 node linear beam elements (B31). The specimen was modeled as a wire part with length 150 mm and a rectangular cross sectional profile (40 mm x 3.12 mm) representing the actual specimen dimension used in the experiments and other 3D FE based bending models. Material properties of AA2024 including stress-strain curve, as presented earlier, were utilized with the isotropic Mises finite strain plasticity constitutive model in Abaqus/Explicit. The bend testing model was compared with a FE V-bending model with the same material properties. The V-bending model was based on a lab based design with punch radius, R_p = 3 mm (see Figure 61(a)). The study was to compare the moment distribution in V-bending that has a significant moment gradient across span, die reaction and friction effects with that of the present design with and rotary clamps to distribute the bending moment across the span and without any die effects. A comparison of bend specimen curvature ($1/r_i$) measured at 24 mm effective bend length at the mid-span is shown in Figure 61(b). The effective bend length was chosen closer to the experimental image width size used for strain mapping and radius measurement. The V-bending curve shows acute rise in curvature. The demarcation between uniform curvature (stage (i)) and non-uniform curvature (stage (ii)) is characterized by sharp increase in curvature ($1/r_i$) shown in Figure 61(b). The evolution of shear force and bending moment obtained for the rotary bending and V- bending cases are shown in Figure 62(a-d) respectively.

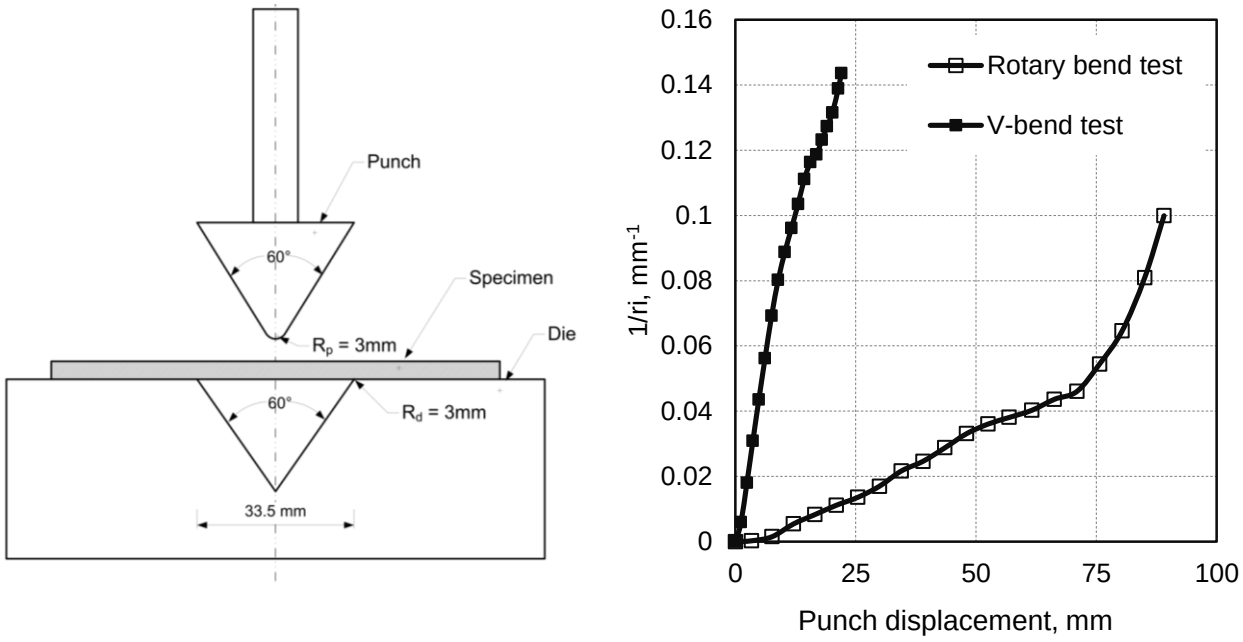

(a) (b)

Figure 61. Bending test models, (a) schematic of V-bend tester used for FE model; (b) comparison of curvature in rotary bending and V-bending cases.

The shear force and bending moment in rotary bending shows relatively uniform distribution across the specimen ends and maximum at the mid-span where the punch meets the specimen. For the V-bending case the shear force and bending moment shows a strong gradient with almost zero in most part of the specimen and peaks at the mid-span. A comparison of effective bend length of the same bending moment plot between the two cases is shown in Figure 62(e-f) respectively. The rotary bending case is initially characterized by constant moment across the span (uniform curvature stage) and gradually peaks at the center providing a narrow pure bending zone (non-uniform curvature). The V-bending comparatively shows a strong gradient in bending moment across the specimen span from the very early stage of bending. The uniform curvature of

the rotary bend specimen is better and this test was utilized in the present work to compare with the pure bending models.

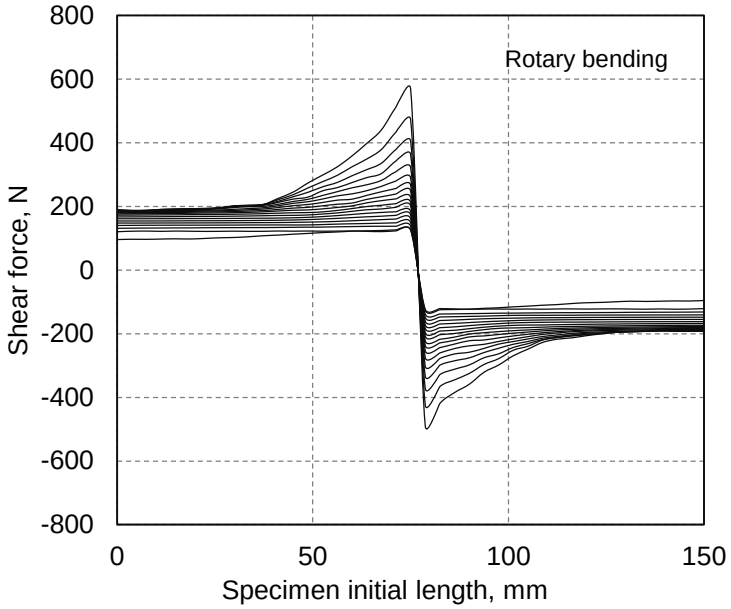

(a)

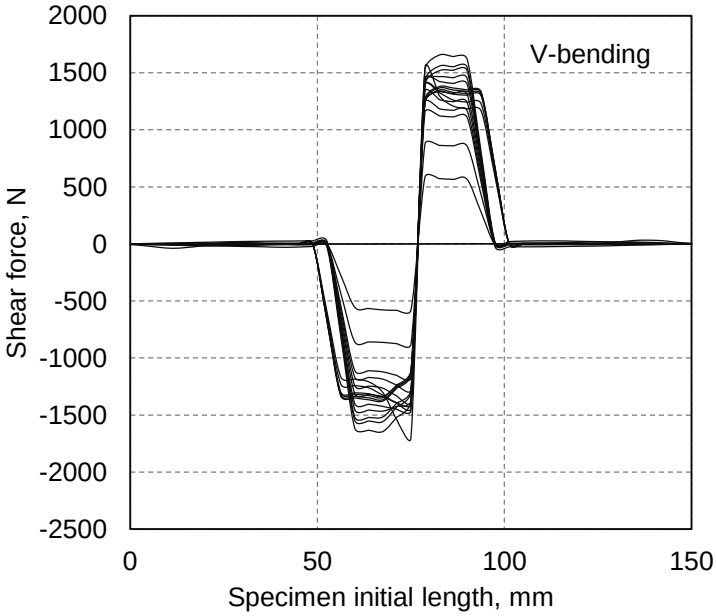

(b)

(figure continued on next page)

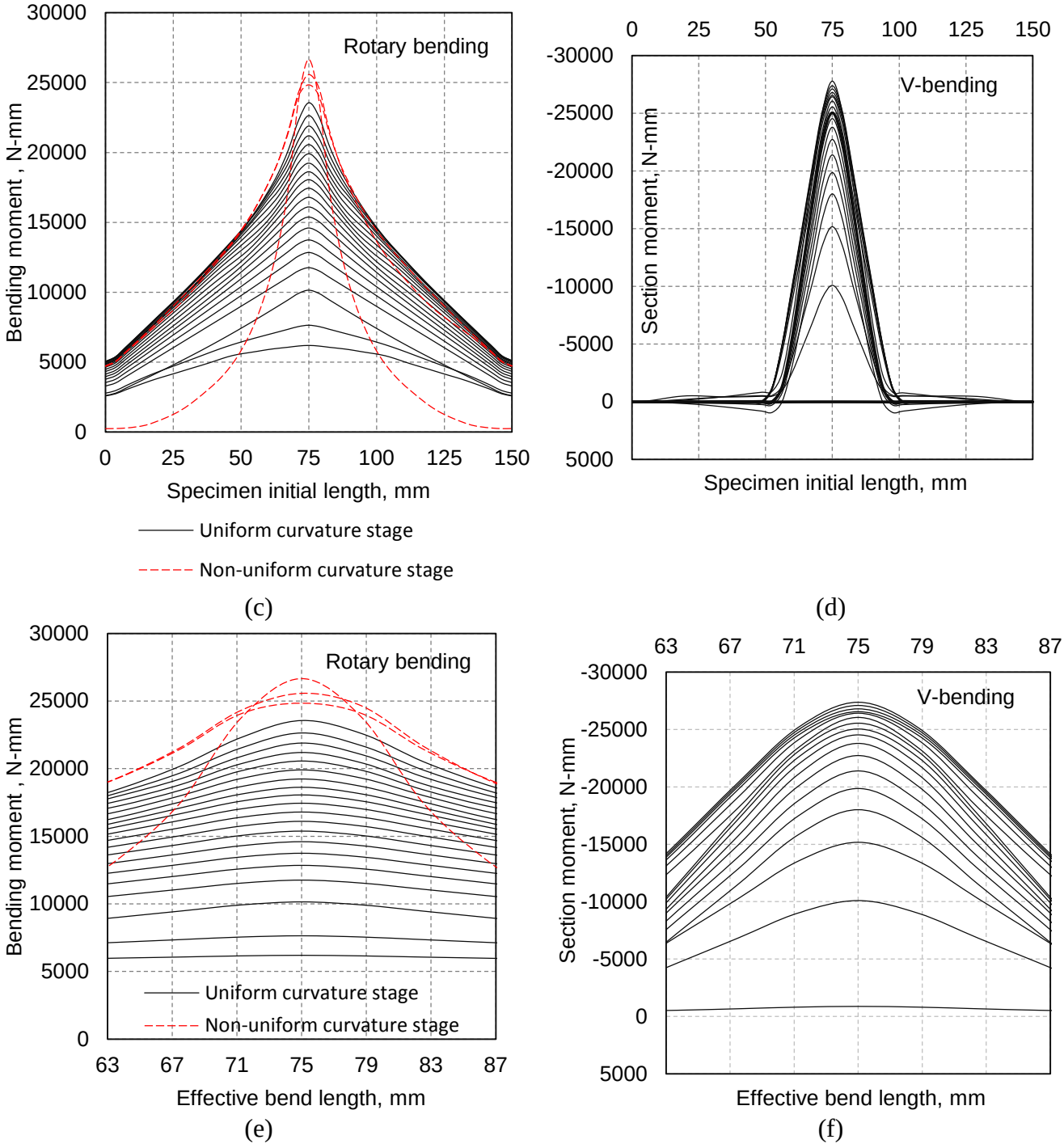

Figure 62. Comparison of rotary and V-bending test characteristics obtained from FE model in terms of (a), (b) shear force for increasing curvature; (c), (d) bending moment across entire span (150 mm) and (e),(f) bending moment within the effective bend length (24 mm) respectively. (V-bend test moment values are negative owing to punch displacement direction).

5.1.4. FE-MK Model

The analytical models of pure bending presented earlier in Chapter 3 deviate from real bending processes in that they involve simplifying assumptions and neglect some important parameters in the analysis. The experimental bend tests performed in the laboratory are closer to real bending conditions but still fall short in measuring through-thickness stresses and thickness change during bending, and especially from through-thickness section at mid-width. Thus, 3D FE models were also developed to analyze strains across any section (edge, center, tension and compression sides of specimen). These models, in principle, are based on Marciniak-Kuczynski test method (Marciniak and Kuczynski, 1979) as described in Section 2.6 (Figure 23). The model is developed in general purpose commercial FE code, Abaqus/Explicit. An 8-noded linear brick element with reduced integration (C3D8R element in Abaqus) is used to represent the sheet material. The material was modeled as homogeneous, rate-independent and following the von Mises yield criterion. In the model, the test specimen was represented by 53 elements along its width and 21 elements though its thickness and 58 elements across the length. The specimen dimension considered for the model is 4 mm (thickness) $\times$ 40 mm (width) $\times$ 25 mm (length). The clamp tooling was considered rigid to simplify the model. The FE model embodied virtual rotary clamps tied to the specimen at its two ends such that, on rotation, the clamps allowed the application of pure bending moments to the specimen, Figure 63(a). A view of the bent specimen through the thickness (Figure 63(b)) and from the width side shows the anticlastic curvature (i.e., edge effect) that develops at the two edges (Figure 63(c)).

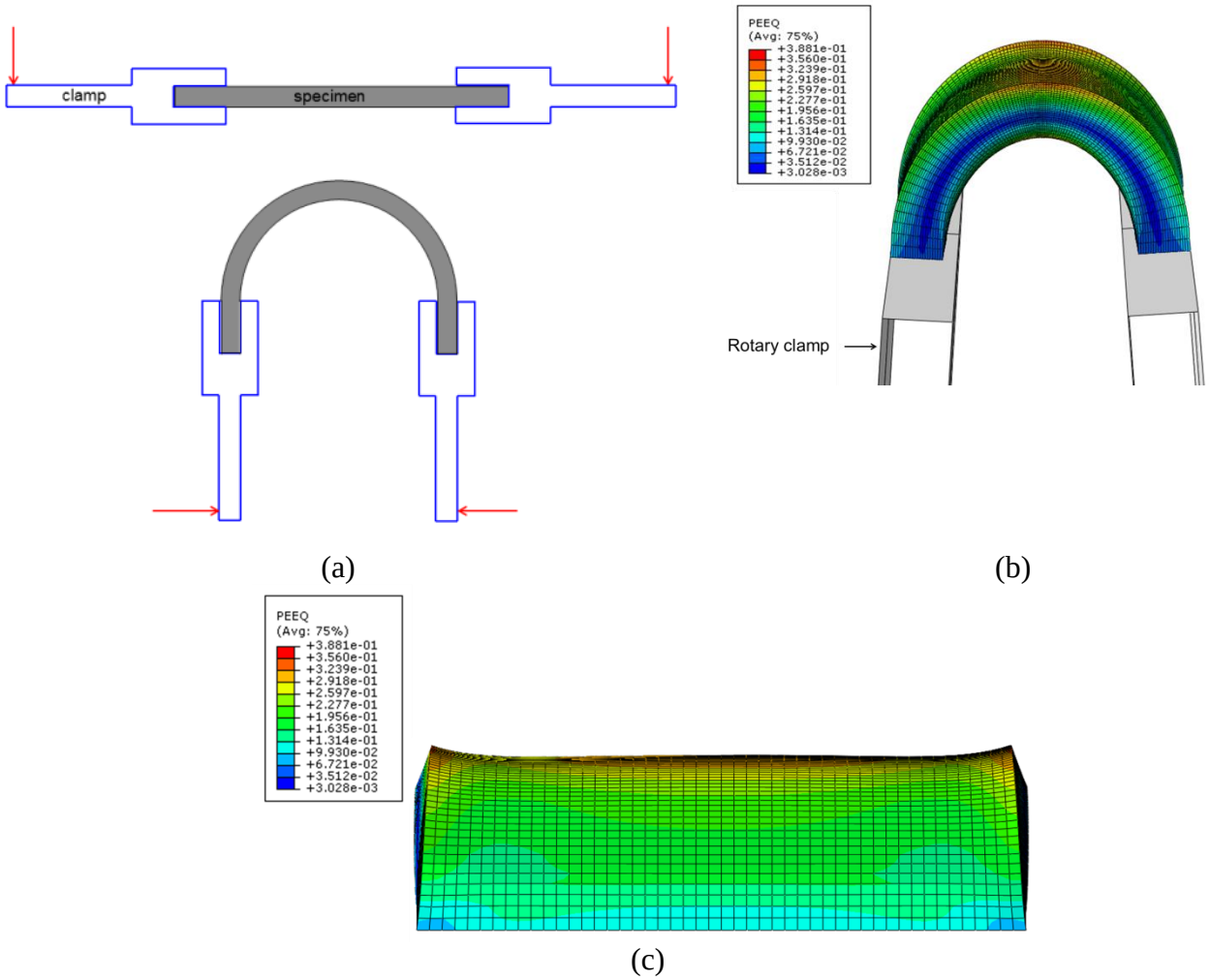

Figure 63. Schematic of simplified M-K model for bending (Marciniak & Kuczynski, 1979); (a) general test specimen geometry with clamp induced bending, (b) FE M-K model specimen undergoing bending; (c) FE-MK model specimen showing development of anticlastic curvature in small radius bending.

5.2. Summary of Chapter

Three FE based bending models were developed to bridge the gap between plane strain analytical model and experimental bending and to overcome the limitations in experimental strain measurement in bending. The model results are compared with the analytical and experimental test results in Chapter 6.

Chapter 6
Results and Discussion

This chapter deals with the results obtained from the analytical and FE bending models and experimental tests in bending. The stress and strain distribution results through the thickness and across width are compared for monolithic, bi-layer and tri-layer laminates. Microscopic thickness measurements for monolithic and bi-layer laminate cases are presented. The limitations and significance of the results are summarized at the end of each section. The later part of the chapter presents the stretch-bendability test results on monolithic and tri-layer aluminum alloy sheets. The strain prediction methodology and practical considerations of the strain acceleration criterion are discussed.

6.1. Bending Characteristics of AA2024 Monolithic Sheets

6.1.1. Strain Distribution in Bending of Monolithic Sheet

The experimental strain map across the through-thickness and width sections of AA2024 (3.12 mm thick) bend specimen are shown in Figure 64 where punch/specimen contact region has been chosen for strain mapping. The tangential strain map of the radial section at two stages of bending (r_i = 5.5 mm and r_i = 4.5 mm) are shown in Figure 64(a) and (b) respectively. As bending progresses, an increase in the tensile strain region and a decrease in the compressive strain region are observed. This is indicative of the shift in the neutral

fiber towards the compressive side of the specimen. The tangential strain map across the width section is shown in Figure 64(c). The effect of non-uniformity in curvature (i.e., deviation from plane strain) is seen in the form of strain concentration at the edges as well as in the mid-width region. The tangential strain plots along the width for the experiment and the FE-NUC model at various stages of bending are shown in Figure 65. The strain distribution is uniform at the beginning of bending and starts to deviate at the edges and centre as the bending progresses. The edges are in uniaxial tension stress state whereas the centre is close to plane strain state (see earlier Figure 59). The end of pure bending is marked by a rapid increase in the tangential strain at the centre, with strain magnitude much above those at the ends. Specimen edge and mid-width regions are potential sites for material approaching its limit strain in bend type deformation. The magnitudes of tangential strain show variation between the experimental and FE model, especially at later stages of increasing curvature. Possible reasons for the discrepancy include (i) some differences in curvature measurement methodology in experiment and model, and (ii) the effect of DIC parameters on strain data such as speckle size and selection of facet size and facet step. Development of anti-clastic curvature at the edges also made experimental curvature measurements difficult. However, the purpose of the plot is to show the evolution of tangential strain across the width during plane strain pure bending. Similar general trends between the experimental and FE model strain distribution were obtained.

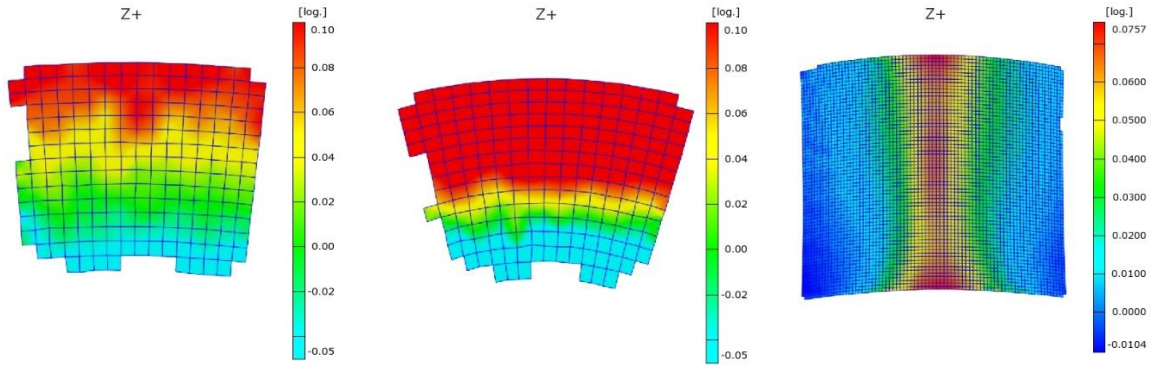

(a) (b) (c)

Figure 64. Experimental tangential strain maps from AA2024 (3.12 mm thick) bend specimen, (a) radial direction (r_i=5.5 mm), (b) radial direction (r_i = 4.5 mm), and (c) convex surface, width direction (r_i=5.5 mm).

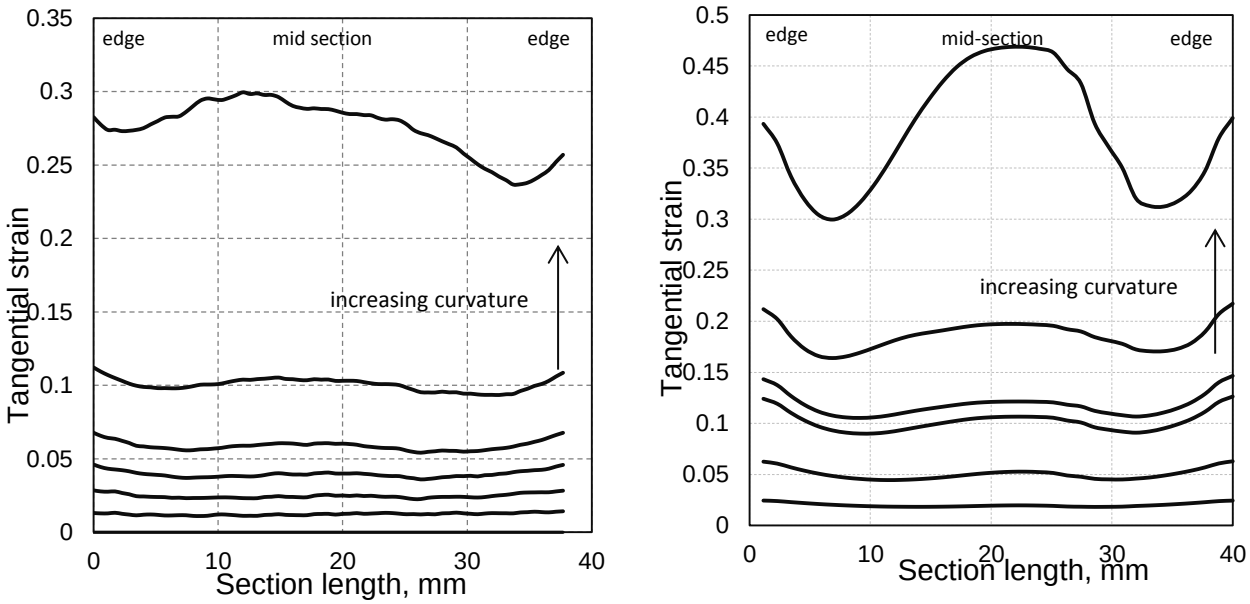

(a) (b)

Figure 65. Tangential strain distribution across the width of the bend specimen; (a) experimental and (b) FE-NUC model for AA2024.

6.1.2. Through Thickness Stress Distributions from Analytical and FE Models

The analytical model of Tan et al. based on Ludwik hardening law, FE plane strain and FE-NUC models at the edge and mid-section are compared for 3.12 mm thick AA2024 sheet. This comparison in terms of through-thickness tangential and radial stress components for specimen inner radius (r_i) of 15 mm is shown in Figure 66(a) and (b) respectively. The analytical model shows a sharp and discontinuous transition in the tangential stress distribution from tension to compression (see Figure 66(a)) compared to the other two FE based models. The FE-MPC model shows a smoother transition from tension to compression, but differs only slightly from the analytical model in the reverse loaded zone, as it employs isotropic hardening rule in the analysis. In the 3D FE-NUC model, the tangential stress at the edges deviates significantly from the mid-section owing to the loss of plane strain state, i.e., edge effect noted earlier in Figure 60(a). Further, in the FE-NUC model, the lateral shift of the tangential stress with increasing curvature is very large at the edges compared to the mid-section. This arises from the non-uniformity in curvature of the specimen. As expected, the radial stress distribution in Figure 66(b) is compressive and shows no through-thickness discontinuity in the stress from any of the models. Note that concave and convex sides of the specimen correspond to left and right x axis in Figure 66(b). However, the analytical model shows the most compressive response in the mid-thickness region compared to the other models. The FE-MPC model shows only minor deviation from zero radial stress state at the concave inner surface perhaps arising from the method of application of MPC constraint to the specimen. In other words, the radial stress is not completely annulled as expected from force

equilibrium considerations and compressive stress remains at the outer surface. The FE-NUC model, on the other hand, shows significantly larger radial stress component at the inner surface of the bend. This is caused by punch penetration of the inner surface that induces normal compressive (i.e., radial) stresses. However, there is considerable variation in radial stress at the inner surface for the edge and mid-width regions. It is likely that the radial stress component at the two inner edges of the specimen is relieved due to the anticlastic curvature whereas the mid-width section of the inner surface maintains continuous contact with the punch.

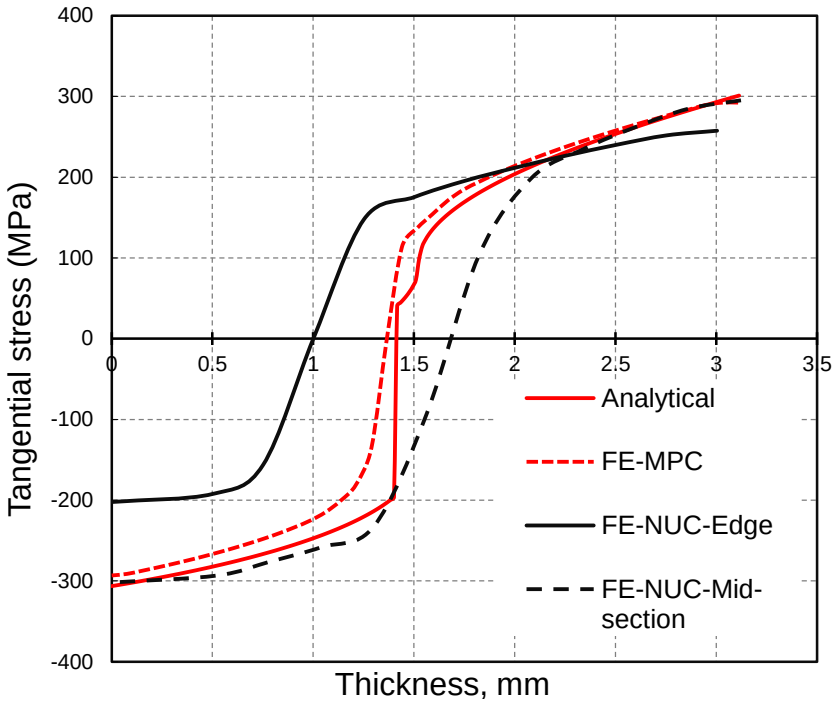

(a)

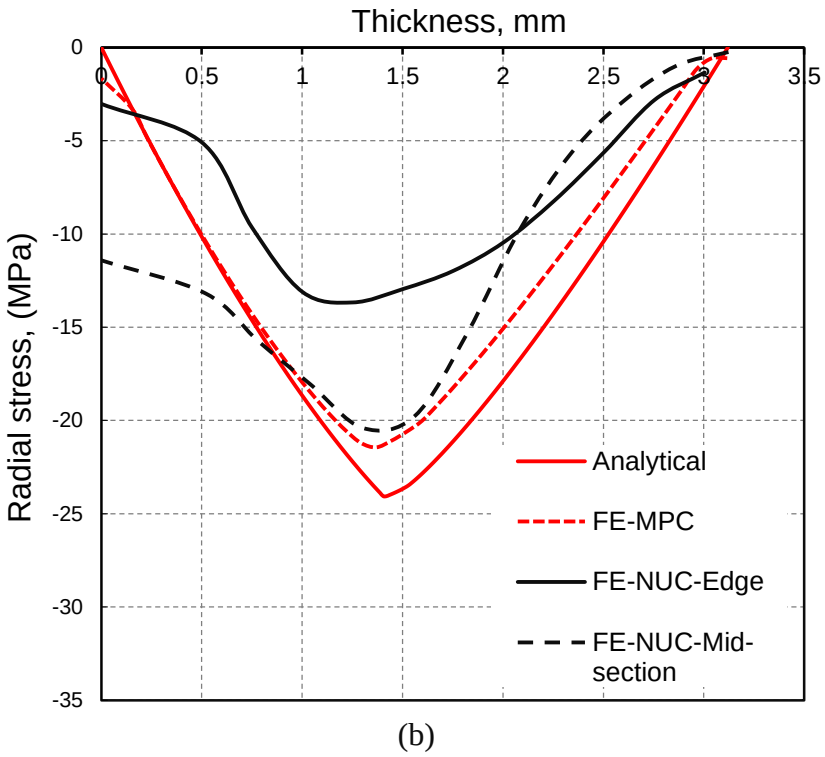

(b)

Figure 66. Comparison of (a) tangential stress distribution and (b) radial stress distribution at r_i=15 mm for 3.12 mm thick AA2024 specimen.

6.1.3. Through Thickness Strain Distributions from Experimental, Analytical and FE Models

Through-thickness tangential strain distribution from the different models (at r_i = 15 mm) is compared with the experimental data in Figure 67. The experimental data is taken from the DIC measurements at the edge of the sample. This data is represented in the form of data points and a polynomial fit to the data. As shown, the experimental compressive and tensile strains are highly unequally distributed about the mid-thickness plane due to significant shift in neutral fiber shift and edge effect. Also, the experimental data from the tensile surface could not be reliably measured due to the edge effect and loss of speckle

pattern at the edges at small curvatures in the DIC strain measurements. The strain is uniformly, and almost equally, distributed between the tension and compression zones in the analytical and FE-MPC models. These two models exhibit very similar through-thickness strain distributions, and similar to the tangential stress distributions shown earlier in Figure 66(a). The strain response of the FE-NUC model in the mid-section region is also similar to the analytical model and FE-MPC model but indicates a slight shift of the curve to the right of the mid-thickness plane. This appears consistent with the earlier tangential stress results of Figure 60(a). The results from FE-NUC model from the specimen edge region are closest to the experimental data. This model appears to closely follow the experimental conditions of the test and measurement locations. Even then, some discrepancy with the experimental data is observed on the tensile surface (rightmost part of the FE-NUC-Edge curve in Figure 67). The model curve indicates a linear rise and a drop at the tensile surface. The discrepancy between experimental result and FE-NUC model in the tensile region is currently unclear and could be attributed to inadequacy of the constitutive model in considering the microstructure and texture characteristics of the surface layer. The discrepancy could also be due to the combined effect of neutral fiber movement towards the compressive side and edge effect. Experimental through-thickness strain profiles during progressive bending of the AA2024 are shown in Figure 68(a). While local oscillations in the experimental strain profiles (oscillations increasing with curvature) are observed, similar trends were observed from the FE-NUC-Edge model results (Figure 68(b)) indicating that the strains became predominantly tensile in the through-thickness region as the specimen curvature increased. The tangential strain

through the thickness are shown for inner radii (r_i) values of 90 mm, 75 mm, 45 mm, 25 mm, 15mm (indicated in red), 7.5mm, 3.5mm and 3mm respectively. The specimen thinning is observed through the contraction in strain distribution plot with increasing curvature.

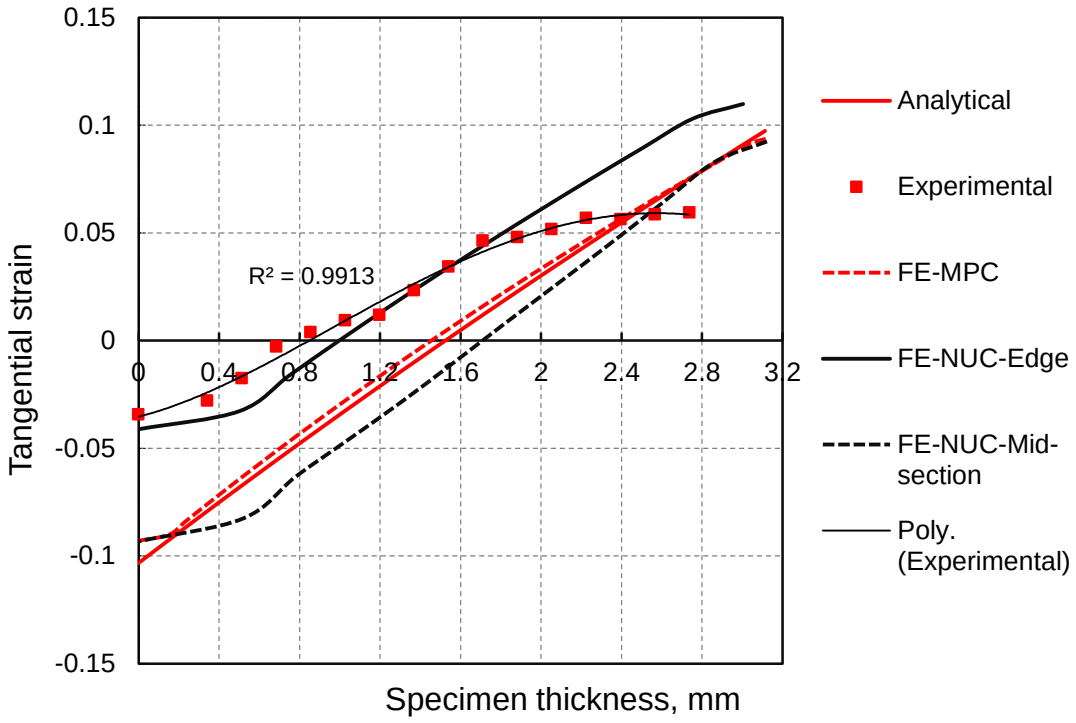

Figure 67. Comparison of tangential strain for different models for r_i =15 mm.

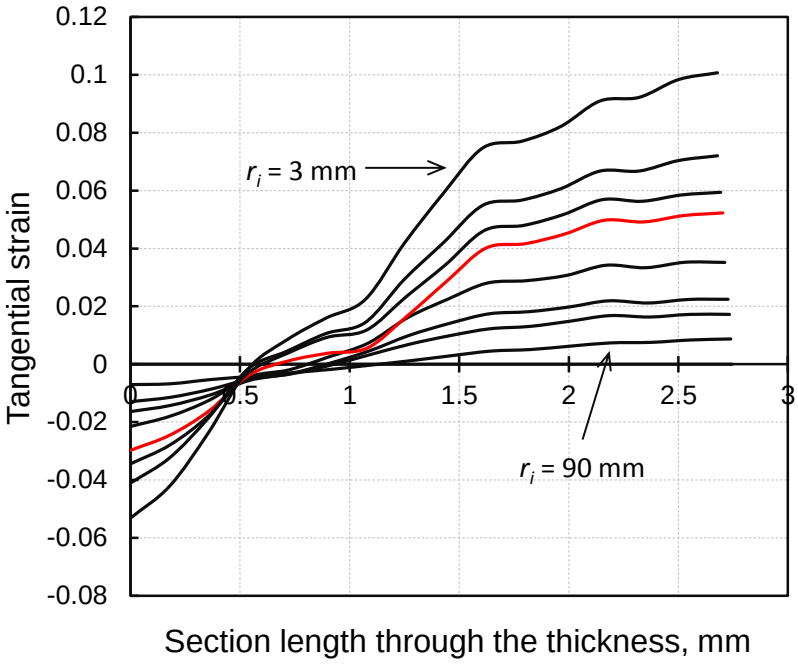

(a)

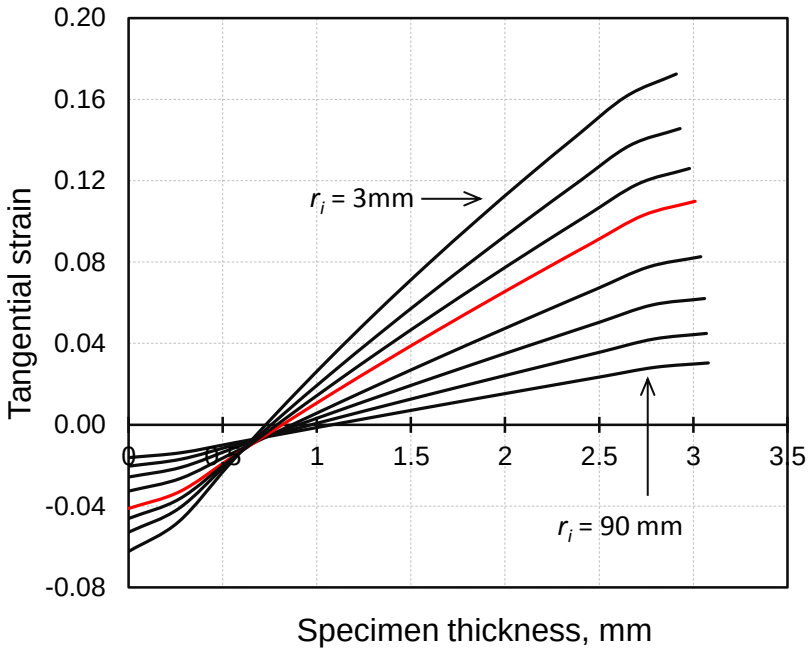

(b)

Figure 68. Through-thickness tangential strain distribution from (a) experimental (DIC) strain measurement and (b) FE-NUC (edge) model for 3.12 mm thick AA2024. The strain data corresponds to inner radii (r_i) values of 90 mm, 75 mm, 45 mm, 25 mm, 15mm (indicated in red), 7.5mm, 3.5mm and 3mm respectively.

Figure 69 shows the variation in width strain across the tensile surface of the specimen at the bend line from DIC measurements (see earlier Figure 46b) and the FE-NUC model data as a function of punch displacement. It is to be noted that width strain is compressive on the tensile surface and *vice versa* on the compressive surface. The FE-NUC model gives tensile width strain on the concave underside of the specimen that is not measureable in the experimental method. The experimental results for the tensile side are in good agreement with the results FE-NUC model. However, FE-NUC model shows that the compressive strain along the outer tensile surface (dashed line) is higher compared to the tensile strain on the inner compressive side (solid black line). This is attributed to the unsupported (and thus more deformable) tensile surface region of the bend compared to the punch supported underside of the specimen which also experiences punch penetration and frictional drag.

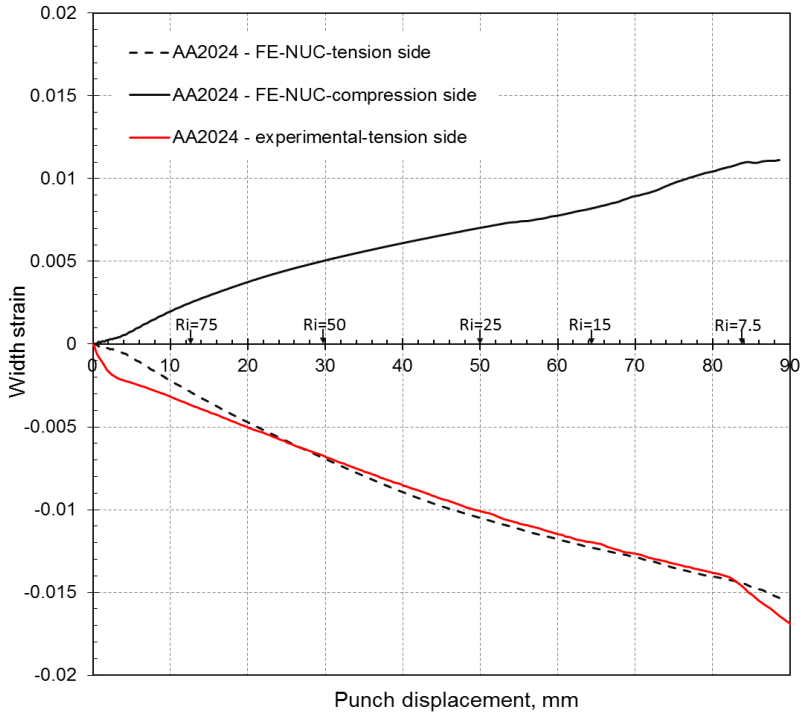

Figure 69. Comparison of width strain from FE-NUC model and experiments.

Figure 70 shows a comparison of relative thickness of the bend sample at the bend line as a function of inner radius of curvature from the experiments and the various models studied in the present work. The experimental data was obtained from DIC strain measurements of the bent specimens at the edge as well as from optical microscope images across the edge and mid-section of the specimen. The results show consistent and systematic drop in the relative thickness with curvature for all of the models (analytical, FE-MPC and FE-NUC) in agreement with the experimental (DIC and optical microscopy) results. The FE-NUC-Edge data, on the other hand, showed significantly lower relative thickness values. This is consistent with the results of Figure 64(a) which indicated significantly higher tangential tensile strains from the FE-NUC-Edge region.

Since this region makes up a substantial part of the through-thickness region, a lower relative thickness is exhibited by this data compared to the mid-thickness data from the experiments and the FE-NUC-Mid-section data. As mentioned earlier, the degradation of speckle pattern at the inner and outer edges of the through thickness section could significantly affect the thickness strain measurement using DIC as maximum strains are at the edges. In other words, the entire span of thickness section was not available for capturing strain data especially at vary sharp curvatures. A loss of 10% of thickness section due to pattern degradation could generally be expected. The microscopic results across the edge were of similar trend to FE-NUC edge data showing that thinning effect was maximum at the edges. However, the microscope based mid-section thickness showed a rapid increase in thickness initially and decreased with the increase in curvature. The thickening effect is very slightly observed in the FE-NUC model data for the mid-section. The variation in thickness across the width is most likely due to the differential stress states that exist at the two edges and mid-section. The edges are in uniaxial tension and compression, whereas the mid-section is in plane strain tension and compression. Punch penetration could also affect the thickness when compressive stresses are combined with the uniaxial and plane strain stress states at the edge and mid-section respectively.

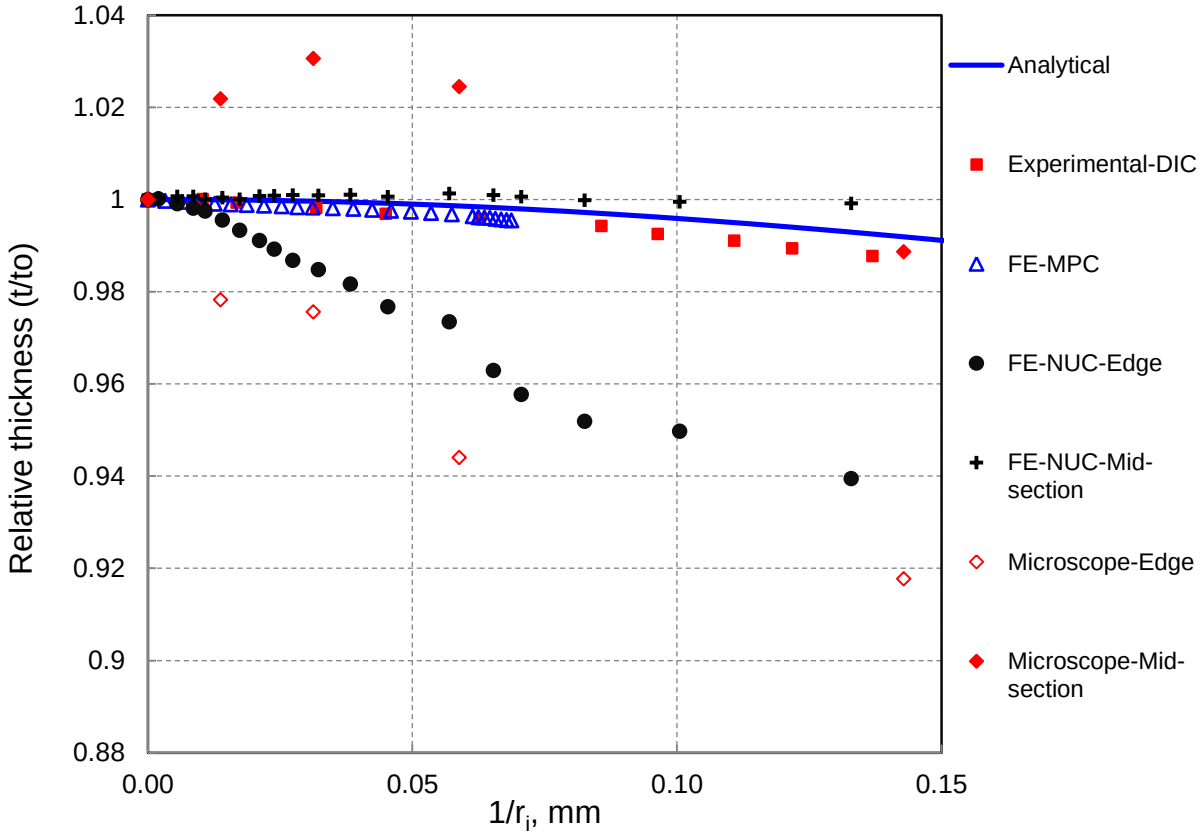

Figure 70. Comparison of relative thickness versus inner surface curvature from models and experiments.

6.1.4. Discrepancy between Models and Experiments

From a comparison of the characteristic plots of bending, it is to be noted that pure plane strain bending is seldom realized in real cases. The experimental test data was based on surface strain measurements and could not reveal the stress and strain distribution at the mid-section and at the compressive side of the specimen. Thus, the strain data from experiments was confined to the tensile surface of the specimen and to the specimen edge where speckle pattern could be applied and then continuously viewed with cameras for

DIC based strain measurements. The specimen edges were quite susceptible to edge effects and speckle pattern degradation that affected the strain measurement at the edges. A 3D FE model (i.e., FE-NUC) was therefore considered to compare with the experimental results wherever possible. The bending characteristics described in the analytical models of bending in the published literature are typically plotted with respect to the relative curvature (κ) which is the ratio of thickness to mid fiber radius. This poses an issue for comparison of model data with experimental results as the mid fiber radius (r_m) is neither uniform across the width nor directly obtainable through experiments. All the more, the physical meaning of relative curvature is not conveniently realized and could even be hypothetical. In order to have a common scale, the characteristic plots in Figure 70 were all represented with respect to the inner radius of the specimen (r_i). The relative thickness decreases for all the models for AA2024 material. The decrease was rather large at the edges due to edge effect combined with the effect of punch penetration and this could not be accounted for in the analytical model and FE-MPC models. It is to be noted that the FE-MPC model could only produce curvature ($1/r_i$) values upto 0.06 unlike the analytical and FE-NUC models that could reach up to 0.12. This is because the FE-MPC model produced perfect curvature unlike the experimental and FE-NUC models where the specimen showed non-uniform curvature rather early in the deformation process.

6.2. Bending Characteristics of SS400/AA1050 Bi-layer Laminate Sheets

In this section, experimental and model results pertaining to SS400/AA1050 bi-layer laminate are presented. Details related to experimental and modelling were provided earlier in Chapters 3-5.

6.2.1. Through-thickness Stress Distributions from Analytical and FE-MK Models

Figure 71(a,b) presents a comparison of through-thickness tangential and radial stress distributions corresponding to inner bend radius of 25 mm from analytical and FE-MK models (hereafter referred to as FE model) for C-T specimen for two different clad to matrix thickness ratios (q_1) of 0.1 and 0.25. For proper comparison, FE model data was obtained from the mid-section of the specimen that is closer to theoretical plane strain condition. Also included in Figure 71, for comparison purposes, are curves for monolithic SS400 steel. Both analytical and FE-MK models exhibit very similar behavior in terms of tangential stress distributions (Figure 71(a)). For example, the tensile tangential stress drops in the soft outer clad region for both models and the amount of drop in the stress is quite similar. The position through the thickness when this drop occurs is clearly a function of the clad to core thickness ratio. The slopes of the curves in the plastic region, in both tension and compression, also exhibit similar responses for the two models. The slope appears slightly higher in the tension region compared to the compression region. A shift in the neutral layer towards the compressive side (i.e., into the core), as indicated by the position zero tangential stress in the curves, is observed with increasing clad thickness. While the shift is consistent for the two models, the shift appears to be

somewhat higher in the analytical model compared to the FE model. Among the differences, the mid-thickness elastic portion of the curve is expressed as a vertical line in the analytical model due to the assumption of rigid work hardening material whereas for the FE model a sloped line in the mid-thickness region is obtained. With respect to the radial stress distributions from the two models, Figure 71(b), consistent trends were once again observed in the two models. The radial stress component reached a maximum in compression in the mid-thickness region of the sheet and dropped to zero and near-zero values in the analytical and FE models, respectively. The radial stress slope declined for the soft clad layer as observed previously in the tangential stress plot. However the maximum radial stress value moves towards the core side as the clad to core thickness increases. The maximum compressive radial stress values from the FE results were almost half of those observed in the analytical model. In addition, the radial stresses develop more slowly in the FE model compared to the analytical model. This variation could be attributed to curvature difference, deviation from exact plane strain condition and free surface effect for FE model respectively. Figure 72(a,b) presents results similar to Figure 71(a,b), for C-C specimen. Many of the observations were similar with regard to the two models. For example, the presence of the soft clad layer on the compressive tangential stress side (Figure 72 (a)) leads to a drop in tangential stress. However, some irregularities were observed in the stress profiles from the FE model data at the free surface that possibly relieved the stress.

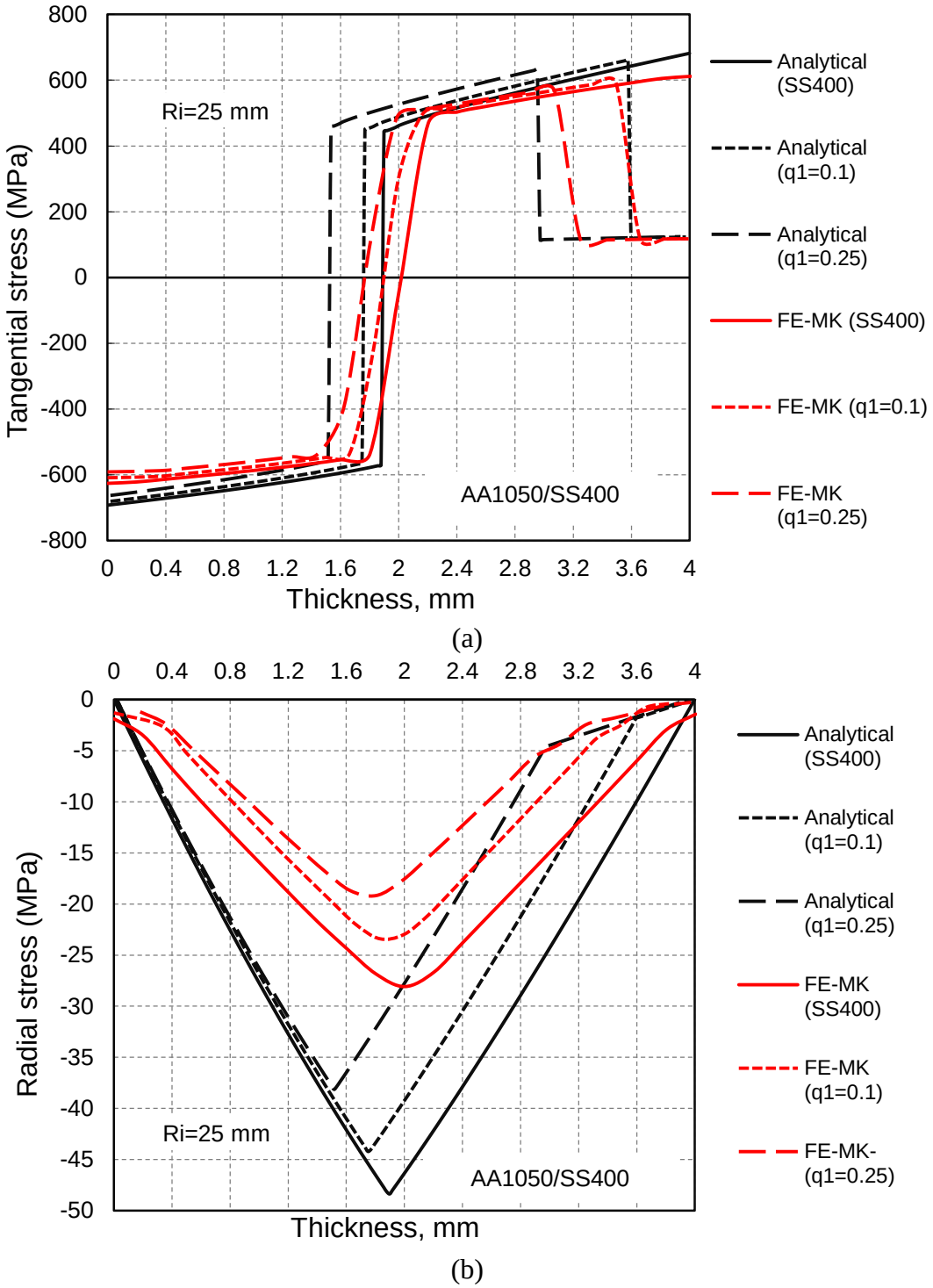

Figure 71. Comparison of through-thickness stress distributions in bi-layer C-T specimen and monolithic SS400 steel layer at an inner radius of 25 mm, (a) tangential stress, and (b) radial stress.

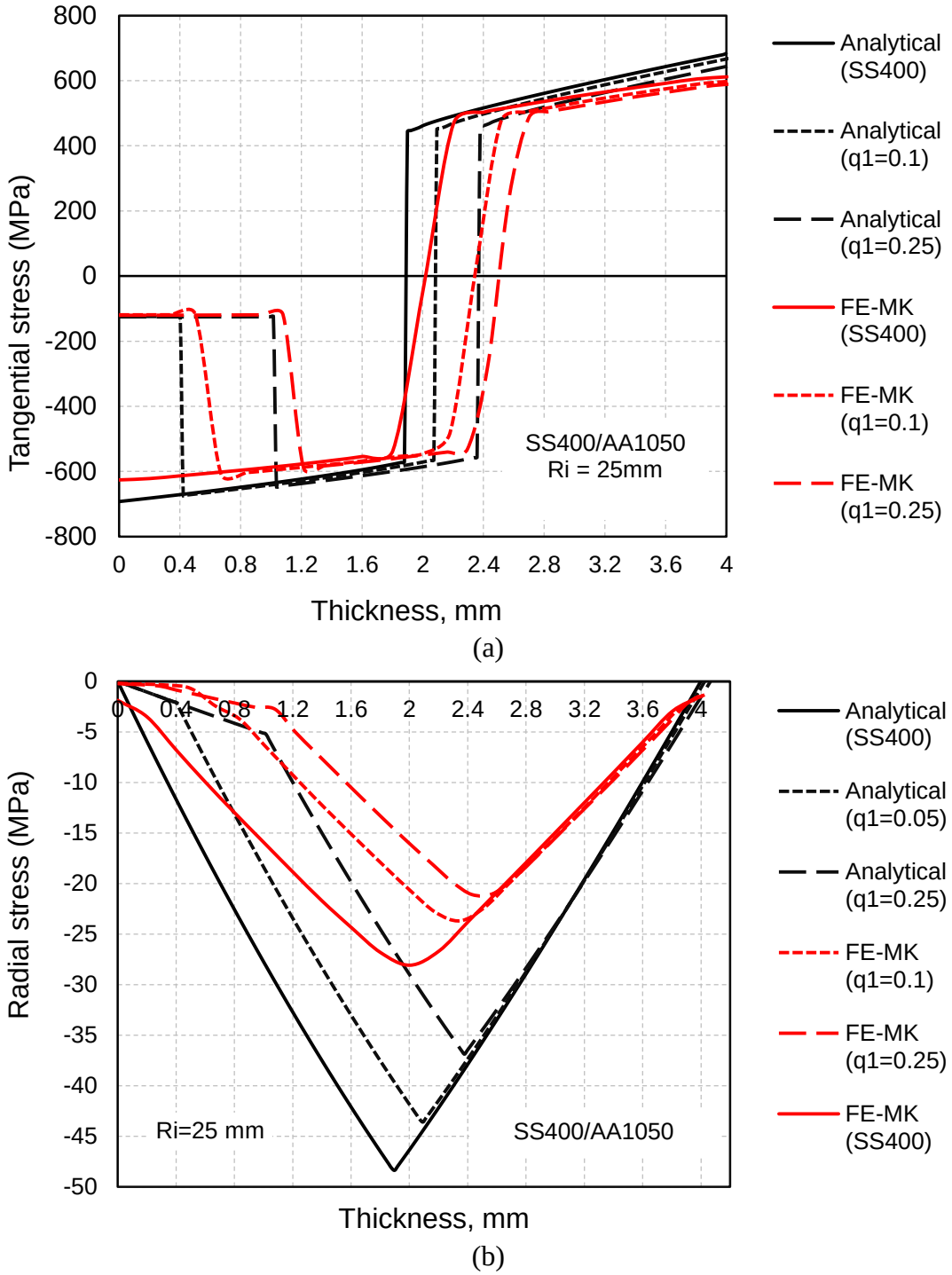

Figure 72. Comparison of through-thickness stress distributions in bi-layer C-C specimen and monolithic SS400 steel layer at an inner radius of 25 mm, (a) tangential stress, and (b) radial stress.

6.2.2. Through Thickness Tangential Strain Distributions from Analytical and FE-MK Models

Figure 73(a) presents tangential strain distribution from C-T specimens in a manner similar to earlier Figure 67 for monolithic AA2024 sheet. The analytical model exhibits a linear curve from compression at the core side to tension on the clad side. The FE model, however, shows lower slope in strain distribution as well as non-linearity especially at larger plastic strains. This is because the specimen undergoes perfect pure bend curvatures without strain along the third axis in the 2D analytical model. The 3D FE model allows the material to adjust along the width direction to cause the drop in strain at the weak clad layer. Similar results were obtained from the two models for C-C specimen (Figure 73(b)) but with a reversal in the positions of the curves in terms of clad to core thickness ratios. In other words, the tangential strain increased in magnitude with increasing clad thickness ratio for C-T specimen but decreased for C-C. The strain variation with respect to soft clad thickness is attributed to the relative difference in strengths between steel and aluminum. Aluminum being a weaker material is deformed to larger strains compared to steel and hence the variation with respect to clad thickness ratio. Overall the C-T specimen produced the maximum strain as AA1050 was subject to higher strain on the outer tensile convex side compared to compression on the inner concave side.

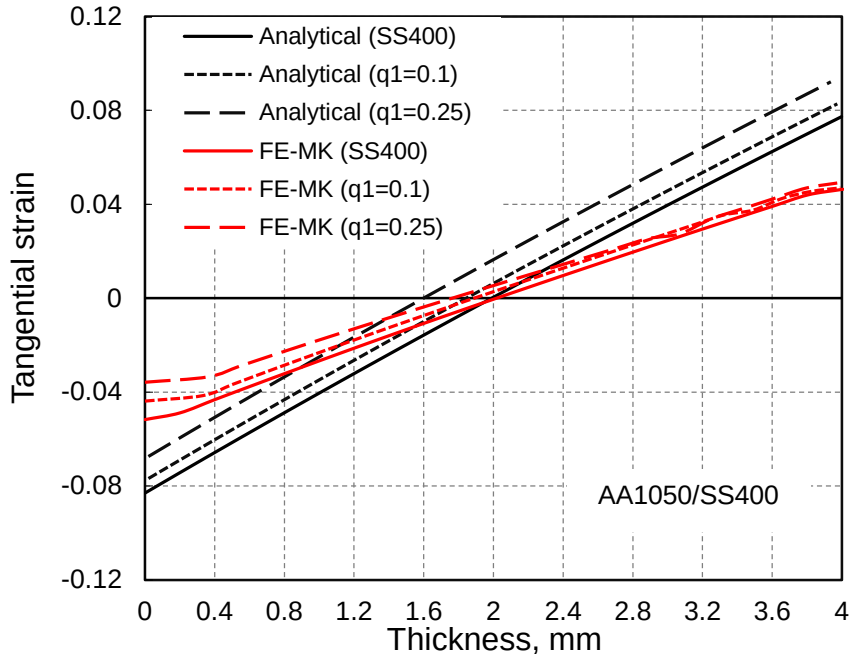

(a)

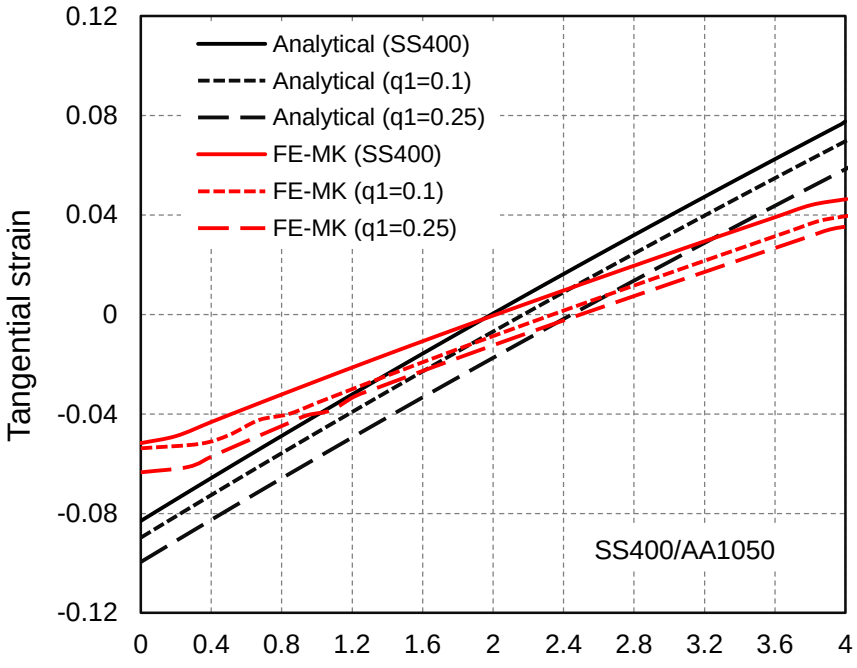

(b)

Figure 73. Through-thickness tangential strain distributions in bi-layer; (a) C-T and (b) C-C specimens with monolithic SS400 steel layer at an inner radius of 25 mm.

6.2.3. Tangential Strain Distributions through the Thickness and Across Width from Experimental and FE Model

Figure 74 shows experimental through-thickness strain distribution for C-T and C-C specimens as obtained from DIC analysis. The strain data is taken from the specimen edge that is largely in uniaxial stress state but does exhibit edge effect (anticlastic curvature) when compared to plane strain state for analytical and FE model. The general trend is similar to the model data shown earlier in Figure 73. However, experimental strain measurements from through-thickness region tended to be rather sensitive to the quality (size) of the speckle pattern, DIC parameters (facet size, facet step, filter size) and the size of the image both of which influenced the accuracy of the strain calculation. The outer fibers of the through-thickness region did not yield any strain due to speckle pattern degradation.

The width strains of the bi-layer C-T and C-C specimens from the two models and experimental DIC measurements are shown in Figure 75(b). In bending, the tension side contracts and compressive side elongates along the lateral (width) direction to compensate for the longitudinal tension and compression (refer Figure 75(a)). The same was observed for C-T specimen, where width strains were compressive on the tension side and tensile on the compression side. For C-C specimen, with increase in thickness ratio (q_1), the width strains became equally proportional on the tensile and compressive sides, i.e., the specimen was subjected to equal tension and compression across the width as observed in C-C-0.25 specimen. However, for the monolithic SS400 and C-T specimen, the strains become disproportional with increasing thickness ratio. For

example, for the C-T-0.25 specimen compressive strains were twice the magnitude of the tensile strains.

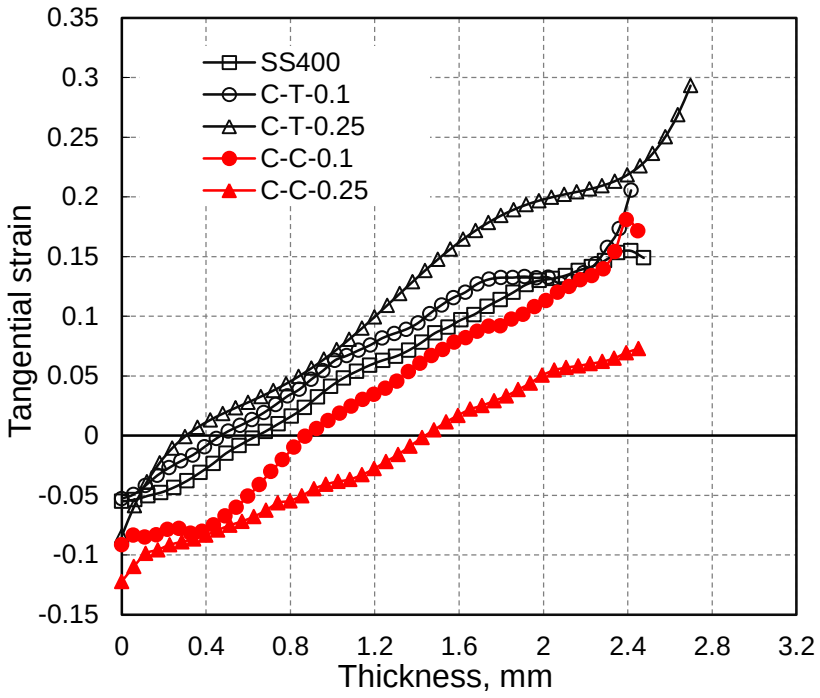

Figure 74. Experimental through-thickness tangential strain distributions for C-T and C-C specimens for two different clad to core thickness ratios and monolithic SS400 steel layer at an inner radius (r_i) of 25 mm.

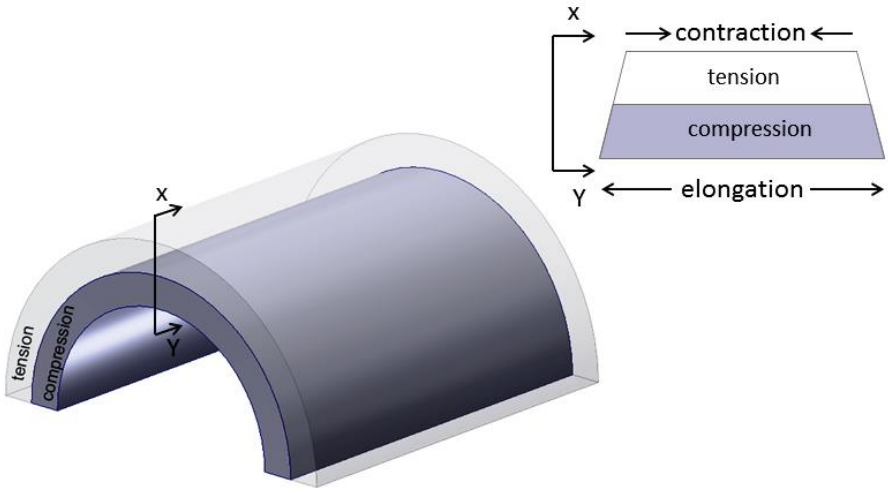

(a) (figure continued on next page)

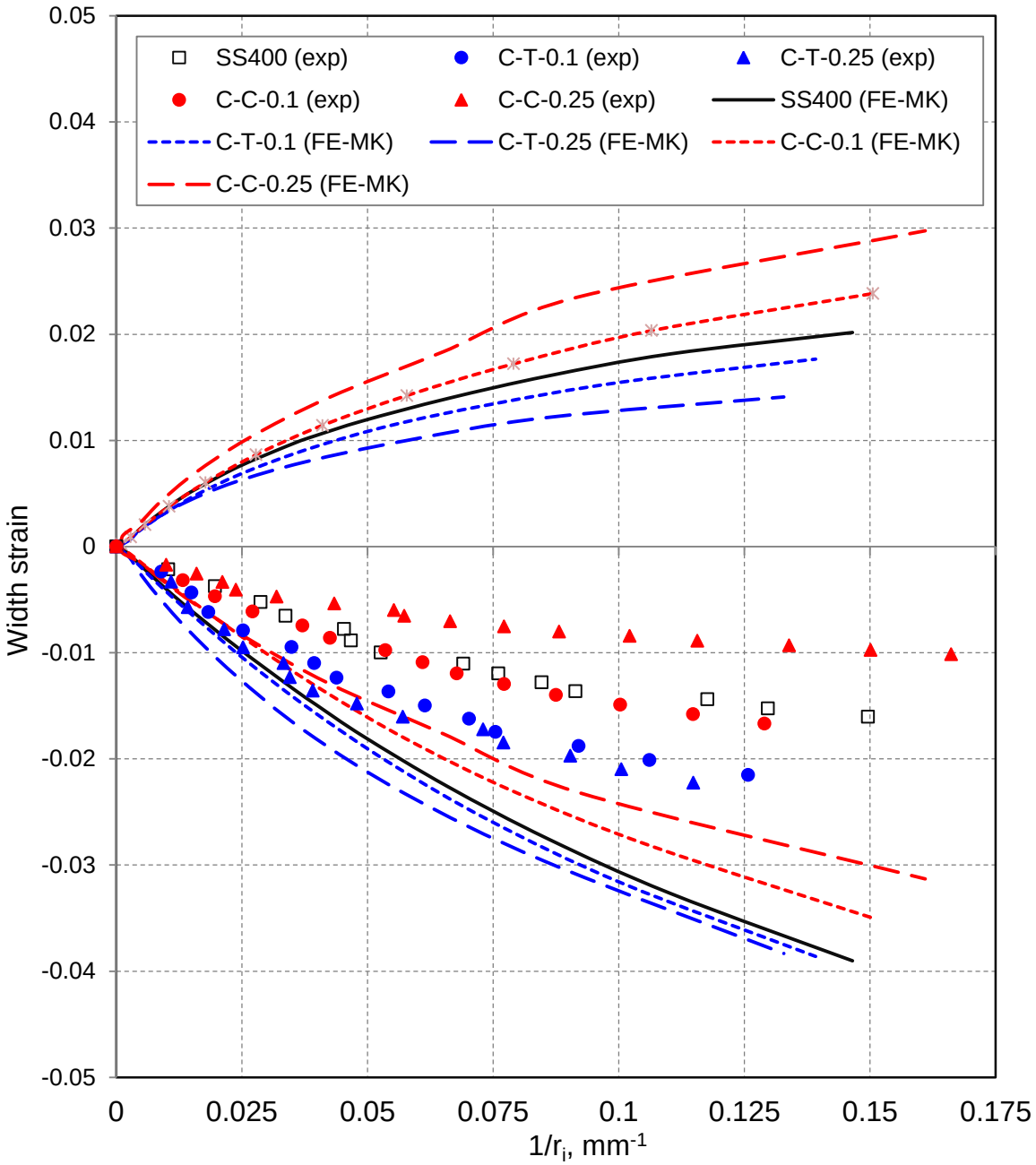

(b)

Figure 75. Bi-layer bending characteristics across width, (a)schematic of elongation and contraction along width section in bending; (b)FE-MK model versus experimental width strain distributions for C-T and C-C specimens for two different clad to core thickness ratios and monolithic SS400 steel layer for a specimen bent to an inner radius of 25 mm. (width strain measurements were made on the convex surface of the specimen).

In general, it is observed that the order of magnitude in tangential and width strains for the C-T and C-C specimen is similar but not the actual magnitude between experiments and model data. The compressive width strain on the tensile tangential stress side is higher for C-T-0.25 that has a soft AA1050 outer clad material. The same effect is seen in the tensile width strain on C-C-0.25. In other words, the tensile strains dominate to produce higher width strain in bending when compared to compressive strain. It is to be noted that width contraction on the tensile side is more than width expansion on the compressive side.

6.2.4. Model versus Experimental Relative Thickness Changes in Bending

A comparison of relative thickness as a function of specimen curvature ($1/r_i$) for analytical and FE models with experimental results from DIC data is shown in Figure 76 and Figure 77. The analytical and experimental data is compared with FE model's mid-section data in Figure 76(a,b) and with edge data in Figure 77(a,b). The analytical model predicts that the relative thickness decreases (thinning), when softer aluminum is in the tension side and increases (thickens) when aluminum is in the compression side. The FE model mid-section data shows trend closer to analytical model that is in plane strain condition, whereas the edge data is closer to experimental data taken from the edge (uniaxial tensile condition). However, the experimental results do not distinctly show thickening for C-C case as seen in the models. Instead the magnitude of thinning is larger for C-T specimen. The primary reason for variations is that the strain data from

experiments are obtained from the specimen edge that is subject to edge effects as described in section 3.2.1. Secondly the window for strain data measurement is slightly smaller in scale compared to the full through-thickness span of the specimen owing to speckle pattern loss at the top and bottom edges. Further the rate at which the material thickness change depends upon the thickness ratio (q_1) and the ratio of the yield strengths of the two materials owing to their different tensile properties.

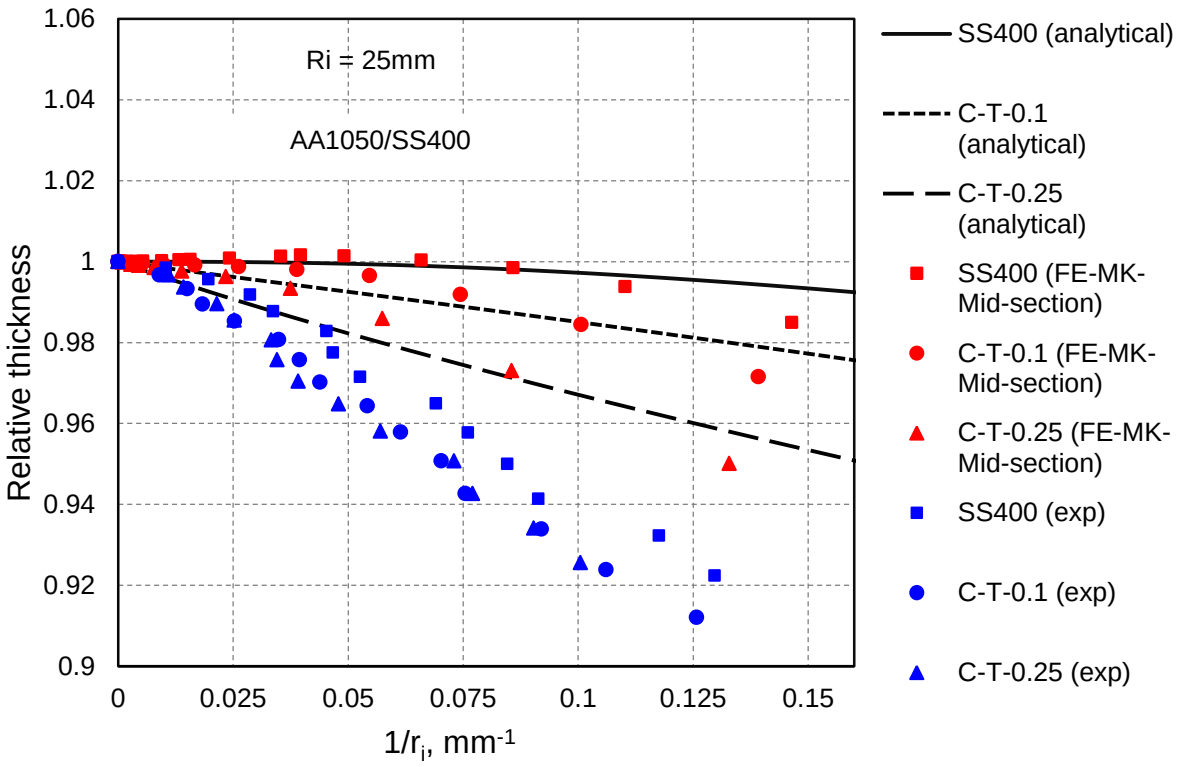

(a)

(figure continued on next page)

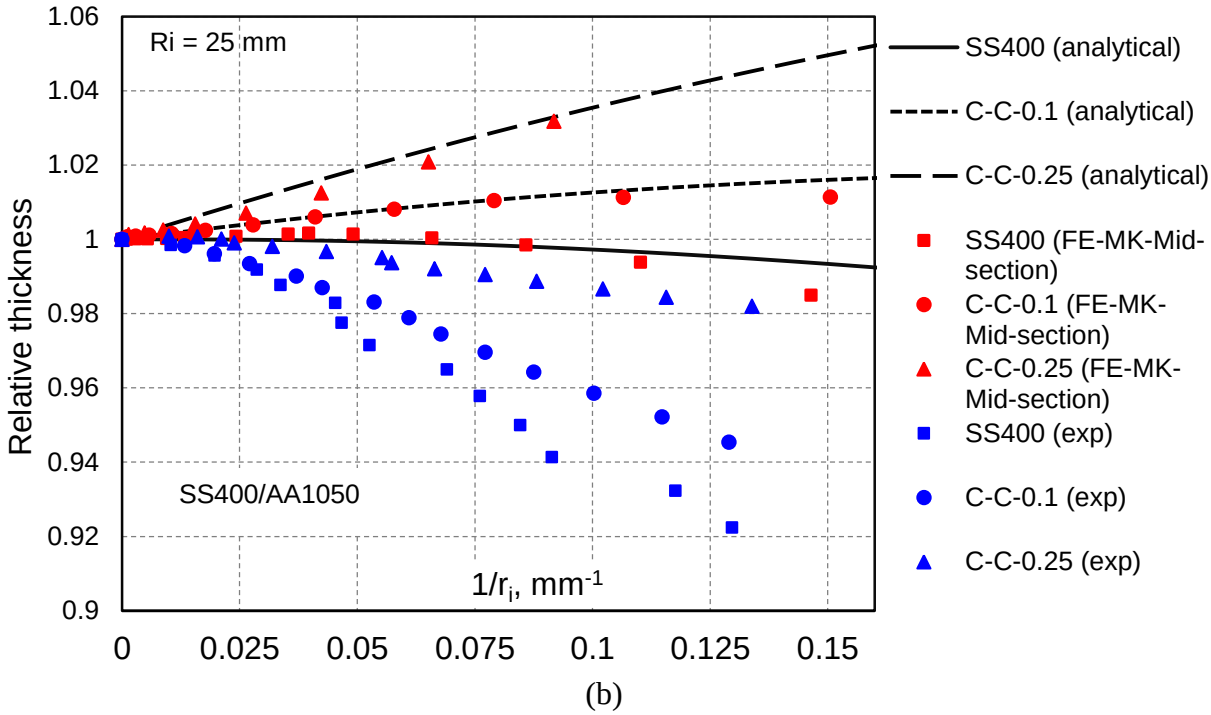

(b)

Figure 76. Models versus experimental (DIC edge) relative thickness as a function of radius of curvature for bi-layer specimens of two different thickness ratios and monolithic SS400 sheet, (a) C-T, and (b) C-C (compared with FE-mid-section data).

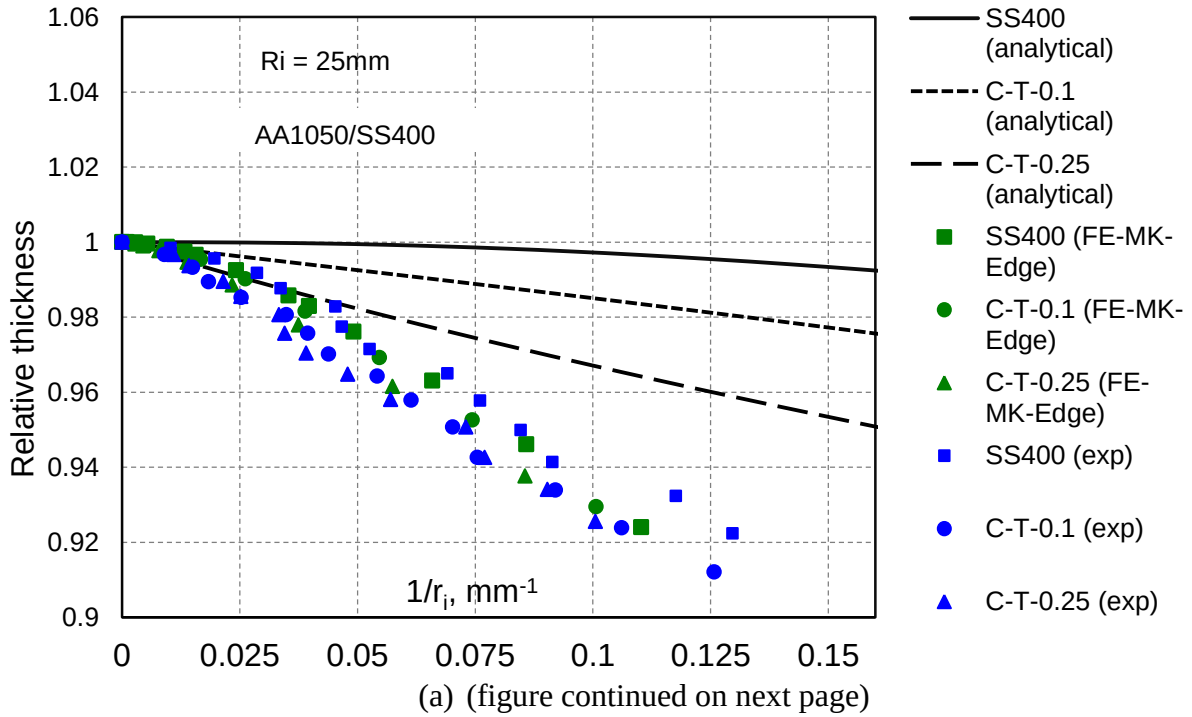

(a) (figure continued on next page)

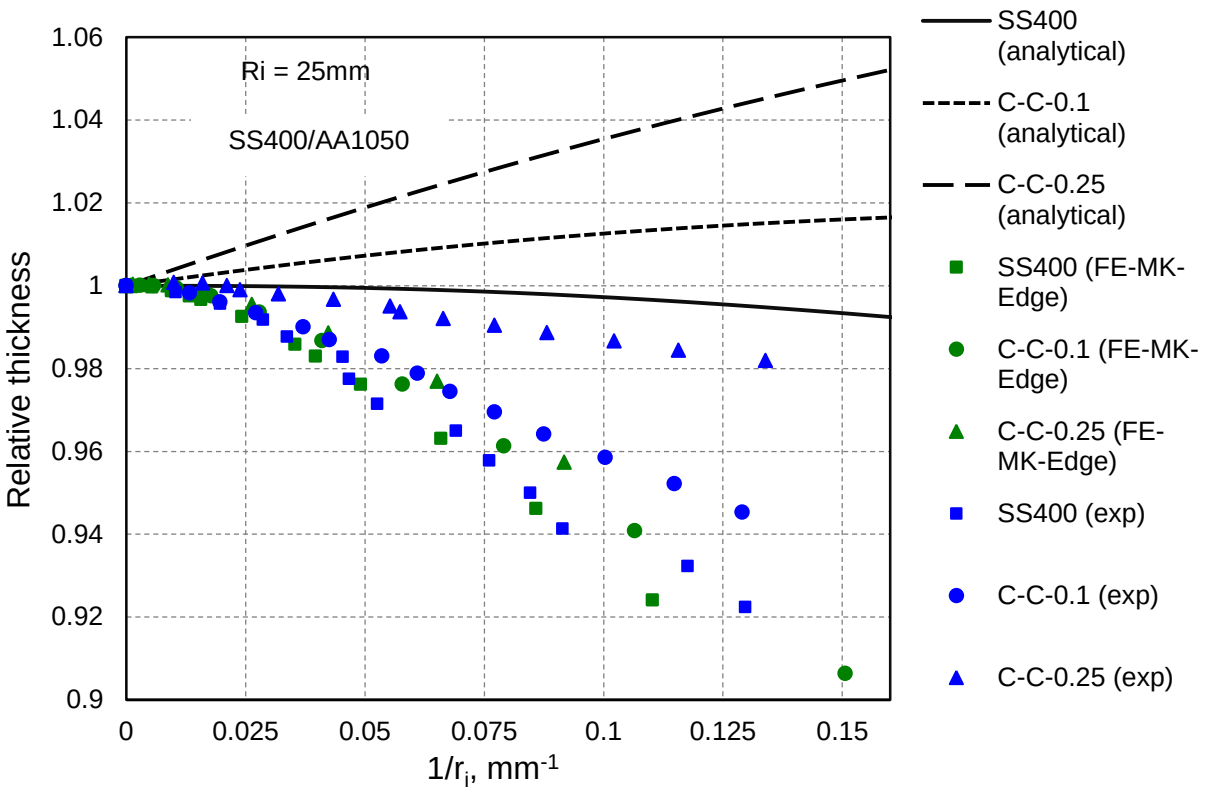

(b)

Figure 77. Models versus experimental (DIC edge data) relative thickness as a function of radius of curvature for bi-layer specimens of two different thickness ratios and monolithic SS400 sheet, (a) C-T, and (b) C-C (compared with FE-edge data).

6.2.5. Relative Thickness across specimen width

The measured data from the photographs is plotted as relative thickness versus width for C-T and C-C specimens in Figure 78, for two different thickness ratios. The thinning for C-T and thickening for C-C specimens across width is analogous to the earlier through-thickness data for monolithic AA2024 sheet, i.e., the clad C-T specimens undergo thinning (with relative thickness less than 1) whereas C-C specimens undergo thickening (with relative thickness values greater than 1). The amount of thinning or thickening was

a function of clad/core thickness ratio. A higher thickness ratio of 0.25 led to significant decrease and increase in relative thickness for C-T and C-C specimens. The fluctuation in thickness profile are largely due to experimental error arising from specimen preparation and thickness measurement procedure rather than any microstructure related surface events.

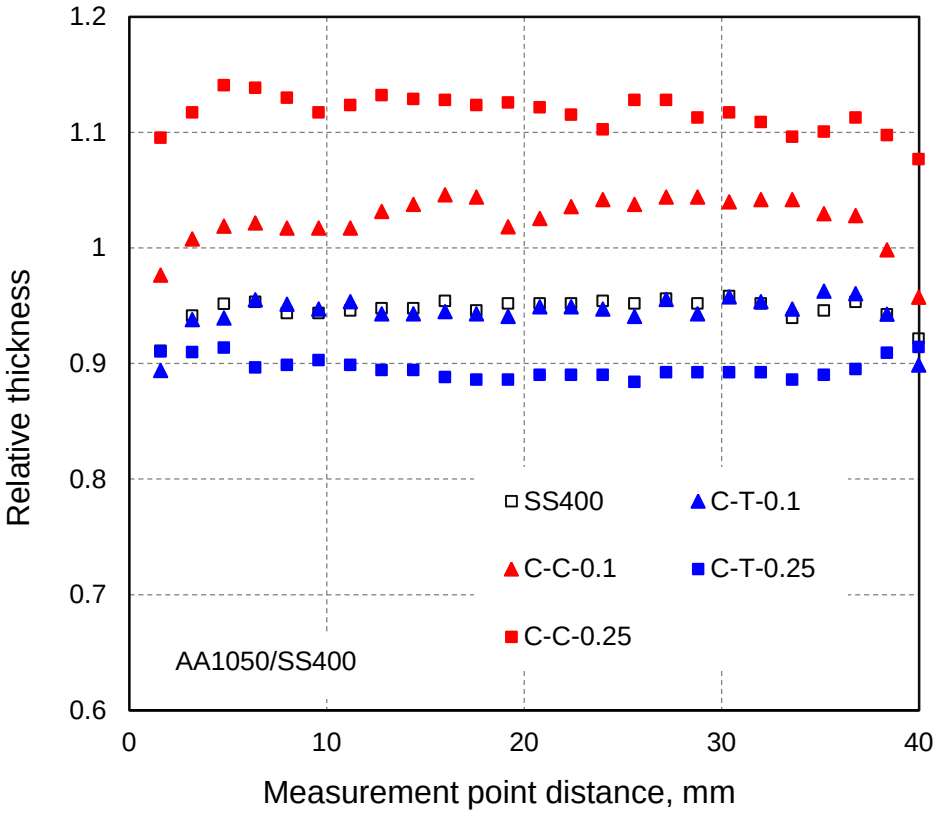

Figure 78. Experimental relative thickness traces across specimen width at the bend line for inner radius of 25 mm.

6.2.6. Discrepancy between Models and Experiments

As shown in the previous section, all of the models capture certain experimental bending characteristics of laminate sheet materials. The 2D (or plane strain) analytical model considers zone-wise strain calculation by applying appropriate material hardening laws to account for stress reversal effects. It is superior in computational efficiency but still theoretical in many ways as properties such as tool-sheet contact and friction are neglected. A 3D FE model (FE-MK), is able to overcome many of the limitations of the plane strain analytical model such as extraction of stress, strain data from any section across the width (not possible in analytical and experimental methods). However, boundary conditions of the experiments are simplified in terms of punch and die reactions and coefficient of friction are assumed from the literature for dry friction. In spite of these differences, a good agreement between the analytical model and FE model has been achieved in predicting the relative thickness change as a function of specimen curvature (see earlier Figure 76 and Figure 77). Both models produce uniform curvature throughout the specimen to realize pure bending. However, the experimental relative thickness measurement do not follow the modeling results closely perhaps due to a combination of change in stress state (analytical model data corresponds to mid-width section where plane strain state exists whereas the experimental data comes from the edge of the specimen where the stress state is closer to uniaxial), punch penetration effect and DIC measurement error as discussed later. The 3D FE model is helpful in obtaining the strain across the width section and thickness gradient. In this sense, it serves to bridge the gap between 2D analytical model and the experimental data.

6.2.7. Comparison with Other Bending Models

Two other models on laminate sheets based on advanced theory of bending and following the zone-wise classification of sheet thickness are available in the literature. The model by Verguts and Sowerby (Verguts and Sowerby, 1975) used a non-strain hardening law for the zones that resulted in linear distribution of tangential and radial stresses, especially in the intermediate zone. The model did not consider the clad-matrix boundary radii, but instead considered the clad thickness ratio in terms of relative thickness and curvature parameters. The model predicted that a weak clad and strong matrix decreased the thickness and the opposite increased the thickness. There were no results on relative thickness variation and effects of clad to matrix thickness ratios on the stress and thickness magnitudes. A second comparison was made between strain hardening clad and non-strain hardening matrix and vice-versa. While the first combination decreased the thickness, the latter increased. However, such arbitrary hardening combinations of laminate systems are not commonly found in sheet metal manufacturing. The work by Majlessi and Dadras (Majlessi and Dadras, 1983) categorized the model specimen based on the position of the neutral fiber with respect to the un-stretched radius. The outer and inner clad layer boundary radii were represented in terms of ratios of the strains of neutral fiber, whereas, the present approach represents them in terms of other boundary radii and thickness ratio. Other major information missing was about the geometrical arrangement of the clad layer and matrix. The work of Dadras and Majlessi generalized that a weak clad and strong core reduced the thickness and the vice versa increased the thickness. However the present work concludes analytically and experimentally that the reduction in

thickness was observed only when the weak clad was in the outer convex side. On the other hand, the material would thicken when the clad layer was placed on the inner concave side. Both of the studies represented the stress distribution in terms of relative curvature of the specimen. Such representation is especially inconvenient when results of the model are being compared with experiments and FE model. The current study thus presents the through-thickness stress distribution in terms of inner radius of the specimen. The above analytical models from the literature and the ones developed in the present work (analytical and FE-based) predict the same thinning or thickening effect based upon the relative strengths, thickness ratio and geometrical arrangement of the clad and laminate layers (i.e., C-C and C-T).

6.2.8. Limitations and Significance of the Results

It is to be noted that the interface between the laminate layers is assumed to be thin and perfect. Therefore, interface characteristics such as strength and thickness are not included in the analysis. The interface thickness was analyzed in the present bi-layer and tri-layer laminates and was found to be in the range 5–10 μm and well below the thickness of each of the layers. Also, the interface in bent specimens was examined by optical microscope and no delamination of the interface was observed up to r_i = 25 mm. Therefore, the assumptions of 'perfect' interface between layers in the analytical and FE models appears reasonable. The properties of the interface obviously depend upon the type of lamination process, and especially when oxide, intermetallics or even voids are

formed during the cladding process and the interface layer thickness is significant. Also, for simplicity, it has been assumed in the development of the 4-zone analytical model that no stress reversal occurs in the innermost and outermost zones for the materials studied in the present work. This was indeed found to be the case in the FE model results where no such restrictions exist. It would be useful to study the role of interface when it lies in the load (or stress) reversal zone.

The DIC methodology has been applied to in-situ bending experiments within a scanning electron microscope (SEM) for studying material flow and strain localization and corresponding through-thickness strain field in a monolithic aluminum sheet (Davidkov et al., 2012) where it was shown that the results are sensitive to the image magnification and other DIC parameters. The images of the deformed through-thickness bend region from larger bend specimens at low magnification, such as in the present experiments, introduce additional errors in terms of speckle size and loss of focus in the image in critical outer and inner fiber regions. Therefore, deviation between the experimental and model relative thickness and width strain data were likely from the inherent errors in the present DIC measurements and analysis.

6.3. Bending Characteristics of AA1100/AA2024/AA1100 Tri-layer Laminate Sheets

6.3.1. Through-thickness Stress Distributions from Analytical and FE-MK Models

Modeling results from analytical and FE-MK models for tri-layer laminate at two different clad to matrix thickness ratios (15% and 25%) are presented in this section. FE method provides stress calculation at any section of the bend specimen which otherwise is not possible by experimental methods. Through-thickness tangential and radial stress distributions for different thickness ratios of AA1100 clad to AA2024 matrix are shown in Figure 79(a,b) respectively. The data for stress values are taken from the mid-width section of the specimen that is closer to plane strain state when compared to the edges (refer to Figure 1). Note that stress values for monolithic AA2024 sheet for an inner radius (r_i) of 15 mm are also included for comparison. Both tangential and radial stresses decrease with increasing clad thickness ratio (i.e., increasing q values). However, the analytical model curve in the matrix layer remain largely unaffected. The tangential stress drop is considerable in the softer clad AA1100 layers in both tension and compression. The FE-MK model shows a smoother transition in tangential stress in the mid-thickness elastic region and a larger tangential stress drop in the soft clad layers. Note that elastic component is not included in the analytical model and it causes a sharp transition to plastic state. As expected, the radial stress components are compressive and continuous across the entire laminate thickness, and their maximum value is slightly shifted towards the center of curvature from the mid-thickness region. The maximum radial stress values

are only about 10% of the maximum tangential stress. There is a slight perturbation in the FE model plots of radial and tangential curves (see Figure 79) seen at the top and bottom surfaces that could be due to the interplay between the layer boundaries that is formed by partitioning the monolithic material in Abaqus. As in the case of bi-layer study, the magnitude of maximum radial stress is lower for the FE model compared to the analytical model. Secondly, variation in exact matching of the curvatures from analytical and FE models could cause this difference. In general, the two models exhibit very similar trends in through-thickness tangential and radial stress distributions. The tangential distribution across the width, i.e., along bend-line of the tension side is shown in Figure 80(a). The stress distribution is compared for inner radius of 15 mm at two laminate thickness ratios and for monolithic AA2024. The stress profile indicates that the maximum tangential (major) stress is at the mid-width location where the material is very close to plane strain state. The stress magnitude is higher for the harder AA2024 monolithic case. The tangential stress distribution at the tensile surface is compared with the data obtained from an approximate depth of 0.8mm. The depth was chosen to observe the stresses in the hard AA2024 matrix. The tri-layer laminates show negligible difference in stress distribution for the two thickness ratios both having similar material in its tensile surface, i.e. AA1100. This shows that that thickness ratio of the laminate material only has a subtle effect on the surface tangential stresses across the width. However the tangential stress magnitudes are closer in the hard AA2024 layer for the laminate and monolithic cases. The same behaviour is observed in the radial stress distribution across the width in Figure 80(b), except that the magnitude increases with depth.

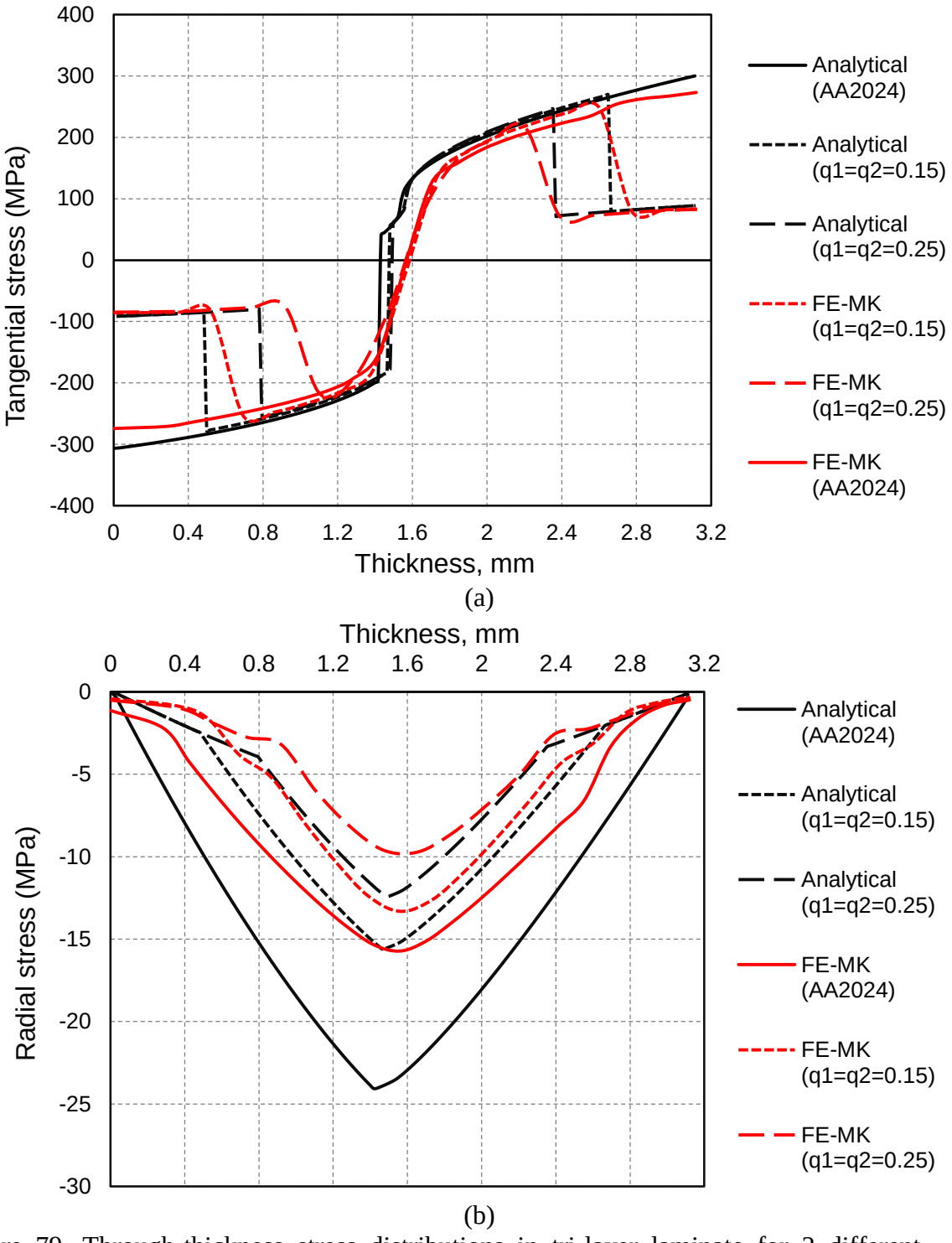

Figure 79. Through-thickness stress distributions in tri-layer laminate for 2 different thickness ratios at a radius of curvature of r_i =15 mm from analytical and FE-MK models. Also included, for comparison purposes, are the curves for monolithic AA2024 sheet.

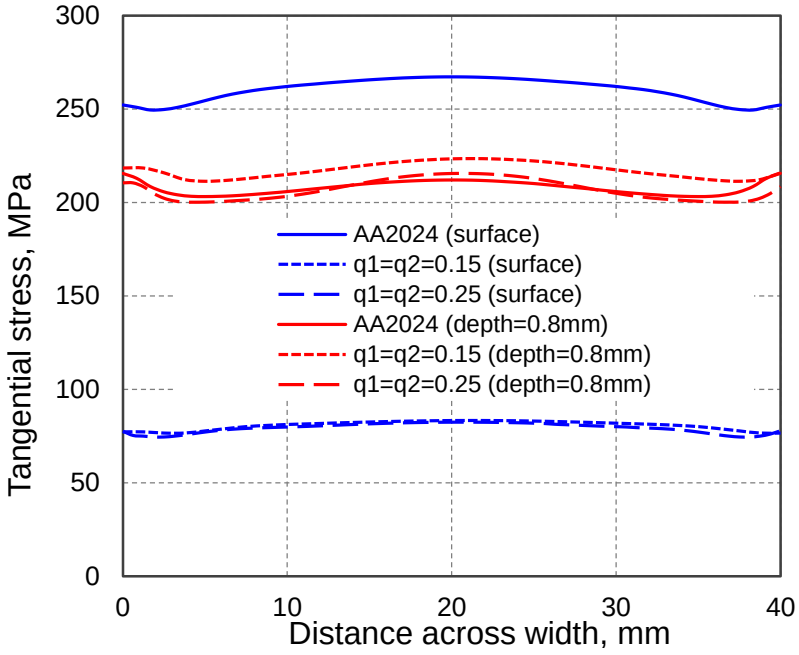

(a)

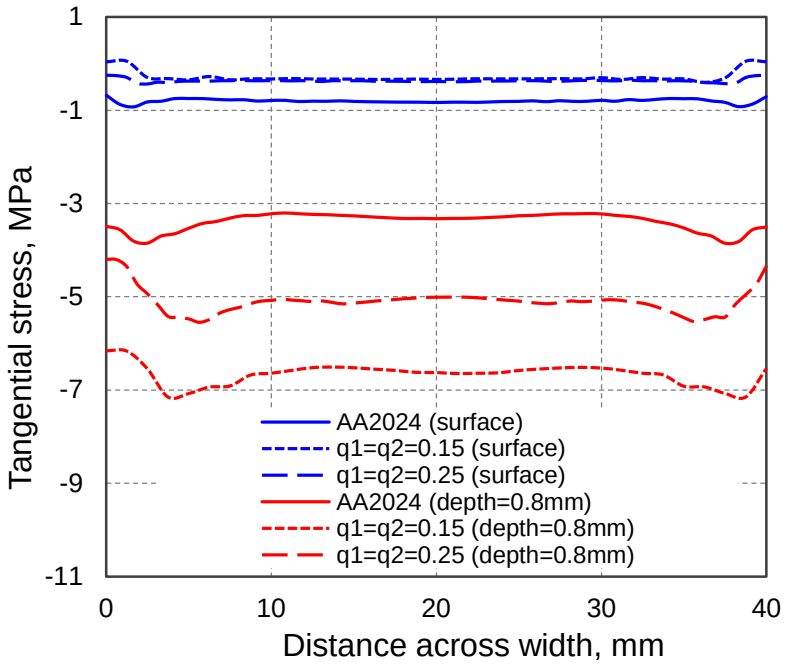

(b)

Figure 80. Tangential stress distributions across width (bend-line) and on (a) the top surface and (b) at a depth of 0.8 mm from the top surface of the tri-layer laminate for 2 different thickness ratios at a radius of curvature of 15 mm from analytical and FE-MK models. Also included, for comparison purposes, are the curves for monolithic AA2024 sheet.

6.3.2. Tangential Strain Distributions through Thickness and Across Width

Figure 81(a) shows tangential strain distributions across the thickness for two different laminate thickness ratios and for monolithic core material (AA2024) from analytical and FE models. The analytical model gives virtually the same curve for all 3 cases whereas 3 distinct curves are obtained from the FE model. Similar to the monolithic material, the FE model for tri-layer predicts a lower slope. The reduction in slope is higher at the outer and inner surfaces for both clad and monolithic specimens, which is not observed in the analytical model. This is possibly due to stress relief at the free surfaces. Figure 81(b) shows the tangential strain along the bend line (i.e., along the width) of the specimen for the same conditions as in Figure 81(a). The strain is compressive on the tensile side and vice versa on the compressive side. Compressive strain on the tensile side is significantly higher from both sets of models compared to the tensile strain on the compressive side due to the shift in the neutral plane towards the compressive side. Note that similar observations were made for bi-layer material (see earlier Figure 75(b)). With respect to laminated sheets, a considerable variation in width strain from monolithic AA2024 is seen only on the tensile side of the specimen. Otherwise, negligible variations are observed among monolithic and laminate cases.

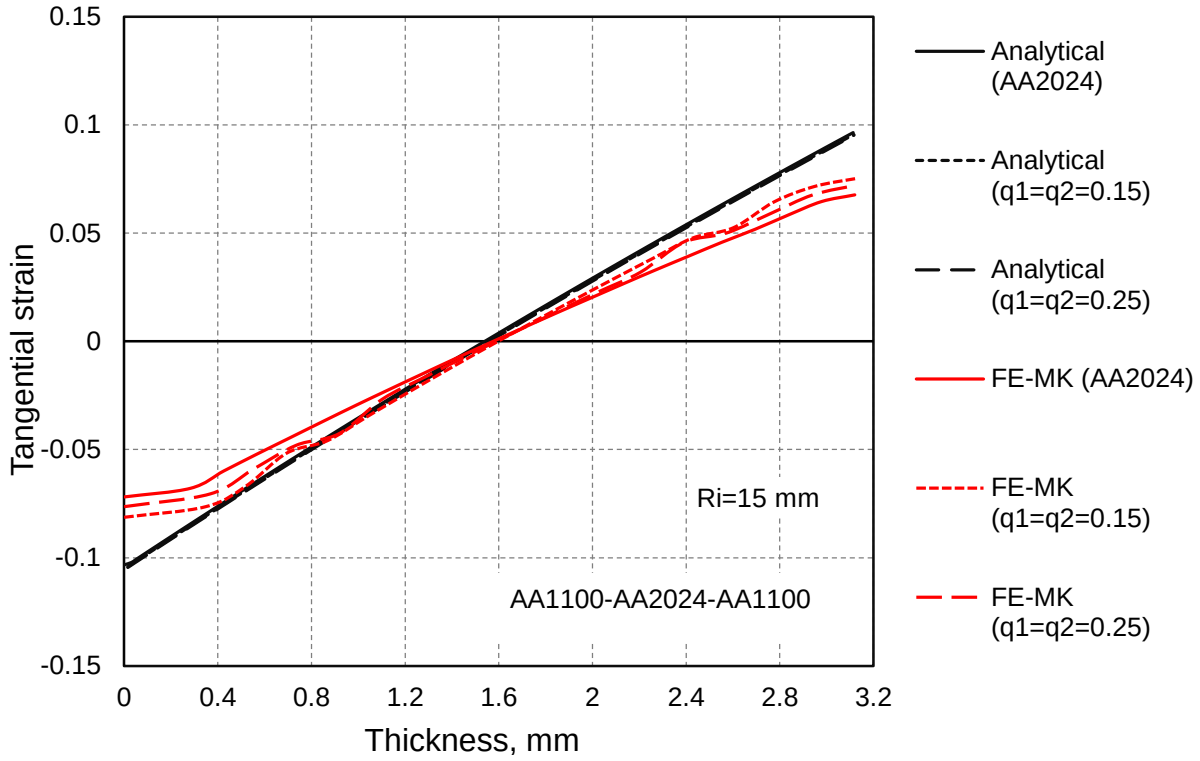

(a)

(figure continued on next page)

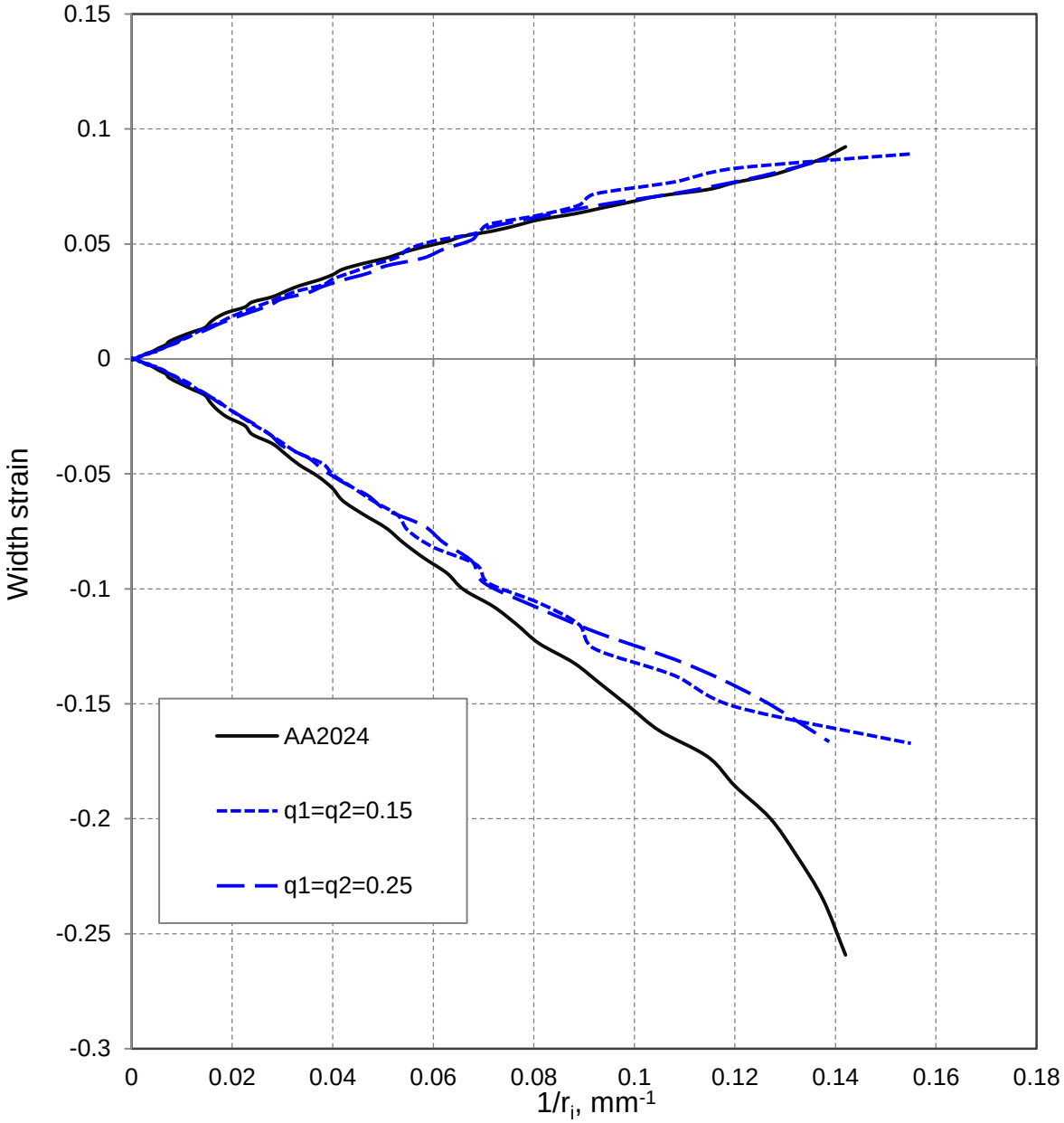

(b)

Figure 81. Strain distributions in monolithic AA2024 and tri-layer laminate, (a) through-thickness tangential strain distributions for 2 different laminate thickness ratios at a radius of curvature of 15 mm from analytical and FE-MK models, (b) width strains from tensile and compressive surfaces at bend line from FE-MK model at different radii of curvature. Also included, for comparison purposes, are the curves for monolithic AA2024 sheet.

Figure 82(a,b) shows the tangential and radial strain distributions across the specimen width. Unlike the tangential stress distribution, as shown earlier in Figure 80, the tangential strain is greater at the specimen edges compared to the mid-width. The radial strain is maximum at a slight offset from the edge compared to the tangential strain. The order of tangential and radial strain compared to the monolithic case shows that the strain is slightly greater for the laminate with 25 % thickness ratio and decreases for 15%.

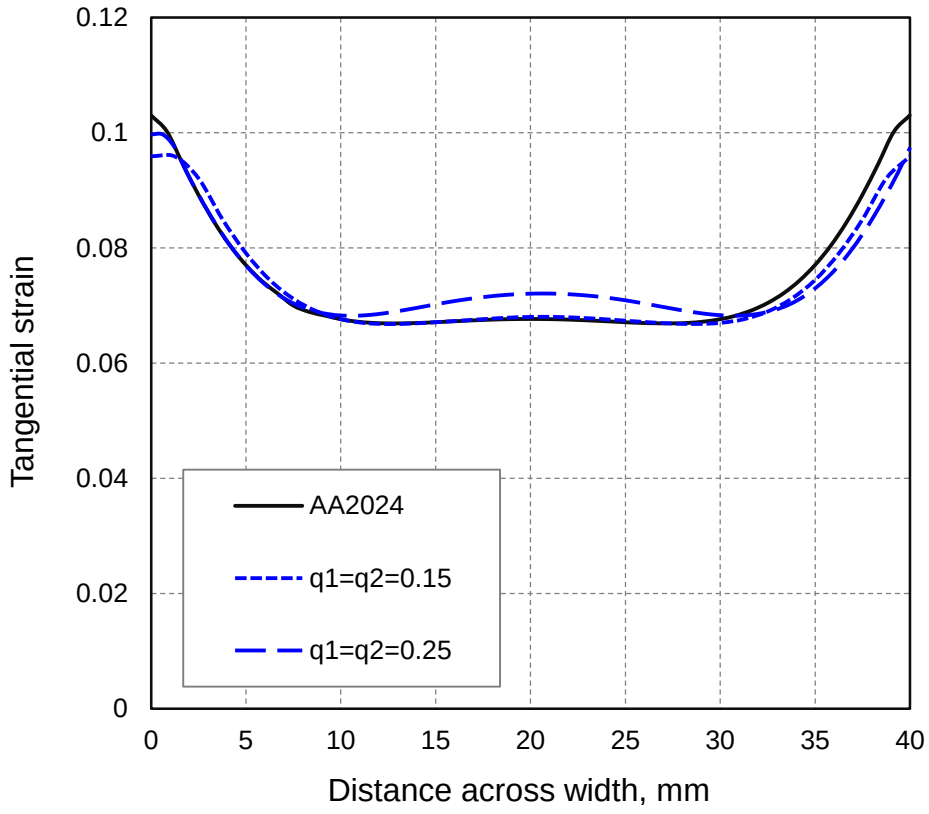

(a)

(figure continued on next page)

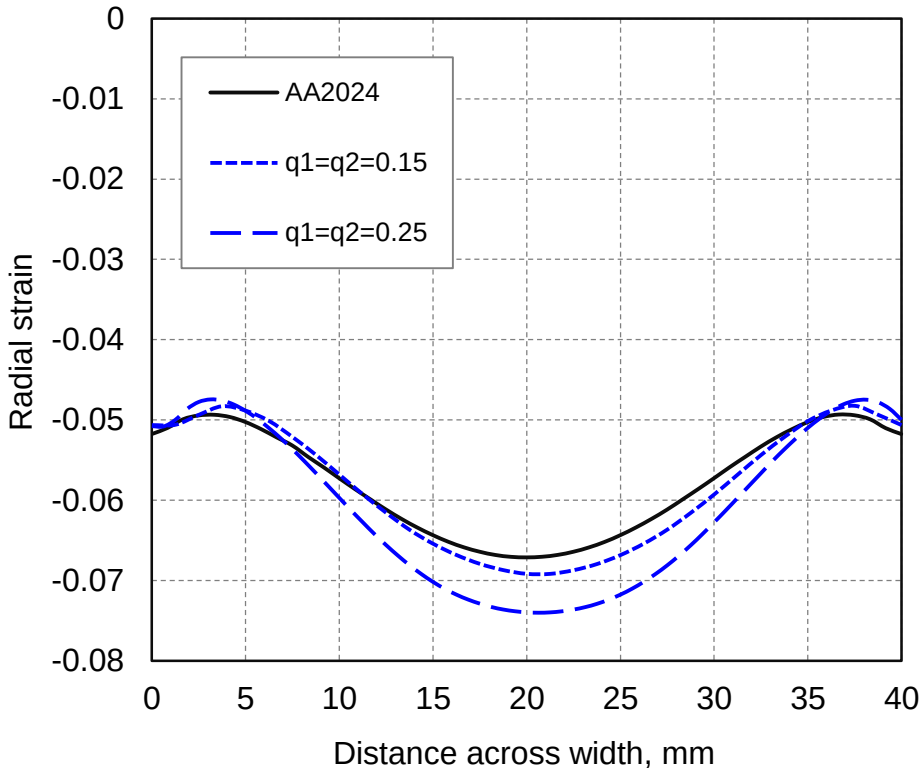

(b)

Figure 82. Bending characteristics of tri-layer laminate sheet, (a) tangential and (b) radial strain distributions across width (bend-line) for 2 different thickness ratios at a radius of curvature of 15 mm from analytical and FE-MK models. Also included, for comparison purposes, are the curves for monolithic AA2024.

6.3.3. Relative Thickness Changes with Curvature

Plots of relative thickness versus specimen curvature from the two models are shown in Figure 83. The FE model data has been extracted from the mid-width cross-section of the bent specimens. The two models clearly yield quite different results. In the case of FE model, the sheet thickens in the early stages of bending and subsequently thins whereas, in the case of analytical model, continuous thinning is observed from the beginning of bending as the curvature is increased. The initial thickening, although only slightly above

the initial thickness, is likely due to the nature of MK bend test design where bending initiates from the ends of the specimen and propagates towards the bend line as opposed to punch actuated bending where bending typically occurs at the mid-span and propagates towards the ends. This accumulates some material at the center that is seen in the form of an increase thickness. To verify this hypothesis, a comparison of relative thickness change between FE-MK and FE-NUC models based on punch actuation is presented in Figure 84(a) and (b) respectively. The FE-MK model is closer to a 'pure' moment condition through rotary clamp actuation. The FE-NUC model, on the other hand, utilizes punch force to initiate bending with clamps that are free to rotate. The relative thickness is measured across the width of the specimen, i.e., along bend line. Both models exhibit similar variation in thickness across the width. The specimen is thinnest at the two edges, increases in thickness at a distance from the edge, and further thins as one moves towards the mid-width region. At this section, FE-MK model increases in relative thickness for initial radii (r_i = 75, 25, 15 mm) and later decreases. In the punch based FE-NUC model the relative thickness continues to decrease up to the mid-width section. Here again, both models coincide in predicting the thinning of both monolithic and laminate specimens with increasing curvature. Also, the thinning effect decreases with increasing clad thickness ratios in both models. Thickening was observed in the model of Majlessi and Dadras (Majlessi and Dadras, 1983) for the strong core and weak clad tri-layer laminate. However, thickening reported was considerably larger than the initial thickness of the material, in variance with the present study. Material thinning has ramifications in terms of limit strain by means of through-thickness strain gradient which can be considerable in

small radius bending when compared to in-plane stretching or deep drawing. In general, forming limit improves with increasing sheet thickness (Hosford and Duncan, 1999) (Rees, 2001). It is interesting to note that increasing thickness has a negative effect on the bending limit (Demeri, 1981). The same was observed in AA2024 sheet through air bending test in the work of Zadpoor et al. (Zadpoor et al., 2011). Bendability tests showed that the minimum bending radius linearly increases as the sheet thickness increases. However, further investigation is needed to conclude the same for laminate sheets with different thickness ratios of distinct materials.

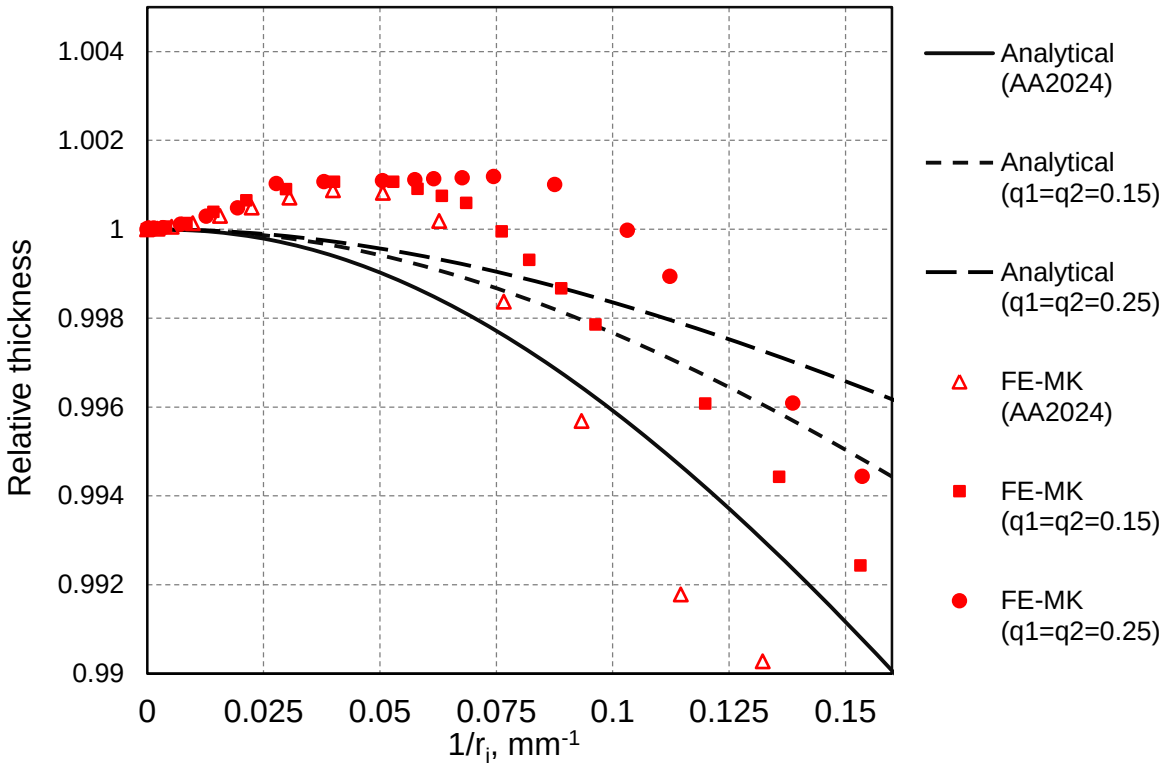

Figure 83. Relative thickness versus specimen curvature in tri-layer laminate for 2 different thickness ratios at a radius of curvature of (r_i) 15 mm from analytical and FE models. Also included, for comparison purposes, is the curve for core AA2024 layer.

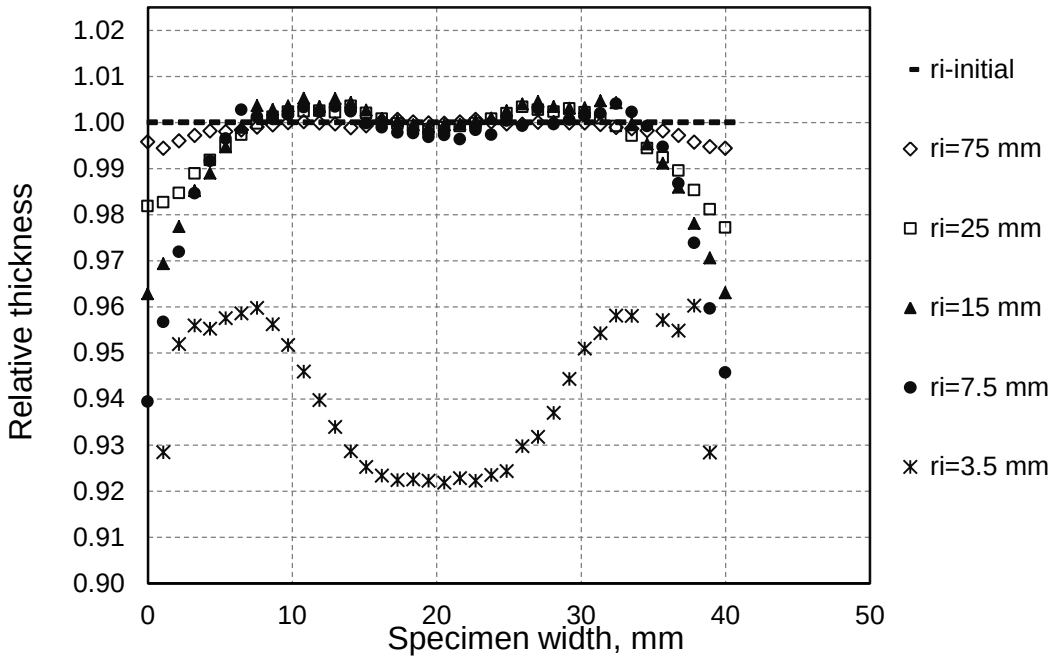

(a)

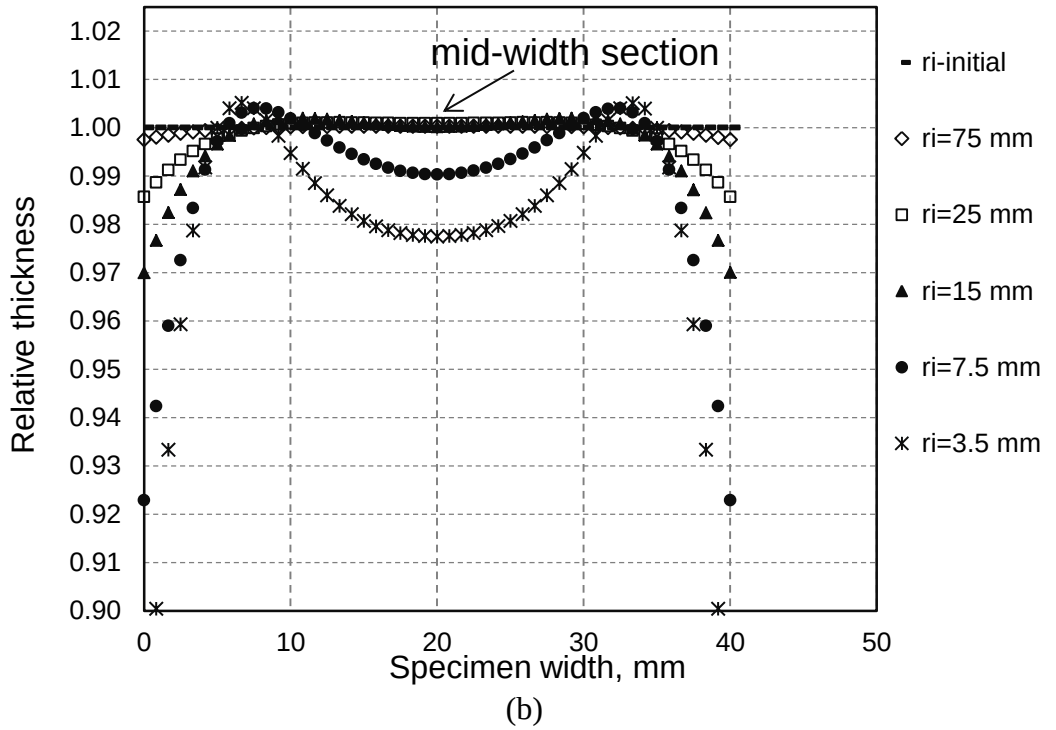

(b)

Figure 84. Distribution of relative thickness along the bend line from (a) FE-MK bending (clamp driven); (b) FE-NUC bending (punch driven) for AA2024 (3.12 mm thick) specimen.

The variation of relative thickness for different outer and inner thickness ratios by keeping one layer thickness constant is shown in Figure 85 (a,b). When the inner layer thickness is varied with a constant outer layer thickness (q_1=0.25), the evolution of the relative thickness with curvature pattern shows an increase in relative thickness for increasing inner layer thickness ratio (q_2) (Figure 85(a)). On the other case, when the inner layer thickness is kept constant (q_2=0.25) the thickness pattern decreases in relative thickness until q_1 = 0.35. For the case of q_1=0.45, the relative thickness again shows to raise as shown in Figure 85(b). It is to be noted that the total sheet thickness remains constant for all these cases.

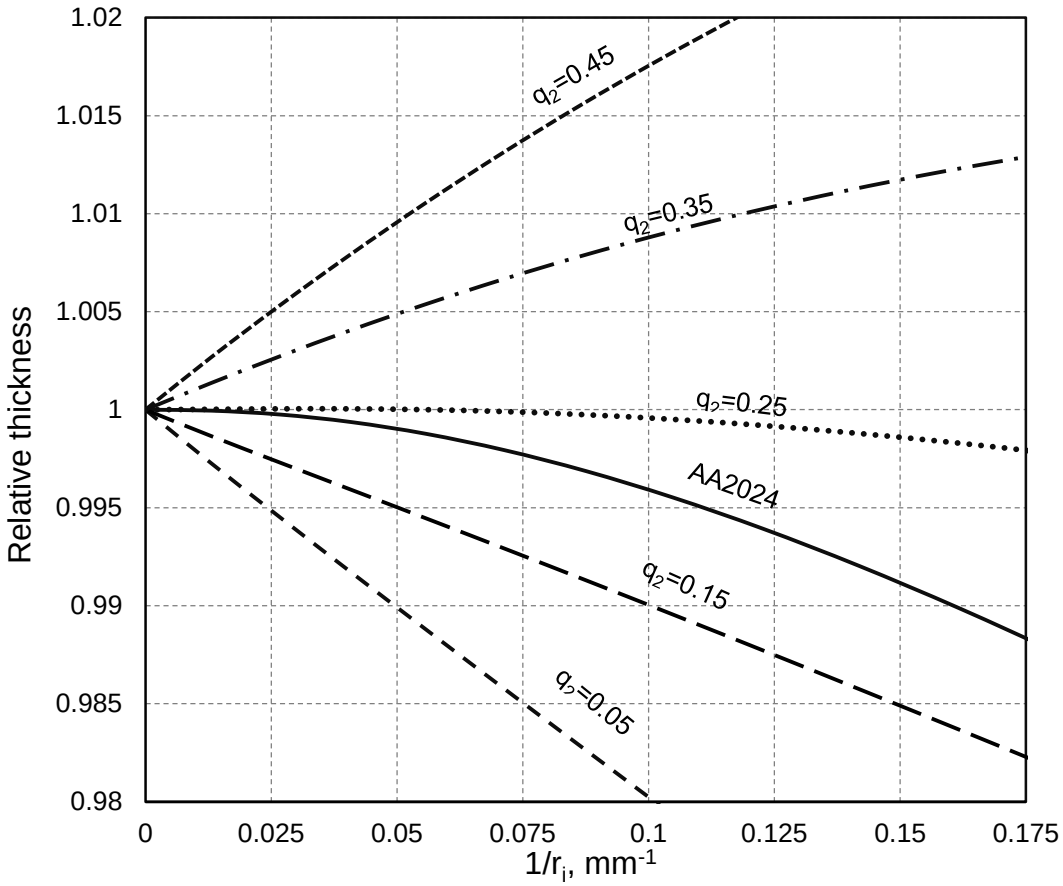

(a) (figure continued on next page)

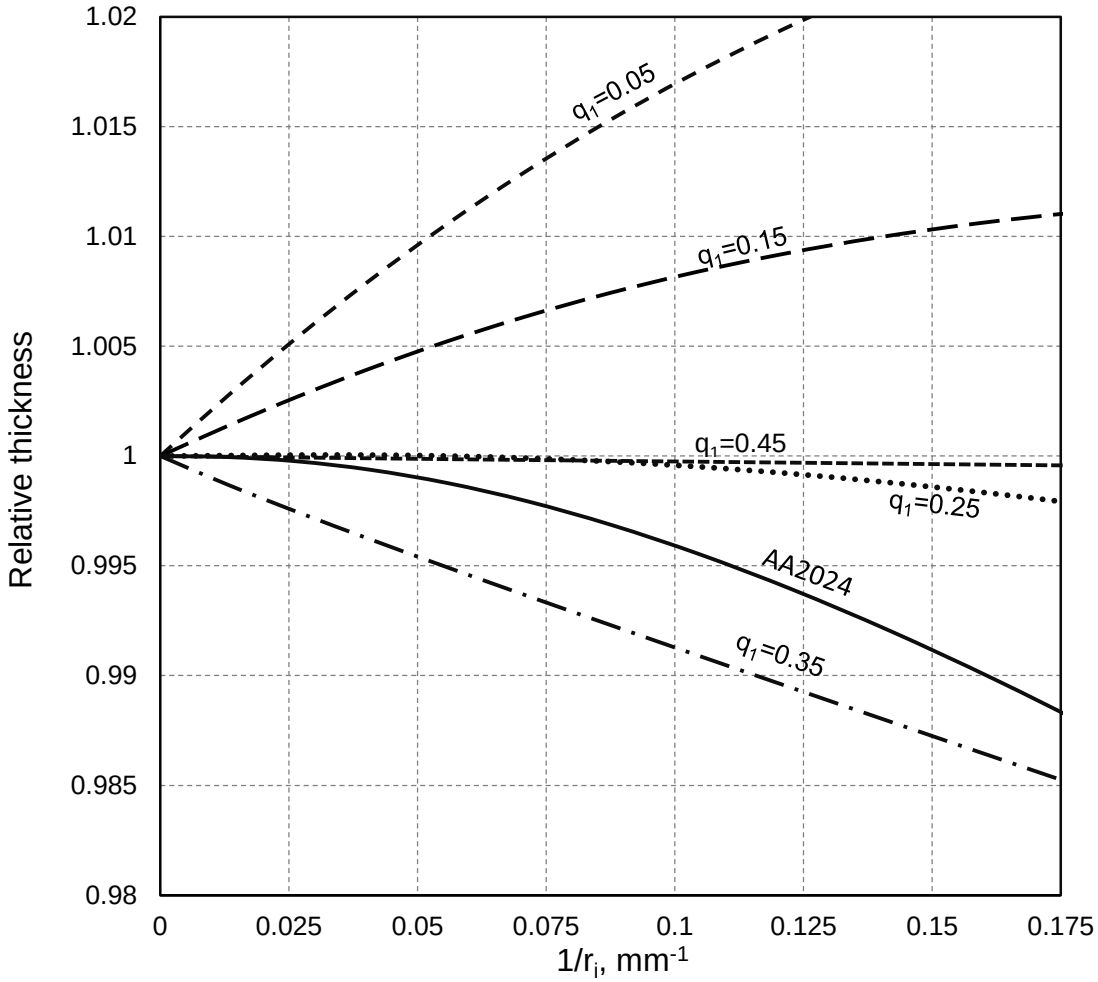

(b)

Figure 85. Comparison of analytical model relative thickness for different thickness ratios of outer an inner layers of the AA2024-AA1100 tri-layer laminate. (a) Outer layer is at constant thickness (q_1=0.25); (b) inner layer is at constant thickness (q_2=0.25). (q_1 and q_2 are the thickness ratios of laminte layers in the outer and inner sides of the tri-layer laminate).

6.3.4. Comparison of Relative Thickness Values from Bi-layer and Tri-layer laminate models

The bi-layer model developed in a similar method and reported in section 3.2 was used to obtain relative thickness of AA1100-AA2024 bi-layer laminate sheet. A comparison of

relative thickness change with curvature for bi-layer and tri-layer laminate with AA1100 as laminate and AA2024 as matrix is shown in Figure 86. Different geometrical arrangement of soft clad and hard matrix in bi-layer shows different response in thickness upon bending. When the soft clad (AA1100) lies on the tensile side of the hard matrix (AA2024) (referred as clad under tension as C-T), the specimen thins with increasing curvature as experimentally confirmed in the bi-layer plots in section 6.2.4. Similar results were reported in Verguts and Sowerby (Verguts and Sowerby, 1975) and Majlessi and Dadras (Majlessi and Dadras, 1983) where thinning increased with increasing clad thickness ratio. The opposite trend is noticed for clad in compression (C-C) type bi-layer laminate that shows increased thickening with clad thickness ratio. However, the thickness change magnitudes for same clad to matrix (0.25) is less in the tri-layer laminate than in the bi-layer laminate. The thinning and thickening effect produced by the soft clad on either side of the specimen could counter each other to produce minor variations in thickness.

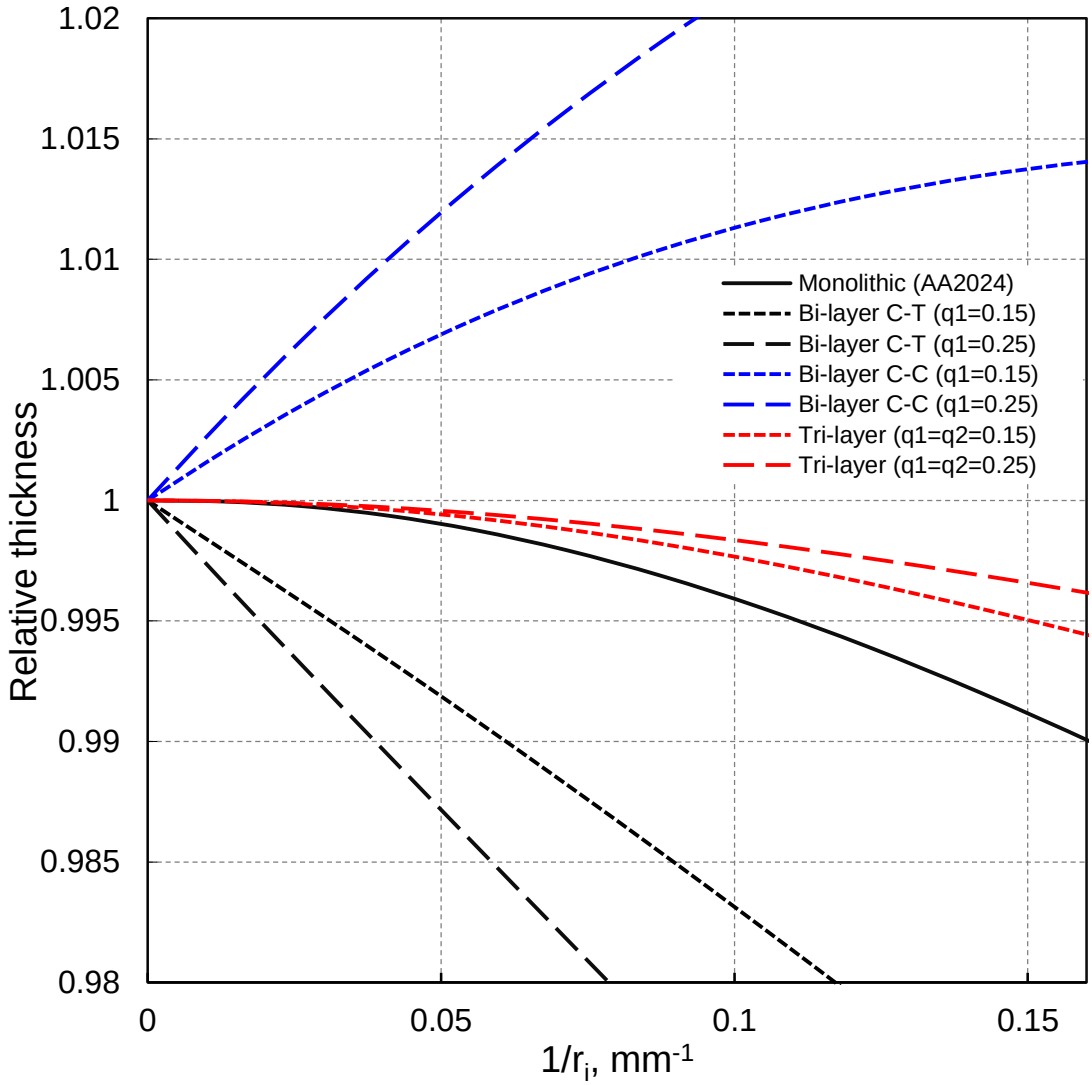

Figure 86. Comparison of relative thickness versus curvature plots for C-T and C-C type specimens for bi-layer AA1100-AA2024 and tri-layer laminates of different thickness ratios.

6.4. Limit Strain Prediction in Stretch-bending using Major Strain Acceleration Criterion

Stretch bending tests were carried on AA2024 – O, 1.25 mm thick specimen using the ASBT test setup as described in Section 4.2. The limit strain in stretch bending are

predicted using major strain acceleration criterion of Situ et al. (2011) applied to experimental DIC data parameters type of curve fitting. The sensitivity of the method is studied by comparing the results with Alclad 2024-O tri-layer laminate sheet of similar thickness. Sources of variability in limit strain prediction are also systematically investigated.

6.4.1. Experimental Strains

Figure 87(a) shows the ASBT test set up with a test sample in the test fixture. The major strain at a certain stage of deformation (or punch displacement) is overlaid on the test specimen. A close-up of the region of interest on the specimen is shown in Figure 87(b) where a major strain map was obtained using facet size 25 x 25 pixels (3.5 mm x 3.5 mm approx). Major strain localization is observed at the edges of the specimen. Two section lines AB and CD along (longitudinal) and across (transverse) the bend line respectively are chosen for determining the evolution of major strain during stretch-bending. Figure 87(c,d) represent curve fitted major strain profiles from sections AB and CD respectively, where strain profiles in Figure 87(c) indicate the presence of a strain gradient at the two edges. The evolution of strain along the transverse direction of bend line, i.e., CD shows maximum strain gradient in the bend line that undergoes maximum bending and stretching compared to the side wall region. This is typical of stretch-bending, whereas strain localization is observed at the edges as well as at the mid-width section in pure bending as reported earlier in Figure 47(b).

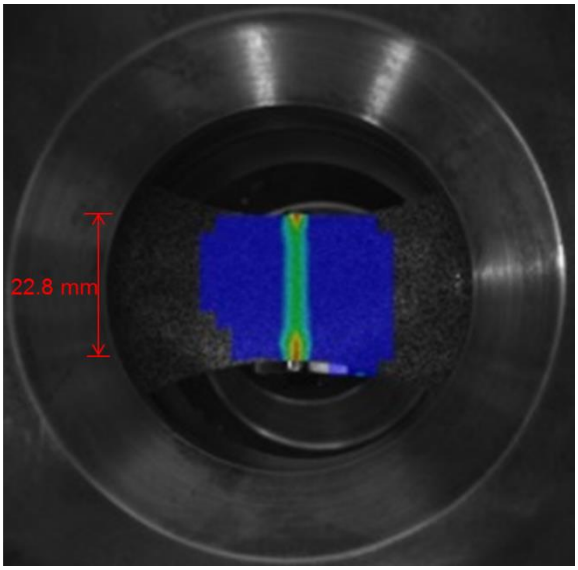

(a)

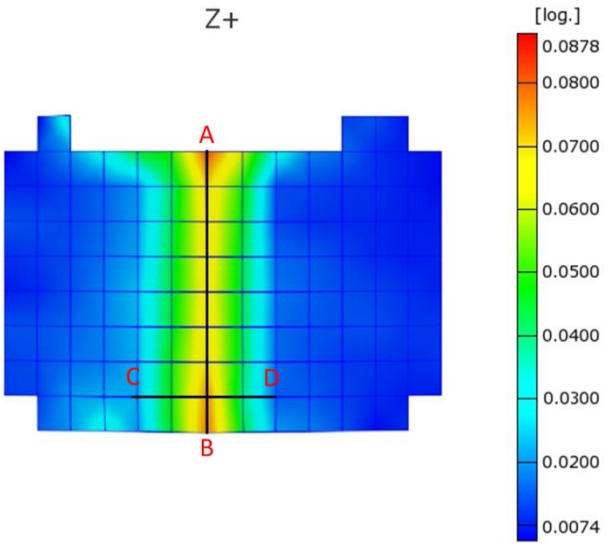

(b)

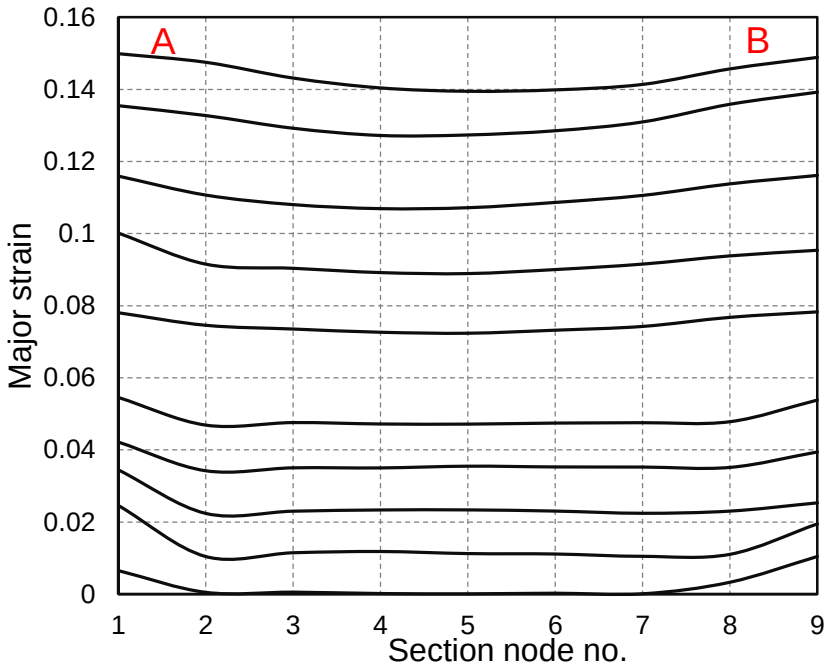

(c)

(figure continued on next page)

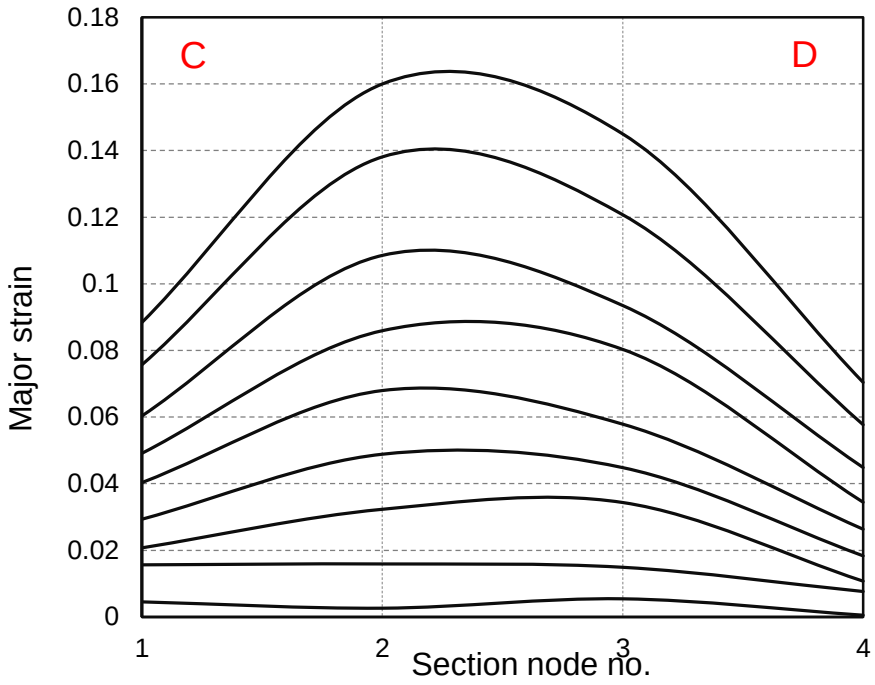

(d)

Figure 87. Experimental major strain maps and evolving strain profiles with increasing curvature, (a) major strain map using a facet size of 25 x 25 pixels is overlaid on the camera image of the test specimen where strain localization can be observed at the edges, (b) strain map with lines AB and CD along longitudinal and transverse direction of the specimen and strain profile along (c) longitudinal and (d) transverse directions.

6.4.2. Practical Considerations of Limit Strain Prediction by Major Strain Acceleration Criterion

Strain measurement by DIC is based on a series of images that reflect the spatial transformation of the specimen surface. The method offers the advantage of providing a complete temporal and spatial history of strain at full-field and localized scales. This capability of DIC method to observe the strain localization process provided an opportunity to predict the onset of necking, and thereby the limit strain, of the material in the work of Situ et al. (Situ, Bruhis and Jain, 2006). Details related to major strain

acceleration criterion of Situ et al. were reported earlier in section 2.8.1. In this work, major strain distribution across a localized neck and its vicinity from a deformed specimens were obtained and plotted as a function of time. Also the first derivative of strain (i.e., strain rate) and the second derivative of strain (i.e., strain acceleration) were plotted as a function of time. The instant at which an inflection point occurred in the major strain rate curve, i.e., a peak in the major strain acceleration, was taken as the onset of localized necking. The criterion was employed with both experimental DIC-based strain field data and FE model data and the approach was applied to predict FLD using punch stretching test.

In the present work, major strain acceleration criterion is studied for its applicability to stretch-bending condition to obtain the limit strain. The nodes in the vicinity of crack are chosen to obtain major strain and major strain acceleration data. A flow chart presenting the procedural steps for limit strain prediction using major strain acceleration cretion is shown in Figure 88. Several factors influencing the major strain and strain acceleration profile were studied in an effort to reduce the variability in the limit strain prediction arising from data analysis considerations.

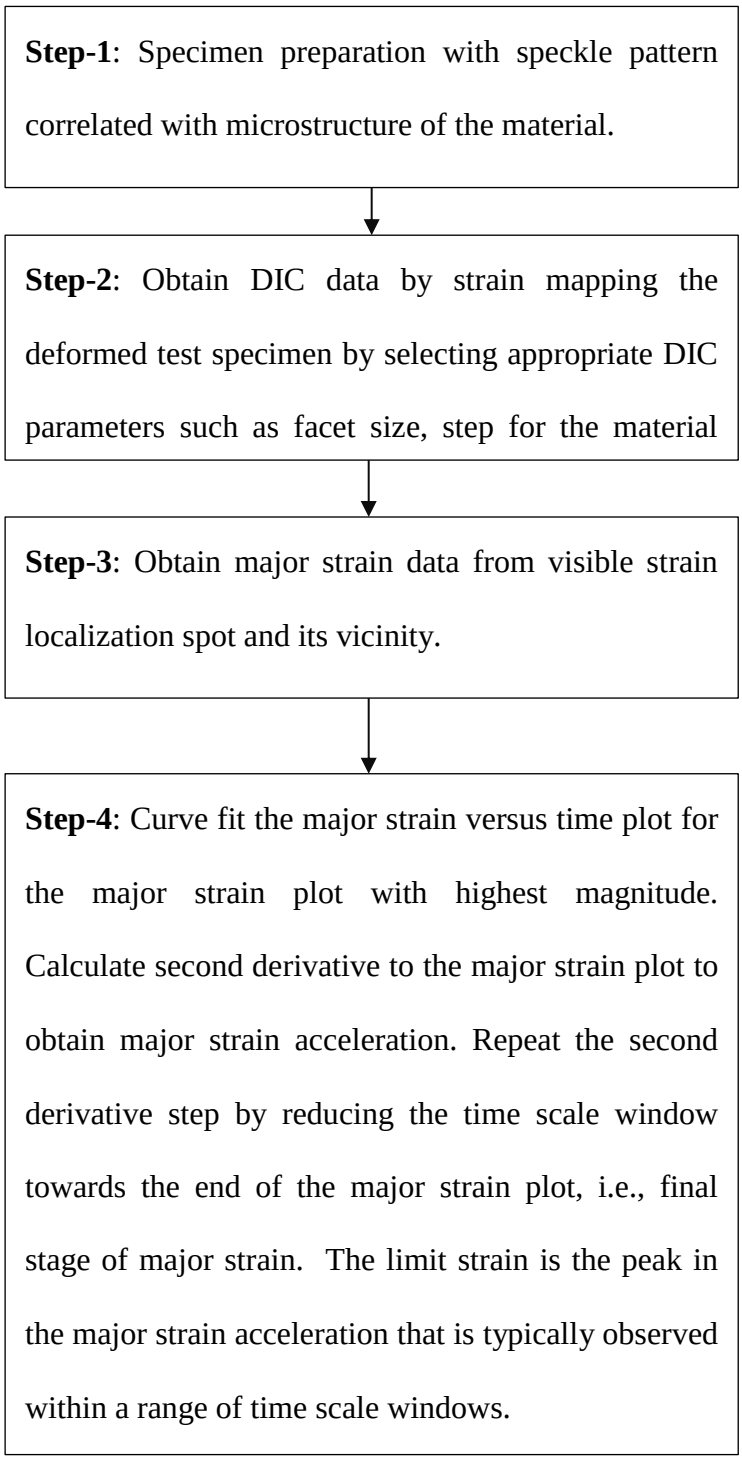

Figure 88. Flow chart presenting the procedural steps for limit strain prediction using major strain acceleration criterion.

6.4.3. Effect of Selection of Major Strain Points on Strain History

Unlike strain localization from large radius hemispherical punch stretching, in small radius stretch bending using an angular punch, the specimen exhibits several distinct potential strain localization regions as shown in Figure 87(a,b). Since the magnitude of strain was highest at the edges, four data points (points 1, 2, 3 and 4 in (a)) in the vicinity of strain localization region near one of the edge (mesh facet size 9 pixel x 9 pixel) (i.e., 1.26 mm x 1.26 mm approx.) were chosen for limit strain study (see Figure 89(a)). These data points were chosen at a slight offset from the edge because of speckle pattern degradation at the edges in DIC strain measurement. The major strain histories at the 4 points are shown in Figure 89(b) where point 2 showed the maximum increase in the strain magnitude. Therefore, major strain history from point 2 was considered for limit strain analysis.

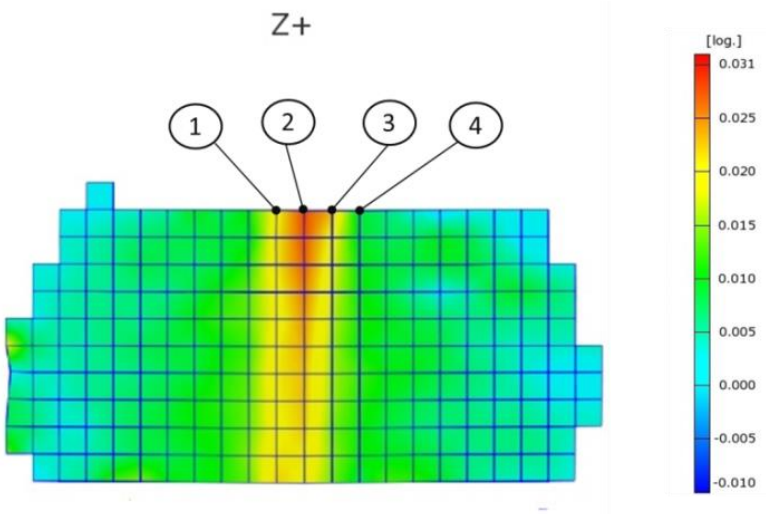

(a)

(figure continued on next page)

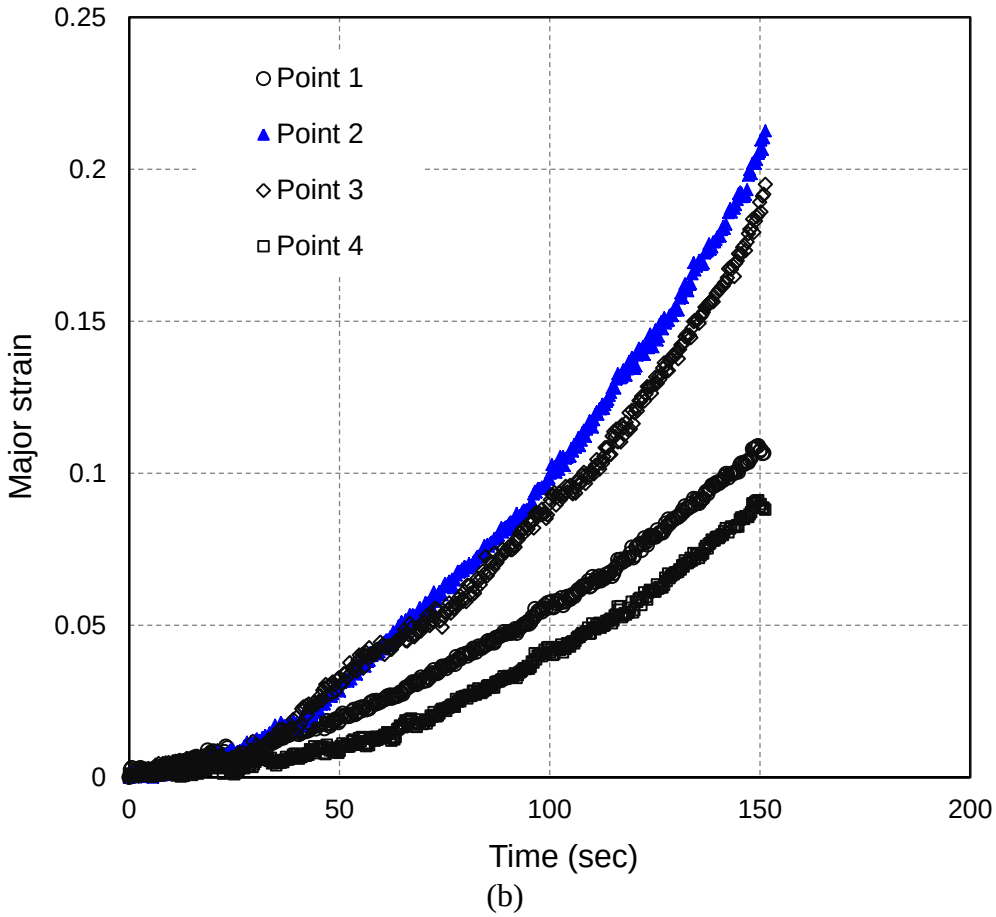

(b)

Figure 89. Strain map at one end of specimen (a) at facet size 9 pixel by 9 pixel and (b) associated major strain history at 4 chosen locations in the critical strain region of ASBT specimen.

6.4.4. Effect of Facet Size and Facet Step on Strain History

As noted earlier in sub-section 4.1, the DIC based strain measurement is influenced by various considerations during data analysis and especially the facet size and facet step. The effect of these two parameters on strain magnitude was studied by selecting three different facet sizes times the number of facet step combinations, (i) 25 x 13, (ii) 17 x 9 and (iii) 9 x 5 within the Aramis DIC software in the calculation of strain history of

critical point 2 (see Figure 90). The results from the DIC analysis in Figure 91 indicate that the rate of strain evolution is quite sensitive to the choice of facet size and the smallest facet size yielded the highest strains at any given time. It is to be noted that facet sizes to facet step lower than 9 x 5 pixels caused loss in data and hence any lower facet sizes were not considered for limit strain study. However, it appears that smaller facets sizes were effective in capturing local curvature effects compared to larger facet sizes that are more suited to situations where strain gradients are significantly smaller such as in large radius hemispherical punch stretching. The effect of facet size was thus assessed for limit strain prediction. The effect of facet with respect to image magnification were reported by Davidkov et al. (Davidkov et al., 2012) for DIC based strain history data in pure bending of an aluminum alloy.

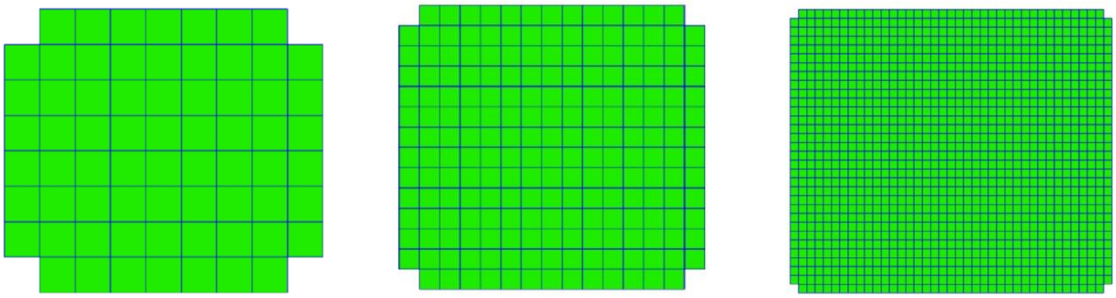

Figure 90. Different facet size and facet step in DIC strain analysis. (The first number corresponds to facet size and second number corresponds to facet step).

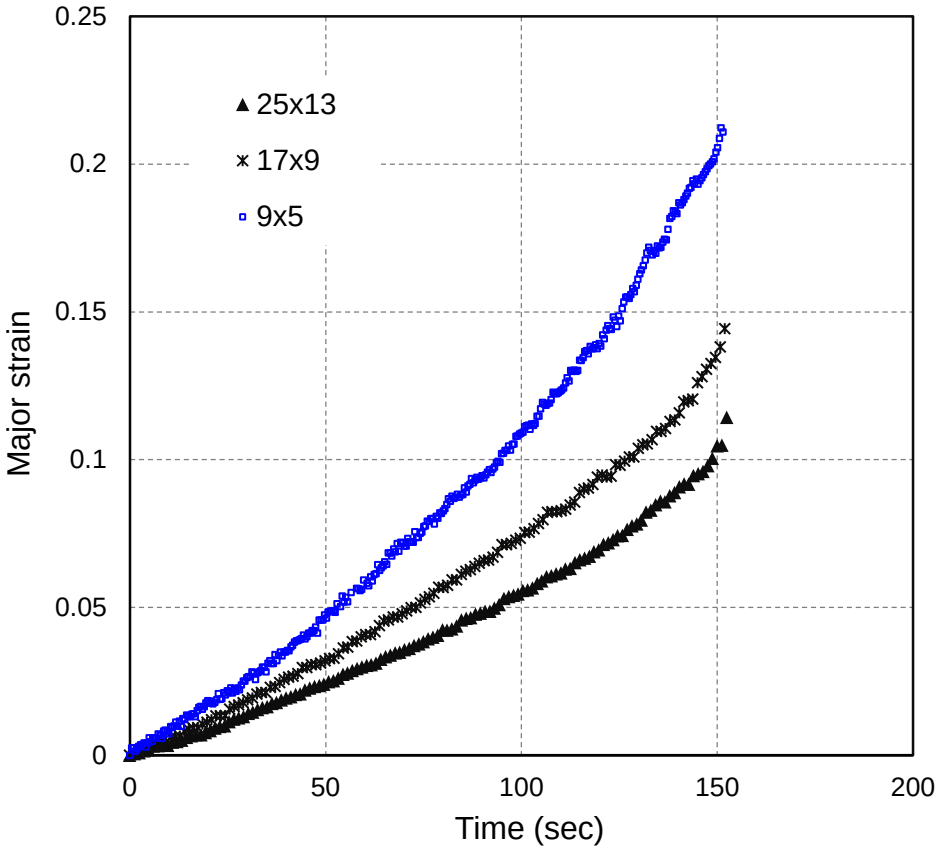

Figure 91. Major strain history at point 2 for three facet sizes in DIC analysis.

6.4.5. Implication of Analyzing Major Strain History by Data Fitting

The choice and effect of curve fitting applied to strain history data on predicted limit strain was also analyzed. Several curve fitting functions were utilized to fit the strain history data ranging from second order to eighth order polynomial as well as Gaussian and exponential functions. The objective of curve fit was to identify the best fit to the strain history data using the simplest (or leanest) form of the function, i.e., with minimum coefficients. Gaussian, exponential and other curve fit models did not offer strain acceleration phenomenon. Second and third order polynomials were not suitable for

obtaining second derivative and the fourth order polynomial failed to produce the strain acceleration phenomenon compared to 5th order in the DIC data. Based on quality of fit, three different curve fitting polynomials namely 4th, 5th and 6th order polynomials were chosen for curve fitting of strain history data. Facet size and facet step combinations of 9 x 5 were chosen from time scale 135.33 to 151.33 seconds in the experimental data, Figure 92(a). Only later stages in the major strain data associated with the strain localization and damage phenomenon were considered for calculating the strain acceleration as these were more relevant for limit strain prediction. This is discussed further in the next sub-section. Curve fitting was done using MS Excel software and second derivative for the major strain equation was obtained using online computational software, Wolframalpha (Wolfram Research, 2009). The coefficients of the polynomial were set to have at least 15 decimal places for accuracy of computation. The major strain acceleration for the 4th order polynomial curve fit responded almost like a straight line and 6th order polynomial provided negative values as shown in Figure 92(b-d). The 5th order polynomial responded with strain acceleration effect in the range of 135.33 seconds to 151.33 seconds with a peak in acceleration at 149.5 seconds, Figure 92(c). This corresponded to a limit strain of 0.205. The 7^{th} and 8^{th} order polynomials, Gaussian second order and Power law curve fit did not produce any strain acceleration behavior as shown in Figure 91(e-h) respectively. The exponential law curve fit did not yield second derivative for strain acceleration. The quality of curve fit to the major strain data are shown by the R^2 value as summarized in Table 12.

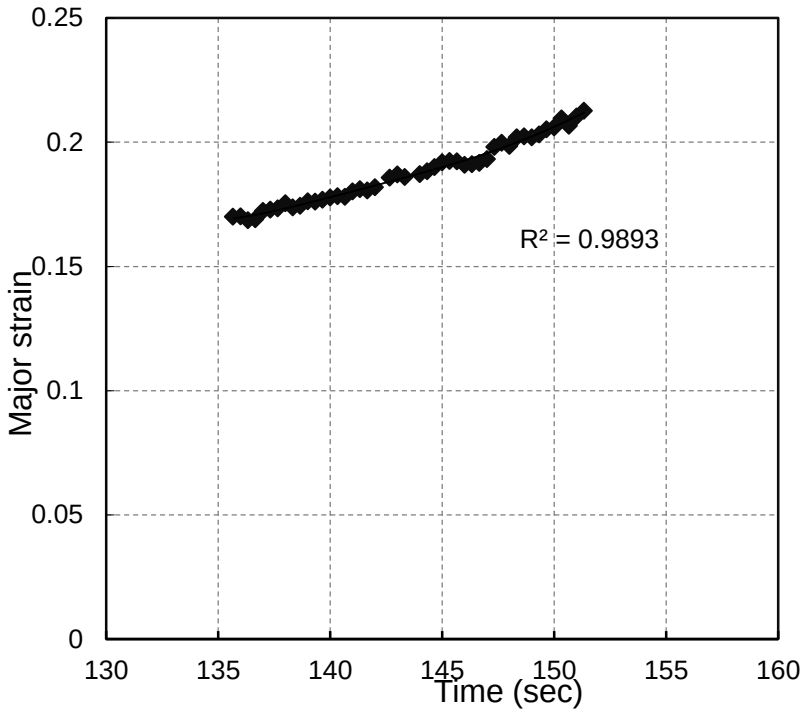

(a)

(Sixth order polynomial used for curve fitting,
$y = -0.000000058431923x^5 + 0.000042474730714x^4 - 0.012339994180089x^3 + 1.791160601069200x^2 - 129.897582861191000x + 3{,}765.552243096220000$

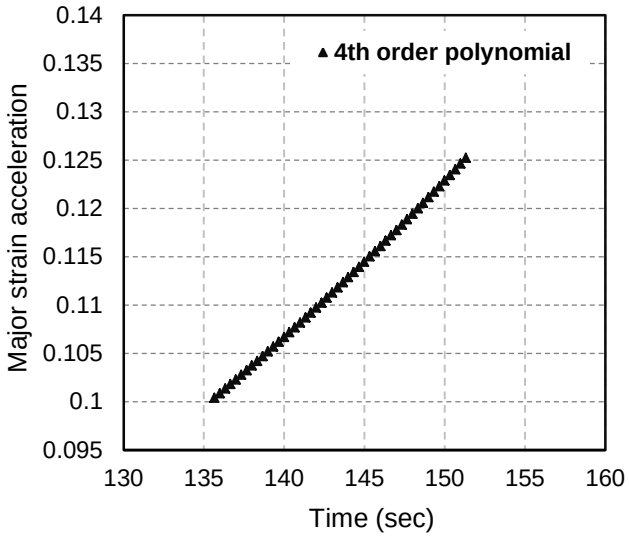

(b)

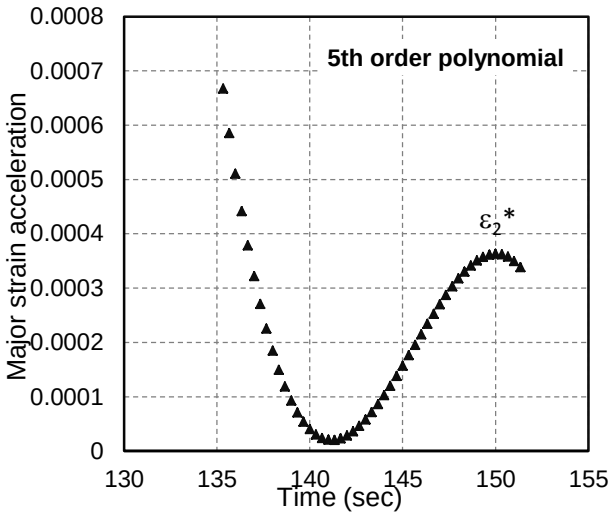

(c)

(figure continued on next page)

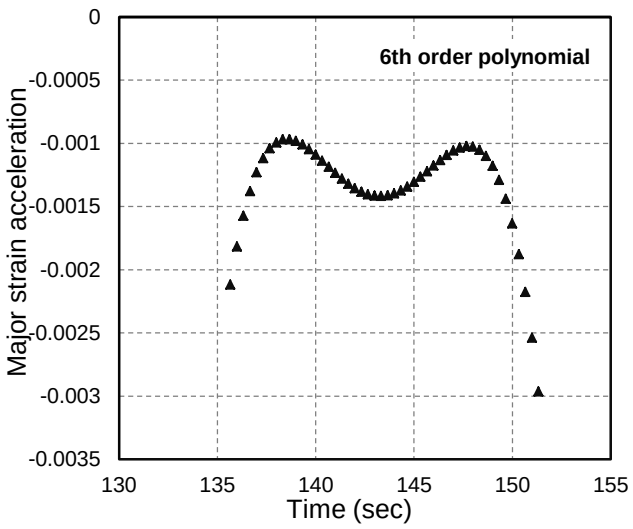

(d)

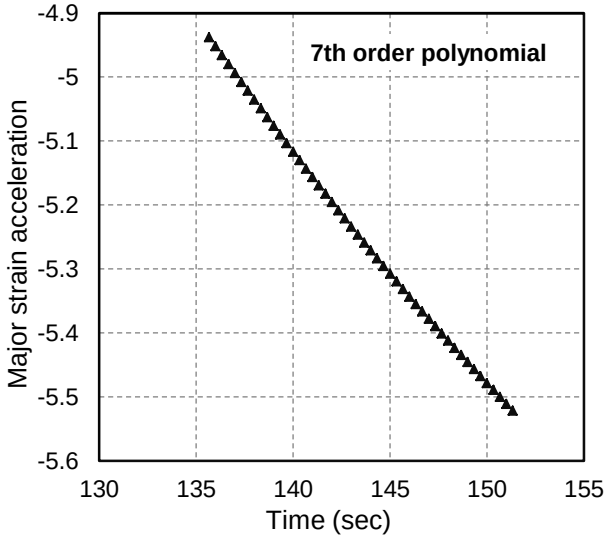

(e)

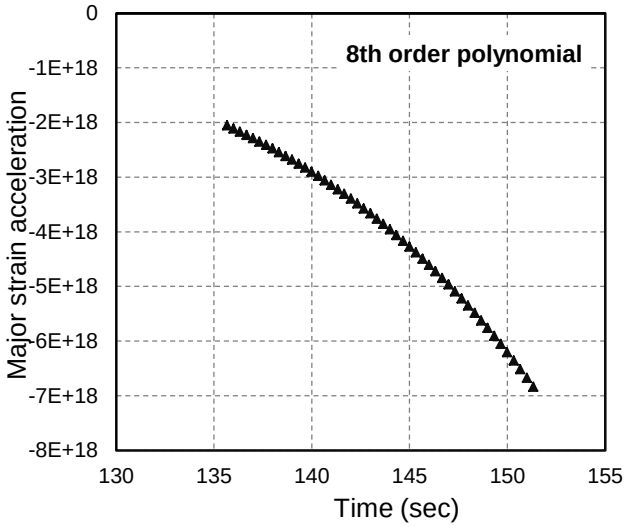

(f)

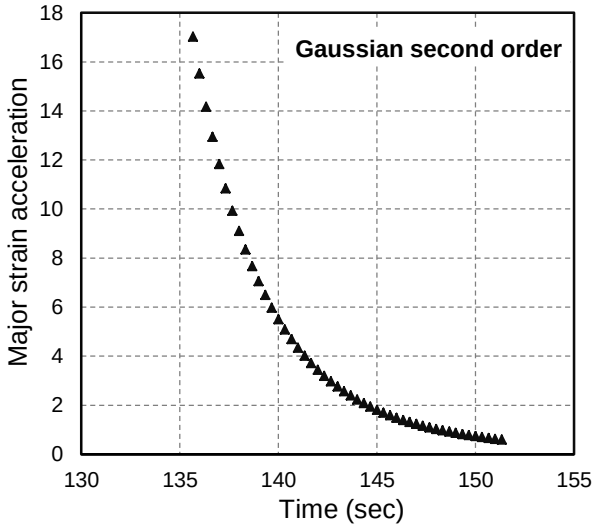

(g)

(figure continued on next page)

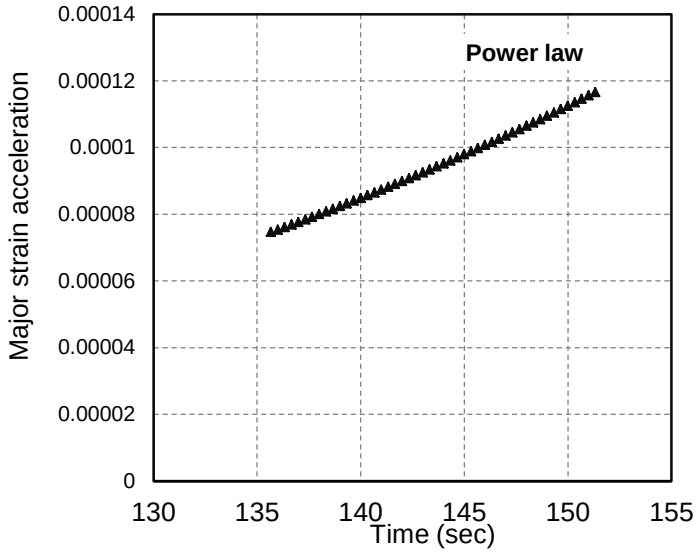

(h)

Figure 92. Effect of curve fitting on DIC major strain history data, (a) major strain history; major strain acceleration curves corresponding to (b) 4th order polynomial, (c) 5th order polynomial, (d) 6th order polynomial, (e) 7th order polynomial, (f) 8th order polynomial, (g) Gaussian second order (h) Power law fits to major strain history data.

Table 12. Different curve fit equation applied to DIC major strain data.

Equation type	R^2
4th order polynomial	0.9895
5th order polynomial	0.9895
6th order polynomial	0.9895
7th order polynomial	0.9895
8th order polynomial	0.992
Gaussian second order	0.9891
Power law	0.987
Exponential	0.977
Std. dev.	0.010

6.4.6. Effect of Choice of Time Scale on Strain Acceleration Characteristics and Limit Strain

The results related to the effect of time scale chosen to analyze major strain history for calculating limit strain via strain acceleration criterion are presented in this sub-section. The major strain acceleration curve was plotted for several time scale windows closer to the end of the major strain curve that is associated with damage. Five time scales 121.33-151.33 (window 1), 128.33-151.33 (window 2), 135.33-151.33 (window 3), 140.33-151.33 (window 4) and 143.33-151.33 (window 5) from the major strain curve and their corresponding major strain acceleration curves are shown as examples in Figure 93(a-f), respectively . No strain acceleration peak was observed for window 1. As the window size was reduced, the peak in strain acceleration was observed for the consecutive windows. The peak strain acceleration (ε_2*) occurred in the same region with minor lateral shift with respect to each other.

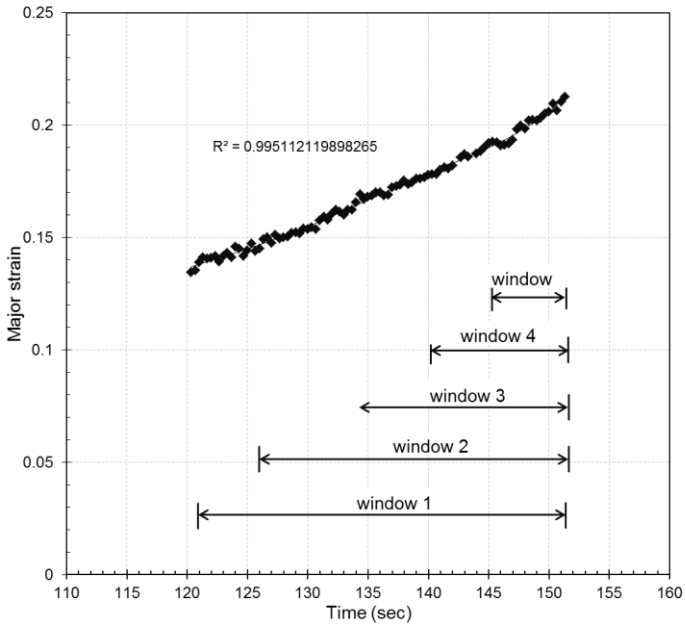

(a)

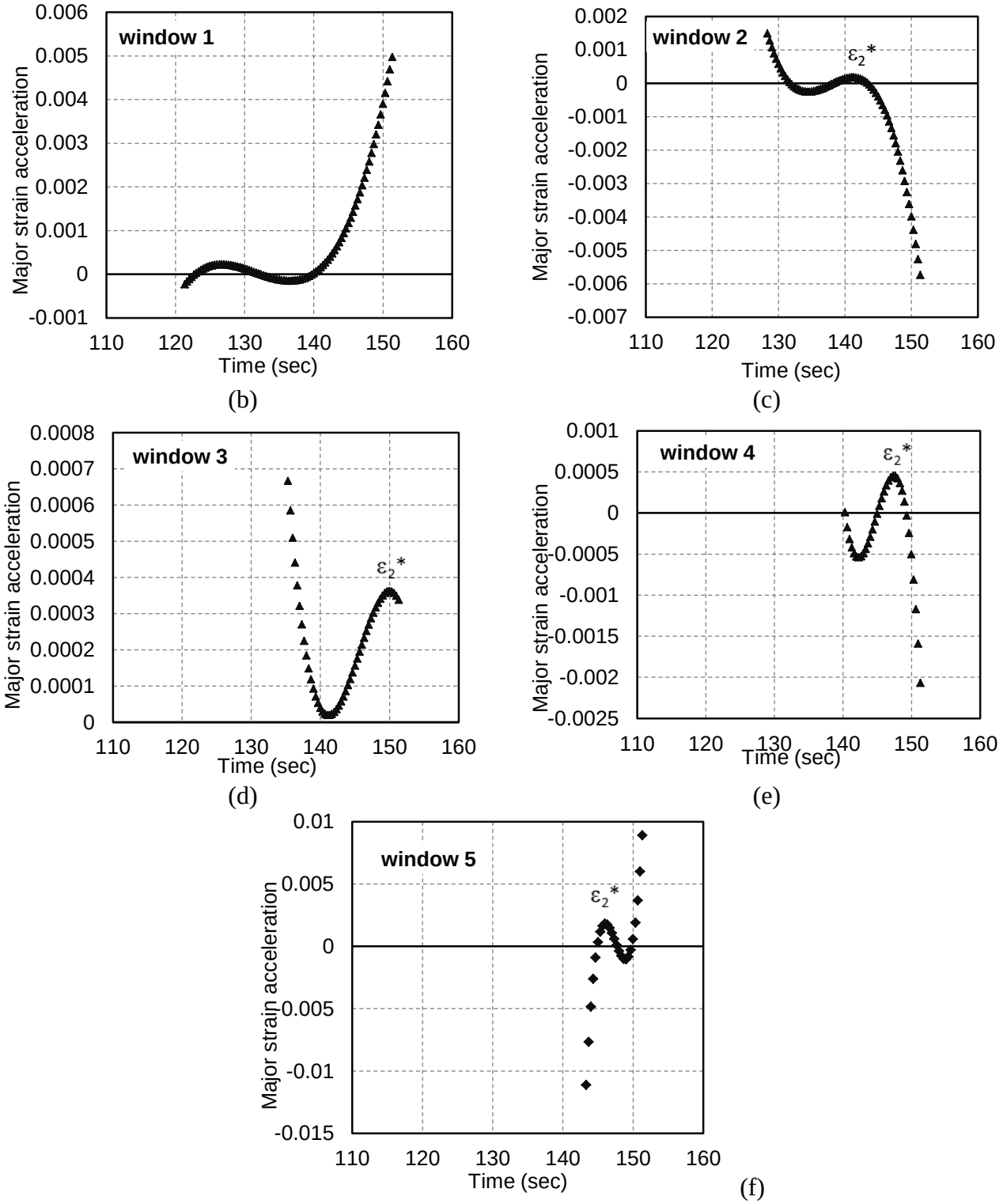

Figure 93. Effect of choice of time scale on strain acceleration characteristics from experiment major strain history data with 5th order polynomial curve fit.

The study shows that choice of time scale also has a bearing on the strain acceleration peak and hence in the prediction of limit strain. By applying different window sizes, the correct location of peak in strain acceleration curves is identified. This conclusion is based on repeated study by applying different time scales study on other locations of the curve and also from multiple tests.

6.4.7. Comparison of Limit Strain Between Monolithic AA2024 and Alclad 2024 Tri-layer Laminate

It was of interest to compare the limit strain in stretch bending for AA2024 and Alclad 2024 tri-layer sheets. Macroscopic response of these two materials in the form of ASBT shown in Figure 94. The presence of softer AA1100 clad layer has caused a minor drop in load compared to monolithic AA2024.

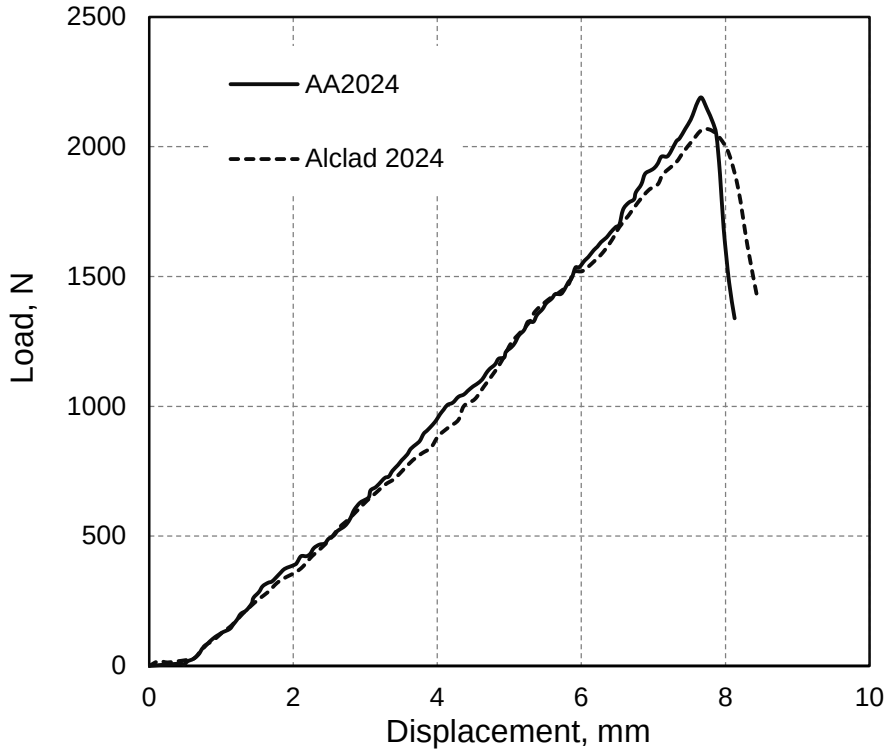

Figure 94. Load versus displacement plot for AA2024-O and Alclad 2024-O of 1.25 mm thickness obtained from ASBT test.

The major strain data obtained from DIC node producing highest magnitude of strain from AA2024 and Alclad 2024 specimen is shown Figure 95. ABST test conditions and DIC parameters such as facet size (9 x 9) for Alclad 2024 were chosen similar to AA2024. The major strain plot for the DIC node with maximum strain is shown in Figure 95. Limit strain based on maximum major strain acceleration criterion were calculated for decreasing order of time scale windows starting from 130 seconds for 21 windows. The quality of curve fit to the major strain data is represented through the goodness of fit (R^2) value. It is observed that the major strain curve fit yields better results for time scale windows chosen closer to the strain localization stage of the deformation and deteriorates

with larger window size. The limit strain values are not deducible at the outer range of the window sizes selected. In other words the initial part of the strain history does not contribute to the strain acceleration effect.

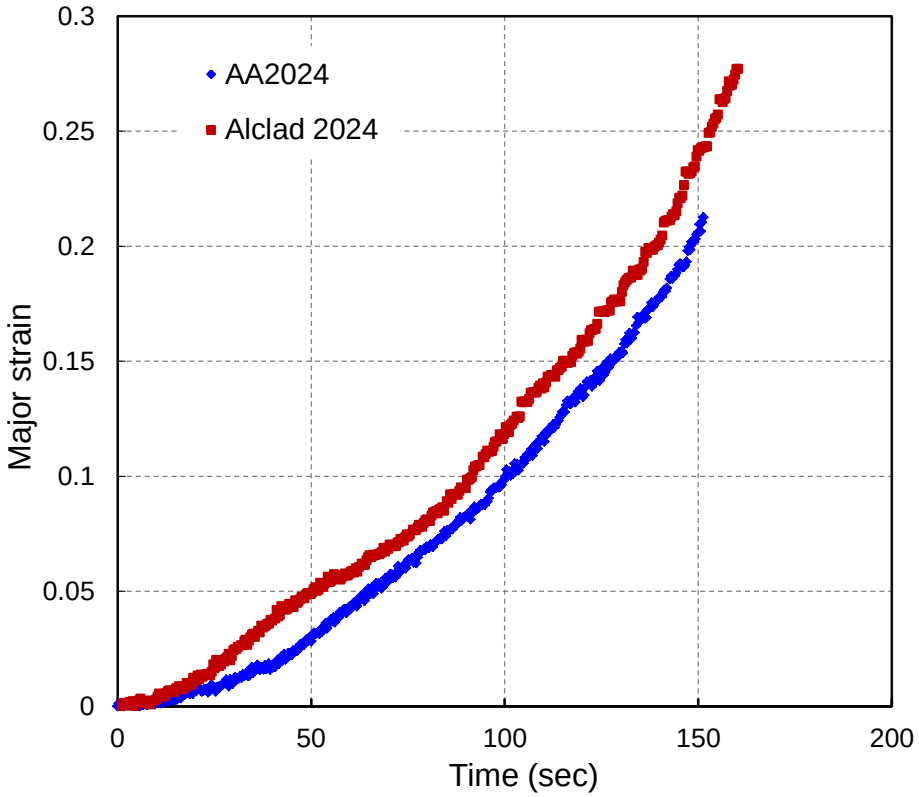

Figure 95. Major strain history from AA2024 and Alclad 2024 stretch bent specimens through DIC analysis.

Table 13. Limit strain values for different time scale windows.

Window number	AA2024			Alclad 2024		
	Time scale (sec)	ε*	R^2	Time scale (sec)	ε*	R^2
Window 1	121.33-151.33	- NA -	0.9926	131.56-160.36	- NA -	0.9959
Window 2	123.33-151.33	- NA -	0.9921	135.56-160.36	- NA -	0.9956
Window 3	125.33-151.33	- NA -	0.9917	137.56-160.36	0.198	0.9952
Window 4	126.33-151.33	0.178	0.9909	139.56-160.36	0.204	0.9949
Window 5	128.33-151.33	0.178	0.9913	141.56-160.36	0.211	0.9944
Window 6	129.33-151.33	0.2051	0.9911	143.56-160.36	0.211	0.9948
Window 7	130.33-151.33	0.198	0.9903	144.56-160.36	0.2517	0.9936
Window 8	131.33-151.33	0.2019	0.9906	145.56-160.36	0.2532	0.9926
Window 9	132.33-151.33	0.2056	0.9902	146.56-160.36	0.2532	0.9923
Window 10	133.33-151.33	0.2051	0.9893	147.56-160.36	0.2532	0.9913
Window 11	134.33-151.33	0.199	0.9881	148.56-160.36	0.2532	0.9902
Window 12	135.33-151.33	0.199	0.9885	149.56-160.36	0.2551	0.9898
Window 13	136.33-151.33	0.2051	0.9874	150.56-160.36	0.2491	0.9889
Window 14	137.33-151.33	0.199	0.9855	151.56-160.36	0.2428	0.9885
Window 15	138.33-151.33	0.2051	0.9821	152.56-160.36	0.2428	0.9883
Window 16	139.33-151.33	0.2065	0.9775	153.56-160.36	0.2428	0.9889
Window 17	140.33-151.33	0.199	0.9736	154.56-160.36	0.2428	0.989
Window 18	143.33-151.33	0.192	0.97	155.56-160.36	0.2432	0.9889
Window 19	145.33-151.33	- NA -	0.9696	156.56-160.36	0.199	0.9881
Window 20	146.99-151.33	- NA -	0.9715	157.56-160.36	- NA -	0.9869
Window 21	147.66-151.33	- NA -	0.9654	158.56-160.36	- NA -	0.9855
Average*		0.2023			0.2485	
Std. deviation*		0.0033			0.0052	

* Average and standard deviation calculations excluded for shaded values.

The deduced limit strain values for AA2024 and Alclad 2024 stretch bend specimens are shown in Table 13. The limit strain values initially showed large fluctuation and stabilized to close values marked within the red dotted lines. The average of the limit strains within the band is considered as the limit strain in stretch bending. For the monolithic AA2024 specimen the average stretch bending limit strain is obtained as 0.202 and for Alclad 2024 specimen it is 0.248. The standard deviation of the limit strain values

is less than 1% for either cases. The 80 μm thin ductile layer of AA1100 clad produced a positive effect of 4% increase on the stretch bendability of Alclad 2024 when compared with monolithic AA2024 specimen.

6.5. Summary of Chapter

The results from the bending models and experiments were presented for monolithic and laminate sheet materials. The differences between the edge and mid-width sections were observed in the 3D FE models and experiments when compared with 2D analytical models that are plane strain in nature. The effects of several aspects of sheet bending such as anticlastic curvature, punch penetration were also observed on the bending characteristics. The relative thickness change results for several geometric and material combinations of bi-layer and tri-layer laminates were observed in the form of thinning and thickening of the sheet. The second part of the results dealt with the limit strain predictions on stretch bending of monolithic and tri-layer laminate sheets. A methodology to arrive at the limit strain from DIC strain data was presented. The effect of DIC parameters, selection of major strain data, and curve fitting to major strain data were studied. The conclusions from the modeling and experimental works are presented in Chapter 7.

Chapter 7
Conclusions

Bending of monolithic and two different laminate sheet material systems has been studied through analytical, FE and experimental methods to understand their small radius plastic bending characteristics, and for tri-layer laminate, predict the limit strain using a strain acceleration criterion from literature. The following conclusions have been drawn from this study.

7.1. Monolithic Sheets

A new test method for conducting bending of sheet materials to produce large strain, small radius, pure bending was developed. The test rig is simple, rigid and robust in design, requires minimum accessories, and is well-suited for laboratory-scale experiments where sample area in the vicinity of the test specimen is available for camera mounting and image acquisition for subsequent analysis of continuous full field strain measurements. The proposed bend test method in conjunction with an online DIC strain mapping method was utilized to assess characteristics of a representative analytical model of pure bending based on advanced bending theory. In addition, three FE models were developed, a 2D model based on uniform curvature assumption similar to the analytical

model extensively studied in the literature, a 3D model that captures the experimental laboratory test set-up and conditions and a 3D model based on Marciniak-Kuczynski model (Marciniak and Kuczynski, 1979) that bends without specimen punch interaction. Various characteristics of the different models were assessed against the experimentally measurable data. While the analytical model captured many of the bend characteristics in an efficient manner, some limitations were also noted. Limitations of the analytical models of pure bending based on advanced bending theory can be significantly improved by utilizing three dimensional FE models that closely incorporated experimental conditions and material properties. The latter provide the best agreement with the experimental data. Specific conclusions from this study are as follows.

- A new experimental bend test jig in conjunction with an online DIC method offers a means of assessing characteristics of existing and new bending models. The test method can subject the bend test specimen to subsequent stretching and thus enable, in future, a study of material characterization and limit strains in bend-stretching mode of deformation.
- The tangential strain map from the edge of the specimen obtained through DIC method indicates a shift in neutral fiber from mid-plane towards the compressive side with increasing curvature. The width section strain map shows the localization of strain at the edges and centre which are possible failure sites for predicting the limit strain under bend-stretching mode.

- Analytical plane strain pure bending model that considers uniform specimen curvature in bending as proposed by Tan et al. (Tan, Persson and Magnusson, 1995) and FE-MPC model yield similar bending stress, strain and relative thickness characteristics for annealed aluminum alloy AA2024. This trend appears in good agreement with the through-thickness edge measurements, using a smaller window in online DIC. However, this model fails to capture the deformation characteristics at the edges of the test specimen. The models are simplistic in comparison to punch (i.e., bending mandrel) based experiments as they fail to account for punch penetration that occurs at the inner surface of the bend, and a likely deviation from pure bending mode of deformation.
- A 3D FE model based on non-uniform curvature arising from punch contact (FE-NUC) captures several experimental bending characteristics of annealed AA2024 alloy such as anti-clastic curvature at the specimen edges, punch penetration into the inner surface, shift in neutral fiber from mid-plane towards the compressive side with increasing curvature, strain development on the tensile surface, and through-thickness edge regions of the specimen. The model allows for an assessment of the edge effect by comparing mid-width and edge region through-thickness stresses and strains. The deviations in the tangential stresses and strains between analytical, FE-MPC and FE-NUC models are largely attributed to the edge effects in bending. While the specimen edge (i.e., anti-clastic curvature) and punch penetration effects complicate the interpretation of 3D FE results and their comparison with limited experimental data, the 3D FE model (FE-NUC) best

represented the overall experimental response. The analytical and FE models and bend test experiment are all capable of revealing various aspects of bending in the context of their assumptions and simplifications. Particular aspects of bending such as anti-clastic curvature arise from different stress state at the edge and mid-section and its role in thickness gradient that develops across the width is clarified.

7.2. Bi-layer Laminate Sheets

A new analytical model based on advanced theory of bending, and Tan's monolithic bending model (Tan, Persson and Magnusson, 1995) was extended to bi-layer laminate sheet material This plane strain analytical model is compared with a 3D FE model based on M-K bend test design to simulate pure bending. The model results were compared with experimental results from a new bend tester that utilized online DIC strain mapping method to obtain through-thickness and convex surface strain data. The model results were compared for SS400/AA1050 bi-layer laminate material for different thickness ratios and geometric arrangements.

- The analytical model was able to predict the variations in tangential and radial stress distribution in the hard SS400 matrix and soft AA1050 clad layer of the bi-layer laminate for two different thickness ratios. The stress and strain magnitudes dropped with an increase in soft clad thickness ratio. The stress profile and

magnitudes were in good agreement with the FE model for values taken at mid-section.

- The model and experiments were in good agreement in the order of strain magnitude strain prediction for different geometrical arrangement of AA1050 and SS400 clad and matrix. The tangential strain was maximum for highest clad thickness ratio (q_1=0.25) and when softer AA1050 clad layer was on the convex side.
- The contraction and elongation in the width direction of tensile and compressive sides of the specimen were observed in FE model and experiment (for tension side). The magnitude of contraction in the width direction on the tensile side was almost double of the elongation on the compression side. The clad layer on tension side produced the highest width strain.
- The material thinned when clad was in tension and thickened when clad was in compression. The same was confirmed through microscopic thickness measurement at mid-section. The amount of thinning and thickening also increased with the clad thickness ratio. The strain and thickness variations were attributed to relative difference in strengths of soft aluminum clad and hard steel matrix leading to different magnitudes of straining.
- The relative thickness at specimen edge and mid-section from FE model clearly showed reasonable agreement with the DIC data from the edge and plane strain analytical model data respectively. The stress state existing at the edge and mid-

section was clearly captured in the 3D FE model as well other experimental characteristics of anticlastic curvature development and punch penetration.

7.3. Tri-layer Laminate Sheets

A new analytical model based on advanced theory of bending, and Tan's monolithic bending model (Tan, Persson and Magnusson, 1995) was also extended to tri-layer laminate sheet material. A 3D FE model was also developed to simulate pure plastic bending of a tri-layer aluminum alloy laminate sheet based on an M-K bend test design. The model results for an aluminum alloy three layer laminate system for different thickness ratios were compared.

- The analytical model provides insight about the stress distribution through the laminate thickness. The analytical model showed similar trend to mid-width data from 3D FE model in predicting the tangential and radial stress distribution for different clad to matrix thickness ratios. The model predicted a continuous reduction in sheet thickness with increasing specimen curvature. Its primary advantage over the FE model is in terms of adaptability to other material systems and rapid prediction of critical bending characteristics such as tangential strain at the outer surface. The model is limited to laminate materials that exhibit similarity in strain hardening behavior. The model is inadequate in describing the stress and strain characteristics along the width direction at the bend line, owing to its two dimensional nature.

- The 3D FE model of M-K bend test design captured all of the general characteristics of the analytical model. In addition, it was able to capture anti-clastic curvature effect, stress and strain variation along the specimen width at the bend line. These features of the model are useful as failures can initiate at the edge. This model showed an increase in specimen thickness at large radii of curvature and a decrease at smaller radii of curvature. This effect was not captured by the analytical model. The increase in thickness at larger radii of curvature is a result of bend propagation from the two ends in clamp driven bending. The thickness variation along the bend line showed the inhomogeneity in strain for wide specimens, a result not obtainable from plane strain based analytical models.

7.4. Limit Strain Prediction in Stretch Bending of Monolithic and Tri-layer Laminate Sheets

An angular stretch bend test was used on AA2024 aluminum alloy and Alclad 2024 tri-layer laminate to predict the limit strain based on the strain data obtained from DIC based strain mapping. A major strain acceleration method from Situ et al. (Situ, Jain and Metzger, 2011) was successfully utilized to predict the limit strain in stretch bending corresponding to the onset of necking was studied. The study was carried out by correlating the three most important DIC parameters namely, microstructure, speckle size and facet size. Major strain history data from the vicinity of strain localization region was utilized in the analysis. Effects of several parameters associated with major strain

acceleration criterion on limit strain prediction were analyzed to optimize the use of major strain acceleration method.

- The DIC based strain mapping served a visual method to locate the strain localization region in stretch bending around the bend line. The maximum major strain in stretch bending occurred on the edge of the specimen.
- The fidelity of DIC based major strain was strongly dependent on the DIC processing parameters namely, facet step and size corresponding with the grain size of the material and speckle size of the random pattern used. Smaller facet size was capable of capturing strain local variations and thereby produced larger strain values.
- Post processing factors such as type of fit to the major strain history data, size of time scale window for data selection had an influence on peak major strain acceleration and thus on limit strains. The major strain curve fit yields consistent strain acceleration results for time scale windows chosen closer to the strain localization stage of the deformation.
- DIC based study utilizing major strain acceleration criterion predicted an average limit strain of 0.20 for stretch bending AA2024-O material with 0.15 uniaxial tensile ductility. This result was comparable with other studies that measured maximum major strain in stretch bending of sheets. The method was also sensitive to predict improved limit strain of 0.24 for Alclad 2024 tri-layer specimen with

80μm thin layer of AA1100, compared to limit strain of 0.20 for monolithic AA2024 specimen.

7.5. Recommendations

Based upon the findings and conclusions of this research the following recommendations can be made for future work.

- The analytical model for predicting bending characteristics reported in this work is confined to Ludwik hardening law and its modified version to represent Bauschinger effect. Developing a model to accommodate other material constitutive laws for a better fit to the material hardening behavior is the next step in the modeling work. This could be further extended to developing a model that is adaptable to any hardening law within its framework.
- The analytical model is still limited to bi-layer and tri-layer materials. Further modifications are required to improve the scope of the model to multi-layer materials.
- Experimental study to precisely measure the shift on unstretched fiber for laminate sheets during bending could be carried through finer speckle pattern and also through in-situ bending under microscope.

- Limit strain prediction could be further studied using different microstructure to continuum scale ratios. Materials with large grain sizes could yield different strain values in DIC strain measurements. Selection of suitable speckle pattern, DIC parameters, camera optics and their effect on the fidelity of the results is an area of study.
- The effect of punch radius on the stretch bendability was not covered in this work. Different punch radii produce different strain gradients and its effect on limit strain could be investigated.
- In the present limit strain study on ASBT test, the camera used for strain measurement was stationary and could lose focus for cases involving large strain out of plane stretch bending. Movable camera system as utilized in the pure bending test could be arranged for constant focus to overcome such limitations.
- Strain measurement through optical methods at macroscopic scale could be verified under the microscope through in-situ stretch bending. The present method could only observe failure shown at the surface. In-situ method could offer details of the location of crack initiation, especially in the case of laminate system where failure could also be from the matrix or interface.
- The limit strain study based on strain acceleration applied to stretch bending of laminate system could be further extended to other in-plane deformation processes to observe the strain acceleration behavior on strain data obtained from strain localization regions in those processes. The effect of clad layer on the forming limits could be assessed in such cases. The same test could be simulated in FE

model and studied for limit strain. Modeling the tri-layer laminate system in FE software considering interface effect is a separate study that could be performed. Forming limit diagram developed through strain acceleration for monolithic and laminate material systems could be compared with those obtained from other FLD development methods.

- The limit strain prediction work through strain acceleration could be automated using suitable software for rapid results. In such case, the software should carry out strain data extraction from Aramis DIC output files, followed by choosing the strain with the highest slope from strain localization region, curve fitting the major strain with different equations and taking second derivative to the fit equations for different time scale window sizes.

References

Alice, J.A. and Danesh, A. (1978) 'Fractue of laminates combining 2024-T3 and 7075-T6 aluminum alloys', *Engineering Fracture Mechanics*, vol. 10, pp. 177-186.

Allwood, J.M. and Shouler, D. (2009) 'Generalised forming limit diagrams showing increased forming limits with non-planar stress states', *International Journal of Plasticity*, vol. 25, pp. 1207-1230.

Aluminum Association (1998) *Aluminum for automotive body sheet panels*, The Aluminum Association.

Amini, S. and Kumar, R. (2014) 'A high-fidelity strain-mapping framework using digital image correlation', *Materials Science and Engineering A*, vol. 594, pp. 394-403.

Antolovich, S.D. and Armstrong, R.W. (2014) 'Plastic strain localization in metals: origins and consequences', *Progress in Material Science*, vol. 59, pp. 1-160.

ASM International, O. (1991) *ASM Handbook, Heat Treating*, Metals Park, Ohio: ASM International.

ASTM-E8 (2008) *Standard Test Methods for Tension Testing of Metallic Materials*, West Conshohocken, PA: American Society for Testing and Materials.

Baba, A. and Tozawa, Y. (1964) 'Effect of Tensile Forces in Stretch Forming Process on the Springback', *Bulleting of Japan Society of Mechanical Engineers*, pp. 834-843.

Bettaieb, M.B., Lemoine, X., Duchêne, L. and Habraken, A.M. (2010) 'Simulation of the bending process of hardening metallic sheets using damage model. Part I: Theoretical development and numerical implementation', *Materials Science and Engineering A*, vol. 528, pp. 434-441.

Bosia, F., Facchini, M., Botsis, J., Gmür, T. and de'Sena, D. (2004) 'Through-the-thickness distribution of strains in laminated composite plates subjected to bending', *Composites Science and Technology*, vol. 64, pp. 71-82.

Caron, E., Pelayo, R., Baserinia, A., Wells, M., Weckman, D., Barker, S. and Gallerneault, M. (2014) 'Direct-Chill Co-Casting of AA3003/AA4045 Aluminum Ingots via Fusion Technology', *Metallurgical and Materials Transactions B*, vol. 45, no. 3, pp. 975-987.

Chakrabarty, J., Lee, W.B. and Chan, K.C. (2001) 'An exact solution for the elastic plastic bending of anisotropic sheet metal under conditions of plane strain', *International Journal of Mechanical Sciences*, vol. 43, pp. 1871-1880.

Considère, A. (1885) 'Mémoire sur l'Emploi du Fer et de l'Acier dans les Constructions', *Annales des Ponts et Chaussées*, vol. 9, pp. 574-775.

Crafoord, R. (1967) 'The mechanism of forming in bending.', *Annals of CIRP*, vol. 15, pp. 253-261.

Dadras, P. and Majlessi, S.A. (1982) 'Plastic bending of work hardening materials', *Transactions of the ASME*, vol. 104, pp. 224-230.

Dassault Systemes (2008) *Abaqus*, Velizy Villacoublay: Corporate Authors.

Davidkov, M.K., Jain, M.K., Petrov, R.H., Wilkinson, D.S. and Mishra, R.K. (2012) 'Strain localization and damage development during bending of Al–Mg alloy', *Material Science and Engineering: A*, vol. 550, pp. 395-407.

Demeri, M.Y. (1981) 'The stretch-bend forming of sheet metal', *Journal of Applied Metalworking*, vol. 2, no. 1, pp. 3-10.

Demeri, M.Y. (1986) 'Strain analysis of the hemispherical stretch-bend test', *Journal of Applied Metalworking*, vol. 4, no. 2, pp. 183-187.

Deqing, W., Ziyuan, S. and Ruobin, Q. (2007) 'Cladding of stainless steel on aluminum and carbon steel', *Scripta Materialia*, vol. 56, no. 5, pp. 369–372.

Doig, M., Kaupper, M., Kraska, M., Eßer, G., Merklein, M., Roll, K. and Keßler, L. (2010) 'Inverse Identification of Kinematic Hardening Parameters with Bending Tests', Proc. 50th Conference of IDDRG, Graz, 555-564.

Drucker, D.C. (1956) 'The effect of shear on the plastic bending of beams', *Journal of Applied Mechanics*, pp. 509-514.

Embury, J.D., Petch, N.J. Wraith, A.E. Wright, E.S. (1967) 'The fracture of mild steel laminates', *Transactions of the Metallurgical Society of American Institute of Mining, Metallurigical and Petroleum Engineers*, vol. 239, pp. 114-118.

Eyckens, P., Bael, A.V. and Houtte, P.V. (2009) 'Marciniak–Kuczynski type modelling of the effect of Through-Thickness Shear on the forming limits of sheet metal', *International Journal of Plasticity*, vol. 25, no. 12, pp. 2249-2268.

Geiger, M. and Merklein, M. (2003) 'Determination of forming limit diagrams – a new analysis method for characterization of materials' formability', *CIRP Annals - Manufacturing Technology*, vol. 52, no. 1, pp. 213-216.

Gom-mbH (2001) *Aramis-deformation measurement using the grating method. User's manual, V4.7-4.2*, Braunschweig, Germany: Gom-mbH.

Guijosa, J.M.M., Cruz, V.R., Cabarello, F.D., Lantada, A.D. and Otera, J.E. (2012) 'Simple testing system for pure bending tests with large deflections', *Experimental Mechanics*, vol. 52, pp. 679-692.

Heller, B. and Kleiner, M. (2006) 'Semi-analytical process modelling and simulation of air bending', *Journal of Strain Analysis*, vol. 41, no. 1, pp. 57-80.

He, J., Xia, Z.C., Zhu, X., Zeng, D. and Li, S. (2013) 'Sheet metal forming limits under stretch-bending with anisotropic hardening', *International Journal of Mechanical Sciences*, vol. 75, pp. 244–256.

Hill, R. (1948) 'A Theory of the Yielding and Plastic Flow of Anisotropic Metals', *Proceedings of the Royal Society of London Series A*, vol. 193, pp. 281–297.

Hill, R. (1950) *The mathematical theory of plasticity*, London: Oxford University Press, pp. 287-294.

Hill, R. (1952) 'On discontinuous plastic states, with special reference to localized necking in thin sheets', *Journal of the Mechanics and Physics of Solids*, vol. 1, no. 1, pp. 19-30.

Hill, R.G. and Zapel, E.J. (1962) *Pure bending test machine*, US Patent 3026720.

Hosford, W. and Duncan, L. (1999) 'Sheet metal forming: A review', *JOM*, vol. 51, no. 11, pp. 39-44.

Kitting, D., Koplenig, M., Ofenheimer, A., Pauli, H. and Till, E.T. (2009) 'Application of a Concave side rule approach for assessing formability of stretch-bent steel sheets', *International Journal of Material Forming*, vol. 2, no. 1, pp. 427-430.

Kruijf, N.F., Peerlings, R.H.J. and Geers, M.G.D. (2009) 'An analysis of sheet necking under combined stretching and bending', *International Journal of Material Forming*, vol. 2, pp. 845-848.

Lesuer, D.R., Syn, C.K., Sherby, O.D., Wadsworth, J., Lewandowski, J.J. and Hunt Jr, W.H. (1996) 'Mechanical behaviour of laminated metal composites', *International Material Reviews*, vol. 41, pp. 169-197.

Liu, J., Sheu, S., Karabin, M.E. and Schultz, R.W. (2008) 'Macro- and micro-surface engineering to improve hot roll bonding of aluminum plate and sheet', *Journal of Materials Processing Technology*, vol. 497, pp. 45-57.

Lopez, A.M. and van den Boogard, A.H. (2011) 'Formability limit curves under stretch bending', 15th International Deep Drawing Research Group Conference, Bilbao, Spain.

Lubahn, J.D. and Sachs, G. (1950) 'Bending of an ideal plastic metal', *Transactions of the ASME*, vol. 72, pp. 201-208.

Ludwik, P. (1903) 'Engineering Study of Sheet Bending. , Böhmen, Technische Blätter', *Verlag des Deutschen Polytechnischen Vereins, Böhmen, Technische Blätter*, vol. 35, pp. 133-159.

Majlessi, S.A. and Dadras, P. (1983) 'Pure plastic bending of sheet laminates under plane strain condition.', *International Journal of Mechanical Sciences*, vol. 25, no. 1, pp. 1-14.

Mamalis, A.G., Szalay, A., Vaxevanidis, N.M. and Manolakos, D.E. (1998) 'Fabrication of bimetallic rods by explosive cladding and warm extrusion', *Journal of Materials Processing Technology*, vol. 83, pp. 48-53.

Marciniak, Z. and Kuczynski, K. (1967) 'Limit strains in the processes of stretch-forming sheet metal', *International Journal of Mechanical Sciences*, vol. 9, no. 9, pp. 609-612.

Marciniak, Z. and Kuczynski, K. (1979) 'The forming limit curve for bending processes', *International Journal of Mechanical Sciences*, vol. 21, pp. 609-621.

Martínez-Donaire, A.J., García-Lomas, F.J. and Vallellano, C. (2014) 'New approaches to detect the onset of localised necking in sheets under through-thickness strain gradients', *Materials & Design*, vol. 57, pp. 135-145.

Martínez-Palmeth, L.H., Martínez-Donaire, A.J., Centeno, G., García-Lomas, F.J. and Vallellano, C. (2013) 'Formability of automotive H240LA steel sheets in stretch– bending processes', *Procedia Engineering*, vol. 63, pp. 669–677.

Martin, G. and Tsang, S. (1966) 'The plastic bending of beams considering die friction effects', *Journal of Engineering for Industry*, vol. 88, pp. 237-250.

Marzouk, M., Shankar, S. and Jain, M.K. (2014) 'Effect of Sr-modification on the bendability of cast aluminum alloy A356 using digital image correlation method', *Material Science and Engineering A*, vol. 598, pp. 277-287.

McClintock, F., Zhou, Q. and Wierzbicki, T. (1993) 'Necking in plane strain under bending with constant tension', *Journal of Physics of Solids*, vol. 8, pp. 1327-1343.

McEwan, K.M.B. and Milner, D.R. (1962) 'Pressure welding of dissimilar metals', *British Welding Journal*, pp. 406-420.

Novelis Global Research (2005) *Novelis Fusion (TM)*, [Online], Available: www.novelis.com [2014].

Patel, K. (2006) *Evaluation of spring back prediction capability using uniform pure bending*, Wichita: Wichita State University.

Perduijn, A.B. and Hoogenboom, S.M. (1995) 'The pure bending of sheet', *Journal of Materials Processing Technology*, vol. 51, pp. 274-295.

Proksa, F. (1959) 'Plastisches biegen von blechen', *Der Stahlbau*, vol. 28, no. 1, pp. 29-36.

Rees, D.W.A. (2001) 'Factors influencing the FLD of automotive sheet metal', *Journal of Materials Processing Technology*, vol. 118, no. 1-3, pp. 1-8.

Situ, Q. (2008) *A New Approach To Obtain Forming Limits Of Sheet Materials, Doctoral Thesis*, Hamilton: McMaster University.

Situ, Q., Bruhis, M. and Jain, M.K. (2006) 'A suitable criterion for precise determination of incipient necking in sheet materials', *Material Science Forum*, pp. 111-116.

Situ, Q., Jain, M.K. and Metzger, D.R. (2011) 'Determination of forming limit diagrams of sheet materials with a hybrid experimental–numerical approach', *International Journal of Mechanical Sciences*, vol. 53, pp. 707-719.

Smith, D.L. (1995) *Thin-Film Deposition: Principles and Practice*, McGraw-Hill Professional.

Sriram, S., Wong, C., Huang, M. and Yan, B. (2003) 'Stretch bendability of advanced high strength steels', *SAE Technical Paper 2003-01-1151*.

Storen, S. and Rice, J.R. (1975) 'Localized necking in thin sheets', *Journal of the Mechanics of Physics of Solids*, vol. 23, no. 6, pp. 421-441.

Swift, R.W. (1948) 'Plastic bending under tension', *Engineering*, vol. 3, pp. 333-359.

Swift, H.W. (1952) 'Plastic instability under plane stress', *Journal of the Mechanics and Physics of Solids*, pp. 1-18.

Tan, Z., Magnusson, C. and Persson, B. (1994) 'The Bauschinger effect in compression-tension of sheet metals', *Materials Science and Engineering: A*, vol. 183, no. 1-2, pp. 31-38.

Tan, Z., Persson, B. and Magnusson, C. (1995) 'Plastic bending of anisotropic sheet metals', *International Journal of Mechanical Sciences*, vol. 37, pp. 405-421.

Tench, D. and White, J. (1984) 'Enhanced Tensile Strength for Electrodeposited Nickel-Copper Multilayer Composites', *Metallurgical Transactions A*, vol. 15A, pp. 2039-2040.

Tharret, M. and Stoughton, T. (2003) 'Stretch bend forming limits of 1008 AK steel', *Society of Automotive Engineers*.

Thomason, P.F. (1990) *Ductile Fracture of Metals*, New York: Pergamon Press.

Triantafyllidis, N. and Needleman, A. (1982) 'On the development of shear bands in pure bending', *International Journal of Solids and Structures*, vol. 18, no. 2, pp. 121-138.

Tvergaard, V. and Needleman, A. (1984) 'Analysis of the cup-cone fracture in a round tensile bar', *Acta Metallurgica*, vol. 32, no. 1, pp. 157–169.

Uko, D.K., Sowerby, R. and Duncan, J.L. (1977) 'Strain distribution in the bending-under-tension test', *CIM Bulletin*, pp. 127-134.

Verguts, H. and Sowerby, R. (1975) 'The pure plastic bending of laminated sheet metals.', *International Journal of Mechanical Sciences*, vol. 17, pp. 31-51.

Voce, E. (1955) 'A practical strain hardening function', *Metallurgia*, vol. 51, no. 307, pp. 219–226.

Wang, C., Kinzel, G. and Altan, T. (1993) 'Mathematical modeling of plane strain bending of sheet and plate', *Journal of Materials Processing Technology*, vol. 39, pp. 273-304.

Weiss, M., Ryan, W., Rolfe, B.F. and Yang, C. (2010) 'The effect of skin passing on the material behavior of metal strip in pure bending and tension', NUMIFORM 2010: AIP Conference Proceedings, Pohang, 896-902.

Wolfram Research (2009) *Wolfram Alpha* , 18 May, [Online], Available: www.wolframalpha.com [2014].

Wu, Y.T., Wei, W.S. and Koo, C.H. (1998) 'Diffusion bonding of Ti-25AI-IONb alloy', *Science and Technology of Welding and Joining*, vol. 3, no. 2, pp. 97-104.

Wu, M., Zhang, J.J., Hunt, W.H. and Lewandowski, J.J. (1995) 'Proceedings of fabrication of advanced materials 4', Warrendale, PA.

Wu, J., Zhou, D., Zhang, L., Zhou, Y.J., Du, C.Q. and Shi, M. (2006) 'A failure criterion for stretch bendability of advanced high strength steels', *SAE Technical Paper 2006-01-0349*.

Yilamu, K., Hino, R., Hamasaki, H. and Yoshida, F. (2010) 'Air bending and springback of stainless steel clad aluminum sheet', *Journal of Materials Processing Technology*, vol. 210, pp. 272-278.

Yoshida, F. and Uemori, T. (2002) 'A model of large-strain cyclic plasticity describing the Bauschinger effect and workhardening stagnation', *International Journal of Plasticity*, vol. 18, no. 5-6, pp. 661–686.

Yoshida, F., Urabe, M. and Toropov, V.V. (1998) 'Identification of material parameters on constitutive model for sheet metals from cyclic bending tests', *International Journal of Mechanical Sciences*, vol. 40, no. 2-3, pp. 237-249.

Yoshida, M., Yoshida, F., Haruyuki, K. and Fukumoto, K. (2005) 'Fracture limits of sheet metals under stretch bending', *International Journal of Mechanical Sciences*, vol. 47, no. 12, pp. 1885-1896.

Zadpoor, A.A., Campoli, G., Sinke, J. and Benedictus, R. (2011) 'Fracture in bending – The straining limits of monolithic sheets and machined tailor-made blanks', *Materials & Design*, vol. 32, no. 3, pp. 1229-1241.

Zhu, H.X. (2007) 'Large deformation pure bending of an elastic plastic power-law-hardening wide plate: analysis and application.', *International Journal of Mechanical Sciences*, vol. 49, pp. 500-514.

Appendices

Appendix A: Summary of Stress Equations and Λ Parameter for Bi-layer and Tri-layer Laminate Sheet Material

The summary of tangential, radial stresses and λ parameter of equality condition for bi-layer (C-T) , (C-C) and tri-layer laminate from the analytical model is presented in sections A1, A2 and A3 as follows.

A1. Summary of Stress Equations and Λ parameter for Bi-layer C-T Laminate

Table 14. Summary of stress equations for bi-layer C-T laminate

Radial stress	Tangential stress
$\sigma_r^{\ I} = -k_3\left(\ln\frac{r_y}{r}\right) - k_4\left[\left(\ln\frac{r_y}{r_u}\right)^{n_{L2}+1} - \left(\ln\frac{r}{r_u}\right)^{n_{L2}+1}\right]$	$\sigma_\theta^{\ I} = \frac{2}{\sqrt{3}}\left[\sigma_{02} + K_2\left(\frac{2}{\sqrt{3}}\ln\frac{r}{r_u}\right)^{n_{L2}}\right] + \sigma_r^{\ I}$
$\sigma_r^{\ II} = -k_1\left(\ln\frac{r_b}{r}\right) - k_2\left[\left(\ln\frac{r_b}{r_u}\right)^{n_{L1}+1} - \left(\ln\frac{r}{r_u}\right)^{n_{L1}+1}\right]$ $-k_3\left(\ln\frac{r_y}{r_b}\right) - k_4\left[\left(\ln\frac{r_y}{r_u}\right)^{n_{L2}+1} - \left(\ln\frac{r_b}{r_u}\right)^{n_{L2}+1}\right]$	$\sigma_\theta^{\ II} = \frac{2}{\sqrt{3}}\left[\sigma_{01} + K_1\left(\frac{2}{\sqrt{3}}\ln\frac{r}{r_u}\right)^{n_{L1}}\right] + \sigma_r^{\ II}$
$\sigma_r^{\ III} = -k_1\left(\ln\frac{r_b}{r}\right) - k_2\left[\left(\ln\frac{r_b}{r_u}\right)^{n_{L1}+1} - \left(\ln\frac{r_u}{r}\right)^{n_{L1}+1}\right]$ $-k_3\left(\ln\frac{r_y}{r_b}\right) - k_4\left[\left(\ln\frac{r_y}{r_u}\right)^{n_{L2}+1} - \left(\ln\frac{r_b}{r_u}\right)^{n_{L2}+1}\right]$	$\sigma_\theta^{\ III} = \frac{2}{\sqrt{3}}\left[\sigma_{01} - K_1\left(\frac{2}{\sqrt{3}}\ln\frac{r_u}{r}\right)^{n_{L1}}\right] + \sigma_r^{\ III}$
(table continued in next page)	

$\sigma_r^{IV} = k_1\left(\ln\frac{r_i}{r}\right) - k_2\left[\left(\ln\frac{r_u}{r_i}\right)^{n_{L1}+1} - \left(\ln\frac{r_u}{r}\right)^{n_{L1}+1}\right]$	$\sigma_\theta^{IV} = -\frac{2}{\sqrt{3}}\left[\sigma_{01} + K_1\left(\frac{2}{\sqrt{3}}\ln\frac{r_u}{r}\right)^{n_{L1}}\right] + \sigma_r^{IV}$

$$\Lambda = \exp\left\{-\left[\begin{array}{l} \frac{k_2}{k_1}\left[\left(\ln\frac{\left(1+\frac{(1-2q_1)\kappa}{2}\right)}{\eta}\right)^{n_{L1}+1} - \left(\ln\frac{\eta}{1-\frac{\kappa}{2}}\right)^{n_{L1}+1}\right] + \frac{k_3}{k_1}\left(\ln\frac{\left(1+\frac{\kappa}{2}\right)}{\left(1+\frac{(1-2q_1)\kappa}{2}\right)}\right) - \\ \frac{k_4}{k_1}\left[\left(\ln\frac{\left(1+\frac{(1-2q_1)\kappa}{2}\right)}{\eta}\right)^{n_{L2}+1} - \left(\ln\frac{1+\frac{\kappa}{2}}{\eta}\right)^{n_{L2}+1}\right] \end{array}\right]\right\} + \frac{q_1.\kappa\left(1-\frac{\kappa}{2}\right)}{\rho^2\eta^2}$$

A2. Summary of Stress Equations and Λ parameter for Bi-layer C-C Laminate

Table 15. Summary of stress equations for bi-layer C-C laminate

Radial stress	Tangential stress
$\sigma_r^{I} = -k_1\left(\ln\frac{r_y}{r}\right) - k_2\left[\left(\ln\frac{r_y}{r_u}\right)^{n_{L1}+1} - \left(\ln\frac{r}{r_u}\right)^{n_{L1}+1}\right]$	$\sigma_\theta^{I} = \frac{2}{\sqrt{3}}\left[\sigma_{01} + K_1\left(\frac{2}{\sqrt{3}}\ln\frac{r}{r_u}\right)^{n_{L1}}\right] + \sigma_r^{I}$
$\sigma_r^{II} = -k_1\left(\ln\frac{r_y}{r}\right) - k_2\left[\left(\ln\frac{r_y}{r_u}\right)^{n_L+1} - \left(\ln\frac{r_u}{r}\right)^{n_L+1}\right]$	$\sigma_\theta^{II} = \frac{2}{\sqrt{3}}\left[\sigma_{01} - K_1\left(\frac{2}{\sqrt{3}}\ln\frac{r_u}{r}\right)^{n_{L1}}\right] + \sigma_r^{II}$
(table continued on next page)	

$\sigma_r^{III} = k_1\left(\ln\frac{r_b}{r}\right) - k_2\left[\left(\ln\frac{r_u}{r_b}\right)^{n_{L1}+1} - \left(\ln\frac{r_u}{r}\right)^{n_{L1}+1}\right] + k_3\left(\ln\frac{r_i}{r_b}\right) - k_4\left[\left(\ln\frac{r_u}{r_i}\right)^{n_{L2}+1} - \left(\ln\frac{r_u}{r_b}\right)^{n_{L2}+1}\right]$	$\sigma_\theta^{III} = -\frac{2}{\sqrt{3}}\left[\sigma_{01} + K_1\left(\frac{2}{\sqrt{3}}\ln\frac{r_u}{r}\right)^{n_{L1}}\right] + \sigma_r^{III}$
$\sigma_r^{IV} = k_3\left(\ln\frac{r_i}{r}\right) - k_4\left[\left(\ln\frac{r_u}{r_i}\right)^{n_{L2}+1} - \left(\ln\frac{r_u}{r}\right)^{n_{L2}+1}\right]$	$\sigma_\theta^{IV} = -\frac{2}{\sqrt{3}}\left[\sigma_{02} + K_2\left(\frac{2}{\sqrt{3}}\ln\frac{r_u}{r}\right)^{n_{L2}}\right] + \sigma_r^{IV}$

$$\Lambda = \exp\left\{-\left[\begin{array}{l}\frac{k_2}{k_1}\left[\left(\ln\frac{1+\frac{\kappa}{2}}{\eta}\right)^{n_{L1}+1} - \left(\ln\frac{\eta}{\left(1+\frac{(2q_1-1)\kappa}{2}\right)}\right)^{n_{L1}+1}\right] + \frac{k_3}{k_1}\left(\ln\frac{\left(1-\frac{\kappa}{2}\right)}{\left(1+\frac{(2q_1-1)\kappa}{2}\right)}\right) \\ -\frac{k_4}{k_1}\left[\left(\ln\frac{\eta}{\left(1-\frac{\kappa}{2}\right)}\right)^{n_{L2}+1} - \left(\ln\frac{\eta}{\left(1+\frac{(2q_1-1)\kappa}{2}\right)}\right)^{n_{L2}+1}\right]\end{array}\right]\right\} - \frac{q_1.\kappa\left(1+\frac{\kappa}{2}\right)}{\rho^2\eta^2}$$

A3. Summary of Stress Equations and Λ parameter for Tri-layer Laminate

Table 16. Summary of stress equations for tri-layer laminate

Radial stress	Tangential stress
$\sigma_r^{\ I} = -k_3\left(\ln\frac{r_y}{r}\right) - k_4\left[\left(\ln\frac{r_y}{r_u}\right)^{n_{L2}+1} - \left(\ln\frac{r}{r_u}\right)^{n_{L2}+1}\right]$	$\sigma_\theta^{\ I} = \frac{2}{\sqrt{3}}\left[\sigma_{02} + K_2\left(\frac{2}{\sqrt{3}}\ln\frac{r}{r_u}\right)^{n_{L2}}\right] + \sigma_r^{\ I}$
$\sigma_r^{\ II} = -k_1\left(\ln\frac{r_b}{r}\right) - k_2\left[\left(\ln\frac{r_b}{r_u}\right)^{n_{L1}+1} - \left(\ln\frac{r}{r_u}\right)^{n_{L1}+1}\right]$ $-k_3\left(\ln\frac{r_y}{r_b}\right) - k_4\left[\left(\ln\frac{r_y}{r_u}\right)^{n_{L2}+1} - \left(\ln\frac{r_b}{r_u}\right)^{n_{L2}+1}\right]$	$\sigma_\theta^{\ II} = \frac{2}{\sqrt{3}}\left[\sigma_{01} + K_1\left(\frac{2}{\sqrt{3}}\ln\frac{r}{r_u}\right)^{n_{L1}}\right] + \sigma_r^{\ II}$
$\sigma_r^{\ III} = -k_1\left(\ln\frac{r_b}{r}\right) - k_2\left[\left(\ln\frac{r_b}{r_u}\right)^{n_{L1}+1} - \left(\ln\frac{r_u}{r}\right)^{n_{L1}+1}\right]$ $-k_3\left(\ln\frac{r_y}{r_b}\right) - k_4\left[\left(\ln\frac{r_y}{r_u}\right)^{n_{L2}+1} - \left(\ln\frac{r_b}{r_u}\right)^{n_{L2}+1}\right]$	$\sigma_\theta^{\ III} = \frac{2}{\sqrt{3}}\left[\sigma_{01} - K_1\left(\frac{2}{\sqrt{3}}\ln\frac{r_u}{r}\right)^{n_{L1}}\right] + \sigma_r^{\ III}$
$\sigma_r^{\ IV} = k_1\left(\ln\frac{r_a}{r}\right) - k_2\left[\left(\ln\frac{r_u}{r_a}\right)^{n_{L1}+1} - \left(\ln\frac{r_u}{r}\right)^{n_{L1}+1}\right]$ $+k_3\left(\ln\frac{r_i}{r_a}\right) - k_4\left[\left(\ln\frac{r_u}{r_i}\right)^{n_{L2}+1} - \left(\ln\frac{r_u}{r_a}\right)^{n_{L2}+1}\right]$	$\sigma_\theta^{\ IV} = -\frac{2}{\sqrt{3}}\left[\sigma_{01} + K_1\left(\frac{2}{\sqrt{3}}\ln\frac{r_u}{r}\right)^{n_{L1}}\right] + \sigma_r^{\ IV}$
$\sigma_r^{\ V} = k_3\left(\ln\frac{r_i}{r}\right) - k_4\left[\left(\ln\frac{r_u}{r_i}\right)^{n_{L2}+1} - \left(\ln\frac{r_u}{r}\right)^{n_{L2}+1}\right]$	$\sigma_\theta^{\ V} = -\frac{2}{\sqrt{3}}\left[\sigma_{02} + K_2\left(\frac{2}{\sqrt{3}}\ln\frac{r_u}{r}\right)^{n_{L2}}\right] + \sigma_r^{\ V}$

$$\Lambda = \exp\left[-1.\left[\frac{k_2}{k_1}\left[\left(\ln\frac{\left(1+\frac{(1-2q_1)\kappa}{2}\right)}{\eta}\right)^{n_{L1}+1} - \left(\ln\frac{\eta}{\left(1+\frac{(2q_2-1)\kappa}{2}\right)}\right)^{n_{L1}+1}\right] + \frac{k_3}{k_1}\left[\left(\ln\frac{\left(1-\frac{\kappa}{2}\right)}{\left(1+\frac{(2q_2-1)\kappa}{2}\right)}\right) + \left(\ln\frac{\left(1+\frac{\kappa}{2}\right)}{\left(1+\frac{(1-2q_1)\kappa}{2}\right)}\right)\right] + \frac{k_4}{k_1}\left[\left(\ln\frac{\eta}{\left(1+\frac{(2q_2-1)\kappa}{2}\right)}\right)^{n_{L2}+1} - \left(\ln\frac{\eta}{\left(1-\frac{\kappa}{2}\right)}\right)^{n_{L2}+1} + \left(\ln\frac{\left(1+\frac{\kappa}{2}\right)}{\eta}\right)^{n_{L2}+1} - \left(\ln\frac{\left(1+\frac{(1-2q_1)\kappa}{2}\right)}{\eta}\right)^{n_{L2}+1}\right]\right]\right] - \frac{(q_2-q_1).\kappa + (q_1+q_2-2.q_1.q_2)\frac{\kappa^2}{2}}{\rho^2\eta^2}$$

Appendix B: Matlab Code For The Bi-layer Bending Model (C-T)

B1. Model Code for Stress Calculation

```
clear all;
clc;
%COMMENTS: Matlab code for obtaining radial and tangential stress ans
strains in bi-layer C-T bending model based on Tan et al. 1995 model.
Ganesh Govindasamy, July 2010. Matlab R2008a. This code is based on
advanced theory of bending.
%Initialising material properties
to=4;
% Properties of SS400
n1=0.83;
K1=1132;
sigma_01=438;
% Properties of AA1050
n2=0.53;
K2=58;
sigma_02=90;
%Initial thickness fraction
global q1
global rho
%Clad to Matrix thickness ratio
q1 = 0.1;
%For Luwik hardening law
k1=sigma_01*(2/sqrt(3));
k2=K1*((2/(sqrt(3)))^(n1+1))/(n1+1);
k3=sigma_02*(2/sqrt(3));
k4=K2*((2/(sqrt(3)))^(n2+1))/(n2+1);
%Initializing the relative curvature and relative thickness
rho=1;
k=0.00;
%
N=1;
count=1;
countr=1;
eta(1:30)=1.0;
% count2 =1;
fid = fopen('stress100.txt','wt');
for k=0.04:0.04:1.2
    [x,y]=ode45('eq22',[k-(0.04-0.0000001),k], eta(count));
    N=y(length(x));
    eta(count)=N;
    t=N*to;
    Rm=t/k;
    Ru=N*Rm;
    Ri=(1-k/2)*Rm;
    R=Ri;
    Ry=(1+k/2)*Rm;
```

```
    Rb=Ry-(q1*N*to);
    q1=(Ry-Rb)./(N*to);
    while ((SIV(Ri,Ru,R)- SIII(Ry,Ru,Rb,R))>0);
        R=R+0.001;
    end
    Rn=R-0.001;
    rho=Rn/Ru;
    kappa(count)=k;
    relative_curavture(count) = rho;
    R_start=Ri;
    R_fin=Ry;
    no_of_points=200;
    rad_stress(1:no_of_points)=0.;
    tan_stress(1:no_of_points)=0.;
    gamma_stress_ratio(1:no_of_points)=0.;
    C_sigbarI(1:no_of_points)=0.;
    C_sigbarII(1:no_of_points)=0.;
    C_sigbarIII(1:no_of_points)=0.;
    C_sigbarIV(1:no_of_points)=0.;
    R_over_Ru(1:no_of_points)=1.;
    Ru_over_R(1:no_of_points)=1.;
    strain(1:no_of_points)=1.;
    R_inc=(R_fin - R_start)/no_of_points;
    Rprime=R_start;
    for Rprime=R_start:R_inc:R_fin
        %Zone 4
        if ((Rprime>=Ri) & (Rprime<=Rn))
            R_over_Ru(countr)=Rprime/Ru;
            Ru_over_R(countr)=Ru/Rprime;
            rad_stress(countr)=SIV(Ri, Ru, Rprime);
            strain(countr)=(2/(sqrt(3)))*(log(Ru_over_R(countr)));
            C_sigbarIV(countr)=-
(2/(sqrt(3)))*(sigma_01+(K1*(strain(countr))^n1));
            tan_stress(countr)=C_sigbarIV(countr) + rad_stress(countr);
gamma_stress_ratio(countr)=rad_stress(countr)/tan_stress(countr);
        end;
%         %Zone 3
        if ((Rprime>=Rn) & (Rprime<=Ru))
            R_over_Ru(countr)=Rprime/Ru;
            Ru_over_R(countr)=Ru/Rprime;
            rad_stress(countr)=SIII(Ry,Ru,Rb,Rprime);
            strain(countr)=(2/(sqrt(3)))*(log(Ru_over_R(countr)));
            C_sigbarIII(countr)=(2/(sqrt(3)))*(sigma_01-
(K1*(strain(countr))^n1));
            tan_stress(countr)=C_sigbarIII(countr) + rad_stress(countr);
gamma_stress_ratio(countr)=rad_stress(countr)/tan_stress(countr);
        end;
%         %Zone 2
        if ((Rprime>=Ru) & (Rprime<=Rb))
            R_over_Ru(countr)=Rprime/Ru;
            Ru_over_R(countr)=Ru/Rprime;
            rad_stress(countr)=SII(Ry,Ru,Rb,Rprime);
            strain(countr)=(2/(sqrt(3)))*(log(R_over_Ru(countr)));
```

```
C_sigbarII(countr)=(2/(sqrt(3)))*(sigma_01+(K1*(strain(countr))^n1));
            tan_stress(countr)=C_sigbarII(countr) + rad_stress(countr);
gamma_stress_ratio(countr)=rad_stress(countr)/tan_stress(countr);
        end;
%         %Zone 1
        if ((Rprime>=Rb) & (Rprime<=Ry))
            R_over_Ru(countr)=Rprime/Ru;
            Ru_over_R(countr)=Ru/Rprime;
            rad_stress(countr)=SI(Ry,Ru,Rprime);
            strain(countr)=(2/(sqrt(3)))*(log(R_over_Ru(countr)));
C_sigbarI(countr)=(2/(sqrt(3)))*(sigma_02+(K2*(strain(countr))^n2));
            tan_stress(countr)=C_sigbarI(countr) + rad_stress(countr);
gamma_stress_ratio(countr)=rad_stress(countr)/tan_stress(countr);
       elseif ((Rprime>Ry))
            R_over_Ru(countr)=NaN;
            rad_stress(countr)=NaN;
            strain(countr)=NaN;
            C_sigbarI(countr)=NaN;
            C_sigbarII(countr)=NaN;
            C_sigbarIII(countr)=NaN;
            C_sigbarIV(countr)=NaN;
            tan_stress(countr)=NaN;
            gamma_stress_ratio(countr)=NaN;
        end;
         fprintf(fid,'%12.8f %12.8f
%12.8f\n',R_over_Ru(countr),tan_stress(countr),rad_stress(countr));

    end
    end
fclose(fid);
```

B2. Radial Stress - I

```
% Subroutine file for Radial stress I
function sigmaI=SI(Ry,Ru,R)
%Initialising material properties
to=4;
% Properties of SS400
n1=0.83;
K1=1132;
sigma_01=438;
% Properties of AA1050
n2=0.53;
K2=58;
sigma_02=90;
%For Luwik hardening law
k1=sigma_01*(2/sqrt(3));
k2=K1*((2/(sqrt(3)))^(n1+1))/(n1+1);
k3=sigma_02*(2/sqrt(3));
k4=K2*((2/(sqrt(3)))^(n2+1))/(n2+1);
```

```
%
sigmaI=(-k3*(log(Ry/R))-k4*((log(Ry/Ru))^(n2+1)-(log(R/Ru))^(n2+1)));
```

B3. Radial Stress – II

```
% Subroutine file for Radial stress II
function sigmaII=SII(Ry,Ru,Rb,R)
%Initialising material properties
to=4;
% Properties of SS400
n1=0.83;
K1=1132;
sigma_01=438;
% Properties of AA1050
n2=0.53;
K2=58;
sigma_02=90;
%For Luwik hardening law
k1=sigma_01*(2/sqrt(3));
k2=K1*((2/(sqrt(3)))^(n1+1))/(n1+1);
k3=sigma_02*(2/sqrt(3));
k4=K2*((2/(sqrt(3)))^(n2+1))/(n2+1);
%
sigmaII=(-k1*(log(Rb/R))-k2*((log(Rb/Ru))^(n1+1)-(log(R/Ru))^(n1+1))-
k3*(log(Ry/Rb))-k4*((log(Ry/Ru))^(n2+1)-(log(Rb/Ru))^(n2+1)));
```

B4. Radial Stress – III

```
% Subroutine file for Radial stress III
function sigmaIII=SIII(Ry,Ru,Rb,R)
%Initialising material properties
to=4;
% Properties of SS400
n1=0.83;
K1=1132;
sigma_01=438;
% Properties of AA1050
n2=0.53;
K2=58;
sigma_02=90;
%For Luwik hardening law
k1=sigma_01*(2/sqrt(3));
k2=K1*((2/(sqrt(3)))^(n1+1))/(n1+1);
k3=sigma_02*(2/sqrt(3));
k4=K2*((2/(sqrt(3)))^(n2+1))/(n2+1);
%
```

```
sigmaIII=(-k1*(log(Rb/R))-k2*((log(Rb/Ru))^(n1+1)-(log(Ru/R))^(n1+1))-
k3*(log(Ry/Rb))-k4*((log(Ry/Ru))^(n2+1)-(log(Rb/Ru))^(n2+1)));
```

B5. Radial Stress – IV

```
% Subroutine file for Radial stress IV
function sigmaIV=SIV(Ri,Ru,R)
%Initialising material properties
to=4;
% Properties of SS400
n1=0.83;
K1=1132;
sigma_01=438;
% Properties of AA1050
n2=0.53;
K2=58;
sigma_02=90;
%For Luwik hardening law
k1=sigma_01*(2/sqrt(3));
k2=K1*((2/(sqrt(3)))^(n1+1))/(n1+1);
k3=sigma_02*(2/sqrt(3));
k4=K2*((2/(sqrt(3)))^(n2+1))/(n2+1);
%
sigmaIV=(k1*(log(Ri/R))-k2*((log(Ru/Ri))^(n1+1)-(log(Ru/R))^(n1+1)));
```

B6. Relative Thickness

```
%COMMENTS: Matlab code for obtaining relative thickness in bi-layer C-T
model based on Tan et al. 1995 model. Ganesh Govindasamy, July 2010.
clear all;
clc;
%Initialising material properties
to=4;
% Properties of SS400
n1=0.83;
K1=1132;
sigma_01=438;
% Properties of AA1050
n2=0.53;
K2=58;
sigma_02=90;
%Initial thickness fraction
global q1
global rho
```

```
%Clad to Matrix thickness ratio
q1 = 0.25;
%For Luwik hardening law
k1=sigma_01*(2/sqrt(3));
k2=K1*((2/(sqrt(3)))^(n1+1))/(n1+1);
k3=sigma_02*(2/sqrt(3));
k4=K2*((2/(sqrt(3)))^(n2+1))/(n2+1);
%Initializing the relative curvature and relative thickness
rho=1;
k=0.00;
%Initializing the relative curvature and relative thickness
k=0.00;
N=1;
rho=1;
%
count=1;
countr=1;
eta(1:50)=1.0;
fid = fopen('ctc101.txt','wt');
for k=0.04:0.04:2
    [x,y]=ode45('eq22',[k-(0.04-0.0000001),k], eta(count));
    N=y(length(x));
    eta(count)=N;
    t=N*to;
    Rm=t/k;
    Ru=N*Rm;
    Ri=(1-k/2)*Rm;
    R=Ri;
    Ry=(1+k/2)*Rm;
    Rb=Ry-(q1*N*to);
    q1=(Ry-Rb)./(N*to);
    while ((SIV(Ri,Ru,R)- SIII(Ry,Ru,Rb,R))>0);
        R=R+0.001;
    end
    Rn=R-0.001;
    rho=Rn/Ru;
    kappa(count)=k;
    relative_curavture(count) = rho;

    fprintf(fid,'%12.8f %12.8f %12.8f %12.8f %12.8f %12.8f
%12.8f\n',k,N,rho,Ru,Rn,Ry,Ri);
end
fclose(fid);
```

Appendix C: Matlab Code for Strain Data Extraction from Multiple Text (.txt) Files From Aramis Strain Measurement

```
% Matlab code for obtaining strain data from multiple text from Aramis
DIC output. Ganesh Govindasamy, July 2012. Matlab R2008a.
%NOTE: This matlab file should be placed in the same folder as the text
%files. Rename the files using BULK RENAME UTILITY software in the
format
%Text001, Text002...(Clue: Use Pad = 3 in numbering)
myFolder = 'C:\<Enter folder path here>’
filePattern = fullfile(myFolder, '*.txt');
txtFiles = dir(filePattern);
j=1;
for k = 1:length(txtFiles)
  baseFileName = txtFiles(k).name;
  fullFileName = fullfile(myFolder, baseFileName);
  fprintf(1, 'Now reading %s\n', fullFileName);
  fid = fopen(baseFileName, 'rt');
  textData =
textscan(fid,'%f%f%f',100,'headerlines',6,'delimiter','space');
  finaldata = cell2mat(textData);
  column3=finaldata(:,[3]);
  column3=column3';
  xlswrite('data.xlsx',column3,1, sprintf('A%d',j));
  fclose(fid);
j=j+1;
    end
```

Appendix D: Convergence Check for Bi-layer and Tri-layer Analytical Bending Models

To check the fidelity of the analytical model for bilayer and tri-layer laminates, convergence check was carried out by assigning SS400 matrix material properties to the bi-layer laminate layers. Similarly AA2024 material properties were applied to tri-layer laminate. The convergence plots for the stresses and relative thickness for Bi-layer C-T and C-C cases are shown in Figure 96 (a-c) and Figure 97 (a-c), respectively. The convergence plots for the stresses and relative thickness for tri-layer are shown in Figure 98 (a-c), respectively. The tangential stress shows very close convergence with the monolithic AA2024 stress profile. A 7.5% deviation in the peak compression radial stress value is observed between the monolithic and laminate for an inner radius of curvature (r_i) of 15 mm. Similarly, minor differences are seen in the relative thickness. The differences are mainly due to the minor variations in the decimal values obtained from the model computation at different stages. The model computation is primarily based on solving the volume constancy equation represented in terms of relative thickness, relative curvature and relative curvature of neutral fiber. Solution from the ordinary differential equation (ODE) yields the above three parameters that are subsequently used to derive the essential radii values. The radii values are utilized to obtain stress values. A three stage processing of data could most likely result in minor differences in computed stress and thickness values.

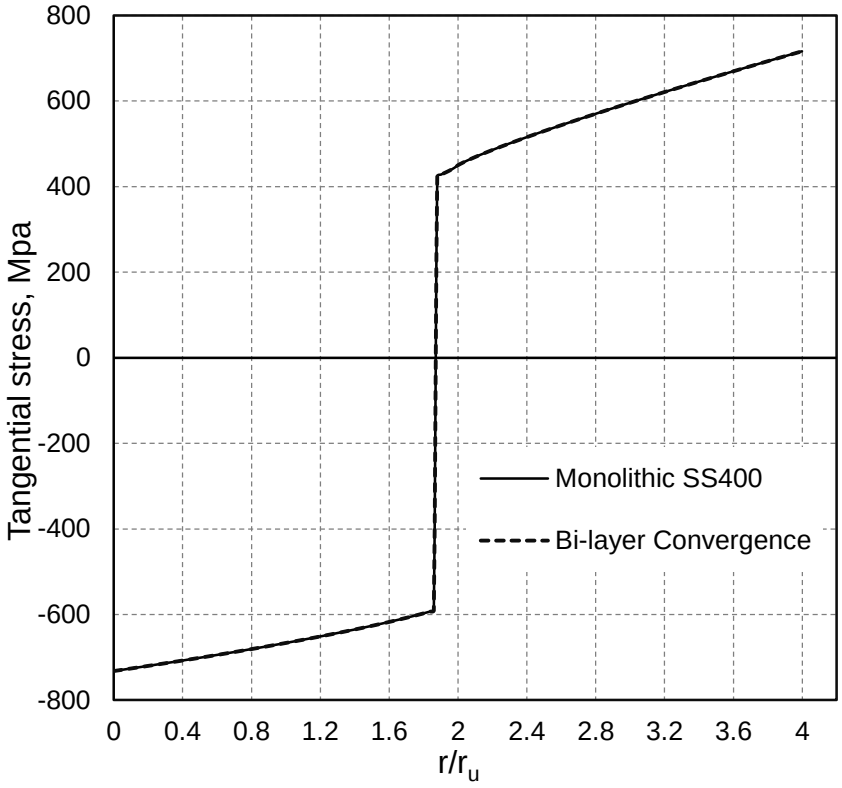
800
600
400
200
0
-200
-400
-600
-800
Tangential stress, Mpa
0
0.4
0.8
1.2
1.6
2
2.4
2.8
3.2
3.6
4
r/r_u
Monolithic SS400
Bi-layer Convergence

(a)

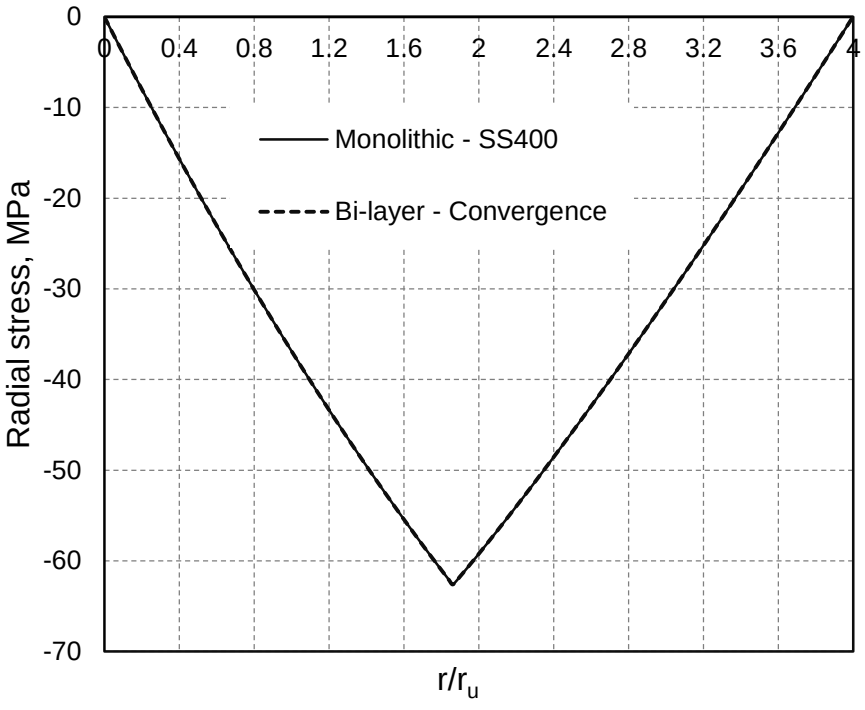
0
-10
-20
-30
-40
-50
-60
-70
Radial stress, MPa
0
0.4
0.8
1.2
1.6
2
2.4
2.8
3.2
3.6
4
r/r_u
Monolithic - SS400
Bi-layer - Convergence

(b)

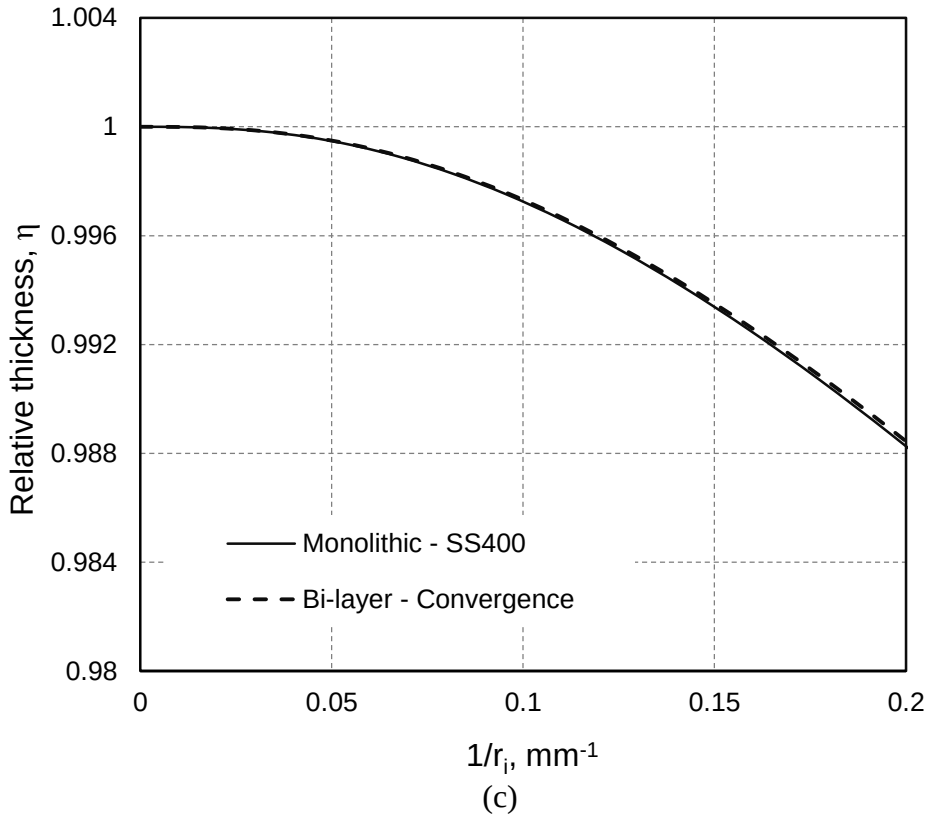

(c)

Figure 96. Convergence check plots for (a) tangential stress, (b) radial stress, (c) relative thickness for bi-layer C-T (AA1050/SS400) laminate and monolithic (SS400) sheets at r_i=25 mm.

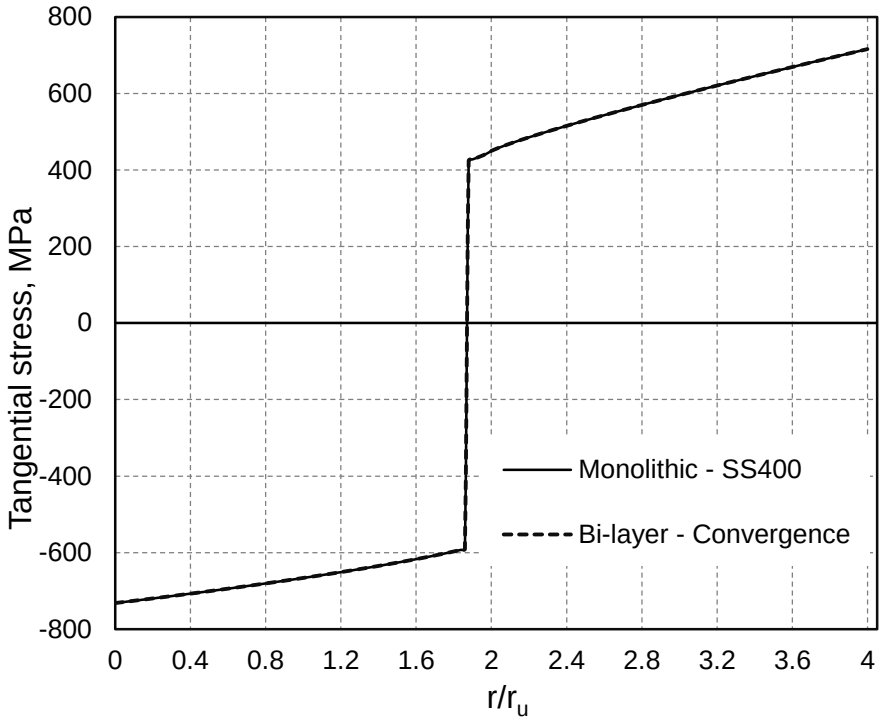
800
600
400
200
0
-200
-400
-600
-800
Tangential stress, MPa
0
0.4
0.8
1.2
1.6
2
2.4
2.8
3.2
3.6
4
r/r_u
Monolithic - SS400
Bi-layer - Convergence

(a)

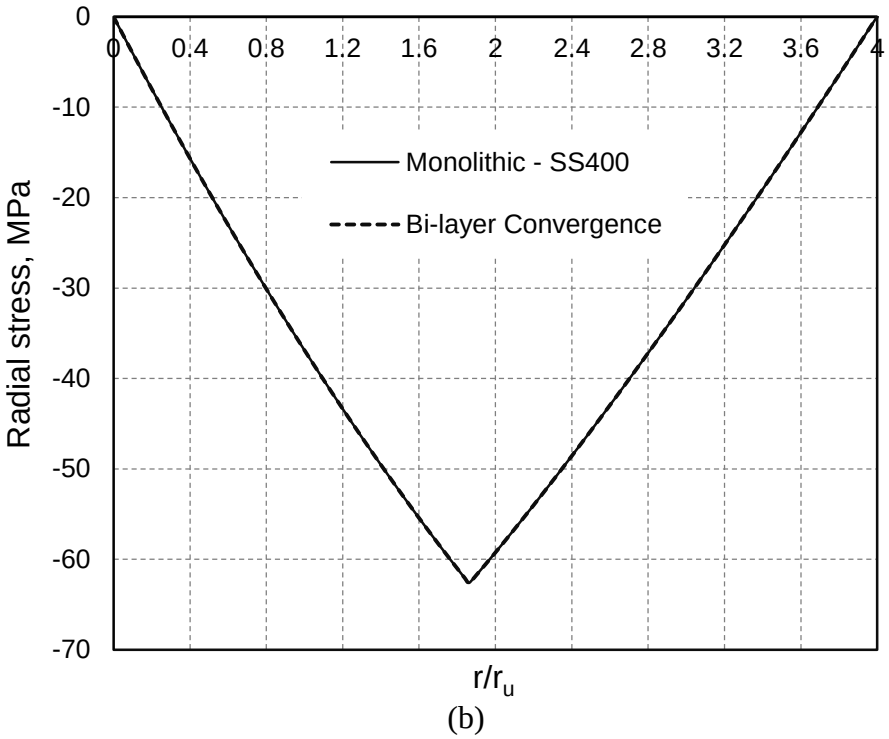
0
-10
-20
-30
-40
-50
-60
-70
Radial stress, MPa
0
0.4
0.8
1.2
1.6
2
2.4
2.8
3.2
3.6
4
r/r_u
Monolithic - SS400
Bi-layer Convergence

(b)

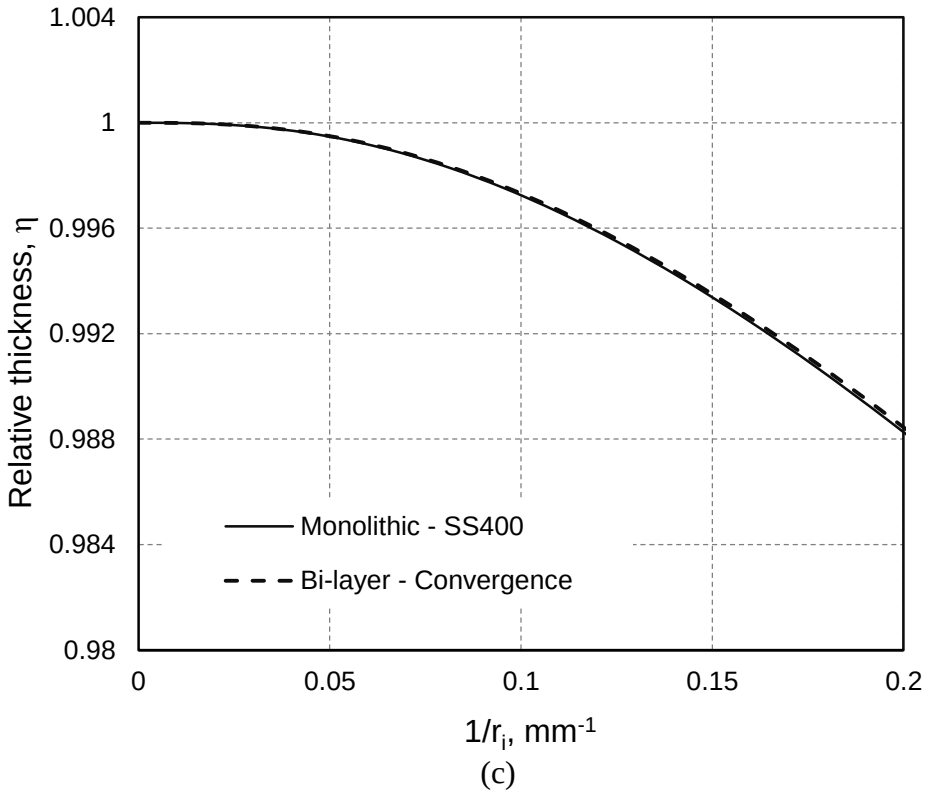

(c)

Figure 97. Convergence check plots for (a) tangential stress, (b) radial stress, (c) relative thickness for bi-layer C-C (SS400/AA1050) laminate and monolithic (SS400) sheets at r_i=25 mm.

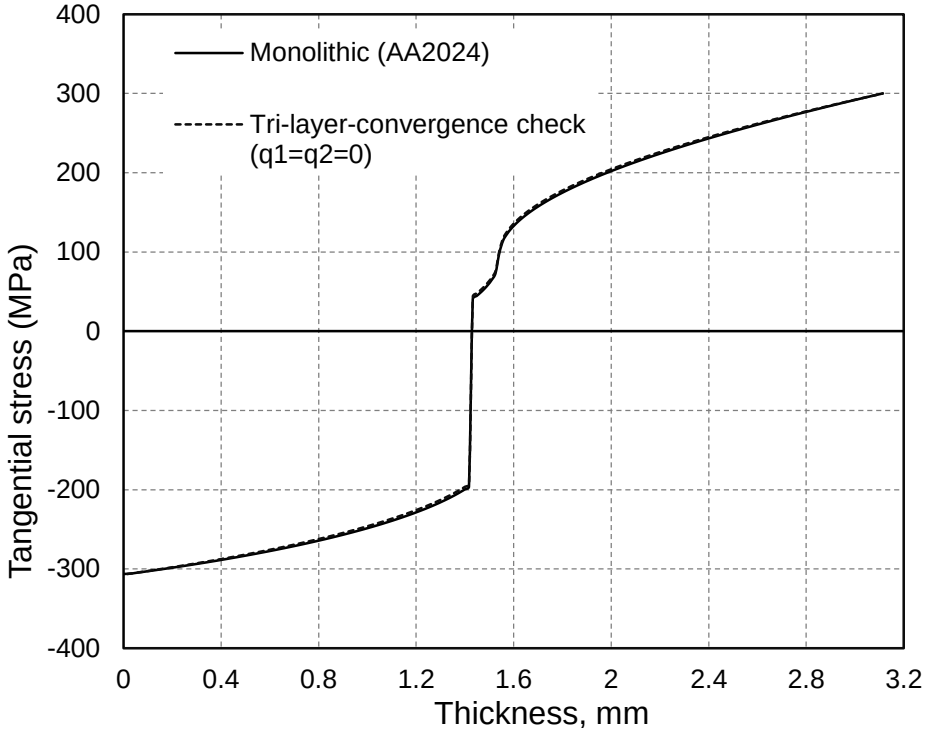
Monolithic (AA2024)
Tri-layer-convergence check
(q1=q2=0)
Tangential stress (MPa)
Thickness, mm
400
300
200
100
0
-100
-200
-300
-400
0
0.4
0.8
1.2
1.6
2
2.4
2.8
3.2

(a)

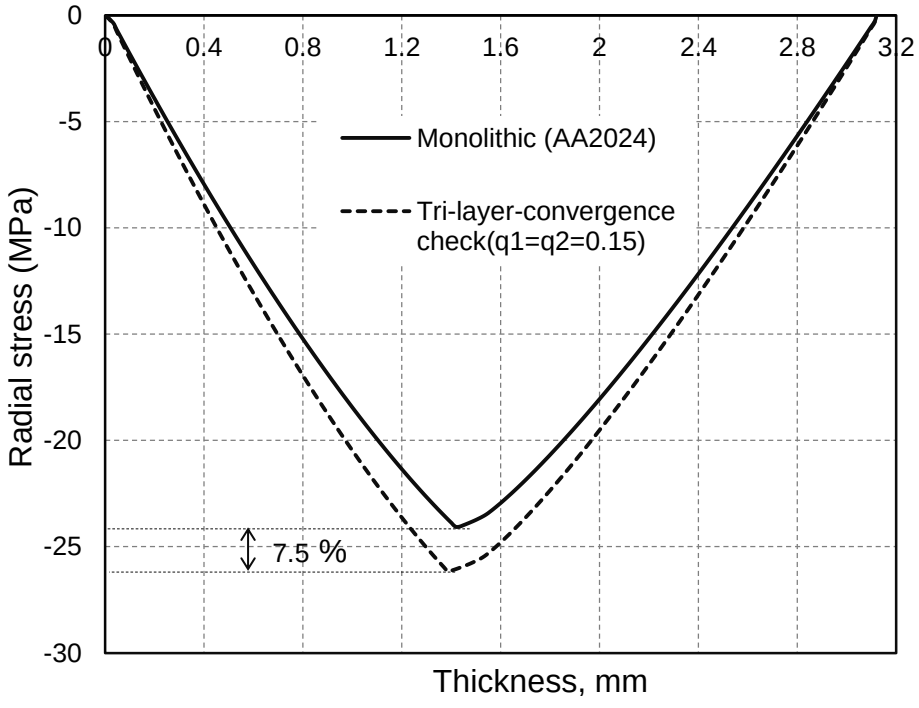
Monolithic (AA2024)
Tri-layer-convergence
check(q1=q2=0.15)
7.5 %
Radial stress (MPa)
Thickness, mm
0
-5
-10
-15
-20
-25
-30
0
0.4
0.8
1.2
1.6
2
2.4
2.8
3.2

(b)

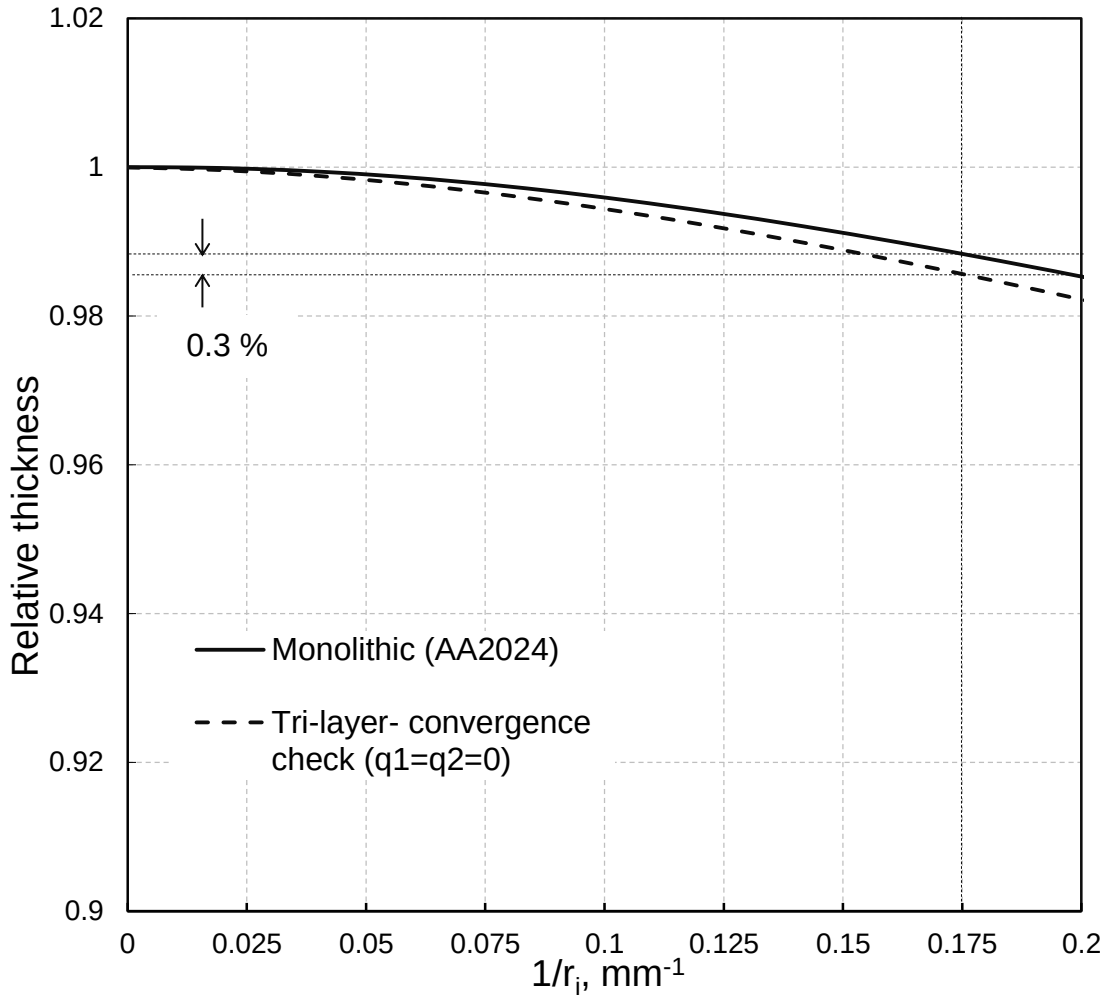

(c)

Figure 98. Convergence check plots for (a) tangential stress, (b) radial stress, (c) relative thickness for tri-layer (AA1100/AA2024/AA1100) laminate and monolithic (AA2024) sheets at r_i = 15 mm.

Appendix E: Error Analysis on the Analytical Model for Pure Bending Characteristics

Error analysis was conducted on analytical pure bending model to check the effect of tensile data curve fit parameters on the bending characteristics. The tensile data curve fit parameters for Ludwik hardening law for AA2024 specimen is shown in Table 10. The curve fit was based on 95% confidence limits. The tensile plot of AA2024 with Ludwik parameters and error bars are shown in Figure 99(a). The effect of upper and lower bound values of the confidence limits on the bending characteristics are shown in Figure 99(b-d) with error bars on the plots. It was observed that the 5% variation on the hardening parameters showed a maximum error of ±1.84 MPa on the tangential stress, ±0.12 MPa on the radial stress and ±0.00018 on the relative thickness plots, respectively.

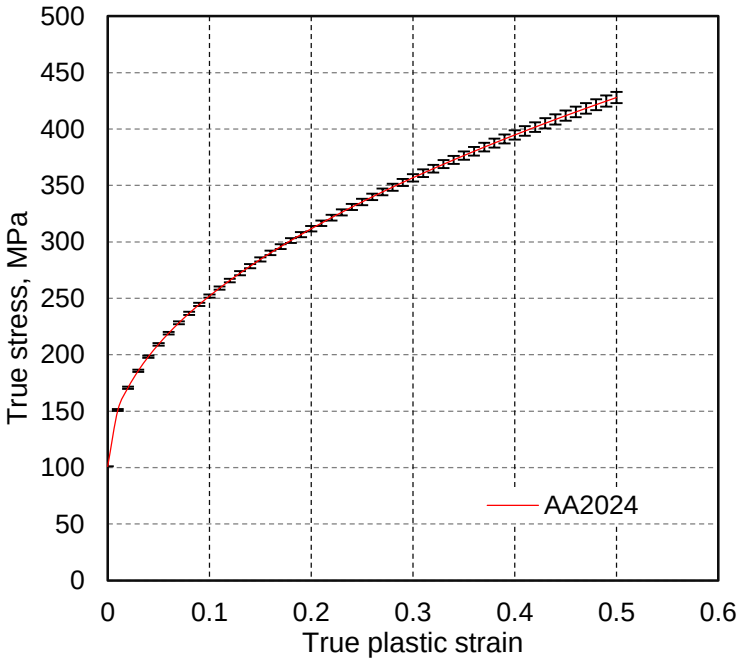

(a)

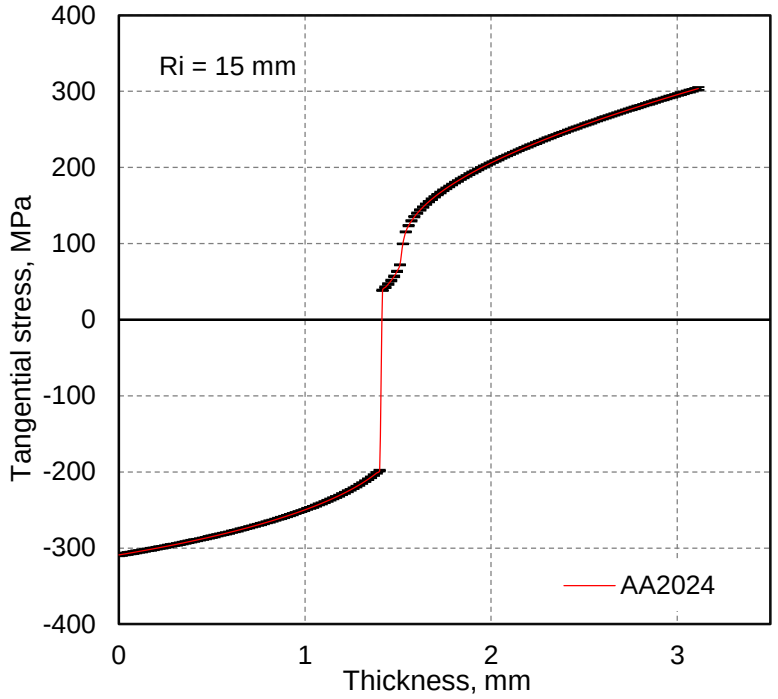

(b)

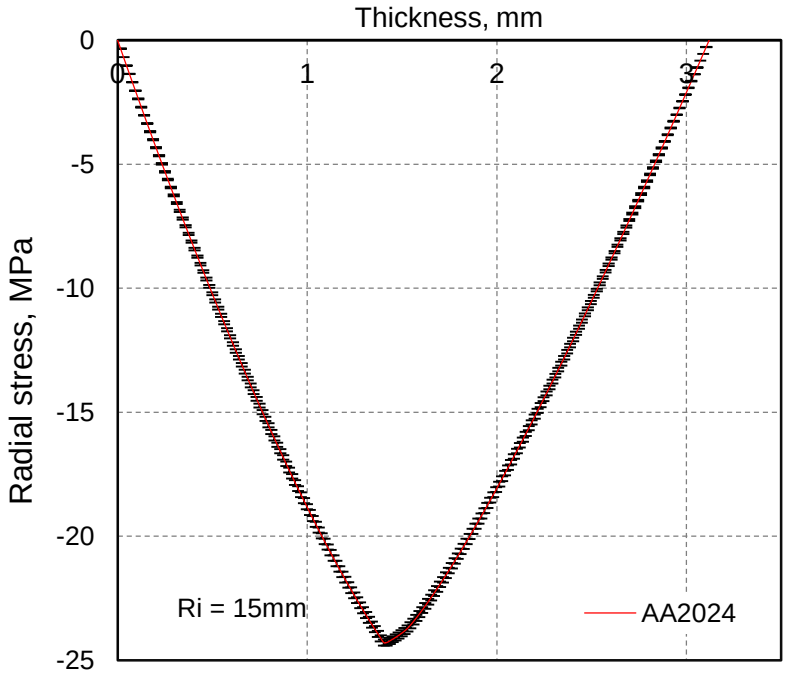

(b)

(figure continued on next page)

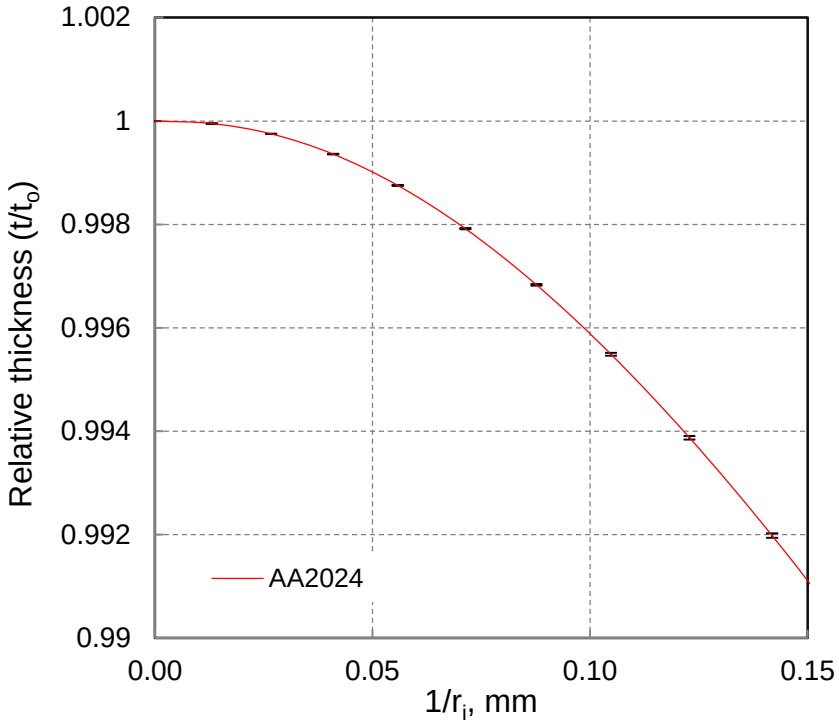

(d)

Figure 99. Error analysis on bending characteristics based on Ludwik hardening properties with 95% confidence limits, (a) tensile plot for Ludwik hardening parameters, (b) tangential stress, (c) radial stress and (d) relative thickness plots.

Appendix F: Mesh Dependency Study on FE-MK Bending Model

To study the effect of mesh dependency on the results, three different mesh sizes and element numbers across the specimen thickness were applied on SS400 monolithic specimen. The mesh element sizes (see Figure 100(a)) chosen are as follows, (i) uniform coarse mesh of 0.4×0.2 (all dimensions in mm) and 20 elements through the thickness, (ii) uniform fine mesh of 0.1×0.1 and 40 elements through the thickness and (iii) biased mesh of bias ratio 15 with 20 elements and largest element dimension of 1×0.2 at the end and smallest element dimension of 0.08×0.2 at mid-section through the thickness. The tangential stress, tangential strain and relative thickness taken at mid-section of width for different mesh sizes were compared for convergence (see Figure 100(b-d)). As suggested by the simulation results and for computational efficiency, the third type of mesh with bias ratio 15 was used in all simulations.

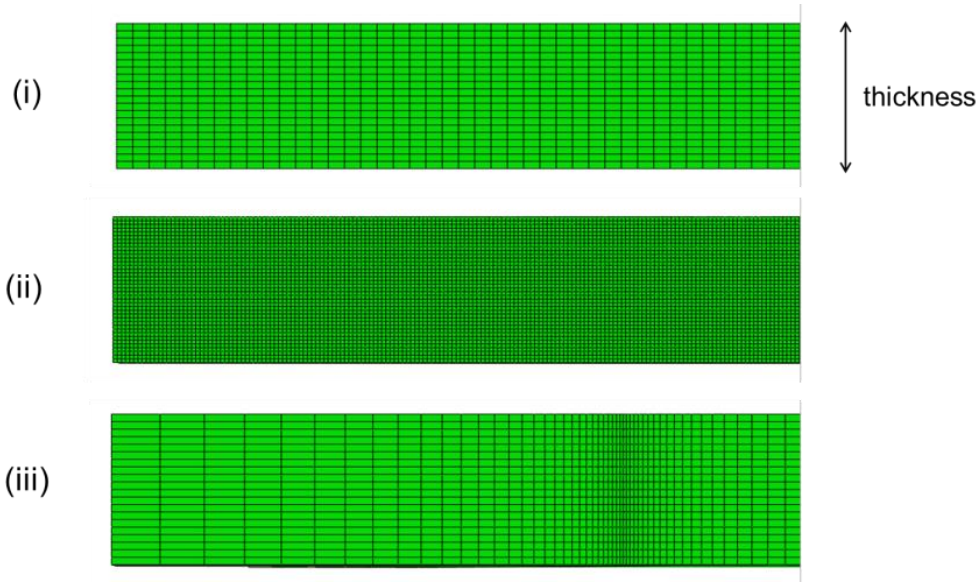

(a)

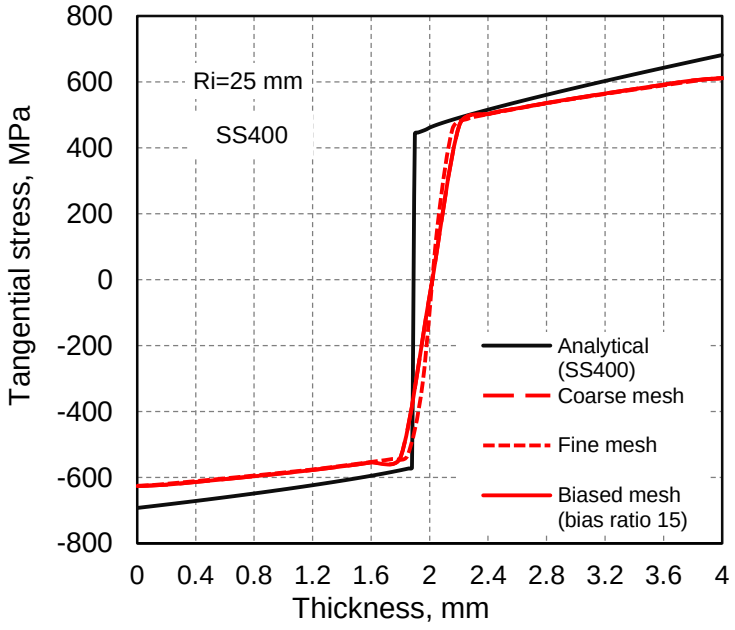

(b)

(figure continued in next page)

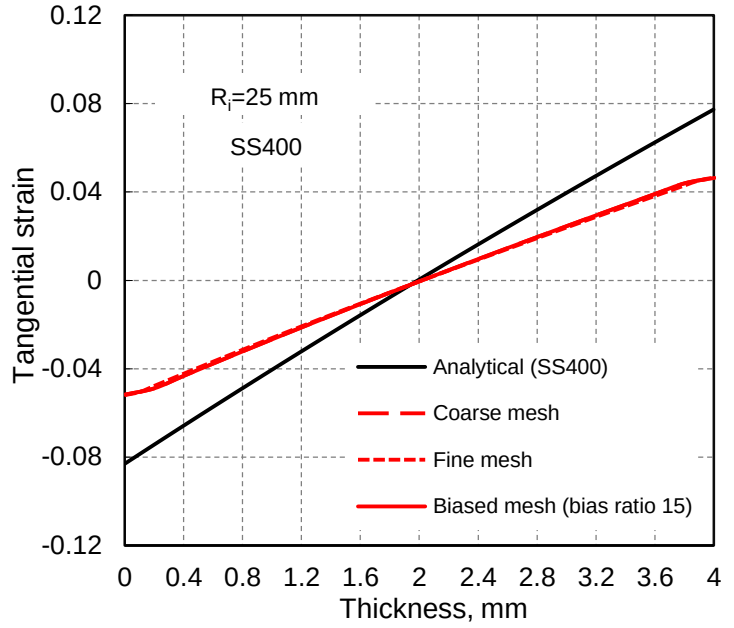

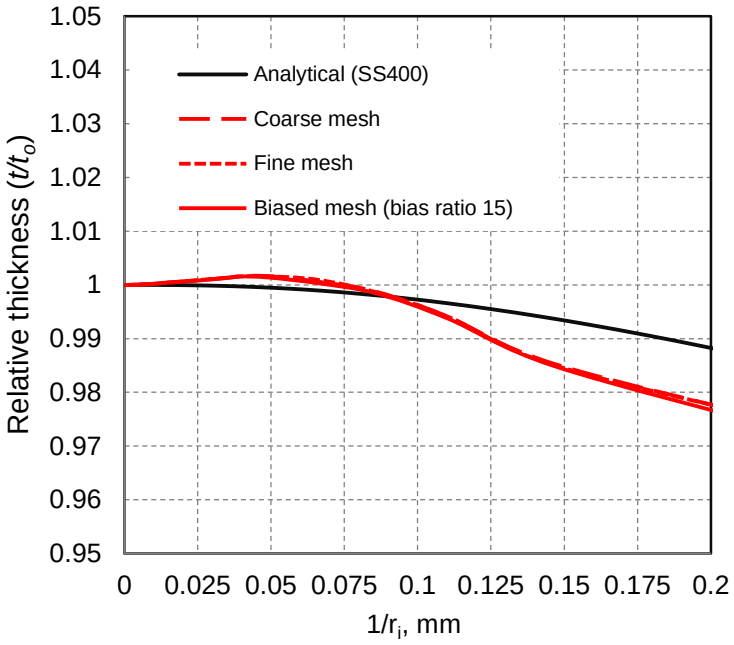

(d)

Figure 100. FE model specimen section for different mesh sizes (i) uniform coarse mesh (0.4 × 0.2 (dimensions in mm)), (ii) uniform fine mesh (0.1 × 0.1) and (iii) biased mesh (bias ratio 15); comparison of through thickness (b) tangential stress, (c) tangential strain and (d) relative thickness for various mesh sizes with analytical model on SS400 monolithic sheet.